University of Trento

department of Physics

# Slow dynamics in colloids and network glasses close to the structural arrest: the Stress-relaxation as a root to equilibrium


*Tutor:*
Prof. Giulio Monaco

*Author:*
Francesco Dallari

# Contents

# Chapter 1

# Introduction

Microscopically disordered materials are at the core of an increasing number of new material technologies, but crucial limitations in their applications come from the physical aging of their properties and the extreme sensitivity on the system's history, which stem from their intrinsically out-of equilibrium nature. A clear understanding of the aging phenomenon, together with the interplay between phenomena that take place at different length-scales are still lacking. In this Thesis the slow dynamics of disordered systems is investigated at different length-scales ranging from the $\mu m$ length-scale probed in optical experiments to length-scales of few $\dot{A}$ probed in wide angle X-ray experiments. The time evolution of the probed out of equilibrium dynamics is thoroughly studied in different glasses exploiting the multi speckle photon correlation technique with different sources.In all probed materials a deep connection emerges between the microscopic dynamics and the relaxation of the stresses that have remained trapped in the glass after its production.
The investigated materials are a set of strong glass-formers (materials that can be found in a wide variety of common glassware) and colloidal suspensions at high volume fractions in an arrested state. The latter class of materials are known as soft glasses and in recent years they are earning great interest and can be found in a lot of industrial products (e.g. wall paint, ink, chocolate) or in production processes (e.g. ceramics). A great deal of the success of colloidal and soft systems in industrial and technological fields comes from the possibility to finely tune the physical and chemical properties of these classes of materials. Being able to effectively know the out-of-equilibrium structural properties of these systems will grant us the possibility to predict the evolution of the several physical properties. Colloidal glasses share with their atomic counterpart the fact of being strongly out of equilibrium disordered systems, but their internal dynamics

is characterized by faster than exponential relaxations and a linear growth of the characteristic relaxation time with the probed length-scale. These latter features have been related to purely stress-release mechanisms and have been observed in many experiments on very different systems: colloidal glasses and gels [1, 2], polymers [3, 4], foams [5], aerogels [6], in metallic glasses [7], and simulations [8].
The fundamental questions that will be tackled in the course of this Thesis will be:

i) What are the effects of the stress-relaxation mechanisms on the dynamical properties of a generic disordered system?

ii) Does stress relaxation proceed microscopically through rupture events randomly distributed in the material, or rather we have to imagine massive displacements occurring through avalanche-type events? Is it possible to associate a length-scale over which such events can occur? Is it possible to know how many particles are involved in a single event?

iii) Is there any general trend in the evolution of the stress dissipation mechanism?

iv) What are the mechanisms at the basis of the internal dynamics developing in different disordered systems?

v) How does the presence of internal stresses affect the time evolution of other dynamical properties?

vi) Is it possible to describe the parameters of the aging process in terms of materials and/or of preparation protocols?

To answer these rather general questions this Thesis is structured as follows: a first general introductory part followed by three chapters focused on experiments carried out during my PhD, all closed by a final chapter where the main results and common traits are summarized.

More in detail, the second chapter is devoted to build a broad scientific background on glasses and colloidal systems. Emphasis is given to the description of the dynamical properties of disordered materials, and in particular to two of the key features of glassy materials, namely aging and dynamical heterogeneities. Both of these properties have quite self explicative names: the first refers to the fact that the physical quantities of a glass explicitly depend on the time elapsed since the formation of the

glass itself; the latter refers to the existence of a microscopic length scale, over which the material's dynamics ceases to be homogeneous.
The third chapter describes the techniques adopted in the experiments reported in this Thesis, focusing on the working principles of photon correlation and on the interpretation of the corresponding autocorrelation matrices. Here the relations that link the intermediate scattering function to the autocorrelation function of the intensity scattered from a sample illuminated with a coherent light source are explained. In this chapter the working principles of the algorithms developed during my PhD time in order to extract the physical quantities from the raw output signals are also reported.

The fourth chapter is devoted to the presentation of the aging of a strong network glass-former. The results concern the diboron trioxide ($B_2O_3$) measured in the glass transition region. Diboron trioxide is a well known glass former with a high viscosity and a very low inclination to crystallize. In this case the measurements where taken at a fixed angle using a visible light source in the Structure and Dynamics of Complex Systems (SDSC) laboratory in Trento. Prior to the production of the out of equilibrium glass, the dynamical properties of the equilibrated undercooled liquid of $B_2O_3$ have been investigated in a wide range of temperatures above and below the glass transition temperature. The measurement of the evolving properties of the aging glass have been carried out with a multi-speckle set-up. The data collected during the aging process have been then analysed and interpreted using models that take into account the macroscopic processes that can occur in a real life glass. At the end of this chapter is discussed how the presence of the aging process affects the dynamical susceptibility.

The fifth chapter presents the results concerning colloidal systems. Among the wide family of colloids, the system composed by $SiO_2$ nanoparticles suspended in a water-lutdine 2,6 solution has been chosen. The advantages in choosing this particular material is that it is possible to tune the inter-particle interaction changing the sample's temperature switching from repulsive hard spheres to sticky attractive particles. The static and dynamical properties of different colloidal systems have been investigated using small angle X-ray scattering (SAXS) and X-ray photon correlation (XPCS) during an experiment at the European Synchrotron Radiation Faculty (ESRF). The SAXS experiments performed using a fast readout, photon-counting pixel detector system (Maxipix), grants the access to a wide range of exchanged wave vectors (and thus length scales). Choosing the appropriate size of the colloidal particles it has been possible to probe more effectively the dynamics

at length scales both larger and smaller than the inter-particle distance. Additional information of the dynamical properties have been obtained using a multi-speckle photon correlation spectroscopy (MPCS) with a visible light source. Among the characteristic features of colloidal systems there is the fact that the dynamical heterogeneities can reach large enough dimensions to be probed in standard SAXS experiments. The dependence of the structural relaxation process on the scattering vector has been studied in detail, providing informations on the nature of the process itself. Interestingly, a clear dependence of the structural relaxation process on the procedure used to prepare the system has been observed, giving a clear hint on the connections between this dynamics and the internal stresses accumulated in the glass during its formation.

In the sixth chapter the X-ray photon correlation spectroscopy (XPCS) results of measurements performed on network glasses are reported, namely lithium borate $(Li_2O)_{0.5}(B_2O_3)_{0.5}$ and silica $(SiO_2)$. It has been observed that, for oxide glasses, the X-ray photons trigger a particular atomic motion resulting in a complete structural rearrangement at a microscopic level. This rearrangement, that cannot be explained by the simple heating of the scattering volume due to X-ray absorption, is quite anomalous, since for these glasses it can be detected up to the glass transition temperature while at higher temperatures this induced dynamics becomes slower than the structural relaxation one. This effect is, by its very nature, extremely dependent on the instrumental details of the performed experiment, and in order to compare different experiments a quantity describing the number of particles that have been set in motion after the absorption of one X-ray photon is defined. To understand this phenomenon, a detailed scattering wave vector dependence study of the induced dynamic has been carried out. In this Thesis, sets of experiments performed in a wide angle X-ray scattering (WAXS) XPCS and SAXS experiments are reported. All these experiments have been performed at room temperature, and have been carried out at two different beamlines in two different large scale facilities, ESRF and PETRA III. It is interesting to observe that the results obtained in these studies appear to be very similar to those obtained for the dynamics of colloidal glasses, pointing to a similar role of internal stresses in both cases.

The seventh chapter is dedicated to the conclusions of this PhD Thesis, and puts the results of the previous chapters in a more general and common framework.

# Chapter 2

# Glasses and colloids

## 2.1 Glasses and disordered systems

Glasses and disordered systems are ubiquitous materials that can be found in a wide variety of scientific and technologic fields. In nature, we can find viterous systems in the most disparate situations, from geological structures to biological systems. Also, since glasses are the first artificial materials ever produced by humankind [9], we can find them in nearly every artifact, from buildings to automotive, and recently a steady increasing interest in glassy physics came from the pharmaceutical sector [10, 11, 12, 13]. But what is exactly a glass? From a microscopical point of view the structure of a glass is no different from the structure of a liquid while its macroscopic properties are more similar to solid crystalline materials. We can use Tammann's words defining a glass as *a liquid that has lost its ability to flow* [14], this definition is strongly related to the most common way to create a glass that is the melt-quench technique. This technique, known since prehistoric times, starts with the material in its liquid state above the melting temperature ($T_m$) and then, thanks to a "fast enough" cooling rate the phase transition can be avoided and the material remains in the liquid state even at temperatures $T < T_m$. A so called undercooled liquid is obtained, and its viscosity will start to increase as the temperature is lowered and eventually a glass will be obtained. But what does a "fast enough" cooling rate means? A precise answer to this question obviously depends on the material under study and on the nucleation and growth of the crystalline phase for that material. However, it is possible to provide a general and extremely simplified description of the phenomena occurring during vitrification, but before going into that , we have firstly to introduce some properties of glass-forming liquids.

### 2.1.1 Relaxation times, strong and fragile glasses

We have seen that between what is called undercooled liquid and what is called glass there isn't a clear cut boundary like in conventional phase transitions. Here we have a liquid material that behaves more and more like a solid. It is possible to gain some more insight on this topic employing a simple model developed by Maxwell in the description of the visco-elastic properties of liquids [15]. Starting from the idea that applying a shear strain $\gamma$ to our sample, we can find both elastic (solid-like) and viscous (liquid-like) response, we get a shear-strain relation given by

$$\dot{\gamma} = \dot{\sigma}/G_\infty + \sigma/\eta$$

Here $\sigma$ is the shear stress, $G_\infty$ is the infinite frequency shear modulus (the elastic response) and $\eta$ is the viscosity (the liquid response). For a step like strain ($\gamma(t = 0^-) = 0$,$\gamma(t = 0^+) = \gamma_0$ ), the previous equation can be easily solved in

$$\sigma = G_\infty \gamma_0 e^{-\frac{G}{\eta}t} = \sigma_0 e^{-t/\tau}$$

Where

$$\tau = \eta/G_\infty \tag{2.1}$$

The quantity $\tau$ is called the structural ($\alpha$) relaxation time and it tells us the time required by our system to completely change its internal structure after a small external perturbation or a thermal fluctuation. For a full-fledged liquid this relaxation time is of the order of few picoseconds, e.g. [16], while in undercooled liquids $\tau$ grows exponentially with the inverse of temperature, and for systems in the glassy state it can easily reach geological timescales [17, 18]. Usually for a given system a glass transition temperature ($T_g$) is defined as the temperature in which $\eta(T_g) = 10^{12}\mathsf{Pa}\cdot\mathsf{s}$ or, since G has typical values in the range $10^9 - 10^{10}\mathsf{Pa}\cdot\mathsf{s}$, another widely used definition for $T_g$ is $\tau(T_g) = 100$s, in the following chapters of this Thesis the latter definition will be employed. For most glasses the temperature dependence of $\tau$ can be described by a simple Arrhenius law

$$\tau(T) = \tau_0 e^{\frac{E}{k_b T}} \tag{2.2}$$

However, as can be seen in fig 2.1, the equation 2.2 cannot describe all the experimental data and thus a more flexible formula, given by Vogel-Fulcher-Tammann, is employed [19, 20, 21]

$$\tau(T) = \tau_0 e^{\frac{B}{k_b(T-T_C)}} \tag{2.3}$$

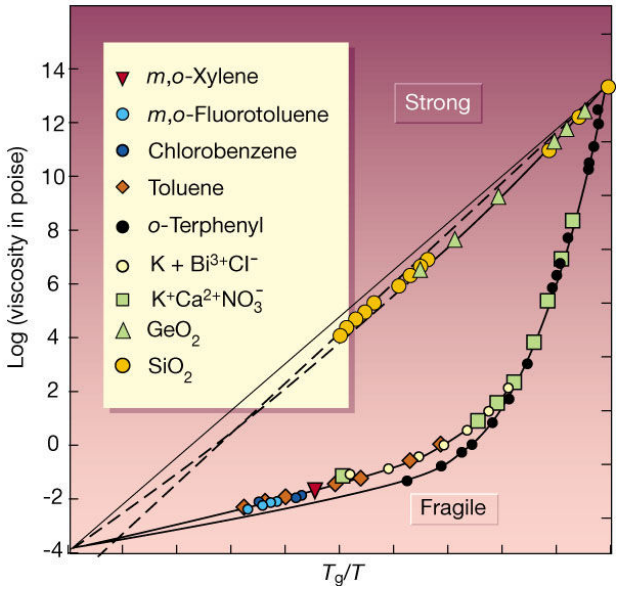


Figure 2.1: $T_g$ rescaled Arrhenius representation of liquid viscosities showing some representatives of the strong and fragile extremes. Strong glasses follow a linear behaviour, indicating an activation energy independent of temperature ($E \propto \partial(log(\eta))/\partial(T_g/T)$) and thus a constant slope. Conversely, the fragile glasses manifest a super-Arrhenius behaviour with an activation energy that increases as $T \to 0$

Equation 2.3 suggest the existence of a divergence at a finite temperature $T_c$, however this equation generally fails to correctly describe the data a low temperatures, predicting too large relaxation times [22, 23, 24].
From graphs like fig 2.1, also called Angell plots, we can recognize two "families" of materials called "strong" and "fragile" glass formers (or strong and fragile liquids). The former are materials that follow quite closely the simple Arrhenius behaviour while the latter strongly deviate from it. Typically, strong liquids are composed of networks of covalently bonded atoms (e.g. $SiO_2$, $GeO_2$ and $B_2O_3$ are typical strong liquids), while on the other hand, fragile liquids are represented by systems in which the inter-particle interactions are due to non-directional dispersive forces such as van der Waals attraction. It is possible to quantify the fragility of a liquid introducing the fragility index $m$ [25], defined as the slope of $log_{10}(\tau(T_g/T))$ when $T = T_g$

$$m = \lim_{T \to T_g} \frac{\partial \log_{10}(\tau)}{\partial(T_g/T)}$$

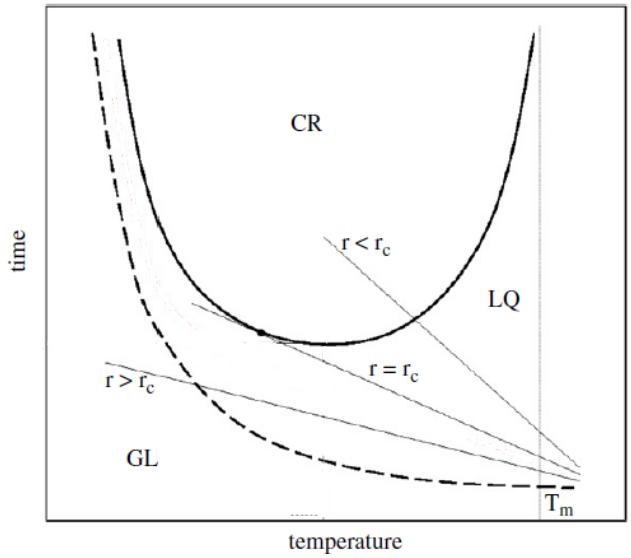


Figure 2.2: example of a time temperature transformation diagram for a glass former. The continous line represents the nucleation time required to the system to initiate the crystallization. The dashed line represents the relaxation time of the liquid, that rise sharply as the temperature is lowered. The straight lines represents three possible thermal treatments at different cooling rates for a material prepared in its equilibrium liquid phase (LQ) above the melting temperature $T_m$ . If the cooling rate is not fast enough ($r < r_c$), we cross the nucleation line and obtain a crystal(CR). Conversely, for $r \geq r_c$, the sample will maintain its liquid state and eventually, when the dashed line is crossed, it will fall out from its metastable equilibrium and we will obtain a glass (GL). Image taken from [26]

### 2.1.2 Approaching the glass transition

With the concept of relaxation time, we can now interpret the graph of fig. 2.2, in which the x axis represents the system's temperature and the y axis the time elapsed since the beginning of our thermal treatment. The "U" shaped continuous line represents the boundary over which the nucleation and growth of a crystalline phase inside the bulk will occur. If with our thermal protocol we cross this region we will end up with a crystalline (or partially crystalline) sample, while for thermal protocols with cooling rates $r$ greater than a certain critical value (namely the lowest cooling rate for the crystal negation in fig 2.2 labelled as $r_c$), then the phase transition is avoided and the system retain its amorphous structure. From the undercooled liquid point of view, the crossing of $T_m$ does not carry any

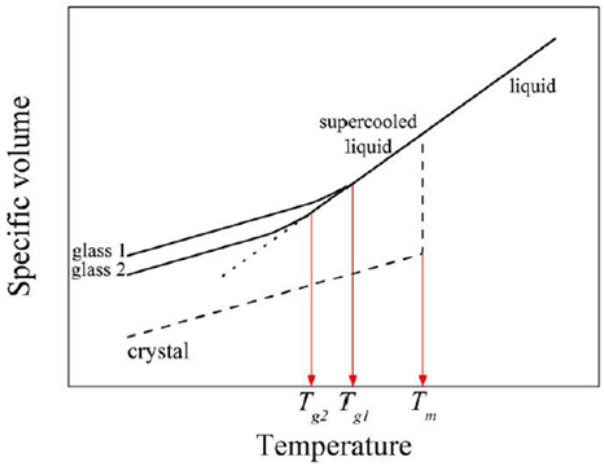


Figure 2.3: Example of the specific volume change for the same material following a rapid cooling and a slower one. The latter thermal treatment produces a glass with a lower $T_g$ and physical properties closer to those of the crystalline phase.

apparent consequence, the microscopic structure is still the same and the thermodynamic properties change continuously. This can be seen from the behaviour of the system's specific volume in fig. 2.3, where it is shown that the system is no longer in thermodynamic equilibrium (represented by the crystalline phase) but instead is in a metastable condition. Despite that, the situation remains unchanged, and the system behaves like a liquid down to a certain temperature range where it starts to slowly change switching to a more solid-like behaviour. This temperature interval is called the glass transition region, identified by the glass transition temperature $T_g$ whose exact value depends on the physical quantity employed to characterize the system. Moreover as can be seen from fig. 2.3, even for the same observable $T_g$ alone cannot be employed to completely characterize a glass, since the location of the glass transition region could change for different cooling rates, the lower the cooling rate the lower $T_g$. This feature can be qualitatively explained looking again at fig. 2.2; recalling that the atomic configurations that can be accessed by a liquid are dictated by its temperature, and $\tau$ is the time required by the system to change from a certain configuration to another, it can be seen that different cooling rates intercept the dashed curve representing the structural relaxation times at different temperatures. Crossing the $\tau(T)$ line with our thermal protocol means that our system will eventually fail to rearrange its internal structure for the new temperature and it will progressively fall out of equilibrium. Once the system cannot

recover anymore the equilibrium condition in an accessible timescale, it is said to be a glass. The other physical properties, in the example of fig. 2.3 the free volume, will be partially determined by the last temperature in which the system was at equilibrium. It has to be noticed that in practice for real glasses the location of the glass transition is not so arbitrary; since the growth of $\tau(1/T)$ is exponential, unless one decides to adopt a quite particular thermal protocol, all the undercooled liquids will leave the equilibrium condition in the same temperature range, typically temperatures where $\tau(1/T) \in [10^2 s, \quad 10^3 s]$.
Here we have encountered another key property of the glassy state, which is the importance of the history of the sample for the determination of the physical properties. We will see this feature and other related properties more in detail later in this and other chapters of this Thesis.

### 2.1.3 Energy landscape

Regardless of the classification of a glass former, we can see from equations 2.3 and 2.2 that the structural relaxation is always an activated process, in which the system needs to overcome energy barriers in order to rearrange its internal structure. A useful framework for the qualitative description of the glassy phenomenology is provided by the energy landscape [27]. This is the name generally attributed to the glass potential energy that for a system composed by $N$ particles is $V((r_1), \ldots, (r_N))$, where the vectors $(r_i)$ specify the degrees of freedom of particle $i$ (position, orientation, vibration etc... ). Strictly speaking, the energy landscape is a multidimensional surface. Even with the simplest case of $N$ identical particles with only translational degrees of freedom, $V$ is a $(3N+1)$-dimensional object. The concept of energy landscape, proposed for the first time by Goldstein [28], has been successfully applied in many fields of complex systems, such as protein folding [29, 30], mechanical properties of glasses [31, 32]and the dynamics of supercooled liquids [33]. For our present purposes it is sufficient to consider a simplified version of this multidimensional surface, i.e. as can be found in [27], where all the $3N$ configurations are projected on a single one-dimensional axis as depicted in fig. 2.4. The energy landscape can give us a better understanding of the distinction between strong and fragile glass formers. For a strong glass, the activation energy remains substantially unchanged for every temperature, indicating that the mechanisms at the basis of structural rearrangements of strong glass formers, presumably the breaking and reformation of covalent bonds, are the same in the whole energy landscape [34]. In contrast, a fragile glass deviates remarkedly from the simple Arrhenius behaviour, showing

an effective activation energy ($E_{eff} = \partial \log(\tau)/\partial(1/T)$) that can increase up to an order of magnitude. This suggests a strong heterogeneity in the basins of a fragile glass. The picture that we can infer from the behaviour of $E_{eff}$ is that at high temperatures, the systems can relax hopping over small potential barriers with the rearrangement of a relatively small number of molecules. Lowering the temperature, the barriers increase meaning that an increasing number of particles is needed for the relaxation. These differences between strong and fragile behaviour imply a corresponding topographic distinction between the two prototypical landscapes as illustrated in the bottom of fig. 2.4. Strong glasses will be characterized by a single mega-basin with smaller local minima, while the fragile systems will be described by a distribution of well separated mega-basins.

## 2.2 Structure of a disordered system

A disordered system, by its very definition, does not have the long-range order of crystalline materials and obviously cannot be described using a simple set of elementary units and symmetry groups. Nevertheless, this does not mean that the microscopic structure is completely unknowable or lacking general rules. there exists in fact, a set of observables that can be accessed both theoretically and experimentally, characterizing the average structure in the proximity of a given molecule.
The first quantity that we want to introduce is the number density of a disordered system $\rho^{(n)}(\mathbf{r^{(n)}}))$, defined as the probability to find $n$ particles in the element of volume $d\mathbf{r^{(n)}}$. The simplest expression for this quantity is $n = 1$, which is exactly the usual definition of density, and thus for an homogeneous system we have $\rho^{(1)} = N/V$, where $N$ is the total number of particles and $V$ is the total volume. Despite its importance $\rho^{(1)}$ does not carry much information about the details of the local environment in which our atoms or nanoparticles are living. The complete and exact description of a disordered system is given by the knowledge of all the $\rho^{(n)}(\mathbf{r^{(n)}}))$ and, strictly related to them, in another important set of observables, by the *particle distribution functions* defined as

$$g^{(n)}(\mathbf{r^{(n)}}) = \frac{\rho^{(n)}(\mathbf{r^{(n)}})}{\rho^n}$$

The particle distribution functions measure the extent to which the structure of a fluid deviates from complete randomness [39]. Luckily, this information is often already embedded in the pair density function $\rho^{(2)}(\mathbf{r_1}, \mathbf{r_2})$ and the pair distribution function $g^{(2)}(\mathbf{r_1}, \mathbf{r_2})$, which for isotropic systems are function

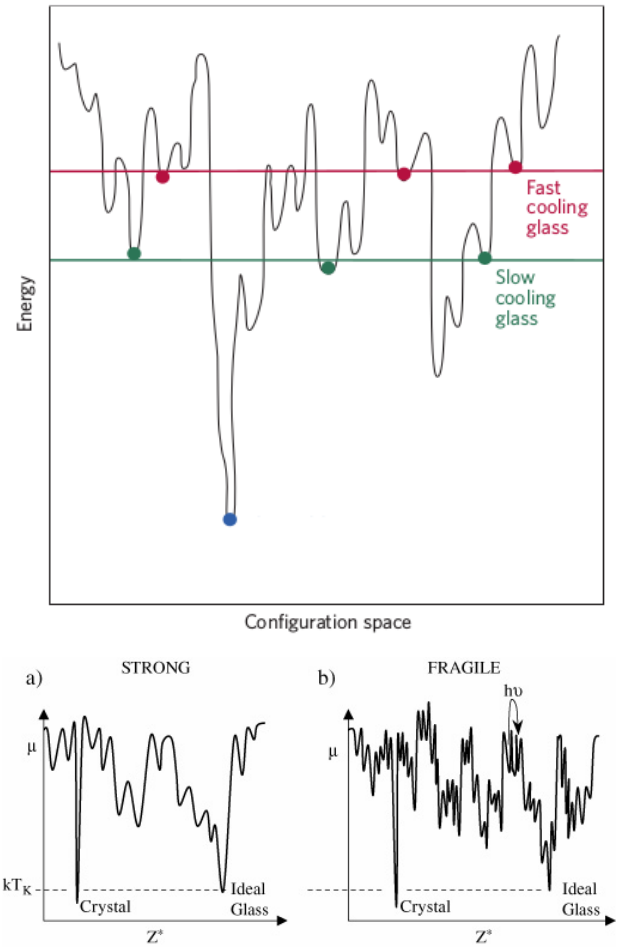


Figure 2.4: top: representations of the energy landscapes for a glass system. On the left, example of the configuration accessed by glassy system after different cooling rates. The slower the liquid is cooled, the longer the time available for configurational sampling at each temperature, and hence the colder it can become before falling out of the liquid-state equilibrium. Consequently $T_g$ increases with cooling rate [34, 35, 36]. Image adapted from [37]. Bottom: qualitative representations of the expected morphology for a fragile (right) and a strong (left) glass. Image taken from [38].

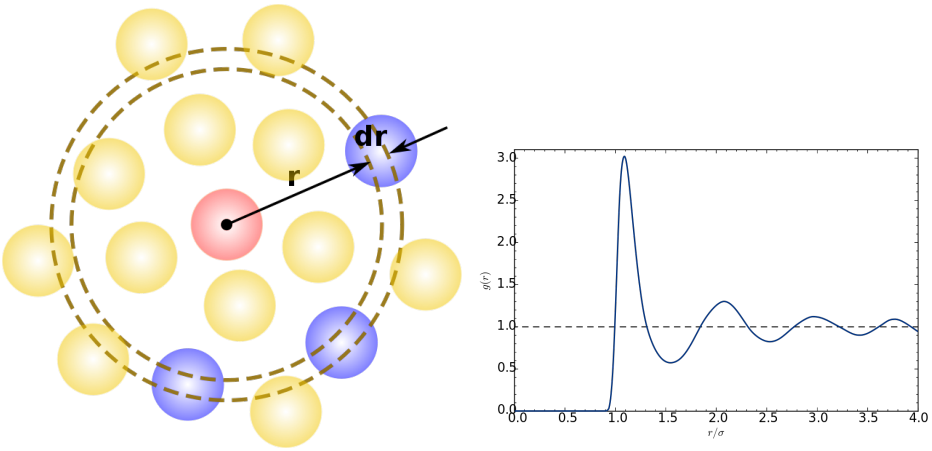


Figure 2.5: representation of a disordered system (left) and of a pair correlation function (right). In the former figure we can observe an example of the meaning of the coordination number, which is the number of particles at a given distance from a reference one (in red). The average over all the possible configurations will generate the pair correlation function.

only of the separation $r$ between particles 1 and 2 at positions $\mathbf{r_1}$ and $\mathbf{r_2}$ ($r = |\mathbf{r_1} - \mathbf{r_2}|$). The distribution function is then simply written as $g(r)$ and is often called *radial distribution function* and basically tells us what is the probability, starting from a given particle to find another particle at distance $r$. In fig. 2.5 we can see an example for a computed $g(r)$. This quantity tells us how much order is still present in the glass. The main characteristics of this function common to all systems, are that $g(r) = 0$ for $r < \sigma$, where $\sigma$ is the radius of a single particle. This means that there cannot be overlap between particles. In the opposite limit $g(r \to \infty) \to 1$, which corresponds to the recovery of the macroscopic density for large separations. At distances of few atomic units, we can see the presence of a certain number of peaks, progressively smaller and broader with $r$. The integral in spherical coordinates of the area under each of these peaks can tells us the average number of molecules at a given distance from the origin (coordination number).

To create a model of the disordered system's structure, we need to define a hierarchy of correlation functions, called *direct correlation functions* $c^n(\mathbf{r^n})$. We are interested in the two-body direct correlation, which is related to the radial distribution function through the Orstein-Zernike relation

$$h(r) = c(r) + \rho \int h(r')c(|\mathbf{r} - \mathbf{r}'|)d\mathbf{r}' \tag{2.4}$$

Here $h(r) = g(r) - 1$. The Orstein-Zernike relation is often adopted as definition of $c(r)$ and can be expressed recursively in the following form

$$h(r) = c(r) + \rho \int c(r')c(|\mathbf{r}-\mathbf{r}'|)d\mathbf{r}' + \rho^2 \int d\mathbf{r}' \int d\mathbf{r}'' c(r'')c(|\mathbf{r}-\mathbf{r}'|)c(|\mathbf{r}'-\mathbf{r}''|) + \dots$$

Looking at this expression we can infer the physical meaning of such direct correlation. The total correlation between two particles, represented by the function $h(r)$, is due to the direct correlation between these two particles (the first term on the right side of the equation) but also to the indirect correlation propagated by an increasingly large number of intermediate particles. A much simpler expression for the Orstein-Zernike relation is obtained taking the Fourier transform of both sides of equation 2.4

$$h(q) = \frac{c(q)}{1 - \rho c(q)} \tag{2.5}$$

where $\mathbf{q} = 2\pi/\mathbf{r}$. Experimentally the measurement of $g(r)$ is quite challenging, and it can be performed only in very specific conditions, i.e. optical microscopy for large colloids [40, 41], or high-resolution transmission electron microscopy for thin samples [42].
A measurement of $g(r)$ comes from scattering experiments, where the probe particles can be either neutrons x-rays or visible photons. Regardless of the details of the scattering event, as long as we remain in single scattering condition (i.e. the probe particle interacts only once inside the sample and then leaves the scattering volume), the intensity recorded at a large distance from the sample will originates from the superposition of all the waves originated at the interaction sites, in other words the atomic positions

$$I(\mathbf{q}) \propto \left\langle \sum_{l,j} f_l f_j e^{i\mathbf{q}(\mathbf{R}-\mathbf{r_l})} e^{-i\mathbf{q}(\mathbf{R}-\mathbf{r_j})} \right\rangle = \left\langle \sum_{l,j} f_l f_j e^{-i\mathbf{q}(\mathbf{r_j}-\mathbf{r_l})} \right\rangle$$

If the system is composed by identical particles $f_l = f_j = f$ and

$$I(\mathbf{q}) \propto \left\langle \sum_{j}^{N} f^2 \right\rangle + f^2 \left\langle \sum_{j \neq l} \int d\mathbf{r} \int d\mathbf{r}' e^{i\mathbf{q}\mathbf{r}-\mathbf{r}'} \delta(r - r_j)\delta(r' - r_l) \right\rangle$$

$$I(\mathbf{q}) \propto Nf^2 + f^2 \int d\mathbf{r} \int d\mathbf{r}' e^{i\mathbf{q}\mathbf{r}-\mathbf{r}'} \left\langle \delta(r - r_j)\delta(r' - r_l) \right\rangle = Nf^2 + f^2 V \rho^2 \int d\mathbf{r} e^{i\mathbf{q}\mathbf{r}} \rho^{(2)}(\mathbf{r})$$

Dividing by $Nf^2$ we get a quantity called *structure factor*, $S(q)$[1]

$$S(q) = 1 + \rho \int d\mathbf{r} e^{i\mathbf{q}\mathbf{r}} (g(r) - 1).$$

[1] the structure factor is usually defined as $S = \frac{1}{N} \langle \rho_q \rho_{-q} \rangle$, where $\rho_q = \sum_j^N e^{iqr_j}$ is the Fourier component of the number density.

In other terms the structure factor is proportional to the Fourier transform of the total correlation function

$$S(q) = 1 + \rho h(q) = 1 + \frac{\rho c(q)}{1 - \rho c(q)}$$

More in detail for a sample composed by identical colloidal particles probed by X-rays, the intensity collected by the detector can be expressed as

$$I(\mathbf{q}) = \frac{d\sigma}{d\Omega}\Delta\Omega \propto \rho V^2 \Delta\rho^2 P(\mathbf{q}) S((q))\Delta\Omega.$$

Where, as usual, $\rho$ is the number density of particles, $V$ is the scattering volume, $\Delta\rho$ is difference in electronic density between the particles and the suspension liquid and $P(\mathbf{q})$ is the form factor. For spherical particles, the form factor can be easily obtained from

$$P(\mathbf{q}) = 4\pi \int_0^\infty \rho(r) r^2 \frac{qr}{qr} dr = 4\pi \int_0^R r^2 \frac{qr}{qr} dr = \frac{4}{3}\pi R^3 3 \frac{\sin(qR) - qR\cos(qR)}{(qR)^3} \tag{2.6}$$

## 2.3 Dynamics in a disordered system

We have seen in the previous paragraphs that the glass transition is a problem of dynamic origin, and consequently the dramatic slowing down of the system's internal rearrangements cannot be characterized effectively by static structural quantities like the structure factor. In fact, snapshots of undercooled liquid configurations are practically identical to the configurations that can be found in the profoundly dynamically different glassy state [43]. However, a clear signature of the glass transition can be easily found looking at dynamical observables. Again, a central role is played by the density function, but this time the positions of the particles are explicitly time-dependent

$$\rho(\mathbf{r}, t) = \left\langle \sum_j^N \delta(\mathbf{r} - \mathbf{r_j}(t)) \right\rangle$$

For more practical use we consider its spatial Fourier transform

$$\rho(\mathbf{q}, t) = \left\langle \sum_j^N e^{i\mathbf{q}\mathbf{r_j}(t)} \right\rangle$$

The $\rho^{(2)}(\mathbf{q}, t_1, t_2)/N$ is the density time autocorrelation function, also called intermediate scattering function

$$F(q, t_1, t_2) = \frac{1}{N} \left\langle \rho_q(t_1) \rho_q^*(t_2) \right\rangle \tag{2.7}$$

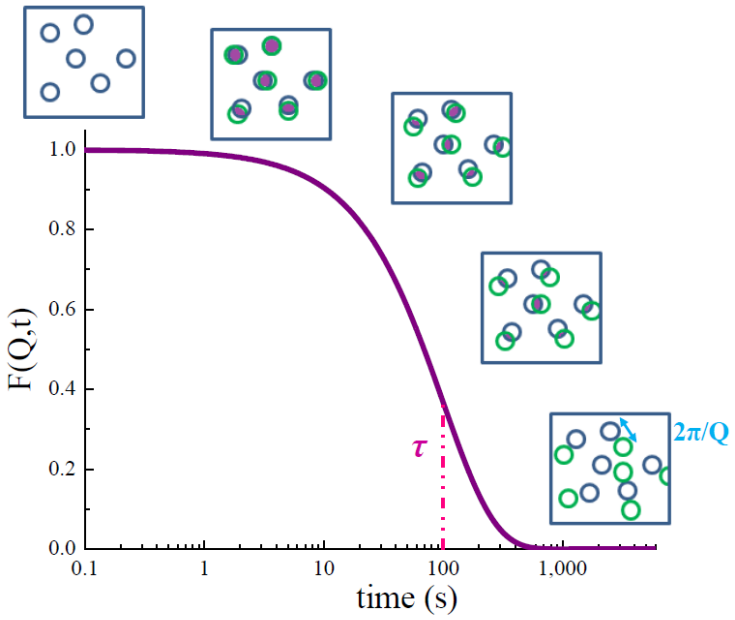


Figure 2.6: schematic example of the intermediate scattering function, the insets at the different values of $F(q,t)$ represent the instantaneous configurations assumed by the system.

This quantity is accessible with neutron and light scattering experiments, and as it can be seen from its definition, it is closely related to the structure factor. In fact for $t_1 = t_2$ we recover the definition of $S$. Usually what is studied is the normalized autocorrelation

$$\Phi(\mathbf{q}, t_1, t_2) = \frac{F(\mathbf{q}, t_1, t_2)}{S(\mathbf{q})}.$$

It is a decreasing function starting from unity for fully correlated configurations and reaching 0 for completely uncorrelated ones.
It is possible to give a quite straightforward interpretation of this quantity. In fig 2.6 an example of the values of $F(q,0,t)$ for a system of spherical particles is reported. Suppose to observe the system at a certain time $t_1 = 0$ and that the system is ergodic, hence $F(q,0,t_2) = F(q,t)$. $F(q,0)$ is simply the instantaneous configuration correlated with itself; at a different $t > 0$ all the particles will have moved from their original positions and the quantity $F(q,t)$ tells us the amount of change occurred in sample during a time $t$. Eventually, for $\tau \to \infty$ every particle will have completely changed its position, and thus $F(q, t \to \infty) = 0$. We can already identify a characteristic

time of the relaxation process which is the time required to the particles to move of $2\pi/q$. If our system is composed by a simple liquid or a diluted colloidal system, then we expect a very short time ballistic regime, where single particles move freely, followed by a dissipative regime described by a normal exponential function

$$\Phi(q,t) = e^{-\frac{t}{\tau}}.$$

For a single diffusive process $1/\tau = q^2 D$, where $D$ is the diffusion constant. Approaching the glass transition the expression for $\Phi$ becomes progressively more complicated, in fig. 2.7 an example is reported . Qualitatively speaking, with the lowering the temperature a plateau is formed so that the decay is no longer purely exponential, but is articulated in a two-step relaxation [44]. This two-step relaxation always appears as a precursor of the glass transition and can be used as a qualitative fingerprint of approaching glassiness. Roughly speaking, we can say that there exists a fast process weakly dependent on the temperature ($\beta$ relaxation), and a slow process strongly dependent on $T$ ($\alpha$ relaxation). A simpple interpretation can be made out from the prototypical scenario of a hard spheres colloidal system. At high densities all the particles are closely packed and from the point of view of an individual particle all its neighbours are forming a cage impeding its free diffusion. Then the first rapid relaxation is due to the movements of the particle rattling inside its cage. After some time, the particle will eventually find a "hole" in the cage escaping and starting the slower diffusive process. The height of the plateau between the two relaxations is often called non-ergodicity level $f_q$.

We have seen this diffusive relaxation from the point of view of a single particle, but we must keep in mind that it is a cooperative process. In fact, even our "protagonist particle" was forming a cage for its neighbours and leaving its initial position it will in turn create a hole in the cage experienced by them and thus one of these neighbours might escape from its own cage allowing another particle to escape etc... .
The potential barriers that the system must overcome to reorganize its internal structure are not identical but will follow a certain distribution, and so inside an undercooled liquid at the same time we expect to observe different microscopic regions relaxing at different rates [46]. The measurement of the total structural relaxation arising from this distribution will then be the Legendre transform of the distribution itself (fig. 2.8) [47, 48]. This Legendre transform is called Kolraush-Williams-Watts (KWW) equation or stretched exponential

$$\Phi_q(t) = \int_0^\infty P(1/\tau) e^{-t/\tau} d(1/\tau) = e^{-(t/\tau)^\beta}. \tag{2.8}$$

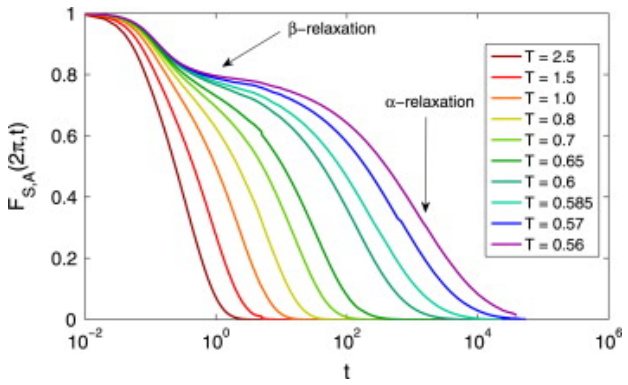


Figure 2.7: computed intermediate scattering functions for a Lennard-Jones liquid at different temperatures. It is clear the initial $\beta$ relaxation weakly dependent on temperature and the subsequent development of a plateau and the final $\alpha$ relaxation. Image taken from [45]

Here $\beta$ is usually named stretching exponent, and for undercooled liquids and glasses it has values less than 1, in fig. 2.8 the profiles of $P(1/\tau)$ for $\beta$ ranging between 0.1 to 0.9 are reported. The processes related to the $\alpha$ relaxation are still diffusive, but the q-dependence of $\tau$ is modified as $\tau^{\beta} \propto q^{-2}$ [49, 50, 51].

Even if nowadays the heterogeneous origin of the stretching exponent is commonly accepted, for long time it has been challenged by the opposite interpretation of a homogeneous distribution. According to this homogeneous explanation, relaxation is equally nonexponential in all regions, so that the stretched nature of the correlation function is not due to a spatial average, but it is an intrinsic phenomenon even at a local level, due to the disordered environment each particle sees around itself.
The reason of this long-lived debate is in the difficulty for the experimentalists to perform a measure local enough to be sensible to these microscopic heterogeneities and even at the present time these dynamical heterogeneities has been directly observed on a rather limited set of samples, mainly colloidal systems or granural materials with particles large enough to be probed by a microscope [40, 41, 52].

### 2.3.1 Dynamical heterogeneity

The consequence of this heterogeneous scenario, is that approaching the glass transition, it becomes progressively difficult to define a “typical particle” and a “typical environment”, because a variety of different behaviours

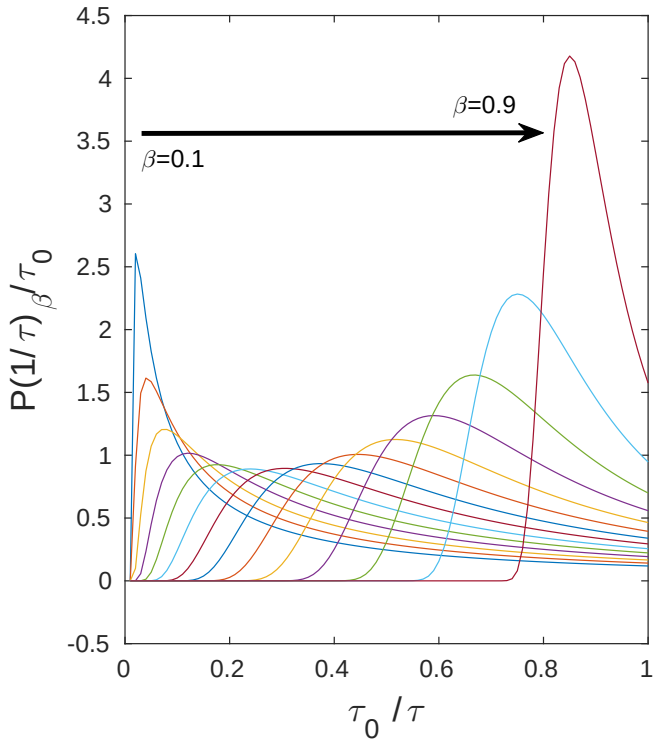


Figure 2.8: Distribution of the inverse of relaxation times computed for different values of $\beta$ using the equations reported in [48]

emerge. Looking at the system on timescale comparable with the structural relaxation, we will see that in the same amount of time some particles have travelled distances comparable with their own sizes, while others have remained localized in their original positions. Thus, at these time-scales we can refer to "mobile" and "immobile" particles. An example is reported in fig. 2.9 in which it is possible to identify regions of high mobility close to regions of stillness. From this picture we can observe a very important feature of the dynamical heterogeneity, that is the clustering of particles with similar dynamic properties, such clusters are also called cooperative rearrangements regions (CRR). In its narrow sense, the term *dynamical heterogeneity* encapsulates the spatial correlations of the CRR; however the term is often used to describe a range of fluctuation phenomena, that arise from deviations from the typical phenomena [53]. Starting from the first years of 2000 [43, 54, 55, 56], it has become possible to define and measure observables related to the CRR that can be determined objectively in a wide range of systems. These observables are known as "four point" correlation functions, and are now commonly accepted as standard tools for analysing dynamical heterogeneities. To begin to work with these four-point correlations, we must find a good quantity to correlate. An appropriate choice is given by the mobility $c_i(t_1, t_2)$ which indicate how much the particle $i$ moves between times $t_1$ and $t_2$. Then, given two particles separated by a distance $r$, one can measure the degree to which their mobilities are correlated, and we can define the quantity

$$C(\mathbf{r}, t_1, t_2) = \sum_i^N c_i(t_1, t_2)\delta(\mathbf{r} - \mathbf{r_i})$$

Then, the spatial correlations of the mobility are naturally captured by the quantity

$$G_4(\mathbf{r}, t) = \langle C(\mathbf{r}, t, 0)C(\mathbf{0}, t, 0)\rangle - \langle C(\mathbf{r}, t)\rangle^2$$

Often the mobilities are by themselves two-point correlations, for example, if we want to know the mobility over length-scales of the order $2\pi/q$, then $c_i(t_1, t_2) = \rho_i(\mathbf{q}, t_1)\rho_i(\mathbf{q}, t_2)^*$ ( and of course $\Phi_q(t_1, t_2) = \langle c_i(t_1, t_2)\rangle$) and the expression for $G_4$ becomes

$$G_4(\mathbf{r}, t) = \langle \rho(\mathbf{r}, \mathbf{q}, t)\rho^*(\mathbf{r}, \mathbf{q}, 0)\rho(\mathbf{0}, \mathbf{q}, t)\rho^*(\mathbf{0}, \mathbf{q}, 0)\rangle - \langle \rho(\mathbf{r}, \mathbf{q}, t)\rho^*(\mathbf{r}, \mathbf{q}, 0)\rangle^2$$

this definition of a real-space correlation function allows the language of field theory and critical phenomena to be used in studying dynamical properties of the glassy state [57]. By analogy with critical phenomena, if there is a single dominant length scale $\xi_4(t)$, then one expects that for large distances

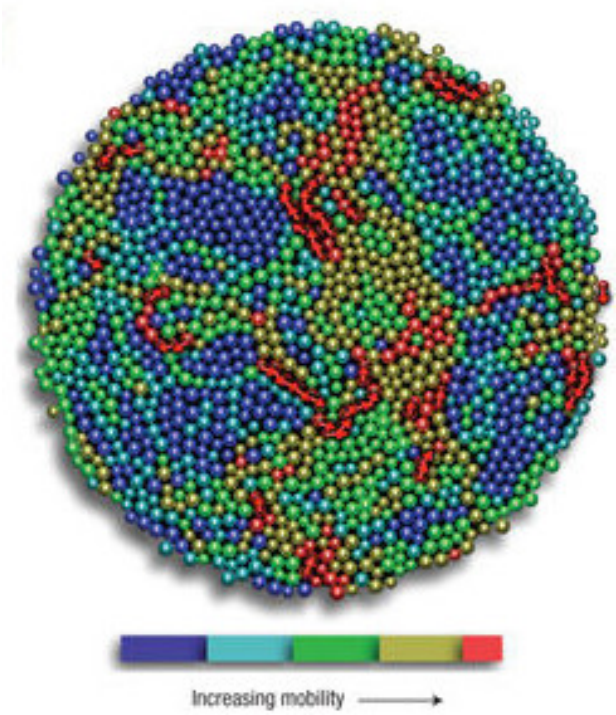


Figure 2.9: Example of dynamical heterogeneities observed in a granular material. The image reports the observed mobility in a system composed by 1:1 bidisperse mixture of steel beads of diameters 0.318 cm and 0.397 cm. confined in a circular region of diameter 17.6 cm and bounded to roll on a horizontal plane. The motion was induced by an upward air flow at fixed speed. Image taken from [52].

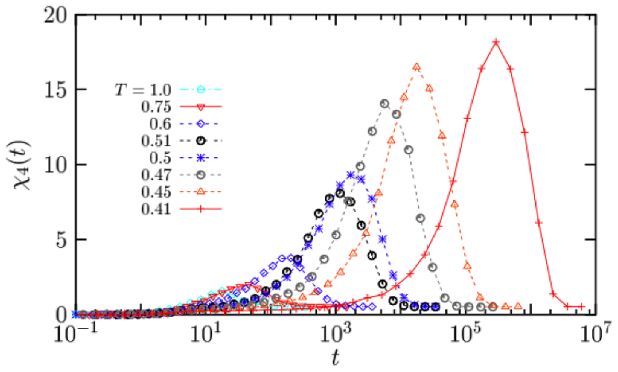


Figure 2.10: Example of the $\chi_4$ obtained from molcular dynamics simulation for different sample temperatures. The general behaviour is an increase of the height of the $\chi_4$, and a shift of the peak position, indicating that as the temperature is decreased, we have a slow down accompained with an enlargement of the dyanmical heterogeneities inside the sample. Image taken from [54].

the correlation function decays as

$$G_4(r,t) \sim \frac{A(t)}{r^p} e^{-r/\xi_4(t)} \tag{2.9}$$

and the quantity $\xi_4(t)$ is the length scale characterizing the CRR's extension and $p$ a critical exponent [54, 57]. At this point we are ready to define the susceptibility

$$\chi_4(t) = \int d\mathbf{r} G_4(\mathbf{r},t)$$

where the integral is taken over the sampled volume, then if 2.9 holds:

$$\chi_4(t) \sim A(t)\xi_4^{d-p}(t)$$

where $d$ is the number of the system's dimensions. The advantages of looking at the $\chi_4$ instead $G_4$ are due to the relatively easy access to the former, both numerically and experimentally. In fact, defining the total mobility $C(t_1,t_2) = \int d\mathbf{r} c(\mathbf{r},t,0)$ and computing its susceptibility, we have that

$$\chi_4(t) = N\left[\left\langle C(t,0)^2\right\rangle - \langle C(t,0)\rangle^2\right] \tag{2.10}$$

The typical behaviour of the $\chi_4$ is reported in fig. 2.10. For short times we do not expect to observe strong signatures of heterogeneities, the particles are still rattling inside their cages and this regime does not corresponds

to significant cooperation, and also at long times $\chi_4 \to 0$ because on that timescales all particles have already diffused. On intermediate time scales we can observe a pronounced peak at time $t^* \sim \tau_\alpha$, and this peak value can be used as a measure of the volume over which the structural relaxation processes are correlated [54, 57, 56]. In fact, if the dynamically correlated regions are compact, $\chi_4(t^*) \sim \xi_4^d$ where the exponent $d$ express the CRR's spatial dimensions, which can be fractal [41, 58, 40]. If there isn't the possibility to determine the value of $d$, or the approximations of eq. 2.9 are not valid it is always possible to define the total number of correlated particles as

$$\chi_4(t^*) = N_{corr} \tag{2.11}$$

Here we can see already one of the complications for the measurements of the $\chi_4$. $N_{corr}$ is a quantity that depends on the studied system, while the $N$ in eq. 2.10 is setted by the experimental conditions (the probed volume), thus the experimentally accessible quantity, $\left[\langle C(t,0)^2\rangle - \langle C(t,0)\rangle^2\right]$, will be inversely proportional to the sampled volume. Along with this restrain for the measurement of the dynamical heterogeneity, another important limitation comes from the crucial role covered by the choice of the probed mobility. There exist in fact a wide number of possible definitions of the mobility that are, a priori, equally acceptable. All these possible definitions involve intrinsically a probe length-scale fixed by the choice of the measurement, in contrast to the dynamic length scale $\xi_4$, which is a physical quantity characteristic of the system. The typical choice for the mobility is the intermediate scattering function $\Phi(q, t_1, t_2)$, in which the probed length-scale is $\sim 1/q$. If the probed distance is of the order of the particle size or smaller, $\Phi(q, t_1, t_2)$ measures local motions, and at this length-scales the heterogeneity is typically more apparent. As the length-scale is increased, contributions to the $\chi_4$ come from couples of particles separated by distances of the order of $1/q$, and typically such correlations weaken with increasing distances, thus reducing the $\chi_4$ [59]. Similarly, also reducing too much $1/q$ reduces the dynamical heterogeneity as we are approaching again to the length scales of the cage motions that are basically uncorrelated thermal vibrations.
Therefore, a good choice of time and length scales, along with small enough scattering volumes, is required if one wants to have the chance of observing the dynamical heterogeneity. However, the optimal choice of $q$ and $t$ does not grant immediately a safe measurement of the $\chi_4$ as its value can be influenced by other factors, as we will see in other chapters of this Thesis.

## 2.4 Colloidal glasses

In modern scientific usage, a colloid is a dispersion of particles or droplets in a liquid that, despite the density difference between the dispersed phase and the dispersing medium, is stable against sedimentation [60]. Typically, in the major part of real life colloidal systems, the dispersed particles have linear dimensions that range between 10 nm and 1 $\mu m$. Even if the focus here is on fundamental science, there are many practical reasons to be interested in colloids. Suspensions of every kind are ubiquitous in every-day life. In fact, may natural substances can be described as colloidal suspensions (e.g. milk or blood) and a lot of industrial products are either colloids in their final state (e.g. wall paint, ink, chocolate) or would have passed through the colloidal stage during their production (e.g. ceramics). Colloids are materials that offer a complete control on an outstanding variety of physical properties thanks to the possibility to work with well characterized particles, with well-defined sizes and other properties, making them an optimal choice as model systems.
The key property of every colloidal suspension is the volume fraction ($\phi$), defined as the ratio between the total volume occupied by the colloidal particles and the total volume of the sample; for $N$ identical particles with volume $V_p$ dispersed in a sample with total volume $V_{tot}$, the volume fraction is defined as $\phi = NV_p/V_{tot}$.
The properties of colloidal suspensions at low volume fractions, are completely described by the Brownian motion. The first quantity that is necessary to describe this kind of dynamics is the mean square displacement

$$\left\langle \Delta r^2(t) \right\rangle = 2nDt$$

Where $n$ is the number of dimensions over which the dynamics is taking place and $D$ is the diffusion coefficient. For a spherical particle that moves in an infinite liquid medium (i.e. the influence of the sample's wall is negligible) with viscosity $\eta$ at temperature $T$, the diffusion coefficient can be described with the Stokes-Einstein relation

$$D = \frac{k_b T}{6\pi\eta a}$$

Einstein also obtained that the number density of particles ($n$) in a suspension that has reached sedimentation equilibrium changes with the height $z$ following an exponential distribution

$$n(z) = n_0 e^{-z/z_0}$$

Where

$$z_0 = \frac{k_b T}{\Delta m g}$$

And $\Delta m = (\rho_p - \rho_l)V_p$ is the buoyant mass.
$z_0$ serves as an upper bound for the colloidal length scale; we can say that a colloidal particle is a particle with radius $a$ for which $a \tilde{<} z_0$.
It has been said that the colloidal systems can be adopted as model systems. In this Thesis the main topic is the physics of disordered condensed matter, thus we want a colloidal system with typical features of a disordered system, in other words we need a colloidal glass (and possibly a colloidal undercooled liquid). To create a glass, or a liquid or a condensed phase in general it is necessary the presence of inter-particle attraction. A first approximation of this interaction is given by the Lennard Jones potential, that for a spherical particle of radius $a$ is written as

$$U_{LJ} = \epsilon \left[ \left( \frac{r}{2a} \right)^{12} - \left( \frac{r}{2a} \right)^{6} \right]$$

where $\epsilon$ is the depth of the potential well. The advantages, and the reason of the success of this model are its simplicity and the fact that practically everything is controlled by two parameters, a and $\epsilon$. In a system described by this kind of potential the condensed (liquid) phase exists for temperatures below the critical temperature $T_C = 1.326\epsilon/k_b$. This model system, even if helpful to get a first insight on the behaviour of colloids at higher volume fractions, cannot describe accurately what is happening with relatively large objects such as colloidal particles and leaves out the physics developing inside our colloidal glass.
In the "nano-world", there is a set of ubiquitous attractive forces known as Van der Waals force. In the case of the interaction between two identical spheres the potential energy arising from this interaction can be expressed as

$$W_{VdW}(D) = -\frac{Aa}{12D} \tag{2.12}$$

Where $D$ is the separation between the two surfaces and $A$ is the Hamaker constant [61]. The Van der Waals interaction alone cannot describe the behaviour of colloidal systems, in fact if we think of a system in which this interaction is the only one present, then we cannot expect any suspended phase to last long in solution, because this attractive force will inevitably lead the particle to be irreversibly stick together and precipitate forming a mass of solid material. Typically, this does not happen because particles suspended in water are usually charged and electrostatic repulsive forces

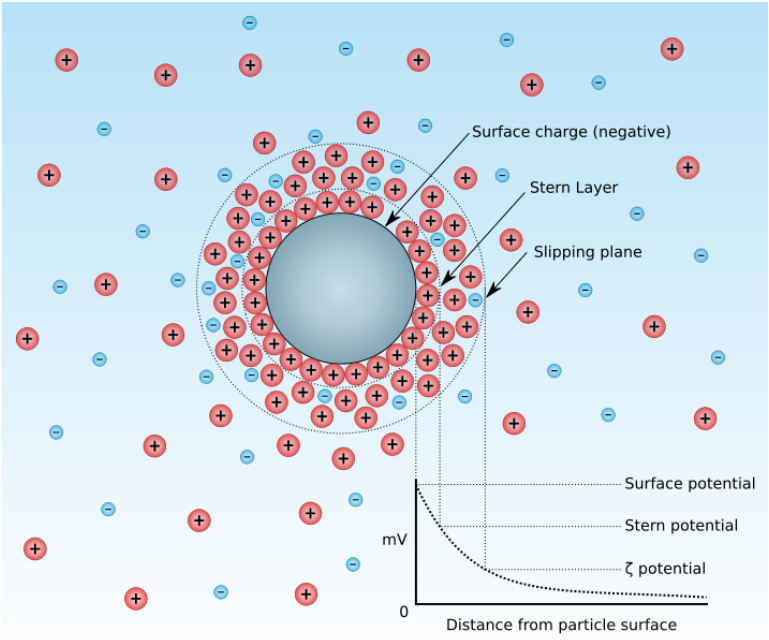


Figure 2.11: Representation of the electric double-layer forming around a charged colloidal particle. On the particle's rim the less mobile counterions forming the Stern layer are present , while for greater distances we see the more mobile counterions forming the diffuse double layer. A direct measure of the surface potential requires particular techniques, thus the quantity typically employed to characterize the charge of the colloidal particles is the $\xi$ potential, or zeta potential.

prevent the coalescence (other repulsive forces might be present, i.e. steric repulsion, but these are outside the aim of this Thesis). The charging of a surface in a liquid can occur for several reasons. Whatever is the charging mechanism, at the end the final surface charge produced by the so called "co-ions" is balanced by the presence of an equal but oppositely charged region of "counterions". Some of the counterions are physisorbed on the surface within the so-called Stern layer, while the others form a cloud of ions with higher mobility known as the diffuse "double layer", see fig. 2.11. In the case of colloidal systems dispersed in pure water the only source for the counterions are those that have come off the surfaces (also the $H_3O^+$ and $OH^-$ naturally present in water); such systems are referred as "counterions only". For low surface potentials (typically less than 25 mV) it is possible to express the surface charge density $\sigma$ of our colloidal particles as $\sigma = \epsilon\epsilon_0 k\psi_0$ [62], where $\epsilon\epsilon_0$ is the dielectric constant, $\psi_0$ is the electrostatic potential and

the quantity $k$ is equal to

$$k = \left( \frac{\sum_i \rho_{\infty i} e^2 z_i}{\epsilon \epsilon_0 k_b T} \right)^{1/2} . \tag{2.13}$$

Here $\rho_\infty$ is the number density of ions of a given charge $ez_i$. The expression for $\sigma$ closely resembles the equation for a capacitor whose plates are separated by a distance of $1/k$. This analogy with the charged capacitor gives rise to the name of "diffuse electric double layer", where $1/k$ is a characteristic length is known as Debye length. For spherical nanoparticles with radius $a$, it is possible to write down the potential energy between two surfaces separated by a distance $D$ [62]

$$W_{DL}(D) = \frac{64\pi k_b T \rho_\infty a \gamma^2}{k^2} e^{-kD} = \frac{Za}{2} e^{-kD}$$

Here $\gamma$ is the reduced surface potential defined as

$$\gamma = \tanh \left( \frac{ze\psi_0}{4k_b T} \right)$$

We can now put together both interactions in what is called the DLVO (Derjaguin, Landau, Verwey, Overbeek) theory; keeping the example of spherical particles we get for the potential energy:

$$W_{tot}(D) = W_{DL}(D) + W_{VdW}(D) = \frac{Za}{2} e^{-kD} - \frac{Aa}{12D} \tag{2.14}$$

The most evident feature is that this expression for the potential energy will always produce a long-range attraction, since the effect of the double layer fade away quite rapidly with an exponential law, while the Van der Waals force scales as $1/D^2$. Depending on the surface charge density and the concentration of electrolytes in solution ($k$) the total effect of the DLVO interaction can be quite different, as can be seen in fig. 2.12. For highly charged surfaces in low concentration of electrolytes (i.e. long Debye length) the potential presents a strong long-range repulsion peaked around $k$ (which is typically in the few nanometres range) and produces a quite high energy barrier. Our colloidal system is then composed by purely repulsive nanoparticles. For smaller values of $k$ a small minimum will appear after the energy barrier, often referred as "secondary minimum" (in contrast with the "primary minimum" represented by two surfaces in contact). For colloidal systems, even if the thermodynamic equilibrium should be represented by the particle in close contact at the bottom of the primary minimum, often

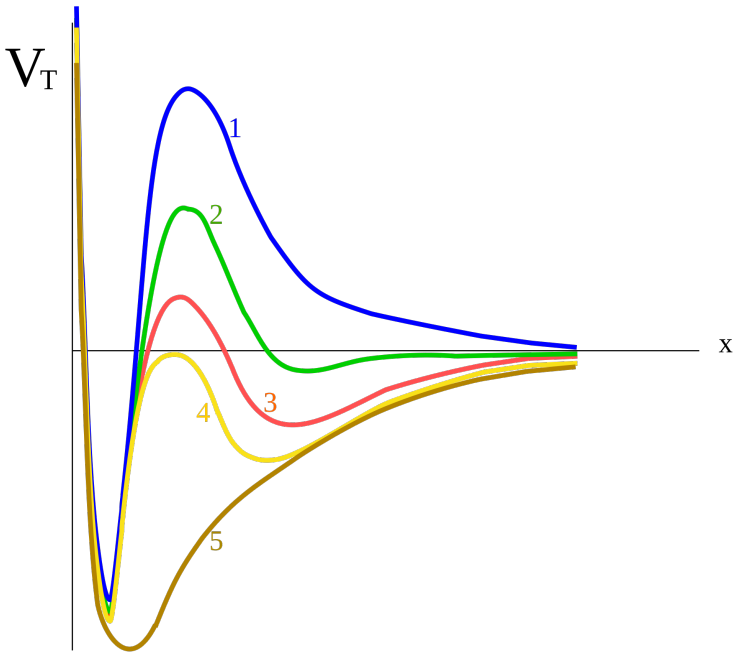


Figure 2.12: Example of the resulting potential energies for the DLVO model for different attraction/repulsion ratios. Curve 1 represent a completely repulsive colloidal system, while curves 2 and 3 are typical of attractive colloids with a marked secondary minimum. Curve 4 and 5 represent the potential energy for unstable systems, in which the particles will immediately flocculate.

the energy barrier is too high to be overcome by the particles in a reasonable timescale. When this is the case the colloidal particles will either sit in the shallow secondary minimum or remain totally dispersed in solution. In the latter case the colloid is referred to as being kinetically stable. Further lowering the charge density (or increasing the electrolyte concentration), the energy barrier will be lower leading to a slow aggregation referred as coagulation or flocculation. Eventually, the energy barrier will fall below $W = 0$ and the particles will start to coagulate rapidly, and the colloid is now referred to as being unstable. It is important to notice that all these scenarios can be obtained for the same colloidal particles changing the Debye length $k$, which by its definition, is a quantity determined only by the solvent's properties.

Increasing the volume fraction, the properties of a colloidal system will become, similarly to more canonical condensed matter systems, determined by the inter-particle interactions. In fig. 2.13 an example of the possible phases that can be obtained with hard spheres colloidal particles is reported. In the low concentration limit, the dynamics of the suspension is still characterized by liquid-like simple diffusion mechanisms, and looking at its intermediate scattering function we will see a single relaxation process. At a certain point the number density of colloidal particles is high enough to initiate a crystallization, however under certain conditions, typically a certain degree of dispersion in the particle's sizes, it is possible to prevent the formation of crystals. Like the situation of undercooled liquids outlined in previous sections, our system has entered a metastable state, and the intermediate scattering function will be split in the fast $\beta$ and slow $\alpha$ relaxation processes. At higher volume fractions the colloidal system will eventually fall off the metastable equilibrium, the alpha relaxation will be so long to be practically impossible to measure and we will have obtained a proper colloidal glass. At this point it is still possible to increase a little more the particle's density, but eventually we will reach the geometrical limit of the random close packing located at $\phi \sim 0.63$.

The $\phi$ value that marks the liquid-crystal transition, and consequently the location of the glass transition region, is strongly dependent on the details of the inter particle potential and for Yukawa-type potentials the phase transition could occur at much lower volume fractions [64]. A colloidal system can reproduce dynamical behaviours of liquids, undercooled liquids and glasses, simply changing the volume fraction, which cover a similar role as the temperature in standard glasses, and in fact it is often identified a colloidal glass transition volume fraction $\phi_g$. As it can be seen in fig. 2.14, the dependence of the structural relaxation time on the volume fraction is

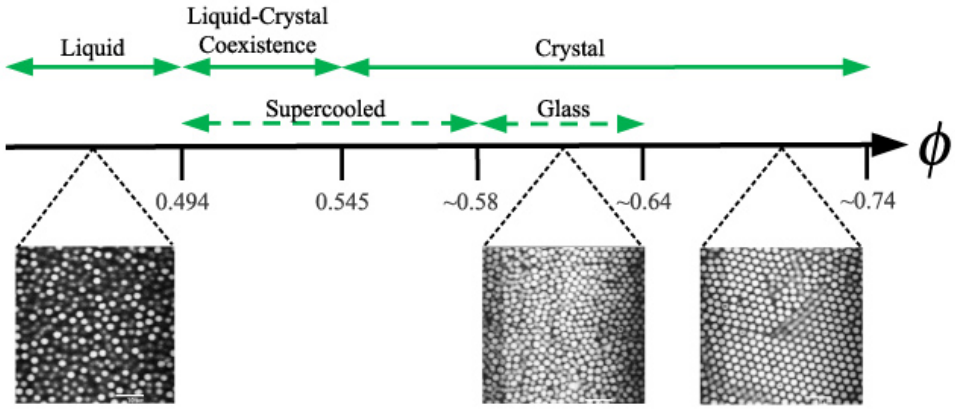


Figure 2.13: Example of the different phases for a colloidal hard-spheres system. The continuous green lines represent the equilibrium configurations, while the dashed lines are the metastable conditions. We can see the images taken with an optical microscope of a colloidal system in the liquid (left), glassy (center) and crystalline (right) phases. Image from [63]

like the one of a typical fragile glass, described by a VFT law

$$\tau \propto e^{-\frac{B}{T-T_0}}.$$

## 2.5 Aging

We will conclude this chapter citing another foundmental characteristic common to all glasses, aging.
It is possible to employ again the concept of the energy landscape, to get a qualitative view of the aging of a glass. We have already seen that when a liquid is cooled, it falls out of equilibrium at a temperature that depends on the cooling rate. The liquid thus remains trapped in the basins that are commonly explored at that temperature; the slower the cooling, the lower the energy of the basin where the system will remain trapped. However, this does not mean that our glass will remain helplessly frozen inside its local minimum; on the contrary, it will begin to sample the accessible regions of the potential energy to find a way to reach more stable minima eventually reaching the configuration of the most stable amorphous system, also referred as ideal glass [37, 17, 66].

The aging regime is an out of equilibrium condition, but as we shall briefly see, a quite particular one. In fact, we can still be able to identify a

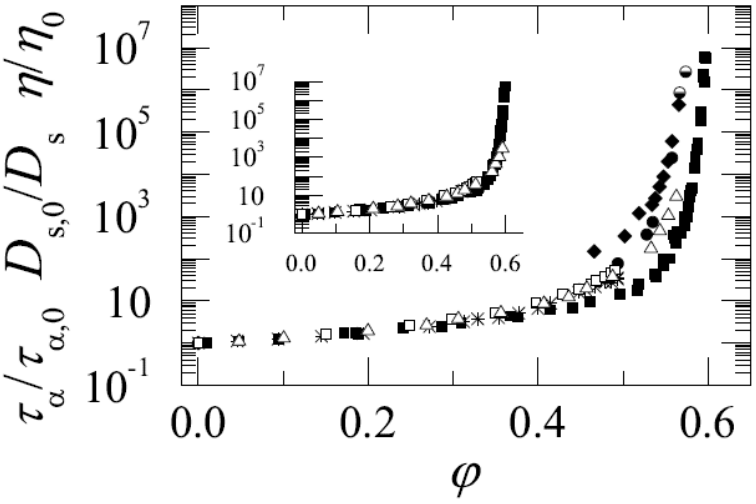


Figure 2.14: comparison of the volume fraction dependence of the structural relaxation time, self diffusion coefficient and low shear viscosity as determined on PMMA colloidal hard spheres. All quantities are normalized with respect to their value in the $\phi \to 0$ limit. Data from [Brambilla et al., 2009; van Megen and Underwood, 1994; van Megen et al., 1998], image from [65].

certain universality, even in this non-equilibrium behaviour [67]. By the very definition of aging, older systems relax in a slower manner than younger ones. It is possible to define the age of the system as the time spent in the phase under study ($t_W$), and a good way to characterize the aging process is using two times quantities such as in eq.2.7. When the system has fallen out of equilibrium, typically at temperatures below $T_g$, the correlation function (here generically described with $C(t_1, t_1 + t) = \langle O(t_1)O(t_1 + t)\rangle$) depends explicitly on $t_W$.

In structural glasses, a pictorial explanation of aging may be put forward recovering again the cage model already described in previous sections. When $t$ is short compared to the structural relaxation time, each particle rattles inside its own cage in a very similar manner to the undercooled liquid case. The difference here is that the cages become stiffer as the system evolves, and thus the time required for diffusion will become longer and longer as $t_W$ increases, in fig. 2.15 an example is reported of the aging intermediate scattering function relative to a simulated Lennard-Jones glass. Thus, similarly to what happens when the undercooled liquid approaches the glass transition, the time scale is separated into two very different "time sectors" [43, 68]. Before reaching the proper aging regime, when the time

elapsed since the beginning of the experiment is still much smaller than the age of the sample, or in other terms $(t - t_W) << t_W$, we have what it is sometimes called a stationary regime during which the system evolves in the same way regardless the sample's age and, from the point of view of the measured observable, it resembles a relaxation towards equilibrium. What is happening is instead that our system is evolving rapidly towards a metastable state.
Then we can separate our generic correlation function, $C(t, t_W)$, in

$$C(t, t_W) = C_{eq}(t - t_W) + C_{ag}(t, t_W).$$

Here the fast relaxation is described by $C_{eq}(t-t_W) = C_{eq}(h_f(t)/h_f(t_W))$ with $h_f(t) = e^{t/\tau_f}$ and $\tau_f$ a characteristic time scale [68], experiments on glycerol [69] have shown that this regime is overcome already for $(t - t_W) \sim 10^{-5} t_W$. This first term describes the stationary approach to the plateau, while the slow, age dependent $\alpha$ relaxation is described by the term $C_{ag}(t, t_W)$.

Often, in many models and measurements, it is reported for the aging part of the correlation function $C_{ag}(t, t_W) = C_{ag}(h_S(t - t_W)/h_S(t_W))$ with $h_S(t_W)$ a system-dependent monotonic function [68, 70, 71] , and thus $\tau_\alpha$ is a function to the age of the system. Typically, this relation between age and structural relaxation time is expressed with a power law $\tau_\alpha = t_W^\mu$ with the exponent $\mu \in [0.5, 1]$. When $\mu = 1$ one speaks of "full aging", while $\mu < 1$ is referred as "sub-aging" [43].
What emerges from this description is that for a glass, once it has started to age, the equilibrated undercooled liquid condition will never be reached again, and its structural relaxation time will continue to increase indefinitely. Indeed, it's the case of a glass window, which is cooled at temperatures so far from its $T_g$, that the time required to perform a simple structural rearrangement is so long [18] that it will require millions of years to reach the most stable configuration [17, 66]. However, if the time window chosen to probe the glass is wide enough or, more realistically, the temperatures are closer to the glass transition region, we expect to observe, at a certain point, values of $\tau_\alpha$ that does not age anymore. This behaviour has been observed in some experiments and simulations [72, 73] and sometimes one refers to this situation as "interrupted aging" [68].
The aging of a glass physical properties can also be described by phenomenological models like the one proposed by Tool, Moynihan and Narayanaswami (further described in chapter 4 of this thesis), so is it possible to say aging related problems are already known? Obviously, the answer is no. First of all, despite being known from about a century, the aging of the glasses is still one of the least understood problems of fundamental physics. From

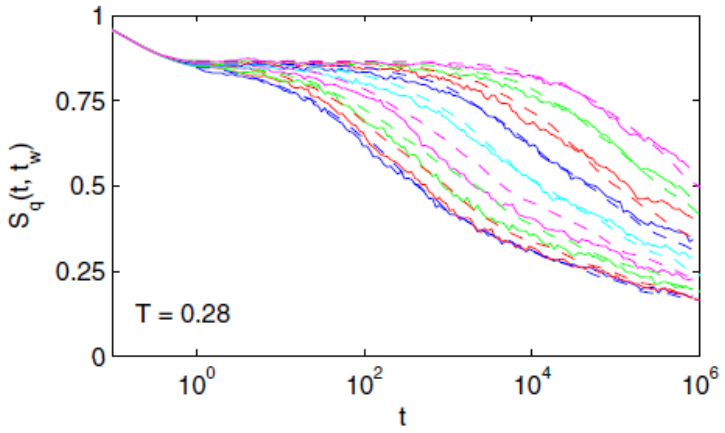


Figure 2.15: Computed aging intermediate scattering functions for a molecular dynamics simulation of a Lennard-Jones glass. For small times the dynamics is nearly the same for different ages, while conversely the long time behaviour changes importantly with $t_W$. Image taken from [72]

the experimental point of view the aging was typically described with the evolution of simple quantites, such as density or refractive index, while direct measurements of aging structural relaxation times are still quite scarce even nowdays. The majority most of this kind of data come from dielectric spectroscopy experiments, and only recently the intermediate scattering function on aging systems have been measured in a reliable way. Lastly, all the previous phenomenological description does not hold for a lot of glassy systems, above all colloidal glasses and gels, for which it has been seen a markedly different behaviour of $\tau_\alpha(t_W)$ [74, 75, 76].From the theoretical point of view the discussion is far to be considered concluded. Several theoretical models have been developed [43, 77, 78, 70] and some of them are able to describe the behaviour of particular systems. However the development of a clear, general and predictive model has yet to come.

# Chapter 3

# Experimental techniques

## 3.1 Speckle patterns

Objects illuminated by coherent light sources are readily observed to acquire a peculiar granular appearance. This complex pattern cannot be described by means of classic geometrical optics, instead, a quantitative description can be achieved by the methods of probability and statistics. The origin of this granularity was quickly recognized shortly after the development of the first lasers [79], in fact, the vast majority of surfaces are extremely rough at lenghtscales of of the illuminating wavelengths; thus, under illumination from coherent light, the wave reflected from such surfaces consists of contributions of many scattering areas [80]. Propagation of this reflected light to a distant observation point results in the additions of various scattered components with relative delays which varies from several to many wavelengths. Interference of this dephased but coherent wavelets, results in the granular intensity distribution known as *speckle pattern*. The speckle pattern consists of a multitude of bright spots, where the interference is highly constructive, dark spots where the interference is highly destructive, and intermediate levels of intensity distributed according a specific statistic.

The refraction from surfaces is not the only way to produce a speckle pattern, random fluctuations of the light source or diffusion from a disordered medium will produce the same intensity distributions, in fig 3.1 is reported the recorded speckle pattern from a concentrated colloidal glass illuminated by a CW green laser. Thus, whenever the source of fluctuations, the description of electromagnetic speckles is based on a statistical approach similar to the one adopted more generally in statistical physics. The field is considered to be a random variable generated by an underlying stochastic process. Using

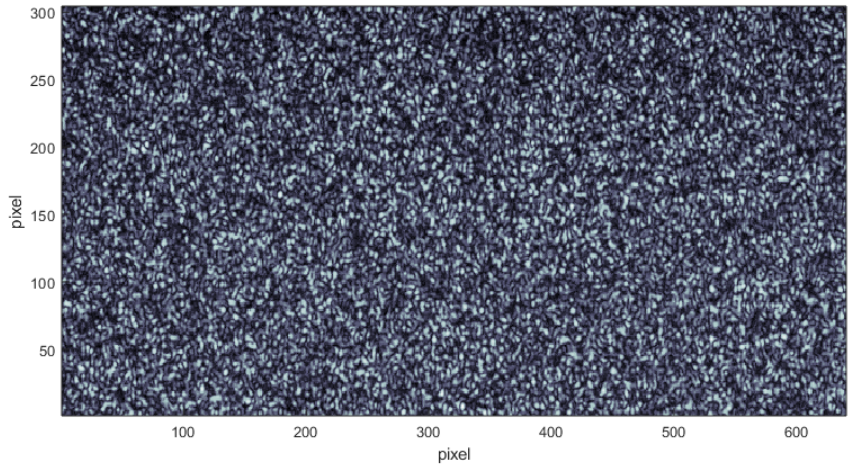


Figure 3.1: example of a recorded speckle pattern produced by scattered coherent light from a colloidal glass.

the notation of [81], the complex amplitude in a certain point $\mathbf{r}$ can be written as:

$$E(\mathbf{r}) = \sum_{\mathfrak{S}_n} A_{\mathfrak{S}_n}(\mathbf{r}) e^{-\phi_{\mathfrak{S}_n}(\mathbf{r})},$$

where $\mathfrak{S}_n$ is a scattering sequence involving n scattering events at position $\mathbf{r1}, \mathbf{r2}, \ldots, \mathbf{rn}($ in a medium made of discrete particles, these are the locations of the n particles involved in the sequence. Both the amplitude $A_{\mathfrak{S}_n}(\mathbf{r})$ and the phase $\phi_{\mathfrak{S}_n}(\mathbf{r})$ are random variables. It is possible to formulate a model of fully developed speckle on the following assumptions [81]:

- The complex amplitudes resulting from two different sequences $\mathfrak{S}_n$ and $\mathfrak{S}_n{}'$ are independent random variables.
- For a given sequence $\mathfrak{S}_n$, the amplitude and the phase are mutually uncorrelated.
- The phase $\phi_{\mathfrak{S}_n}(\mathbf{r})$ is uniformly distributed on $[0, 2\pi]$.

defining $X = Re(E(\mathbf{r}))$ and $Y = Im(E(\mathbf{r}))$ the real and imaginary part of the complex field respectively, under the three hypothesis of the fully developed speckle pattern one find: $\langle X \rangle = \langle Y \rangle = 0$, $\sigma^2 = \langle X^2 \rangle = \langle Y^2 \rangle = 1/2 \sum_{\mathfrak{S}_n} A_{\mathfrak{S}_n}(\mathbf{r})^2$ and $\langle XY \rangle = 0$. The central limit theorem states that, both X and Y are Gaussian variables with zero mean and equal variance, and the joint probability of X and Y is also Gaussian

$$P(X, Y) = P(|E|) = \frac{1}{2\pi\sigma^2} e^{-(X^2+Y^2)/2\sigma^2}$$

but $X^2 + Y^2$ is the intensity $I$, thus adopting a change of variables

$$P(I) = \frac{1}{\langle I \rangle} e^{-\frac{I}{\langle I \rangle}}, \tag{3.1}$$

where the average intensity is equal to $\langle I \rangle = 2\sigma^2$. From the distribution of eq. 3.1 it is possible to easily obtain the second moment $\langle I^2 \rangle = 2 \langle I \rangle$. The ratio $A = \sigma_I^2 / < I >^2$ is called contrast and in the ideal case of a fully coherent source it is equal to 1. In figure 3.2 is reported the intensity recorded from a speckle pattern produced by a $B_2O_3$ sample. It is evident that the actual distribution is not exactly the one described by 3.1, the key parameter is the contrast value that here is reduced to a value of 0.45. The reasons for this reduction reside in experimental conditions, often far to be ideal, which could be spurious background illumination, dynamic nature of the speckle pattern, or not fully coherent light sources. The latter case, typical of X-ray sources, can offer a quite straightforward interpretation for the contrast reduction [82]. In that case we can imagine the total scattered intensity as the intensity produced by $M$ independent speckle patterns (where $M$ is the ratio between the scattering volume and the coherence volume) leading to a modified intensity distribution

$$P(I) = M^M \left( \frac{I}{\langle I \rangle} \right)^{M-1} \frac{e^{-M\frac{I}{\langle I \rangle}}}{\Gamma(M) < I >}, \tag{3.2}$$

where $\Gamma$ is the gamma function. The new value for the intensity fluctuations is $\sigma^2 =< I >^2 /M$ and the contrast is now $A = 1/M$. Another reason for the reduction of the contrast is that the sensitive area, i.e. the single pixel for a CCD, records more than a speckle at the same time. In this case the recoded contrast will be inversely proportional to the number $N$ of speckles per pixel $A \propto 1/N$. In a freely diffusing speckle pattern, i.e. with no optical elements between the speckle's source and the screen, the linear speckle size, also called coherence length, at a fixed point in space is given by [83]

$$l_c = \frac{\lambda}{\delta\theta}, \tag{3.3}$$

where $\lambda$ is the radiation wavelength, and $\delta\theta$ is the angle of the source subtended at the screen. For a source with linear dimension $L$ and a screen placed at a distance $D$, the speckle size becomes

$$l_c \approx 1.22\lambda \frac{D}{L} \tag{3.4}$$

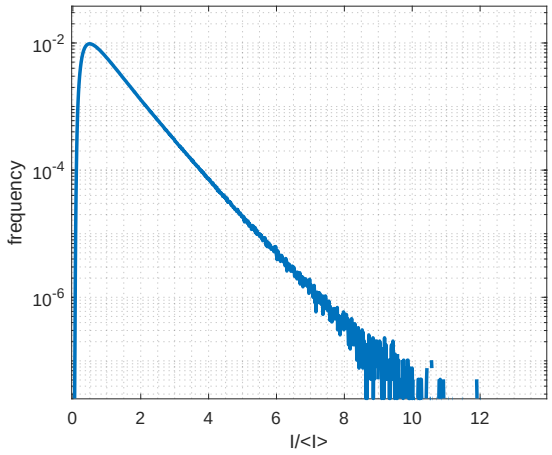


Figure 3.2: Example of the intensity distribution in a real speckle pattern produced by the scattering from a $B_2O_3$ glass.

## 3.2 From the scattered intensity to the intermediate scattering function

When the light travel inside a medium it can be diffused by small local density fluctuations $\delta\rho$, which create small changes of the dielectric constant $\delta\epsilon$. If we send an electromagnetic field with initial amplitude $E_0$, frequency $\omega$ and wave-vector $\mathbf{k_i}$, the resulting field at a certain distance $\mathbf{R}$ from the scattering volume is described by [83]

$$\mathbf{E}(\mathbf{R},t) = -\frac{k_f^2 E_0}{4\pi R\epsilon_0} e^{-i(\mathbf{k_f}\mathbf{R}-\omega t)}\delta\epsilon(\mathbf{q},t),$$

where

$$\delta\epsilon(\mathbf{q},t) = \int_V e^{-i\mathbf{qr}}[\mathbf{n_f}\cdot(\mathbf{k_f}\times(\mathbf{k_f}\times(\delta\epsilon(\mathbf{r},t)\cdot\mathbf{n_i})))]d\mathbf{r},$$

with $V$ being the scattering volume, $\mathbf{n_f}, \mathbf{n_i}$ the final and initial polarizations respectively, $\mathbf{k_f}$ the final wave-vector, and $\mathbf{q} = \mathbf{k_f} - \mathbf{k_i}$ exchanged momentum. The former is a fundamental quantity in all scattering experiments, determined by the experimental parameters its magnitude is given by

$$q = \frac{4n\pi}{\lambda}\sin(\theta/2), \tag{3.5}$$

where $n$ is the refractive index, $\lambda$ is the probe wavelength and $\theta$ the angle between $\mathbf{k_i}$ and $\mathbf{k_f}$.

The recorded physical quantity is the intensity, and its instantaneous value, at a fixed point in space, depends on the positions and momenta of all the particles inside the scattering volume. Thus even if individual particles are described by deterministic laws, the time evolution of $I(t)$ resemble a noise pattern. The instantaneous values measured at two different instants $t$ and $t + t'$ are in general different $I(t_1) \neq I(t_1 + t')$, but if $t'$ is small enough, then the two intensities will be partially correlated. The measure of this correlation is the autocorrelation function $< I(t_1)I(t_1 + t') >$, that for ergodic systems, i.e. when the time average $\bar{I}$ is equal to the ensemble average $< I >$, is defined as

$$< I(t_1)I(t_1 + t') >= \frac{1}{T}\int_0^T I(t_1)I(t_1 + t')dt', \tag{3.6}$$

where the time interval $T$ is much longer than the characteristic time of the internal dynamics. If the system is stationary, then $\langle I(t_1)\rangle = \langle I(t_1 + t')\rangle = \langle I\rangle$ for all $t'$, and the mean physical property does not depend explicitly on the value of $t_1$ which will be put equal to zero. For $t' = 0$ the autocorrelation function is $< I^2 >$, while in the limit $t' \to \infty$, $I(0)$ and $I(t')$ will eventually become uncorrelated, thus $\langle I(0)I(t')\rangle =< I >^2$. Since $\langle I^2\rangle \geq \langle I(0)I(t')\rangle$, the autocorrelation function of an non periodic property decay from $\langle I^2\rangle$ to $\langle I\rangle^2$ in the course of time.
The physical quantity usually measured is the normalized intensity autocorrelation function

$$g_2 = \frac{\langle I(0)I(t)\rangle}{\langle I\rangle^2} \tag{3.7}$$

which, for an ideal speckle pattern is a function that decay from 2 to 1. This $g_2(t)$ is called homodyne autocorrelation function, since it is obtained uniquely from the scattered intensity. Another type of detection is possible when one mix a small quantity of unscattered light (local oscillator) with the diffused light on the detecting surface. In this case one talks about heterodyne detection and the autocorrelation of the intensity is

$$\langle I(0)I(t)\rangle \simeq \langle I_{LO}\rangle + 2Re\left(\langle E(0)E(t)\rangle\right),$$

where $\langle I_{LO}\rangle$ is the mean intensity of the local oscillator, and $Re\left(\langle E(0)E(t)\rangle\right)$ is the heterodyne autocorrelation function.
In the previous chapter we have seen that the dynamic structure factor is the normalized autocorrelation of the density fluctuations, in practice this quantity is strictly related to normalized autocorrelation function of the electric fields, since

$$g_1(t) = \frac{\langle E(0)E(t)\rangle}{\langle I\rangle} = \frac{\langle \delta\epsilon(q,0)\delta\epsilon(q,t)\rangle}{\langle \delta\epsilon(q,0)\rangle^2} \simeq \frac{\left\langle \delta\rho_q(0)\delta\rho_q^*(t)\right\rangle}{\langle \delta\rho_q\rangle^2} = \Phi_q(t).$$

But how can we link this object to the measured quantities? For the heterodyne case this is quite straightforward, since we have directly access to the real part of $g_1(t)$. For the homodyne detection case, we can easily access to the square modulus of the $g_1(t)$ thanks to the Sighert relation

$$g_2(t) - 1 = A|g_1(t)|^2 \tag{3.8}$$

where $A \in [0, 1]$ is a parameter determined by the experimental set-up.

The experimental techniques described above are usually referred as Dynamic Light Scattering (DLS) or Photon Correlation Spectroscopy (PCS), and they are nowadays a classical experimental technique used to measure the average translational and rotational dynamics in many different systems [83], and in particular to probe the structural rearrangements in glass-forming materials in time domain [84].
The most popular approach, mainly due to its relatively easy implementation and straightforward interpretation, is the homodyne configuration. The autocorrelation function $g_2(t)$ can be clearly seen (i.e. has a higher contrast) if a single speckle is collected by the detector which, in typical DLS set-ups, is a photomultiplier. The main drawback of this scheme is that, in order to obtain an autocorrelation function of good statistical quality, i.e. in order to perform a reliable time average of the measured signal, and thus being able to apply eq. 3.6 the data have to be collected over a time interval several orders of magnitude longer than the characteristic time of the probed dynamic. This requirement clearly becomes critical when investigating the structural relaxation dynamics across $T_g$, and in fact only few experiments report DLS results of glass-formers in this temperature range [84].
In the last years, thanks to the increasing availability of high-quality bi-dimensional sensors such as charged coupled devices (CCD), a growing number of DLS experiments are carried out relying on new schemes based on multi-speckle detection [5, 2, 85, 86, 7, 87]. The main advantage in these schemes is the capability of measuring a large amount of independent statistical events (speckles) simultaneously. This is achieved e.g. designing the optical setup in order to have one speckle collected by each pixel of a bi-dimensional detector. It is possible in this way to obtain an autocorrelation function of good statistical quality even with measurement times of the same order of magnitude as the relaxation time.

### 3.2.1 DLS experiments on slow systems

In a typical DLS experiment the measured quantity is a temporal series of the light intensity, $I(t)$, scattered by the sample. From this temporal series

a normalized time autocorrelation function is calculated:

$$g_2(\tau) = \frac{\overline{I_1(t)I_1(t+\tau)}}{\overline{I_1(t)}^2}, \tag{3.9}$$

where the average is calculated over time $t$. In single scattering conditions, it is possible to connect the intensity fluctuations to the intermediate scattering function via the Siegert relation [83]: In a multi-speckle DLS setup, instead, $I(t)$ can be additionally averaged over the independent speckles simultaneously collected by the CCD. In this case, an autocorrelation matrix $C_I(t_1, t_2 = t_1 + t)$ is often introduced defined as:

$$C_I(t_1, t_1 + t) = \frac{\langle \delta I_p(t_1) \delta I_p(t_1 + t) \rangle_p}{\langle I_p(t_1) \rangle_p \langle I_p(t_1 + t) \rangle_p}, \tag{3.10}$$

where $I_p(t)$ is the intensity collected by pixel $p$ at time $t$, $\langle \ldots \rangle_p$ indicates the average over the pixels and $\delta I_p(t) = I_p(t) - \langle I_p(t) \rangle_p$. The element $C_I(i, j)$ of this autocorrelation matrix is the correlation coefficient between the image taken at time $i$ and the image taken at time $i + j$. The diagonal elements of $C_I$ correspond to the autocorrelation coefficients at the same lag time ($\tau$), and the autocorrelation function at time $t$ is obtained simply averaging the $C_I$ values along a line parallel to the main diagonal and separated by a time $t$ from it, i.e.

$$g_2(t) - 1 = \overline{C_I(t_1, t_1 + t)}. \tag{3.11}$$

The Siegert relation is then used again to get $\Phi_q(t)$, the observable of physical interest.

In glass-forming materials close to $T_g$ the intermediate scattering function is dominated by the structural relaxation and shows a universal, stretched exponential shape [88]:

$$\Phi_q(\tau) = f_q e^{-(\tau/\tau_r)^\beta}, \tag{3.12}$$

where $f_q$ is known as the non-ergodicity factor, $\tau_r$ is the structural relaxation time and $\beta$ is the stretching exponent, with $\beta \leq 1$. The structural relaxation time, the non-ergodicity factor and the stretching exponent are the three relevant physical parameters that are then extracted from a DLS experiment on a glass-former close to $T_g$.

The advantages in employing the autocorrelation matrix, are not limited to only slow systems. In fact, being $C(t_1, t_2)$ a two-time quantity, it is possible to correctly describe out of equilibrium dynamics. A classic example are aging systems, and in fig. 3.3 the autocorrelation matrix of an aging

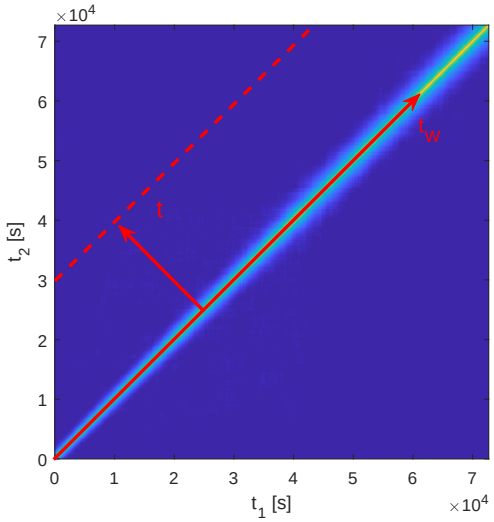


Figure 3.3: example of an aging 2-times correlation matrix. The main diagonal represent the istantaneous contrast of the speckle patterns at different sample's ages, the diagonals parallel to the $t_W$ axis are the collections of the correlations at a certain lag-time t.

$B_2O_3$ glass is reported. Along the main diagonal, are located the points corresponding to $t_1 = t_2 = t_W$, with $t_W$ the sample's age, while on lines parallel to the main diagonal we find all the points $C(t_w, t_w + t)$ in which the intensities are separated by the same lag-time $t$. There exist several ways to deal with such out-of equilibrium quantities. The most straightforward, further described in chapter 4, consist of selecting smaller sub-matrices spanning intervals of $\delta t$, over which one can compute the time average of eq. 4.4. This simple approach is useful when the dynamic is evolving following simple linear function, like for full-aging systems in which $\tau(t_W) \propto t_W$. If in the chosen sub-matrix the dynamics does not evolve excessively, i.e. $(\tau(t_w + \delta t) - \tau(t_W))/\overline{\tau}$ is small, the one can safely attribute the results from 4.4 to the mean age of the considered sub-matrix (i.e. the resulting relaxation time can be considered as $\tau = \tau(t_W + \delta t/2)$). The limitation to slowly evolving dynamics can be quite problematic when someone wants to investigate strongly out of equilibrium systems, and in fig. 3.4 are reported some limit-cases in which adopting the simple approach will inevitably produce wrong or inconclusive results. In fact, reducing $\delta t$ in order to compensate the quickly varying dynamic will not work forever. At a certain point, typically when $\delta t \sim \tau$, the fitting procedures for the determination of the dynamical parameters (for processes described by eq. 4.6, $f_q, \beta, \tau$)

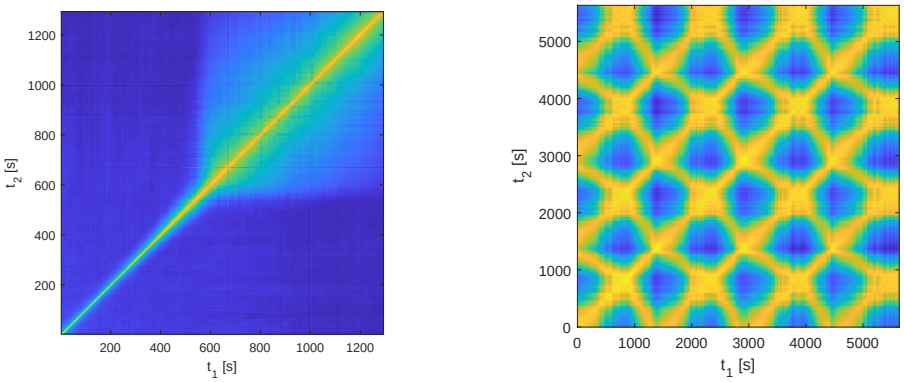


Figure 3.4: autocorrelation matrices of fast, and non-linearly varying processes. Left a glass sample has been rapidly cooled. Right autocorrelation matrix of a slightly turbid sample in presence of small periodic thermal drifts in the optical set-up.

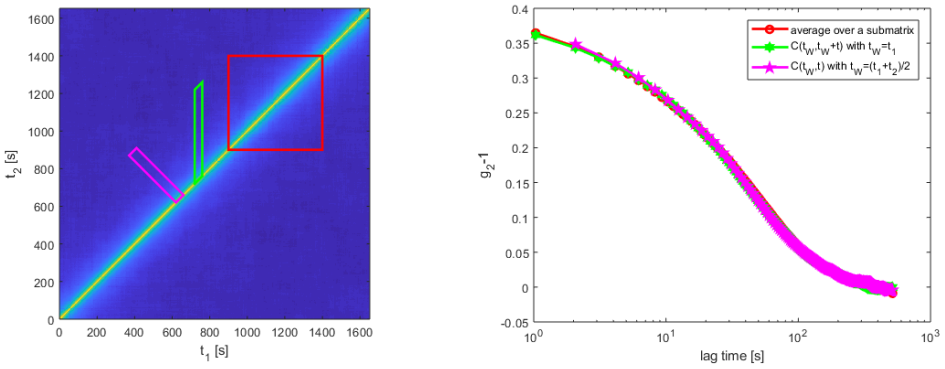


Figure 3.5: Example of possible ways to analyse the autocorrelation matrix, red is the the "sub-matrix" approach, magenta area correspond to $C(t_w, t)$ defining $t_w = (t_1 + t_2)/2$, while the green area is $C(t_W, t_W + t)$ with $t_W = t_1$. The matrix obtained from a measure on an equilibrated undercooled liquid of $B_2O_3$ near its glass transition temperature.

will start to produce less and less reliable results. A way to overcome such situation is to consider "slices" of the autocorrelation matrix. One possibility described also in [89], is taking the "cuts" orthogonal to the main diagonal, thus one obtains $C(t_w, t)$ defining $t_w = (t_1 + t_2)/2$, and $t = |t_2 - t_1|$. The other approach, adopted in this thesis, is to consider cuts parallel to one of the time axes, thus $C(t_W, t_W + t)$ with $t_W = t_1$ [1]. These two approaches are nearly equivalent, see fig. 3.5, and the principal differences are due to operative considerations linked to the finite size of the autocorrelation matrix, i.e. with the latter approach one can easily see the autocorrelation of a very young system also at large lag times, while with the former definition for a given lag time $t$ the minimum age accessible is $t_W = t/2$.

### 3.2.2 Visible photon correlation spectroscopy

Photon correlation spectroscopy is a technique originally developed precisely to be adopted with visible laser sources. The general features of a typical set-up are a focusing and collecting optics, which depending on the experimental requirements can be composed by a simple convergent leness [90] or more sophisticated objects [91], and a detector to record the scattered intensity. In standard PCS set-ups the detector is often composed by a fast photon-counting units, often an avalanche photo-diode, which produce a signal for every photon hitting their sensitive area. Typical outputs of such devices are time series of recorded events which are then correlated by dedicated electronics (correlator), and finally recorded and analysed by a computer. With these set-ups, the requirement to obtain signals with good contrast is to completely fill the sensitive area with a single speckle. These detectors,often referred as point-detectors, are capable of accessing very fast time-scales and are able to span many decades of lag times (from $\mu s$ to $100s$ ), but are limited by the contraints associated by the time average pointed out in the previous sections.
For slow or non-ergodic samples, a better approach is to employ a bi-dimensional detector, often a CCD or a CMOS. In this case the speckle-size must not be smaller than the pixel size. Depending on the pourposes the collecting optics can be of various kinds. The simples configuration is certainly the freely propagating speckle pattern. In this case the speckle-sizes are determined by eq. 3.4, but since in most of the cases the scattering volumes are highly anisotropic, gaussian beams with lengths of few millimetres and waists of $\sim 200\mu m$, the resulting speckles will be elongated in the vertical direction. One possibility to obtain a better aspect-ratio of the speckle pattern is to place a limiting aperture ( a pin-hole) between the detector and the sample. The drawback that one could often ecounter in doing so is that

the light impinging on the CCD will be below the instrument's sensitivity. Placing a convergent lens the speckle size will be mofied according to [92]

$$L_c = 1.22\frac{\lambda}{d}\left(Z_2 + Z_1\left(1 - \frac{Z_2}{f}\right)\right), \tag{3.13}$$

where $d$ is the lateral extension of the source, often defined by a pin-hole, $Z_1$ and $Z_2$ are respectively the lens-source and lens-detector distances, and $f$ is the focal length.
In case both the detector and the source are placed on the lens's focal plane it can be easily shown that the speckle size become

$$L_c = 1.22\frac{f}{d}.$$

Also, if the lens is placed to project the image of the scattering volume on the detector (imaging condition) it is possible to demonstrate that the speckle size become

$$L_c = 1.22\lambda\frac{s}{d}|M|, \tag{3.14}$$

with $M$ being the optical magnification, $d$ the pin-hole diameter, and $s$ the source - pin-hole distance. In imaging conditions the speckle aspect ratio is determined by the limiting aperture, and a good way to determine if the sample image is correctly projected on the detector is to check if the speckles have a symmetrical shape. The minimum value for $L_c$ attainable in imaging conditions is when $s$ is the lens-object distance and $d$ the lens diameter, in other words the minimum speckle-size is the lateral resolution of the collecting optics. Equations 3.13 and 3.14 are obtained here for a single lens, but in first approximation can be easily extended to more complex optical compounds.
Regardless the details of the collecting optics, when performing a multi-speckle detection with a CCD, one has to always perform some corrections to the recorded quantites to obtain the true scattered intensity. In fact, the signal, $S_p(t)$, measured by a certain pixel $p$ is affected by a time dependent electrical noise, $b_p(t)$, and by the non uniform illumination of the CCD, that in imaging conditions corresponds to the image of the beam profile. This latter contribution introduces a time independent factor $m_p$ that affects the measured intensity in the following way [2]:

$$S_p(t) = I_p(t) * m_p + b_p(t). \tag{3.15}$$

Assuming the noise contribution to be a pure random term, only its temporal average affects the final result. Therefore, it is a good practice to take a

set of dark images for each measurement (this latter advice depends on the kind of detectors one is working with, in most cases it is sufficient to collect a dataset of dark images only once in a wile). Averaging out this set of dark images one obtain $\overline{b_p}$. Then supposing the electrical noise to be completely random and uniformly distributed both in time and in space ($\overline{b_p} = \langle b_p \rangle$), subtracting $\overline{b_p}$ from the acquired data the noise contribution is then cancelled out once the average is performed. Moreover, to account for the non uniform illumination an image $M_p = \overline{S_p(t) - \overline{b_p}}$ was calculated averaging over all of the recorded frames and then normalized by its mean value obtaining $m_p = M_p / \langle M_p \rangle_p$. For experiments whose duration is much longer than the characteristic time of the probed dynamics this procedure gives a smooth function since the spatial fluctuations due to the speckle dynamics are completely averaged out. On the contrary, for measuring times comparable with the characteristic time of the probed dynamics the $M_p$ image is heavily influenced by the location of the single speckles. Therefore the $M_p$ image was further smoothed applying a median filter. In case of even slower systems, the smoothing of the mean image is not sufficient, and for these situations it is better to renounce to normalize by $m_p$ because it might affect the results for the dynamical quantities. Intuitively this is explained considering a sample with an extremely slow relaxation rate, each imaged speckle will light up or shut down following a certain distribution given by sample's properties. This means that, in the case of very slow dynamic, a certain number of speckles will persist for a considerably long period of time; if we normalize the collected images with $m_p$, even if it's smoothed, we will end up altering the contribution of the very slow speckles treating them as a static contribution.

### 3.2.3 X-ray photon correlation spectroscopy

Storage-ring based synchrotron radiation sources are chaotic sources since the emission processes of the individual relativistic electrons (or positrons) are independent and spontaneous. The coherence properties of radiation can be characterized by the energy spread of the photons, which is described by their spectral purity $\lambda/\Delta\lambda$, and the phase-space volume in which the photons are contained $(d \cdot \theta)^2$, where $d$ is the measure of the photon-beam widht and $\theta$ is the photon-beam divergence [93].
The degree of coherence of the radiation along its propagation direction, i.e., its longitudinal (or temporal) coherence, is the length (or time) over which the phase of the field amplitude undergoes no fluctuations. Let us consider two wavefronts, one at wavelength $\lambda$ and the other at a slightly different wavelength $\lambda + \Delta\lambda$,which simultaneously depart from a single point. Let

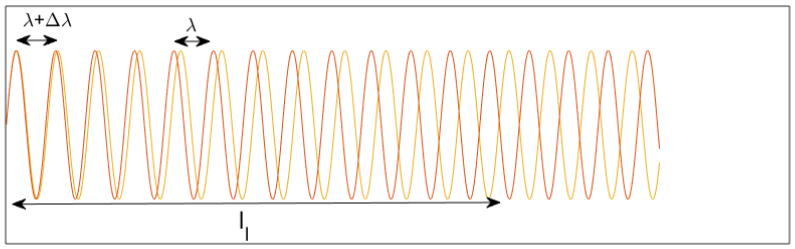


Figure 3.6: , example of two propagating waves with wavelengths $\lambda$ and $\lambda + \Delta\lambda$. The coherence lenght is defined as the distance required to produce a dephasing between the two waves of $\pi$.

us assume that after some distance $l_l$ the two wavefronts are in antiphase; see figure 3.6. If the first wave has made $N$ oscillations over that distance, the second wave must have made$N - 1/2$ oscillations. One therefore has $N\lambda = (N - 1/2)(\lambda + \Delta\lambda)$. Solving for $N$ and substituting in $N\lambda = l_l$ we find for this distance

$$l_l = \frac{1}{2}\frac{\lambda^2}{\Delta\lambda}.$$

Thus the longitudinal coherence is directly proportional to spectral purity, or inversely proportional to bandwidth.

Incoherent radiation, from sources such as ordinary light bulbs, has a broad spectral content and emits from a large area into the largest possible solid angle. Fully coherent radiation has a narrow spectral content and a phase-space volume given by the relation $(d \cdot \theta)/2 = \lambda/\pi$ [93]. Partially coherent radiation does not fully possess these limiting properties. Its spatial coherence is defined by the previous relation, but its longitudinal coherence is limited by the value of $l_l$. Because of the direct relation between the electron oscillation and the resulting radiation, the energy spread of the electrons should be small, and the phase-space volume of the electrons ( given by the product between beam width and angular divergence $\sigma_h\sigma'_h$) must be contained in the phase-space of the photons, obtaining the relation

$$\sigma_h\sigma'_h = \frac{\lambda_{min}}{4\pi},$$

where $\lambda_{min}$ is the shortest wavelength over which coherence is expected. In the X-ray regime such condition can be achieved only placing collimating apertures in the beam, this obviously greatly reduces the total photon flux and before the development of the udulator technology exploiting coherence properties of synchrotron radiation was prohibitive. Undulators are third

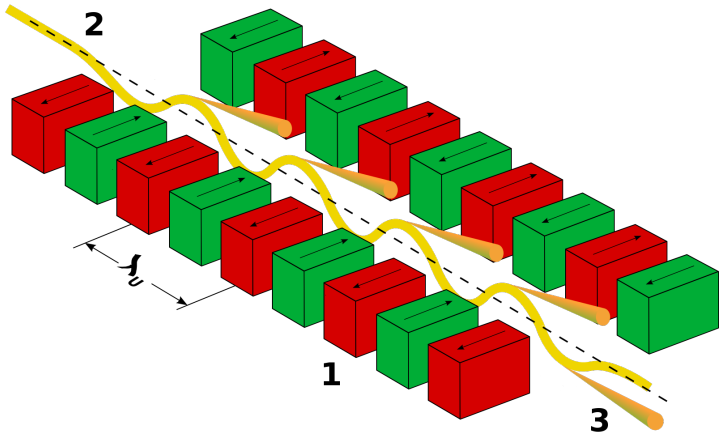


Figure 3.7: Example of the working principle of an undulator. Two sets of magnetic arrays (1) induce an oscillatory trajectory in a bunch of relativistic electrons (2) which emit synchrotron radiation in the forward direction (3).

generation synchrotron radiation light sources, they are composed by a periodic array of magnetic dipoles arranged as in fig. 3.7. If the magnet's periodicity is $\lambda_u$ and $\gamma$ is the electrons Lorentz factor, then the produced radiation will be a discrete spectrum with a fundamental wavelength given by [94]

$$\lambda_0 = \frac{\lambda_u}{2\gamma}\left(1 + 2K\right),$$

where $K$ is the undulator parameter, and the other photon energies will be multiples of the one $\epsilon_N = N\hbar c/\lambda_0$. Undulators can be extremely brilliant sources of X-rays, reaching brilliances of $10^{20}$photons/s/mrad2/mm2/0.1% bandwidth or higher. The width of the collimating aperture is determined by another transverse coherence length $l_t$ of the photon beam which can be defined via the visibility of interference fringes, that for a circular monochromatic source of diameter $\Sigma$ seen at distance $D$, is

$$l_t = \frac{\lambda}{2}\left(R/\Sigma\right)$$

Having access to a large number of coherent photons, allow the extension of the photon correlation techniques even to the X-ray regime reaching probed length-scales smaller than typical inter atomic distances (fg. 3.8). Carrying out dynamical experiments like the ones described in the previous section imply that all the scattering volume has to be illuminated by a coherent radiation, implying that the maximum path-length difference (PLD) for rays

in the sample has to be equal to or smaller than the longitudinal coherence length $l_l$ of the beam. In addition, the lateral size of the illuminated sample volume must be smaller than or comparable to the transverse coherence length $l_t$. In forward scattering the PLD between waves scattered from the centre of the sample and from the outer edge equals to

$$PLD1 = d\sin(2\theta) \tag{3.16}$$

where $d$ is the beam diameter, and $\theta$ the scattering angle. Also the sample thickness $W$, contribute to the $PLD$ . The PLD between waves scattered from the front and the back of the sample equals

$$PLD2 = W(1 - \cos(2\theta)) = 2W(\sin(\theta))^2. \tag{3.17}$$

From equations 3.16 and 3.17 we get the conditions for coherence that is [95]

$$\frac{\lambda^2}{\Delta\lambda} > max(PLD1, PLD2) \tag{3.18}$$

typically, in samll angle X-ray scattering experiments (SAXS) the strictiest requirements came from $PLD1$ [95], and starting from that, we get restrictions on the maximum q that can be probed in a coherent conditions [95]; recalling the definition 3.5 and imposing the limitation $l_l > PLD$ one obtain

$$\frac{\lambda^2}{\Delta\lambda} > \frac{dq}{k},$$

where $2\theta$ is the angle between $\mathbf{k}_{in}$ and $\mathbf{k}_{out}$. The penalty in which we will incur exceeding $q_{max}$ or violating restrictions 3.16, 3.17 will be a decrease in the experimental contrast and an intensity distribution given by equation 3.2.

### Optimal thickness of the samples

X-rays are typically strongly absorbed by condensed matter phases, but more the X-ray beam travel inside the sample, more photons will have the chance to interact with the atoms, thus to obtain good signals one has to find a compromise between these two effects. In the case of an incoming X-ray beam with initial intensity $I_0$, signal collected at scattering angle $2\theta$ and a material with absorption coefficient $\mu$ we get that the recorded intensity arising from a small portion of the scattering volume is

$$dI = I_0 e^{-\mu x} s_i e^{-\mu \frac{W-x}{\cos(2\theta)}}, \tag{3.19}$$

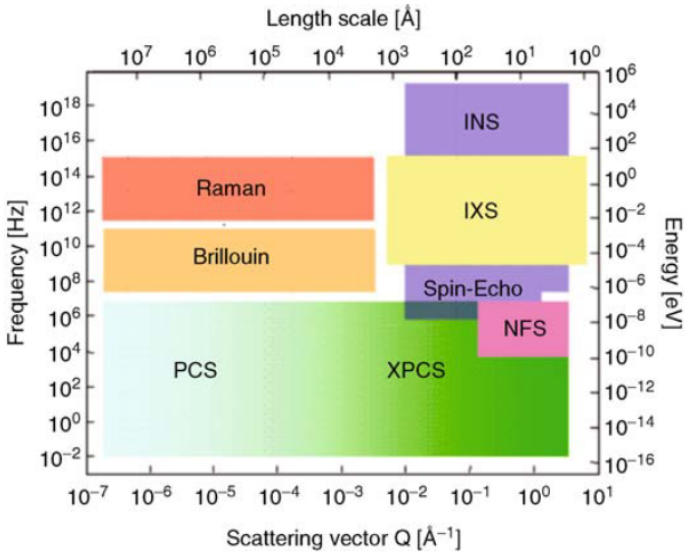


Figure 3.8: Frequency–scattering vector space covered by different experimental techniques X-ray photon correlation spectroscopy (XPCS) is a continuation of photon correlation spectroscopy with visible coherent light (PCS) in the very small length-scales. Image taken from [96]

where $s_i$ is an isotropic scattering factor and $W$ is the total sample's width. Integrating $x$ over the width we get the total scattered intensity at angle $2\theta$

$$I = I_0 s_i \frac{e^{-\frac{\mu W}{\cos(2\theta)}} - e^{-\mu W}}{\mu(1 - 1/\cos(2\theta))},$$

and we find that the value of $W$ that maximize the scattered intensity is [97]

$$W = \frac{\ln(\cos(2\theta))}{\mu\left(1 - \frac{1}{\cos(2\theta)}\right)},$$

and in the small angles limit

$$W \approx \frac{\cos(2\theta)}{\mu}. \tag{3.20}$$

These relations must always be considered taking in account the conditions imposed by the partial coherence of the light source. In the small angle regime the requirements deriving from relation 3.18 allow sample thickness of few millimetres and the only conditions derive from the absorption considerations of eq. 3.20. The situation radically changes when the experiment is performed

on scattering angles larger than few degrees, here the conditions imposed by relation 3.17 are the strictest and to satisfy them the samples would be extremely thin, i.e. for $1\mu m$ of longitudinal coherence, beam diameter of $3\mu m$ and we want to perform the experiment at 20° we need a sample thickness of $20\mu m$. For most materials this would means a loss in total number of scattered photons, so what happen in WAXS experiments is often a compromise between signal and contrast.

## 3.3 Higher order correlations

We have seen in the previous chapter that it is possible to measure the properties of the dynamical heterogeneities with the aid of four point correlation functions.

The optimal quantity for this task would be the $G_4(r,t)$, however its detection, altought possible with appropriate techniques [98], cannot be always implemented, especially in XPCS experiments. A more accessible quantity is the dynamical susceptibility $\chi_4$ which is directly linked to the variance of $C_I(t_1, t_1+t)$, ideally one has:

$$\chi_4(t) \propto \left\langle C(t_1, t_1+t)^2 \right\rangle_{t_1} - \langle C(t_1, t_1+t) \rangle_{t_1}^2 = \sigma^2_{C_I}(t) \tag{3.21}$$

and the proportionality constant would be the total number of particles in the scattering volume.
The variance of $C_I(t_1, t_1+t)$, $\sigma^2_{C_I}(t)$, is the lowest moment of the data that provides information on the fluctuations. similarly, $\sigma^2_{C_I}(t)$ quantifies the fluctuations of the intensity correlation function as the system evolves through statistically independent configurations. Intuitively, one can expect the variance of the fluctuations of the dynamics to scale as the inverse number of "dynamically independent" regions in the scattering volume, and thus to increase as the spatial range of the correlation of the dynamics increases. Inspection of the t dependence of $C_I(t_1, t_1+t)$ at fixed lag time allows temporally heterogeneous dynamics to be discriminated from homogeneous dynamics. Indeed, in the former case a large drop or increase of $C_I(t_1, t_1+t)$ is observed whenever the dynamics is faster or slower than average giving a non zero contribution to $\sigma^2_{C_I}(t)$, while in the latter case the degree of correlation keeps a constant value. This approach is quite general, since it can be applied to any experimental configuration where an autocorrelation matrix can be defined (thus any multispeckle photo-correlation experiment). However, experiments on diluted suspensions of colloidal Brownian particles have shown that the degree of correlation exhibits some fluctuations even

in the absence of dynamic heterogeneity [99]. These fluctuations are due to statistical noise stemming from the finite number of speckles in the collected images. In order to exploit quantitatively the informations obtained with $\sigma^2_{C_I}(t)$ it is thus necessary to separate the contribution to the fluctuations of $C_I(t_1, t_1 + t)$ due to the noise from that due to dynamic heterogeneity. Several strategies have been developed for such purpose, and in the present thesis the extrapolation method developed by Duri et al. [2] will be adopted. This method is based on the consideration that the temporal fluctuations of the degree of correlation $C_I(t_1, t_1 + t)$ at a fixed lag time have only two independent sources: the statistical noise due to the finite number of speckles probed in the experiment and the intrinsic fluctuations of the sample dynamics. The first contribution, referred as the measurement noise, is always present. The second contribution, on the contrary, is present only if the dynamics is temporally heterogeneous and thus represents the physically valuable information that we aim to extract from the fluctuations of $C_I(t_1, t_1 + t)$.To highlight the two different contributions, we rewrite Eq 4.3 as

$$C_I(t_1, t_1 + t) = g_2(a_1(t_1), ..., a_m(t_1), t) - 1 + n(t_1, t), \tag{3.22}$$

where $n(t_1, t)$ is the measurement noise and $\overline{n(t_1, t)} = 0$ and $g_2(a_1(t_1), ..., a_m(t_1), t) - 1$ is the two-time correlation function that will be obtained in limit of an infinite number of recorded speckles. $a_1(t_1), ..., a_\nu(t_1)$ are parameters that depend from the measurement if the dynamics are heterogeneous, but are constant for homogeneous case. Let us consider the contributes to $\sigma^2_{C_I}$ due to only the noise term. Assuming a temporally homogeneous dynamic, for example a Brownian motion, the parameters $a_1, ..., a_n$ are constant and the only fluctuations arise only from $n(t_1, t)$. Since MPCS experiments are typically performed on a large number of pixels, the central limit theorem can be applied and $\sigma^2_{C_I}$ are Gaussian distributed. Accordingly only $\overline{C_I}$ and $\sigma^2_n$ are needed to completely describe the full probability distribution of $C_I$ (since $\sigma^2_{C_I} = \sigma^2_n$). To compute $\sigma^2_{C_I}$ we recall that for a given quantity $f$ function of $n$ random variables $x_1, ..., x_n$ its variance can be expressed as a Taylor expansion

$$\sigma^2_f = \sum_{i=1}^{n} \left( \frac{\partial f}{\partial x_i} \right)^2 \sigma^2_{x_i} + \sum_{i \neq j} \left( \frac{\partial f}{\partial x_i} \frac{\partial f}{\partial x_j} \right) \sigma_{x_i, x_j}, \tag{3.23}$$

where $\sigma^2_{x_i} = \overline{x_i^2} - \overline{x_i}^2$ is the variance of the variable $x_i$ and $\sigma_{x_i,x_j} = \overline{x_i x_j} - \overline{x_i}\,\overline{x_j}$ is the covariance between $x_i$ and $x_j$. By applying eq. 3.23 to the definition of $C_I$ we find

$$\sigma^2_{C_I}(t) = \frac{1}{\overline{I}^4} \sigma^2_{G2}(t) + 2 \frac{\overline{G2(t)^2}}{\overline{I}^6} \sigma^2_I + 2 \frac{\overline{G2(t)^2}}{\overline{I}^6} \sigma_{I,J}(t) - 4 \frac{\overline{G2(t)}}{\overline{I}^5} \sigma_{G,I}(t)$$

where $G2(t) = \overline{\delta I(t_1)\delta I(t_1+t)}$, and $J(t) = I(t_1+t)$ ($\overline{I} = \overline{J}$). The origin of the fluctuations of $I$ and $G2$, and their covariances, stems from the finite number of pixels. In [2] is demonstrated how $\sigma_I^2, \sigma_{G2}^2, \sigma_{I,J}$ and $\sigma_{I,G2}$ scales as $1/N$ where $N$ is the number of probed pixels, and that, due to the definition 4.3, the fluctuations of the statistical noise can be expressed as a third order polynomial dependence from $\overline{C_I(t)}$

$$\sigma_n^2(t) = \frac{1}{N}\sum_i^3 \alpha_i \overline{C_I(t)}^i = \frac{\Omega(t)}{N}. \tag{3.24}$$

Thus for $N \to \infty$ $\sigma_n^2(t) \to 0$.
When the sample dynamic is heterogeneous, the measured fluctuations fluctuations will be described by

$$\sigma_{C_I}^2(t) = \frac{\Omega(t)}{N} + \sigma_{g_2}^2(t),$$

where the first term is the measurement statistical noise, and the the second is the physically relevant dynamical heterogeneity. The latter, contrary to the noise term, does not depend on the number of pixels over which $C_I$ is averaged. This argument is easy to understand when the scattering experiments are performed in the far field geometry in which each pixel receive light scattered by the whole illuminated sample. Thus, any spatial or temporal heterogeneity of the dynamics affects in the same way the signal measured by each pixel. The different pixel-number dependence of the noise and the fluctuations suggests a way to discriminate between these two contributions. Thus as described in [2], analysing the speckle images by processing different number of pixels, and plotting $\sigma_{C_I}^2(t)$ as a function of $1/N$, as shown in fig. 3.9. The slope of a linear fit to the data yields $\Omega(t)$ , while the intercept at $N^{-1} = 0$ is $\sigma_{g_2}^2(t)$, the desired variance of the correlation function due to dynamical heterogeneity. Operatively, the procedure is as follows. First, all pixels of each image are processed and $C_I(t)$ and its variance $\sigma_{C_I}^2(t)$ are calculated. Each image is then divided into two regions of interest (ROI) of equal size. For each ROI, $C_I(t)_2$ and its variance are calculated and the values of $\sigma_{C_I}^2(t)_2$ obtained for the two ROIs are averaged, yielding the variance of $\sigma_{C_I}^2(t)$ when only N/2 pixels are processed. This scheme is iterated as long as the size of each ROI contain a meaningful quantity of different speckles.

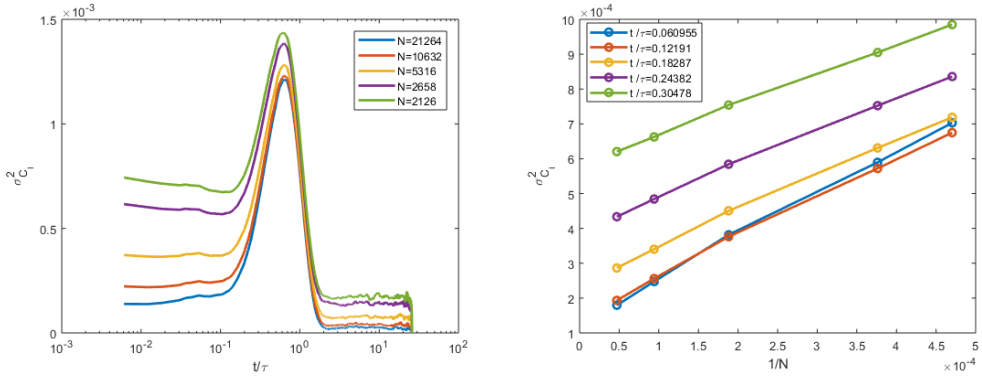


Figure 3.9: Left: $\sigma^2_{C_I}(t)$ at various ROI sizes. Right: $\sigma^2_{C_I}(t)$ as a function of $1/N$ for different lag times. Data obtained from an aging sample of $B_2O_3$.

### 3.3.1 General properties of the dynamical heterogeneity arising from stretched exponentials relaxations

We have now a tool to extract $\sigma^2_{g_2}(t)$ from the experimental data, and we can introduce a general approach to the interpretation of the observed results. Many relaxation processes in glassy systems (and in many other situations) are described by a stretched exponential function

$$g_2(f_q^2(t_1), \tau(t_1), \beta(t_1), t) - 1 = f_q(t_1)^2 e^{-2(t/\tau(t_1))^{\beta(t_1)}}, \tag{3.25}$$

where $f_q^2$ is the non ergodicity level, $\tau(t)$ the relaxation time and $\beta(t)$ the stretching exponent. Here we are considering the most general case in which all the parameters can in principle fluctuate in time. Applying equation 3.23 we get :

$$\left(\frac{\partial g_2 - 1}{\partial f_q^2}\right)^2 \sigma^2_{f_q^2} = e^{-4(t/\tau)^\beta} \sigma^2_{f_q^2}$$

$$\left(\frac{\partial g_2 - 1}{\partial \beta}\right)^2 \sigma^2_{\beta} = 4(f_q^2)^2 \left(\frac{t}{\tau}\right)^{2\beta} \ln^2\left(\frac{t}{\tau}\right) e^{-4(t/\tau)^\beta} \sigma^2_{\beta}$$

and lastly for the relaxation time

$$\left(\frac{\partial g_2 - 1}{\partial \tau}\right)^2 \sigma^2_{\tau} = 4(f_q^2)^2 \frac{\beta^2}{\tau^2} \left(\frac{t}{\tau}\right)^{2\beta} e^{-4(t/\tau)^\beta} \sigma^2_{\tau}$$

if the three parameters are independent their covariances are equal to zero, and we get

$$\sigma^2_{g_2-1} = 4(f_q^2)^2 \left(\frac{t}{\tau}\right)^{2\beta} \left[\left(\ln^2(t/\tau)\,\sigma^2_{\beta}\right) + \left(\frac{\beta^2}{\tau^2}\sigma^2_{\tau}\right)\right] e^{-4(t/\tau)^\beta} + e^{-4(t/\tau)^\beta} \sigma^2_{f_q^2} \tag{3.26}$$

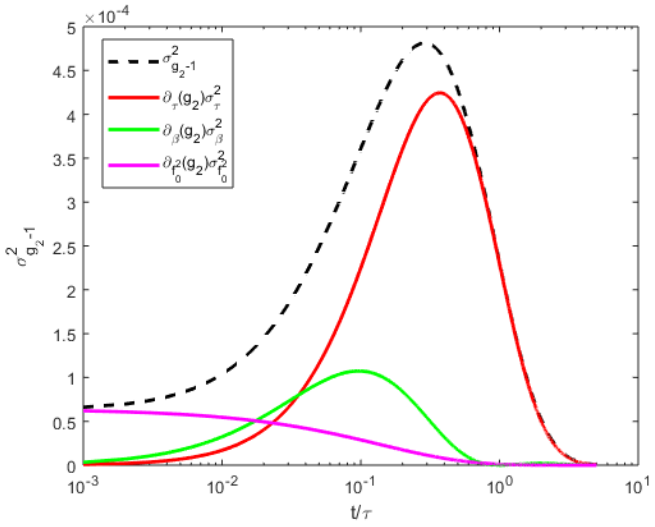


Figure 3.10: Example of the expected dynamical heterogeneity for a stretched exponential function with $\beta = 0.7$, $\tau = 1000$ and $f_0^2 = 0.8$. Red: contribution due to the fluctuations in $\tau$,green: contribution due to the fluctuations in $\beta$,magenta: contribution due to the fluctuations in $f_0^2$, black: fluctuations of $g_2 - 1$ .

In figure 3.10 is represented a numerical example for the expected $\sigma^2_{g_2-1}$ for a stretched exponential without the cross-correlation terms, the conrtibution arising from contrast fluctuations is a monotonically decreasing term, while the contribution from the fluctuations of the relaxation time is a peaked function at values close to $\tau$, the term due to the fluctuations in shape ($\beta$) is still a peaked function, but with a maximum located at shorter time-scales. It is interesting to point out that both the contributions to $\sigma^2_{g_2-1}$ coming from the relaxation time and the stretching exponent are directly proportional to the squared value of the non ergodicity level. Typically, the fluctuations of $\tau$ are the main contribution to $\sigma^2_{g_2-1}$, and considering only this term, it's easy to compute the lag time $t^*$ corresponding to the dynamical susceptibility peak

$$t^* = \frac{1}{2^{1/\beta}}\tau.$$

# Chapter 4

# Aging in diboron trioxide glass

## 4.1 Aging in structural glasses

We have seen that in general therms, what differentiates a glass from an undercooled liquid is its out of equilibrium condition and consequently that its physical properties explicitly depend on the time elapsed since the glass creation, or more generally, they depend on the thermal history of the sample.
Glassy materials, such as polymers, alloys, silicates and so on, change their properties even years after the time when they have been produced [43, 100]. The basis of this physical aging is the process of establishing equilibrium, usually studied after a decrease in temperature below the glass transition temperature $T_g$. Aging is the key to understand the gradual changes in volume, density, transport coefficient and other properties as a function of time after the departure from equilibrium. The mechanisms responsible for aging are the same that govern the structural relaxation in the undercooled liquid state, with the added complication that the aging rate depends not only on the temperature but also on the internal structure of the glass that changes during aging [101].
The aging phenomenon is now a known topic and it has been described at many theoretical levels. An important phenomenological model developed to describe the aging process is the Tool-Narayanswanmy-Moynihan (TNM) framework [102, 35, 103], specifically designed for the treatment of structural glasses. The first quantitative description of the aging phenomenon can be dated back already in the forties [102] and a complete formulation was given in the seventies [103]. The description stems out from an initial simple consideration: after a temperature jump the properties of the sample change as a function of the new temperature and of the internal dynamics that

evolves in the glass. The temperature dependent change, which occurs almost instantaneously, leads to a slight change of the average distance between the atoms. The time dependent changes are more complex and can be imagined to be brought by several mechanisms of atomic rearrangements. Thus to describe structural state of a nonequilibium glass exactly, it is necessary to specify not only its pressure, temperature and other order parameters, but also an additional set of parameters that describes the progress of the relaxation mechanisms. Given $p$ a generic physical property (e.g. the free volume or the density) and considering its dependence in temperature in the linear approximation ($p \propto T$) the coefficient in the liquid region is described by

$$\alpha_{pl} = \frac{1}{p}\frac{\partial p}{\partial T} \qquad \alpha_{pl} = \alpha_{pg} + \alpha_{ps}$$

where $\alpha_{pg}$ is the coefficient that describes the temperature dependent change, while $\alpha_{ps}$ describes the structural changes. In the liquid region the structural rearrangements are very fast and practically, only $\alpha_{pl}$ can be measured, while in the glassy state the internal dynamics becomes nearly arrested and typically only $\alpha_{pg}$ is observed. We can think of $\alpha_{pg}$ as the short time response and $\alpha_{pl}$ as the long time response to a temperature change. Another important quantity that we have to define is the response of our generic property $p$ after a temperature jump $\Delta T = T_1 - T_2$

$$M(t, \Delta T) = \frac{p(t) - p_{2\infty}}{p_1 - p_{2\infty}} = \frac{T_f(t) - T_2}{T_1 - T_2}$$

where $p_1$ is the initial value of the equilibrated property, $p_{2\infty}$ corresponds to the asymptotic value of the equilibrated property at the new temperature $T_2$. With this relation we have operatively defined an important concept: the fictive temperature $T_f$ for the observable $p$. It is important to outline the fact that as it is defined, the fictive temperature is in general different for different physical properties. Before proceeding with a more detailed description it is useful to clarify the assumptions over which this model is based: i) structural relaxation is treated here as a single stretched exponential mechanism with a constant activation energy, This assumption is equivalent to postulating the existence of several relaxation mechanisms with identical activation energies; ii) The slope of the equilibrium response curve is assumed to be fixed and changes in actual and fictive temperature are assumed to simply alter the time scale; iii) The intrinsic relation between force and flow is assumed linear, in other words this model works with constant temperature coefficient only, i.e. physical properties as expansions coefficients, heat capacity etc... are assumed not to change significantly in the temperature range over which the

experiment is performed. With these assumption it is possible to describe the generalized equation of the evolution of the property $p$ in response to an arbitrary temperature jump $T(t)$

$$p(t) - p(0) = p(0)\alpha_{pl}(T - T_0) - p(0)\alpha_{ps}\int_0^{\xi} M(\xi - \xi')\frac{dT}{d\xi'}d\xi'$$

where $\xi$ is the reduced time

$$\xi = \int_0^t \frac{dt'}{\tau(T, T_f)}$$

and from [102, 35, 103]

$$\tau(T, T_f) = \tau_0 e^{\left(\frac{xE}{k_b T} + \frac{(1-x)E}{k_b T_f}\right)} \tag{4.1}$$

In the original idea proposed by Tool [102] it was stated that for every non equilibrium state there exists a single corresponding equilibrium state. Thus the original definition of fictive temperature was the actual temperature of an hypothetical equilibrium condition that corresponds to the given non equilibrium condition. As a consequence of this interpretation of the fictive temperature, the memory effect wasn't appropriately described by the simple Tool's model. Here the non equilibrium state is described as a mixture of different equilibrium states, accordingly the fictive temperature can be defined as:

$$T_f = T + \int_{\xi(T)}^{\xi(t_0)} M(\xi - \xi')\frac{dT}{d\xi'}d\xi'$$

or in the more compact way [35]

$$T_f = T_0 + \Delta T\left(1 - e^{-\left(\int_{t_0}^{t}\frac{dt'}{\tau(T,T_f)}\right)^{\delta}}\right) \tag{4.2}$$

with $\delta \in [0, 1]$.

This phenomenological model has been proven to be very effective in the description of the time evolution of the glassy physical properties with the "only" requirement of knowing exactly the thermal history of the sample.The physical observable measured in the experiments here reported is the internal dynamics itself and so a little deeper description of the aging glass is needed. Let's recall briefly what was previously said in chapter 2. We have seen that for a general correlation function it is possible to identify a fast equilibrated dynamics and a long time aging relaxation.

$$C(t_w, t_w + t) = C_{eq}(t) + C_{aging}(\frac{t_w + t}{t_w})$$

where the characteristic time of the aging part corresponds to the $\alpha$ relaxation $\tau_\alpha$, and typically it is seen that $\tau_\alpha(t_w) \propto t_w$ [43]. In these cases one talks of full aging. Actually, for many systems a milder dependence is reported, namely $\tau_\alpha(t_w) \propto t_w^\mu$ with $\mu \in [1/2, 1]$, and one refers to these cases as sub-aging [104]. It has been found through numerical simulations that the occurrence of sub-aging or full-aging depends on how far from eqilibrium the observed glass is [72]. From these models another requirement is deduced for $C_{aging}$, that is the property that all the $C_{aging}$ taken at different $t_w$ rescale onto a single master curve, this property is often called time aging-time superposition [43, 104]. This time-aging time superposition principle has been challenged by some experimental results [101, 73] and also some fundamental consideration are against it. In fact, in the hypothesis that the structural dynamics is of heterogeneous origin, then is is legit to expect that each microscopic region will reach equilibrium on timescales dictated by its own dynamics. Thus, during the aging, the overall distribution of relaxation frequencies will results distorted, and hence the final shape of the observed relaxation function will emerge altered in respect to an equilibrated one.
For most glasses of common use, this aging process takes place on very long time scales, few experiments have been performed in these conditions, and the time required to observe a significant change is definitively too long for the current capabilities of a DLS set-up, even with the multispeckle approach[100, 105]. Nevertheless looking not too deep in the glass transition region it is possible to observe aging phenomena on more reasonable time scales.

## 4.2 Diboron trioxide

Diboron trioxide, together whit silica and germania, is one of the most widely used glass formers and can be found mixed with other oxides and other elements in a lot of common use objects, for example the main ingredients of the majority of cooking glassware are $SiO_2$ and $B_2O_3$. The glasses obtained mixing boron oxide and silica are usually characterized by high chemical stability and low thermal expansion coefficient making them the best choice for the containment of chemically reacting materials in a lab or food in the kitchen. However in its pure form, boron oxide presents very different characteristics, starting from the coefficient of thermal expansion higher by about 2 orders of magnitude whith respect to borosilicates [106], to the low chemical stability, in fact diboron trioxide reacts with water forming boric acid $BH_3O_3$, and even the presence of very small quantities of water can strongly affect the final dynamical properties of the glass and it is sufficient

to expose the samples to ambient humidity to see a significant change in the glass transition temperature. Despite all these complications, pure boron trioxide presents some properties that make it a very good sample when one wants to study a system in the glass transition region; in first place, its $T_g$ is quite close to room temperature in respect to the other oxides (ranging from 525 K to 570 K [107, 108, 109, 110, 111, 112, 113]) and above all the crystallization of molten $B_2O_3$ at ambient pressure is strongly kinetically disfavored [114] making it possible to cool the samples even with very slow cooling rates and to keep the samples in the undercooled liquid state for very long periods without worrying about the occurrence of the crystallization.

## 4.3 Sample preparation

All samples were prepared starting from anhydrous powder of $B_2O_3$ purchased from Sigma Aldritch. Small quantities, typically between 2 to 3 grams, of this powder were loaded inside quartz glass test tubes, with 10 mm of inner diameter, 80 mm of height and 1 mm of wall thickness.
in order to obtain water-free samples, before melting the powder the loaded test tubes were slowly heated to $140°C$, enhancing the degradation of boric acid and the dessication of the powders [115]. Boron oxide melts at $T_m = 650°C$, however since it is a rather viscous material, the test tubes were carried at $950°C$ and held at that temperature for a long period (typically 48 hours) in order to let all the bubbles formed inside the melt to exit from the bulk; then, taking advantage of the exceptional glass-forming ability of boron oxide, the samples were slowly cooled to $330°C$ in order to minimize the creation of stresses between the $SiO_2$ glass of the tube and the $B_2O_3$. A typical thermal treatment for the glass production was:

- from room temperature to $140°C$ at 1 K/min
- held at 140 for 3 hours
- from $140°C$ to $950°C$ at 1 K/min
- held at $950°C$ for 48 hours
- from $950°C$ to $330°C$ at 0.5 K/min

Actually, for the production of bubble free samples, $950°C$ for 48 hours is an oversized amount of time, however we noticed that the reduction of the duration of this step strongly influenced the glass transition temperature in the final glass, indicating the presence of contaminating substances trapped

inside the network (most probably water molecules) [107].
Once the samples reached $330°C$ (603 K) they were immediately transferred inside a furnace (ready at the same temperature of the preparation oven) specifically designed for light scattering experiments. All of the samples obtained in this way appeared, with a simple visual examination, completely transparent and homogeneous. This "hot" transfer between furnaces was necessary in order to minimize the stresses between the sample and the quartz tube containing it. In fact, the first sample were cooled down to room temperature, and the subsequent attempts to reheat them resulted in an explosion of the couvette and in the shattering of the boron oxide glass.

## 4.4 Experimental set-up

The DLS setup was based on a 532 nm green laser as light source with a beam attenuated to powers ranging between $\simeq 15\ mW$ and $\simeq 100\ mW$ at the sample position on a spot of $\simeq$100 $\mu$m in size. The sample was held in a silica cilindrical couvette (inner diameter of 7 mm) placed in a furnace with a temperature control to within 0.1 K. The radiation scattered at an angle of $90^o$ from the incoming beam was first selected by an aperture and then imaged by a lens on a CCD (Atik 11000) connected to a PC. The CCD has pixels 9 $\mu$m in size. It was possible to change the lens-sample position in order to reach different magnifications of the scattering volume, the aperture, composed by an adjustable iris, was changed for every configuration in order to maintain a similar pixel size to speckle size ratio. In fig 4.1 is reported a drawing of the implemented set-up, the distances are not in scale, in fig 4.2 a picture of the actual set up, and of the sample holder. For the experiments reported in this chapter, the magnifications of the scattering volume where setted to be 1:1 for the measurements of the undercooled liquid, and 3:1 for the measurements of the aging system.

## 4.5 Results for $B_2O_3$

The details of the two time autocorrelation matrix and the autocorrelation function have been reported in the previous chapters, but let's recall briefly the most important definitions: the autocorrelation matrix

$$C(t,\tau) = \frac{\langle \delta I_p(t) \delta I_p(t+\tau) \rangle_p}{\langle I_p(t) \rangle_p \langle I_p(t+\tau) \rangle_p}, \tag{4.3}$$

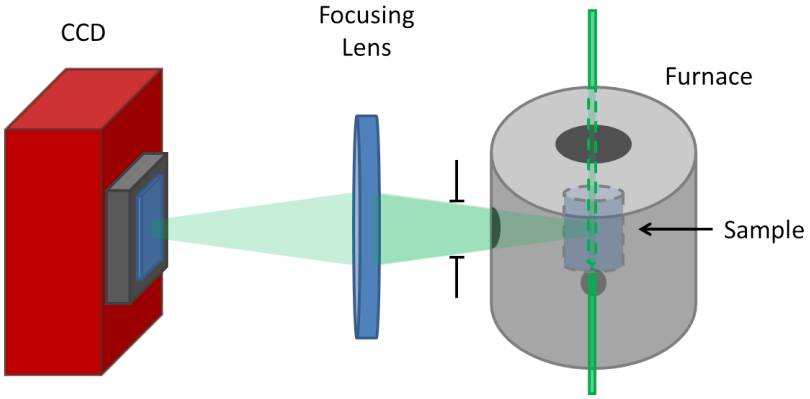


Figure 4.1: schematic representation of the set-up implemented for the measurements carried out in the present chapter

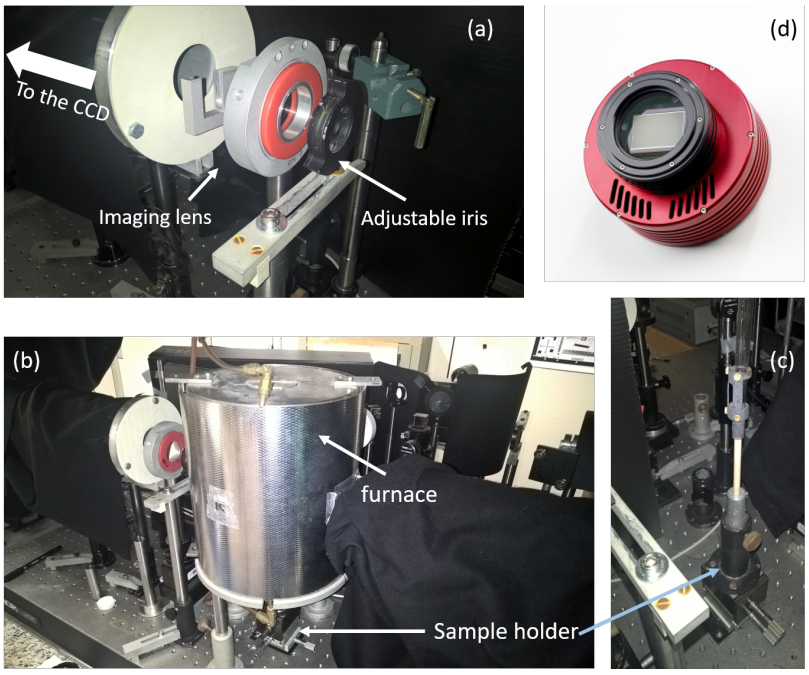


Figure 4.2: picture of the various components of the set-up. (a) picture of the adjustable iris and imaging lens. (b) Picture of the furnace placed inside the optical set-up. (c) picture of the sample holder, usually located inside the furnace. (d) picture of the Atik 1100 camera.

where $I_p(t)$ is the intensity collected by pixel $p$ at time $t$, $\langle \ldots \rangle_p$ indicates the average over the pixels and $\delta I_p(t) = I_p(t) - \langle I_p(t) \rangle_p$.
The autocorrelation function:

$$g_2(\tau) - 1 = \overline{C(t,\tau)}. \tag{4.4}$$

And lastly the Siegert relation:

$$g_2(\tau) - 1 = A|\Phi_q(\tau)|^2, \tag{4.5}$$

An example of an autocorrelation matrix $C(t,\tau)$ computed for measurements collected at $T$=503 K is reported Fig.4.3.

We can use an equilibrated undercooled sample to test the robustness of the multispeckle photon correlation (MPCS). In Fig. 4.4 are reported different curves that correspond to different time intervals (ranging from 5 minutes up to 3 hours) used to compute the time averages in Eqs. 4.4 and 4.5 starting from the same autocorrelation matrix shown in Fig. 4.3. These curves are all mutually consistent, indicating that i) the MPCS is a reliable technique also for integration times similar and even smaller than the characteristic time of the probed dynamics, ii) even with relaxation times of thousands of seconds we are observing an equilibrated undercooled liquid.

### 4.5.1 Equilibrated undercooled liquid

The measurements were carried out starting from 553 K, i.e. above the glass transition temperature ($T_g$ =526 K for our samples). Between measurements at one temperature and the following one, the sample was cooled down at a rate of ∼3 K/min. The CCD data were collected only in the region of interest (ROI), corresponding to the image of the sample (30x500 pixels in size). With this choice of the ROI a rate of ≃1 frame/s was achieved. Every CCD image was collected with an integration time of 0.1 s/frame. The collecting lens was positioned in a imaging condition with a magnifying factor M=1 and a pin-hole aperture chosen in order to obtain an average speckle-size of $\approx 3$ $\mathsf{pixels}^2$.

In figure 4.5 the final autocorrelation functions are reported for different temperatures across the glass transition. The data are fitted using a stretched exponential function

$$g_2(t) - 1 = A|f_0 e^{-(t/\tau_\alpha)^\beta}|^2 \tag{4.6}$$

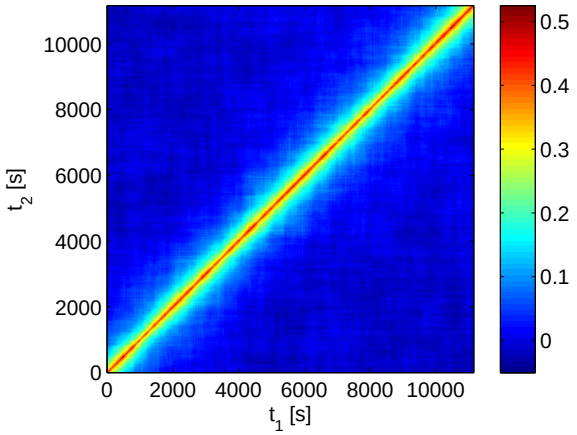


Figure 4.3: Autocorrelation matrix computed for a temporal sequence of scattered intensity images collected at $T$=503 K. This sequence lasted 4 hours in order to see the decorrelation of the signal.

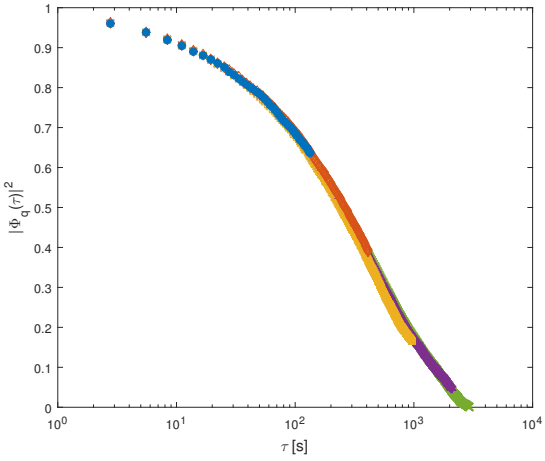


Figure 4.4: Square modulus of the normalized intermediate scattering function, $|\Phi_q(\tau)|^2$, calculated for different lengths of the temporal sequence of images, $T_m$. The different curves correspond to $T_m$=280 s, 837 s, 1953 s, 4185 s and 8649 s (blue, orange, yellow, purple and green symbols, respectively). In terms of fractions of $\tau_r$ they range from $T_m/\tau_r = 0.18$ (blue circles) to $T_m/\tau_r = 5.7$ (green crosses).

from which $\tau_\alpha$, $\beta$ and $Af_0^2$ are deduced. The stretched exponential function follows the experimental points quite closely in the first time lags. For longer time lags the experimental data show larger statistical fluctuations since the number of $C(t,\tau)$ elements decreases as $\tau$ increases.

The values obtained for the stretching exponent $\beta$ come out to be equal to 0.67±0.09 and don't show a marked temperature dependence in the investigated region, as can be seen from figure 4.7. This result is consistent with the ones that can be found in literature, i.e. $\beta$=0.65±0.03 [111, 84] and $\beta$=0.6 [117]. However, it has been observed a weak temperature dependence that tend to produce more stretched autocorrelations for lower temperatures [111].

The results obtained for the mean value of $\tau_\alpha$ are reported in Fig. 4.6 where they have been calculated as $\langle\tau_\alpha\rangle = \Gamma(1/\beta)\tau_\alpha/\beta$ [47]. The temperature dependence of $\tau_\alpha$ follows an exponential behaviour that can be described by the empirical formula $\tau_\alpha = \tau_0 exp(B/T)$. The quantity $B$ is proportional to the activation energy, $E = B \cdot k_B$, or to the fragility index $m = B/T_g$. The results here obtained for $\langle\tau_\alpha\rangle$ are compared on an Arrhenius plot to the data of previous experiments on $B_2O_3$ [116, 111, 84]. While the three sets of data show the same slopes within the experimental error (i.e. the same activation energies), the glass transition temperatures, e.g. the temperatures where $\langle\tau_\alpha\rangle$=100 s, are quite different: $T_g$=526 K for our sample ($q \sim 0.0242 nm^{-1}$), 556 K for that of Ref. [111] ($q \sim 0.0264 nm^{-1}$) and 569 K for that of Ref. [116] ($q \sim 0.0251 nm^{-1}$). A possible explanation for this difference can be found in the fact that, as previously anticipated, several physical properties of $B_2O_3$ are very sensitive to the presence of residual water molecules, and therefore critically depend on the sample preparation procedure [109]. As a matter of fact, the values of $T_g$ reported in the literature span a temperature range of about 45 K between 525 K and 570 K [107, 108, 109, 110, 111, 112, 113].

The $\langle\tau_\alpha\rangle$ data here presented follow quite closely an Arrhenius behaviour as shown by the linear fit reported in Fig. 4.6. From the slope of this linear fit it is possible to calculate the fragility index, $m$ [117]. We obtain for $m$ a value of 29±1, well compatible with the value of 27±3 obtained from the literature [84].

In addition to $\tau_\alpha$ and $\beta$, it is possible to obtain also the non-ergodicity level $f_q$ from the fits reported in Fig. 4.5 once the instrumental factor $A$ appearing in Eq. 4.5 is known. The factor $A$ is in turn evaluated in two

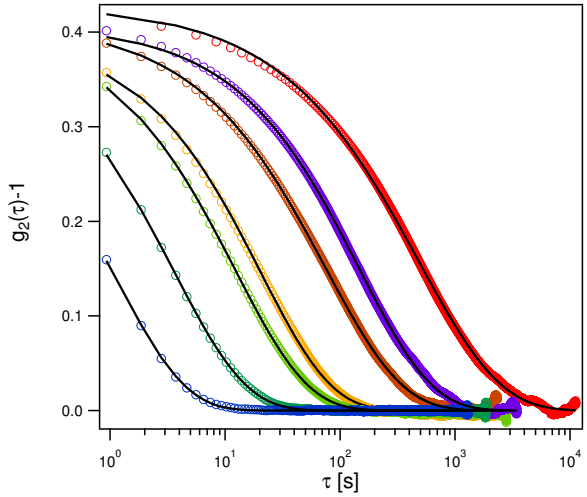


Figure 4.5: Circles : autocorrelation functions obtained for different temperatures across the glass transition region of $B_2O_3$ (from left to right: $T$= 553 K, 543 K, 533 K, 528 K, 518 K, 513 K, 503 K ). Solid lines: fitted curves using Eq.4.6.

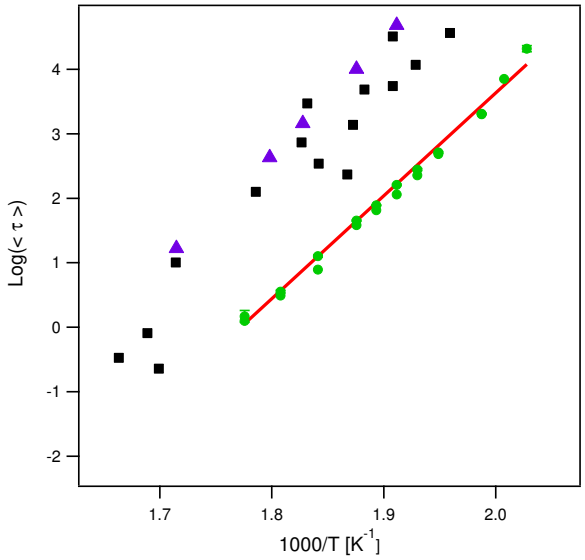


Figure 4.6: Average relaxation times obtained in the present work (green circles) and compared to literature data obtained using a traditional single-speckle setup [111](black squares) and obtained via DLS and volume relaxation measurements [116] (purple triangles). Red line: linear fit to the present data, indicating that $\langle \tau_r \rangle$ follows closely an Arrhenius behaviour in the investigated temperature range.

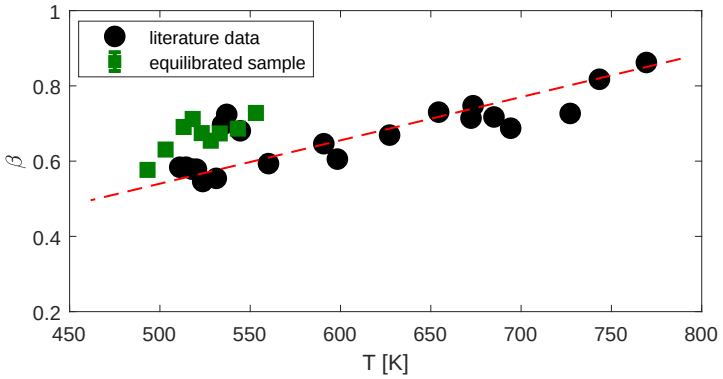


Figure 4.7: measured $\beta$ in the undercooled liquid regime compared with literature data from [111], the red dashed line is a guide to the eye.

steps: i) comparing a correlation function measured using the multi-speckle setup here presented and that measured using a conventional setup based on a photomultiplier on the same sample in the same conditions; ii) evaluating the instrumental factor relative to the photomultiplier setup measuring a standard dilute solution of 100 nm diameter silica spheres in water. Using the data reported in Fig. 4.5 and the instrumental factor evaluated in this way it is possible to estimate for $f_q$ a value of 0.82±0.05. This result is consistent with the value $f_q$=0.75±0.03 reported in Ref. [84]. Moreover, it is also interesting to compare the value of $f_q$ here obtained with the values of the zero-frequency longitudinal elastic modulus, $M_0$ and the infinite-frequency longitudinal elastic modulus, $M_\infty$, given that $f_q = 1 - M_0/M_\infty$ [88]. Using literature values for the elastic modulus in the low frequency limit [116, 118] and in the high frequency limit obtained with ultrasonic and Brillouin light scattering techniques [119, 120], respectively, we find $f_q = 0.86 \pm 0.03$ at $T$=523 K, which is well consistent with the result obtained here.

We have seen how this diboron trioxide behaves in the glass transition region in the equilibrated undercooled condition and how, with the right amount of patience, slow cooling rates and time for the sample to equilibrate, we can reach relatively low temperatures below $T_g$. But what happens if we do not wait this much time to cool before measuring our samples? Then our system will eventually fall out of the equilibrium and start to age, what we have inside our furnace will then be a proper glass.

### 4.5.2 Aging glass

Even for these measurements the experimental set-up didn't change substantially: green laser, 90° scattering geometry and imaging configuration. The main difference it the increased magnify factor, now 3:1.The increased enlargement is the best compromise between good statistic (i.e. for a fixed speckle size, larger the images, larger the number of pixels exploitable to compute the autocorrelation matrix) and physical extension of the experimental set-up which is directly linked to the thermal stability of the whole apparatus. In fact even small changes in the laboratory's temperature ($\sim \pm 0.25k$ in 20 minutes ) can induce changes on the optical apparatus in the order of few $\mu m$, these shifts are magnified by the collecting optics and if this magnified thermal drift covers a distance comparable with the pixel size then it will begin to affect even the measured dynamical properties limiting de facto the maximum observable relaxation time.Even in this case the pin-hole aperture was chosen in order to have the average speckle-size of $\sim 3$ $\mathsf{pixel}^2$.
In order to create our out-of-equilibrium system we let our sample equilibrate at temperatures 10 K above $T_g$ and then we change the set point of the furnace to a value below $T_g$. Thus the sample will change its temperature with a rate defined by the furnace's heat capacity, that in our case is $4.4K/min$. In figure 4.9 three thermal histories are shown. After this cooling, we give some time to our system to equilibrate at the new temperature, typically 20 minutes, and we start the analysis, in other words we set $t_W = 0$. One could argue that a more precise identification of the $t_W = 0$ can be obtained identifying the exact instant in which the sample's internal dynamics is outrun by the changing temperature, namely looking at the intercept between the equilibrium Arrhenius curve and the curve of the sample's thermal history like how is is done for the more canonical phase transitions in a TTT diagram [26], see fig 4.8. However doing so we would take in our analysis even times at which our sample is still driven out of the equilibrium by the thermal treatment. This choice of the origin of the sample's age is indeed quite arbitrary, but given our quite "mild" temperature treatment it is the safest way to distinguish between an undercooled liquid driven in an out of equilibrium condition with a temperature jump and the proper glassy phase. More pragmatically, this choice allows us to look at our glass knowing, at least macroscopically, that there are not strong "artificial" temperature gradients inside the scattering volume.

The speckle patterns are recorded during the whole process and we can look the effects of cooling on the autocorrelation matrices. In fig 4.9 some examples are reported, it can be seen that at the beginning the system is

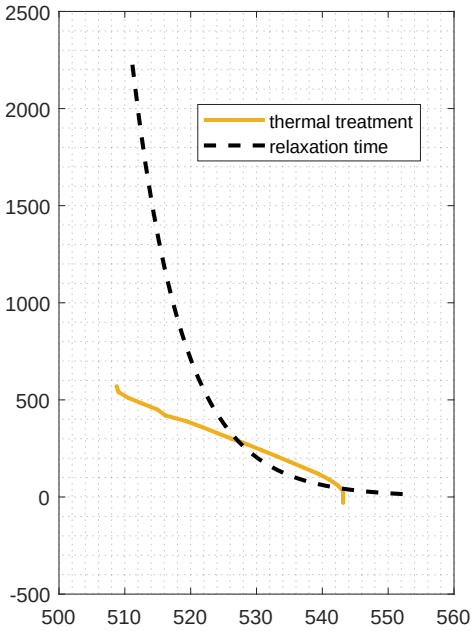


Figure 4.8: one of the thermal treatments of fig.4.9 plotted alongside the equilibrium relaxation times computed from the fit parameters of the Arrhenius law. The intersection between the thermal protocol and the Arrhenius curve can be seen as the first instant in which the internal dynamic of the system is outrun by the external temperature change.

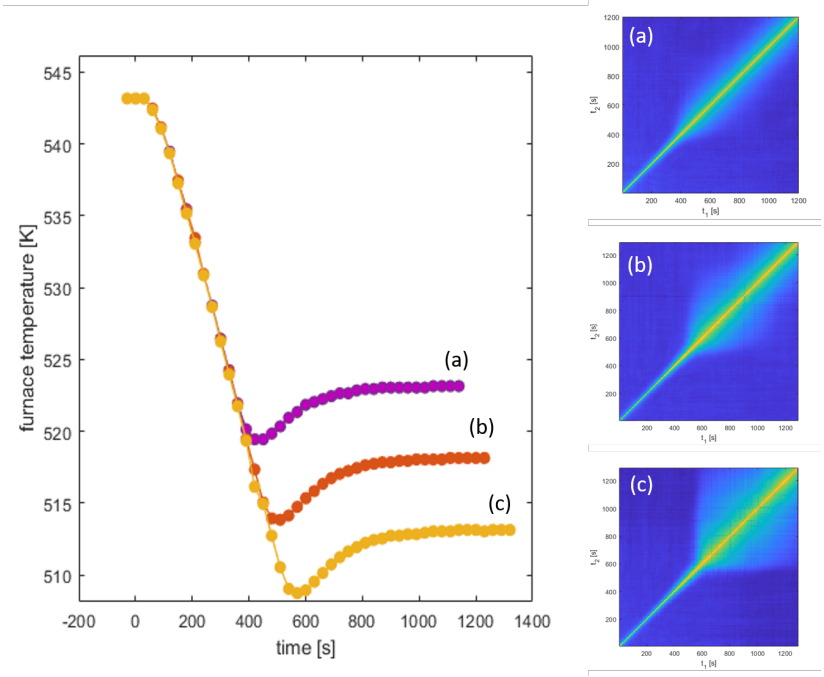


Figure 4.9: examples of three different temperature jumps. On the left, the recorded fournace temperature is reported against the time elapsed since the change of the setpoint. The final temperatures are $250°C$ (a), $245°C$ (b) and $240°C$ (c). On the right the corresponding two times autocorrelation matrices are reported

still in equilibrium with a relaxation time of about 30s. Then, when the temperature of the furnace starts to change, the correlation begins to increase in a quite steep way (about 1 or 2 orders of magnitude in few minutes) until it reaches the new temperature and then begin to slowly increase with the waiting time as reported in fig 4.10. The relaxation times shown in fig. 4.10 are obtained computing Pearson autocorrelation function (i.e. $C(t,t) = 1$ and $C(t,t') = 0$ for $t' - t \to \infty$) and then finding the lag time at which $C(t_W, t_W + \tau) = e^{-2}$. In the cooling regime we can observe how the values obtained for this "effective relaxation time" increase quickly indicating that the system's dynamic appears to be completely determined by the external temperature.

When the temperature settled at the final value and the sample's bulk has thermalized we can begin our aging measurements. Obviously the rough thermal treatment, that inevitably goes with every experiment on aging, and the finite size of our sample will lead to the formation of internal stresses inside the bulk, and we will shorty see what are the consequences of these

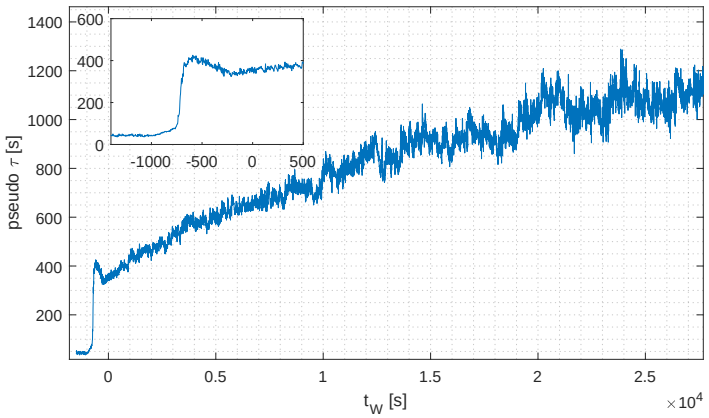


Figure 4.10: relaxation time defined as the lag-time at which the autocorrelation functions reach the value exp(-2) for an aging sample. In this case the temperature jump was from 543.15 K to 513.15 K. In the inset the initial time behaviour is reported. The very first data points correspond to the equilibrated undercooled liquid, while the sharp jump corresponds to the temperature decrease

stresses.

There exist several ways to deal with an autocorrelation matrix for an aging process; the most straightforward one is simply to select small matrices from the total autocorrelation matrix and compute the $g_2 - 1$ for each sub-matrix collecting the autocorrelation functions at different waiting times. The advantage of this approach is a more robust and simple interpretation of the results, while on the other side we have a rather coarse sampling of the ages of the sample giving a sensitivity on $t_W$ bounded to be a multiple of the $\alpha$ relaxation time, (i.e. in order to obtain reliable fits of the data is always a good practice to see a full decorrelation for the $g_2 - 1$).

For deep temperature jumps it is not possible to reach the equilibrium in a reasonable time or, for very low temperatures, avoid the shattering of the sample as a consequence of the building up of the internal stresses. In this regime, the time required to reach equilibrium is much longer than the relaxation time and a full aging regime can be easily observed. Moreover the aforementioned "loss" in sensitivity on $t_W$ is not a crucial task in this case, since the aging rate is quite small compared to the relaxation time itself. In figure 4.12, three different full aging cases are shown. In all three situations the aging rates are quite similar.

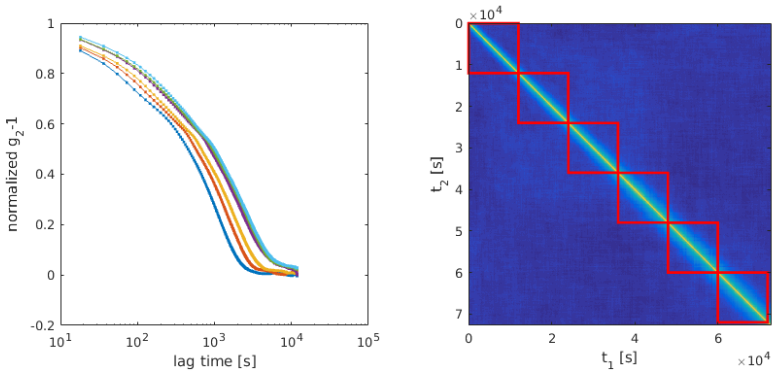


Figure 4.11: Example of an aging autocorrelation matrix analysed dividing it in small submatrices

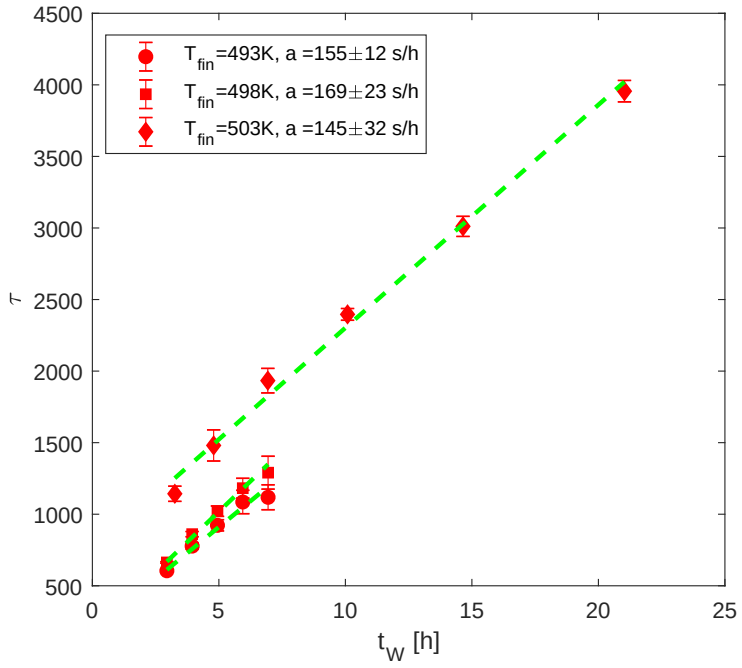


Figure 4.12: relaxation times observed in three aging samples at three different temperatures. The first ones (493 K and 498K ) are measures lasted 7 hours and each relaxation time is obtained integrating 1 hour. The third one is a measure toward the deepest temperature reported in this thesis and lasted 24 hours. The data points here reported are computed with an increasing integration time, adopting the procedure illustrated in fig 4.10.

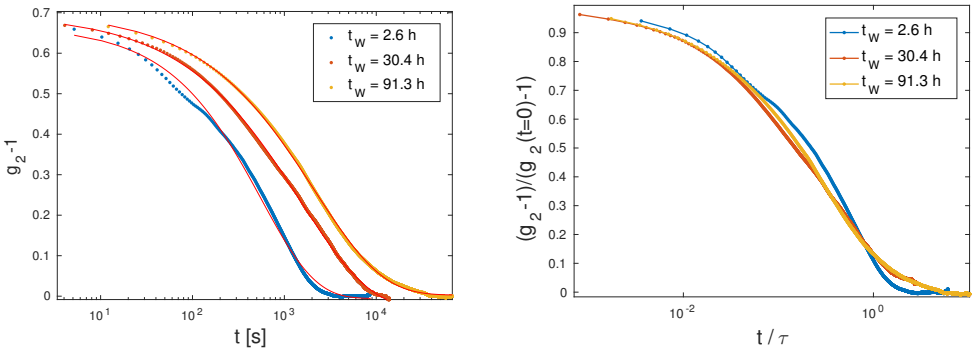


Figure 4.13: Left, autocorrelation function for a sample at 503,15 K measured at three different ages (2,6 hours, 30,4 hours and 91,3 hours). The continuous red lines are the stretched exponential fits to the data. Right, the same autocorrelation functions rescaled by the apparent relaxation time.

### A straightforward approach

As can be already seen in fig 4.11 and more clearly in fig 4.13, the autocorrelation functions from the "fast aging" regime appear more compressed than the ones corresponding to the equilibrated undercooled liquid. The stretched exponential is obviously no more the correct function to describe the data, but it can still be useful to get a glimpse on the main features of our aging glass.

Looking at the evolution of the KWW's parameters it is clear to see that both the relaxation time ($\tau$) and the shape ($\beta$) follow a simple exponential law of the form

$$\tau(t_W) = \tau_\infty - (\tau_\infty - \tau_1)exp\left(-\frac{t_W}{\tau_{rel}}\right) \tag{4.7}$$
$$\beta(t_W) = \beta_\infty - (\beta_\infty - \beta_1)exp\left(-\frac{t_W}{\tau_{\beta,rel}}\right)$$

similar simple phenomenological laws has been readiliy observed in many other aging systems [73, 121, 105]. In fig 4.14 the results for $\tau(t_W)$ are reported. The parameter $\tau_1$ represents the the relaxation time immediately after the final temperature has been reached, and it is clear how, for temperatures further away from $T_g$, the difference between $\tau_\infty$ and $\tau_1$ becomes progressively larger while, the asymptotic value $\tau_\infty$ falls on the Arrhenius line extrapolated from the equilibrated undercooled liquid. It is worth noticing that for long enough measurements, the relaxation times of the oldest

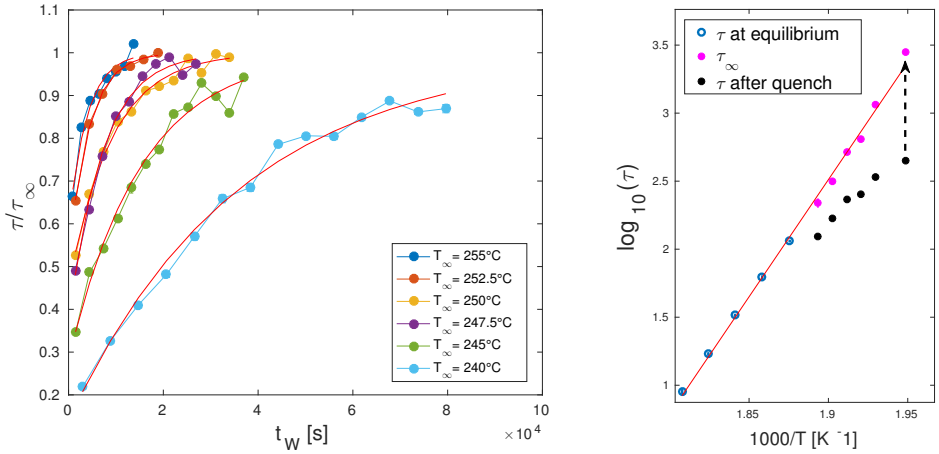


Figure 4.14: Left, relaxation times at different ages for 6 temperature jumps, the datapoints are rescaled by the asymptotic value $\tau_\infty$ computed from 4.7. The red lines are the fits to the data with equation 4.7. Right, Arrhenius plot for the equilibrated undercooled liquid (blue symbols) compared with the initial values of the relaxation time (black dots) and the asymptotic values computed from 4.7. It is clear that the values of $\tau_\infty$ fall on the Arrhehnius line extrapolated from the equilibrium values (red line)

samples are compatible within the experimental uncertainty with the values of $\tau_\infty$ and do not depend anymore from the waiting time, i.e. the sample had managed to equilibrate and can be referred to as to a very viscous undercooled liquid.

From the behaviour of $\beta$ we can understand how the shape of the autocorrelation function evolves in time. As already stated before, the dynamic of the younger samples cannot be described by a simple stretched exponential due to the presence of a clearly visible "distortion", this feature has the qualitative effect to compress the relaxation curve and looking at the evolution of the shape parameter we can be able to track this deformation at different times. In fig 4.15 we can see the results for $\beta(t_W)$. Also in this case the asymptotic value $\beta_\infty$ is aligned with the values of the equilibrated undercooled liquid with a slight tendency to decrease with temperature, as already observed in other experiments [111]. The initial value $\beta_1$ is also interesting, it tells us that the net effect of this anomalous shape is a compressed decay at early stages, and the further away we are from $T_g$, the more the initial decay function is closer to an exponential.

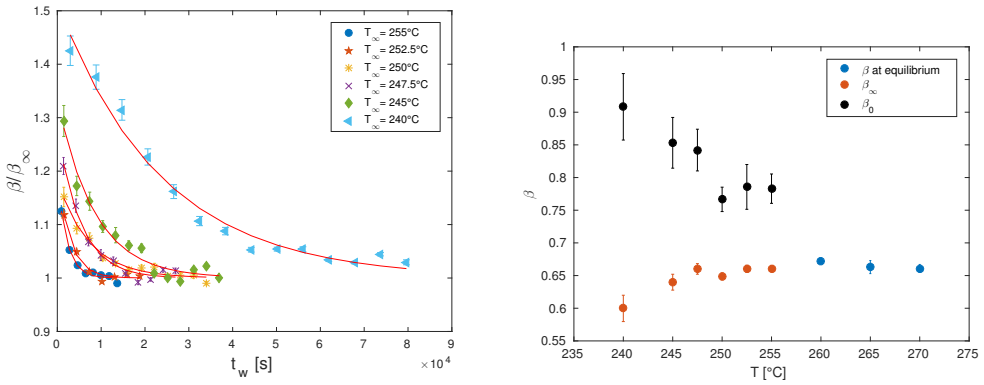


Figure 4.15: left, rescaled values of the exponent $\beta$ as a function of $t_w$, red lines are a fit to the data with equation 4.7. Right, equilibrium values of $\beta$ (blue symbols) compared with the initial (black) and asymptotical ones (red)

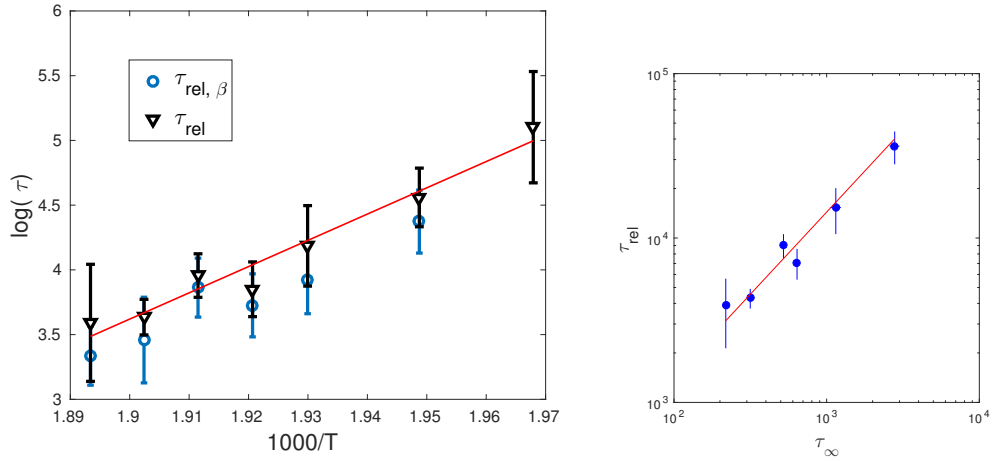


Figure 4.16: Left, recovery times for $\beta$ (blue circles) and $\tau$ (black triangles). Both times appear to follow an Arrhenius-like law and appear to be consistent within their experimental error bars. Right, recovery time for $\tau$ plotted against $\tau_\infty$; the two quantities appear to be proportional with a proportionality constant of $14 \pm 3$.

### Beyond a stretched exponential fitting

Among the consequences of the rapid quench there is the creation of internal stresses inside the glass volume. Now, in order to infer a more complete understanding of the physical phenomena that were developing in our samples it is necessary to consider the origin and the implications of these stresses. Due to the finite dimensions and the low thermal conductivity common to all glasses, when the sample is cooled different portions of the volume experience in practice a different cooling rate; at any instant during the cooling, the structural evolution of the surface will precede that of the interior of the sample. Thus temporary differences must exist between the specific volumes of layers of glass near the surface and in the center of the sample [122]. This difference in specific volumes produces strains and hence stresses inside our sample.
The final temperatures at which all our experiments were carried out are not too far from $T_g$ and actually they lay in the temperature range in which the annealing of glasses is typically carried out [102, 123]. Then inside the samples volume we have to expect alongside the intrinsic structural $\alpha$ relaxation also the rearrangements related to the dissipation of the internal stresses that have been created after the quench. The mechanisms regulating this dissipation imply an equalization of the mass density and thus a motion of a certain amount of atoms from the denser center [122, 102], this macroscopic movement will produce then a motion of the centroids of the speckles across the pixels. Since this phenomenon is of dynamical origin, it will affect the autocorrelation in a way that can be described using the approximations reported in [124]. Qualitatively speaking the "natural" autocorrelation will be truncated by a fast decaying function, that strictly depends on the velocity $v$ of the process that is taking place inside our sample

$$g_2(t) - 1 = |\Phi_q(t)|^2 G(v,t)$$

where $G(v,t)$ is the term arising from the macroscopic motion, that in the simplest approximation is a Gaussian function

$$G(v,t) = exp\left(-\left(\frac{v}{\sigma}t\right)^2\right)$$

where $v$ is the velocity of the speckle crossing the pixels and $\sigma^2 = \sigma^2_{speckle} + \sigma^2_{pixel}$, where $\sigma_{speckle}$ and $\sigma_{pixel}$ are the speckle diameter and the pixel size respectively [124]. Adopting this correction it is now possible to fit our data with the function:

$$g_2(t) - 1 = A|\left(e^{-(t/\tau_\alpha)^\beta}\right)|^2 \cdot e^{\left(-(\Gamma t)^2\right)} \tag{4.8}$$

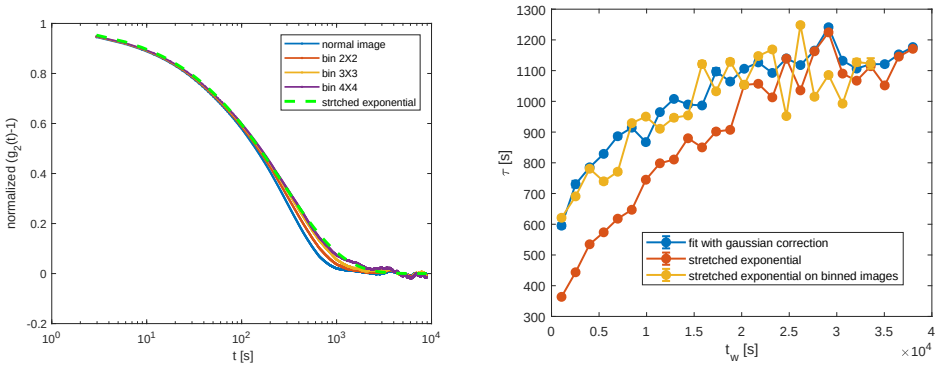


Figure 4.17: Left, normalized autocorrelation functions computed for the same subset of images but with different binning applied on the original data. It is clear that adopting a bin size of at least 3 pixels, the tail of the autocorrelation is already completely compatible with a stretched exponential (green dashed line). Right, comparison between the relaxation times obtained following different approaches starting from the same images. In blue are the relaxation times obtained employing eq. 4.8, in orange the relaxation time obtained from a fit with a simple stretched exponential, and in yellow the relaxation times obtained from a stretched exponential fit on the autocorrelations obtained from binned images (bin size of 3 pixels).

where now $\tau_\alpha$ is meant to be the real structural $\alpha$ relaxation time and $\beta$ the real stretching exponent, while $\Gamma \propto v$ is a parameter monotonically decreasing with $t_W$.

We can test this hypothesis computing the autocorrelation functions obtained sampling the original images into progressively larger bins. In fact if the distortion is due to the movements of the single speckles across the detector, increasing the effective dimension of the pixels will reduce this effect, i.e. we are increasing the value of $\sigma_{pixel}$ and $\Gamma \propto 1/\sigma^2$. As can be seen from the images in fig. 4.17 considering bins of the size of 3X3 pixels, the characteristic tail of the stretched exponential is already recovered. The drawback of this approach is a rapid decrease in contrast which scales as $1/N$, where $N$ is the number of coherence areas recorded by a single pixel [83].

Another consideration in support to this hypothesis can be found looking at the signal arising from the rims of the scattering volume or more in general, from the the portions of the image where a small percentage of reflected laser light is present. In fact, since boron trioxide is a very clear

and transparent material even the faintest reflection can affect greatly the observed autocorrelation function polluting the signal with a small heterodyne signal [125]. One advantage of working in an imaging configuration is that such polluted regions can be quite easily identified. Normally one avoids to consider such regions, and typically they are excluded via software masks; but it is possible also to take advantage of the presence of this kind of information to take a glimpse at the heterodyne autocorrelation function. In these regions, in fact, we can express the measured autocorrelation function with a modified Siegert relation [125, 83, 126]:

$$g_2(t) - 1 = A\left(C^2|g_1(t)|^2 + 2C(C-1)Re(g_1(t))\right)e^{-(\Gamma t)^2}$$

in our case $g_1 = e^{i\mathbf{q}\mathbf{v}t} f_0 e^{-(t/\tau_\alpha)^\beta}$, and the previous equation become

$$g_2(t) - 1 = A\left(C^2|f_0 e^{-(t/\tau_\alpha)^\beta}|^2 + 2C(C-1)\cos(\mathbf{q}\mathbf{v}t)|f_0 e^{-(t/\tau_\alpha)^\beta}|\right)e^{-(\Gamma t)^2} \tag{4.9}$$

where $A$ is the instrumental contrast, $C$ is the parameter that express the percentage of homodyne signal and $\mathbf{v}$ is the velocity of the scatterers inside the sample. In this framework a linear dependence between $\Gamma$ and $v$ is expected. In figure 4.18 an example of an autocorrelation measured on a spot with a 99% of homodyne signal in a young sample is reported. The presence of beatings can clearly be seen on the tail of the relaxing autocorrelation confirming the presence of a velocity field inside the scattering volume.

With this concept in mind we can then proceed to interpret the data with a more complete approach. As can be seen in fig. 4.19, now the fitting function can describe reasonably well the data at all the time-scales. First of all we see that the $\Gamma$ parameter, as already anticipated, is a decreasing function of $t_W$. In fig 4.20 it is shown an example of the aging of $1/\Gamma$ compared with the one observed for $< \tau_\alpha >$. In the beginning the value of $1/\Gamma$ is lower than the corresponding $< \tau_\alpha >$, meaning that in the young samples this internal motion is developing at a much faster pace than the structural relaxation; the situation changes rather quickly, in fact $1/\Gamma$ manifest a faster aging rate than $\tau_\alpha$ and eventually a crossover occurs before $\tau_\alpha$ has reached the equilibrium value. In the end this contribution will became too small to be detected (typically this is the case for the higher final temperatures). In fig 4.20 we see that both the initial value $\Gamma(t_W = 0)$ and the rate at which $\Gamma \to 0$ decrease with decreasing final temperature. From these observations we can infer some preliminary conclusions regarding this Gaussian contribution. In fact since this term is dependent both on the sample's age and on the final temperature then: i) it must be a phenomenon that takes place inside the

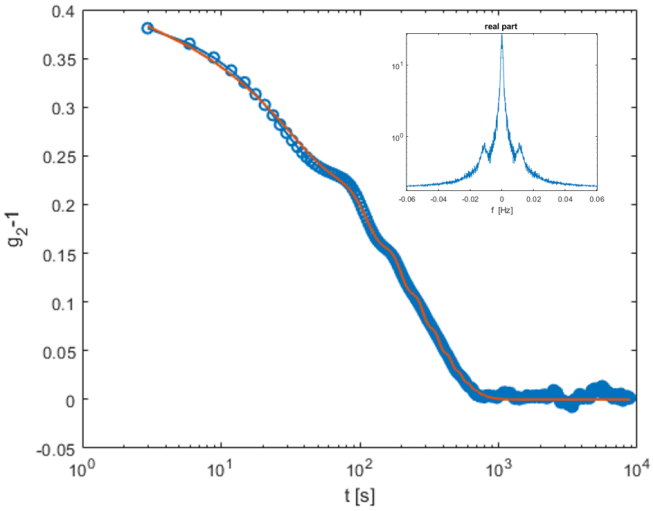


Figure 4.18: Autocorrelation function computed selecting a portion of the detector with a small contribution of light reflected from the couvette's wall. In this specific example the percentage of the heterodyne signal is less to 1%, however the beatings due to the heterodyne detection of a moving sample can be clearly seen on top of the autocorrelation function. In the inset the Fourier transform of the autocorrelation function is reported, showing the presence of a periodic component in the spectrum. In order to see clearly the beatings it is necessary to select a rather small $t_W$ interval when computing the autocorrelation because the detected velocity is evolving and an average on too large waiting times will eventually cancel out all the ripples leaving only a large bump on the side of the autocorrelation function.

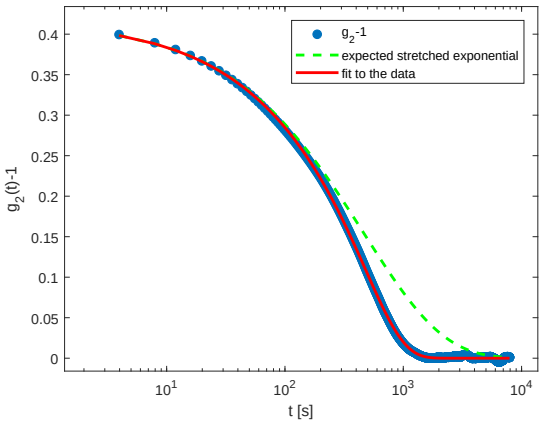


Figure 4.19: Example of an autocorrelation function for a "young" sample (blue dots) and the fit employing equation 4.8 (red line). For comparison the stretched exponential expected for this sample age is shown as well (green dashed line)

scattering volume and not a spurious effect due to the sample holder or the optical set-up, ii) $1/\Gamma$ is related to $\tau_\alpha$, suggesting a link between the internal dynamics of the sample and the value of $\Gamma$. This $\Gamma(t_W)$ then describes the evolution of the velocity field inside the sample's bulk developed as a consequence of the dissipation of the internal stresses.

Another important observation is that thanks to this Gaussian correction the value of $\beta$ does not depend any more on the sample's age, thus preserving the concept of the time aging-time superposition, see fig 4.21. Moreover it appears evident that, for what concerns $\tau_\alpha$ the difference between the initial and the asymptotic values ( $\tau_\infty - \tau_0$) is greatly reduced, see fig 4.22. This is true to the point that equation 4.7 can be used to describe effectively only the points corresponding to temperature jumps larger than 10 K. In fact, looking at the values that can be obtained for $\tau_{rel}$, and comparing them with the data from the previous approach, fig. 4.22, we can see that the two results for $\tau_{rel}$ are consistent within their respective errorbars, but this is mainly thanks to the increasing uncertainty on the newly computed $\tau_{rel}$. This huge errorbars are due to the significant decrease of the difference $\tau_\infty - \tau_1$, that for the highest temperatures is so small to be comparable with the experimental fluctuations of the measured $\tau_\alpha$. However, it is now possible to employ the more complete Tool-Moynihan-Narayanaswanmi model to describe our data fig. 4.23, using a slight modified version of equations 4.1

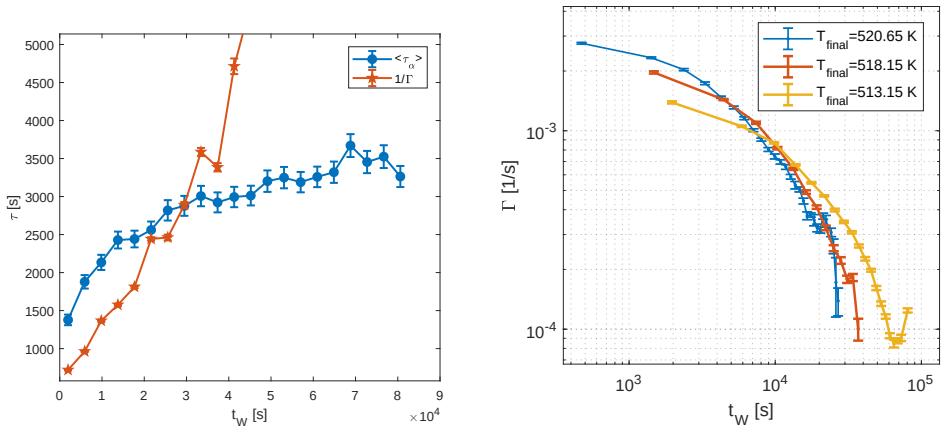


Figure 4.20: Left, comparison between the aging of $< \tau_\alpha >$ and $1/\Gamma$. It is evident that the latter has a faster aging rate and that it grows almost linearly with $t_W$. Comparison of the measured aging of $\Gamma$ at three different final temperatures. For lower $T_{final}$ we can observe lower initial values of $\Gamma$ and longer equilibration times.

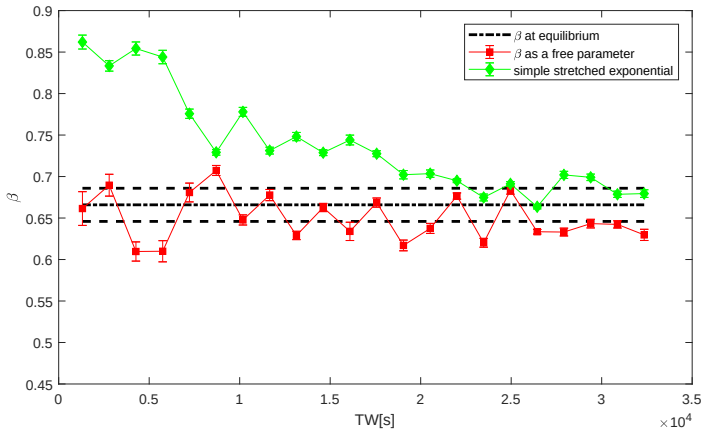


Figure 4.21: red squares, exponent $\beta$ evaluated at different ages for a single temperature jump (final temperature 518,15 K) using the modified equation 4.8. For comparison on the same plot the values of $\beta$ obtained with the stretched exponential are reported (green diamonds). The black dash-dotted line is the value of $\beta$ at equilibrium, while the dashed lines are the error upon this final value

and 4.2

$$\tau(T, T_f) = \tau_0 e^{a\left(\frac{xE}{k_b T} + \frac{(1-x)E}{k_b T_f}\right)} \tag{4.10}$$

$$T_f = T_0 + \Delta T \left(1 - e^{-\left(\int_{t_0}^{t} \frac{dt'}{\tau(T,T_f)}\right)^{\delta}}\right) \tag{4.11}$$

where $\tau_0$ and $E$ are obtained from the Arrehinus curve of the equilibrated data, $\Delta T$ is the temperature difference between the starting temperature $T_0$ and sample's temperature, $x$ describes the relevance of the fictive temperature in the determination of $\tau_\alpha$ and $\delta$ describes the broadening of the relaxation time spectrum [102, 35, 103], while $a$ is a parameter necessary to compensate the presence of systematic errors that can have occurred in the determination of $\tau_0$ and $E$. In order to work, this model needs the complete thermal history of the sample and in all cases it is able to describe quite well the data keeping as free parameters $a$, $x$, and $\delta$ see figure 4.23. For each temperature jump, the results from such fits are consistent within their experimental error bar and performing a weighted average of the parameters $a$,$x$,$\delta$, obtained from each temperature jump, we get $a = 1.002 \pm 0.001$, $x = (0.005 \pm 5)10^{-2}$and $\delta = 0.25 \pm 0.06$. The result for $a$ substantially tells us that the systematic errors in $\tau_0$ and $E$ are not too big, the value for $x$ tells us that the aging mechanism in this case is unaffected by the sample's temperature and is completely determined by $T_f$ and from $\delta$ we learn that in order to describe the observed dynamics one has to consider a rather large distribution of relaxation times. These facts can seem in contrast with what has been observed in the aging of $B_2O_3$ in some previous works [35, 127], these differences can be justified looking at the probed temperature ranges. In the historical works of Moynihan and DeBolt the sample measurements were always carried out at temperature well above $T_g$, while in the present work the samples were carried at much deeper temperatures. Another possible explanation for this discrepancy can be provided by the presence of the strong stress relaxation mechanism, which interferes with the normal thermally activated aging process delaying the time evolution of $\tau_\alpha$.
From the data shown in fig 4.22 and 4.23 it appears that smaller values of $\tau_\infty - \tau_1$ are related to greater values of $\tau_{rel}$. We can now test this qualitative hypothesis knowing the values for equations 4.10 and 4.11. In fig. 4.24 are reported the expected relaxation times at different temperature jumps towards the same final temperature slightly below $T_g$. For higher initial temperatures the sample has the possibility to better arrange its internal structure and thus to find itself, at the end of the temperature ramp, with a relaxation time closer to the equilibrium one. However as soon as the temperature has ceased to change, the aging rate of the samples with an

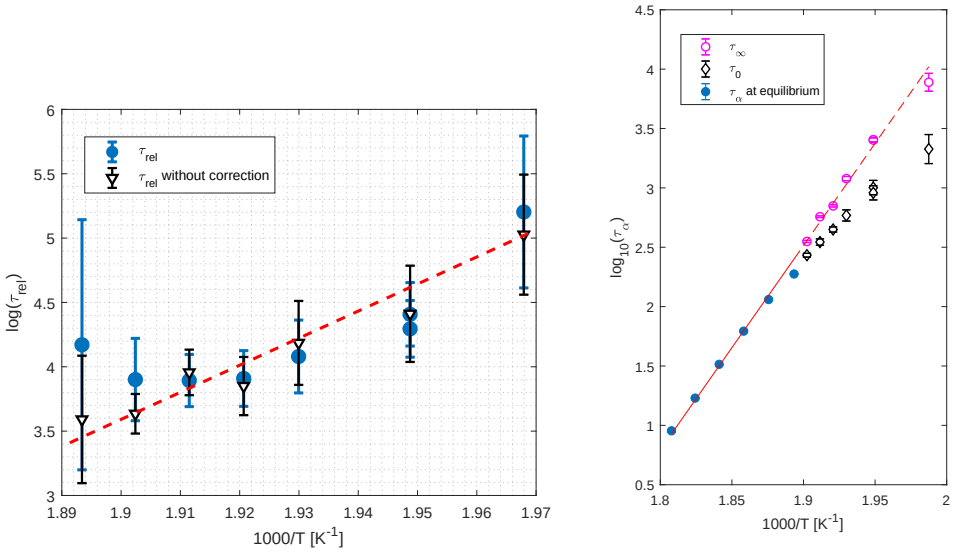


Figure 4.22: left, $\tau_{rel}$ at different temperatures obtained using equation 4.7 on $\tau_\alpha(t_W)$ (blue circles) compared with the values reported in fig. 4.16 (black triangles). The two results are compatible, within their respective errorbars. The dashed line here is just a guide to the eye. Right, Arrhenius plot with the real values of $\tau_\alpha$ at $t_w = 0$ (black diamonds) and $t_w \to \infty$ (magenta circles), compared with the values of the undecooled liquid (blue dots). The red line is a linear fit considering both the values of the equilibrated undercooled liquid and the asymptotic values. In respect to the values reported in fig. 4.14 the values of $\tau$ after the quench depart more mildly from the equilibrium Arrhenius line, wile the asymptotic values of $\tau_\infty$ maintain their position substantially unchanged.

initial more stable configuration is much slower than the one corresponding to smaller temperature jumps. Thus the systems that were initially further from equilibrium age more quickly and in the end reach the equilibrated undercooled liquid condition before systems starting from more advantageous positions.

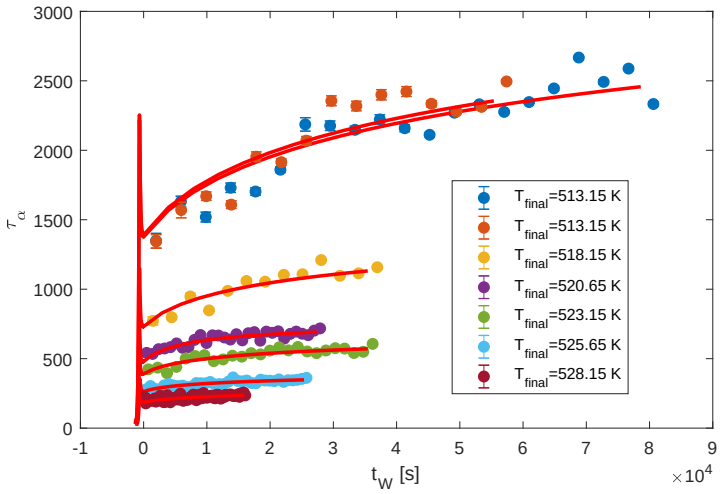


Figure 4.23: Aging of $\tau_\alpha$ at different temperatures, red lines are fits to the data using equations 4.10 and 4.11. The sharp peaks just before $t_W = 0$ are due to the furnace's overshoot during the cooling procedure (see fig 4.9)

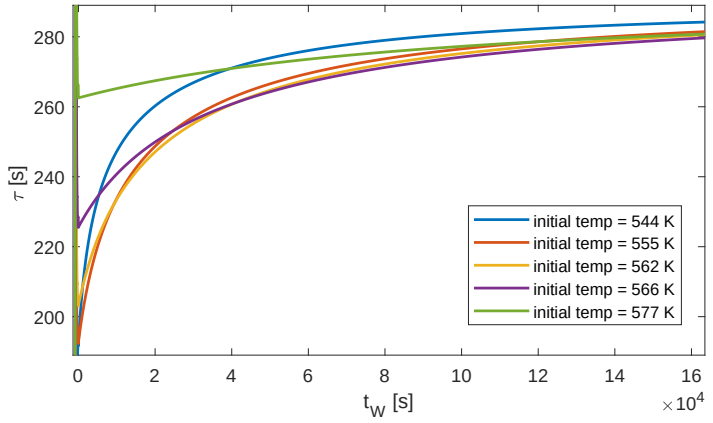


Figure 4.24: simulated values for 5 different temperatures jumps towards the same final temperature, $T_{final} = 528K$. For the simulations the experimental values of $\delta$, $a$, and $x$ where employed. The virtual thermal histories are obtained from a real thermal treatment, comprehensive of the furnace's overshoot, in which the initial linear cooling was opportunely prolonged.

## 4.6 Effects of aging on the dynamical susceptibility

We have seen in previous chapters that the dynamical susceptibility can grant the access to the dynamical heterogeneity, an important physical quantity for the glass transition. At the end of chapter 3, we have seen a way to purify the variance of the $g_2 - 1$ from spurious contributions arising from the finite number of pixels. The tool of the extrapolation grant the access to the $\chi_4$ only in a q-resolved scattering geometry, thus in the imaging configuration employed in the present chapter, one does not expect to find non-Gaussian contributions when computing the $\sigma^2_{g_2-1}$, moreover for boron oxides the spatial extensions of dynamical heterogeneity is of few nanometer, thus it should be impossible to see a non-Gaussian contribution employing visible light sources.
However, if one compute the susceptibility

$$\sigma^2_{g_2-1} = \overline{\left(C(t_w, t_w + t) - \overline{C(t_w, t_w + t)}\right)^2}$$

for an aging glass of $B_2O_3$ it is possible to see a clear signal even after the extrapolation method of [2] has been applied, see fig.4.25. It is easy to understand the origin of this "non-Gaussian" contribution, in fact $\sigma^2_{g_2-1}$ is a tool to detect all the temporal heterogeneities and a relaxation time continuously growing with the sample's age is a very specific kind of temporal heterogeneity.
Having at our disposal a complete description of the relaxation function with eq.4.8, we can test the simple model described at the end of chapter 3 with the dynamical susceptibilities arising from full-aging samples. In this peculiar condition the only quantities that are varying with a non-Gaussian process are the structural relaxation time $\tau_\alpha$ and the parameter $\Gamma$, and both $\tau_\alpha$ and $1/\Gamma$ are described by a simple linear relation $\tau(t_W) = a \cdot t_W + b$. It is easy to show that the variance $\sigma^2_\tau$ of a quantity linearly growing between the ages $t_1$ and $t_2$ can be written as

$$\sigma^2_\tau = \frac{a^2}{12}\left[(t_2 + t_1)^2 + t_1^2\right]$$

and adding the term

$$\left(\frac{\partial g_2 - 1}{\partial \Gamma}\right)^2 \sigma^2_\Gamma = 4(f_q^2)^2 \left(2\Gamma(\Gamma t)^2\right)^2 e^{-4(t/\tau)^\beta} e^{-2(\Gamma t)^2} \sigma^2_\Gamma$$

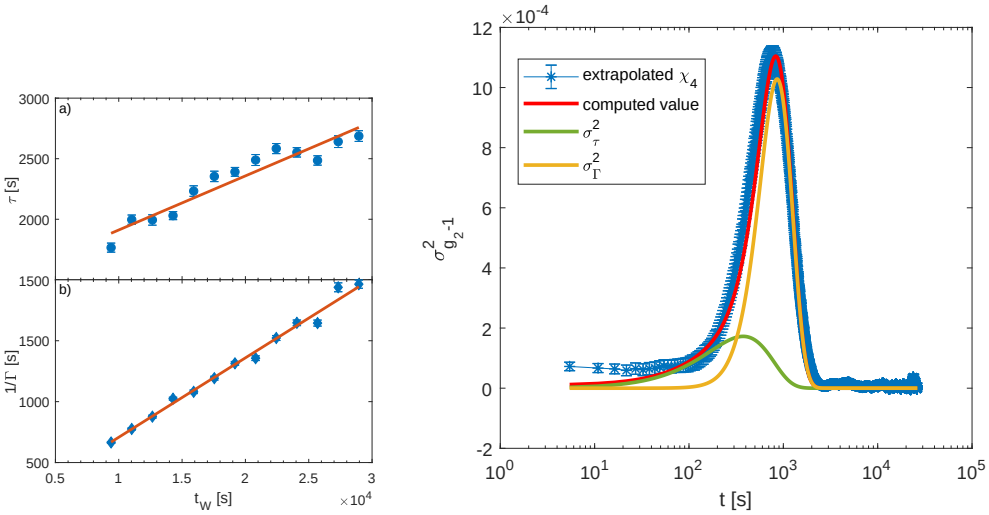


Figure 4.25: Left: aging behaviour of the structural relaxation time $\tau_\alpha$(a) and the inverse of the Gaussian parameter $1/\Gamma$ (b), the red continuous lines are linear fits $\tau(t_W) = a_\tau \cdot t_W + \tau_0$ and $1/\Gamma(t_W) = a_\Gamma \cdot t_W + 1/\Gamma_0$ which give an aging rate of $a_\tau = 0.045 \pm 0.008$, $\tau_0 = (1.46 \pm 0.16)10^3 s$ and $a_\Gamma = 0.065 \pm 0.004, 1/\Gamma_0 = 55 \pm 80$ respectively. Right: extrapolated dynamical susceptibility (blue asterisks) compared with the results from the simple model of eq.4.12 (red line), the green and yellow lines are the contributions arising from the growth of $\tau_\alpha$ and $1/\Gamma$ during the measurement.

to the equation 3.26 we obtain

$$\sigma^2_{g_2-1} = 4(f_q^2)^2 \left[ \left(\frac{t}{\tau}\right)^{2\beta} \left( \left( \ln^2(t/\tau)\, \sigma^2_\beta \right) + \left( \frac{\beta^2}{\tau^2} \sigma^2_\tau \right) \right) + \left(2\Gamma(\Gamma t)^2\right)^2 \sigma^2_\Gamma \right] \cdot e^{-4(t/\tau)^\beta} e^{-2(\Gamma t)^2} + e^{-4(t/\tau)^\beta} e^{-2(\Gamma t)^2} \sigma^2_{f_q^2} \quad (4.12)$$

and we can reproduce reasonably well the observed dynamical susceptibility of the full-aging glass (red line in the left panel of fig.4.25). This result imply that if the time evolution of the dynamical parameters is described with enough precision (in this case $\tau_\alpha$ and $\Gamma$), it is possible to reproduce with a reasonable precision the contribution to the $\chi_4$ that arise to the solely aging parameters. Further refined, this technique can be employed in the measurements in which a real dynamical heterogeneity is expected, but the sample's dynamic is not stationary, allowing to obtain a more precise measure of the $\chi_4$.

# Chapter 5

# Slow dynamics in colloidal systems of silica nanoparticles

## 5.1 Silica nanoparticles in the water-lutidine mixture

One of the most interesting features of colloidal systems is the possibility to tune the inter-particle interactions. Typically, this tuning is performed adding salts or polymers to the solvent to change the strength or even the nature of the forces between the nanoparticle dispersed into the liquid phase [62]. As long as one is interested only in the low volume fraction limit this approach presents very few side effects; however, if one is interested in the glass transition region of such materials this approach is all but trivial. In fact, colloidal glasses, like most disordered materials, are very difficult to reproduce (especially if one wants to finely characterize the glass transition region), and changing the glass properties inserting exogenous substances like a salt, de facto irreversibly destroys the previous glass. An alternative to this approach is to change the inter-particle potential with an external field. With this kind of approach, it is possible to obtain a homogeneous change of the potential inside the sample, moreover in most cases it is also possible to have a completely reversible process. To attain such condition either the colloidal nanoparticles or the solvent must have a strong coupling with the external filed, like for example magnetically active colloidal particle [104], or like in our case a binary mixture near its critical concentration.
The solvent of the colloidal samples described in this chapter is a binary mixture of water ($H_2O$) and lutidine 2,6 ($C_7H_9N$). The change in the inter-particle interaction in this peculiar binary mixture arises from a wetting mechanism.

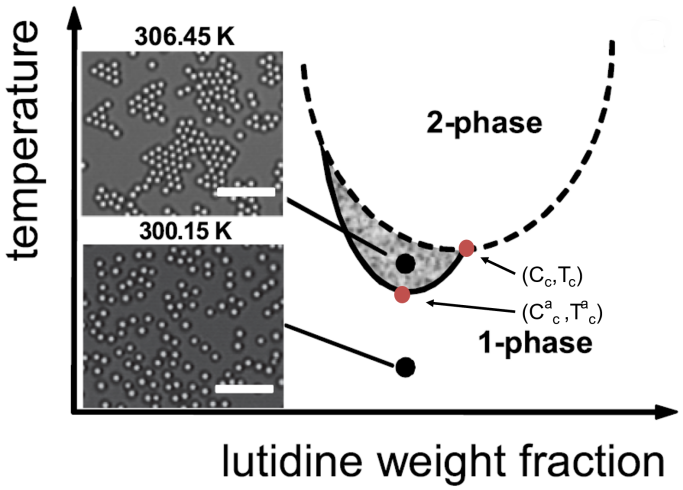


Figure 5.1: water-lutidine phase diagram. The small shaded area just before the critical point $(C_c, T_c)$ indicate the pre-wetting region for this bynary mixture. The insets are images of a bi-dimensional colloidal system composed by micron-sized colloidal particles in a near-critical water-lutidine binary mixture, taken with an optical microscope. Image adapted from [41]

Wetting phenomena on a wall appear in multicomponent systems close to their critical point when one of the components exhibits different interactions with the interface to a third phase (be it the wall of the container or the liquid-air interface). What happens is that one of the two liquid phases tends to completely cover the third phase eliminating the existence of three phases interfaces, in other words a first-order transition between partial wetting (finite contact angle between the wall and the two phases) and complete wetting (one phase wets the wall and surrounds the other phase) occurs in the region where the system exhibits two phases. This process is based on van der Waals interactions and can be found in a wide variety of binary mixtures [128, 129, 130]. For the water-lutidine system the lower critical solution temperature is $T_c = 34°C$ and occurs at mass concentrations of $C_L^m = 0.28$ (volume concentrations of $C_L^v = 0.27$), see the phase diagram reported in fig 5.1.

The interesting part is that before this phase transition another equilibrium line exists that marks another first order phase transition from a one component system and a "pre-wetting" region that ends with a critical point $(T_a = 33.743°C, C_a = 0.275)$ (different from the critical point of the liquid-liquid transition)[130]. When the third solid phase is represented by a colloidal particle, the effect of this pre-wetting regime is a change of the

inter-particle interaction [131]. In fact, silica nanoparticles are negatively charged (typically $\sim 140e^-$ [130] for small nanoparticles) and when dispersed in pure water they behave as hard repulsive particles. When the critical point is approached, then lutidine starts to form a thin layer around every nanoparticle and the inter-particle interaction switches from repulsive to attractive. Since lutidine is a weak base one is tempted to interpret this phenomenon as a simple screening process, however experimental observations suggest a more radical change of the nature of the interaction [130]. In fact, if a fluctuating medium is confined, the ensuing perturbation of its fluctuation spectrum generates Casimir-like effective forces acting on its confining surfaces. Thermal fluctuations in condensed matter typically occur on a molecular scale. However, upon approaching the critical point of a second-order phase transition the fluctuations of the order parameter of the phase transition become relevant and detectable at a much larger length scale, and its confinement produce a fluctuation-induced Casimir force acting on the confining surfaces [132, 133].
From the point of view of the colloidal suspension, this effect causes a drop in the absolute value of the zeta potential, and the particles start to flocculate and aggregate into large clusters and, for low volume fractions, we can talk of a gas-liquid transition for our colloidal system [131] (i.e. the system switches from a condion in which the system is composed by freely diffusing non interacting particles to one in wich the particles are still able to diffuse, but the inter-particle distance is much smaller and the inter-particle interactions are stronger). If the initial volume fraction is already high enough to have a colloidal glass, then this transition has an even more interesting effect. Approaching the transition from an arrested phase causes a melting of the colloidal glass and a subsequent freezing in a new configuration [134], thus corresponding to a transition from a repulsive glass to an attractive liquid to an attractive glass. In a more detailed way, in the hard sphere repulsive glass at the glass transition volume fraction ($\phi_g$) each particle is both caged and is part of a cage for its neighbours and all particles tend to stay away from each other. This glassy state is perturbed by short range interparticle attraction (stickiness), because now the particles does not repel each other anymore, but on the contrary they tend to shorten the interparticle distance. Such an attraction first melts the hard sphere glass and then a second, qualitatively different, glassy state is formed. Sticky hard spheres, therefore represent the simplest system in which multiple glassy state can occur [135]. The neat thing is the complete reversibility of the whole process, as long as one does not goes too far in the demixing region; the problem is that all of this happens in a very narrow temperature range of less than 1 K.

In this chapter we will see the results of scattering experiments (carried out with both visible and X-ray photons) performed on concentrated suspensions of silica nanoparticles in near critical water-lutidine solutions. Two "families" of colloidal samples were produced, one made of silica nanoparticles with nominal diameter of 450 nm, and one of silica nanoparticles with nominal diameter of 100 nm. The reasons for these choice are manifold; the form factor of the bigger particles can be measured even with a standard dynamic light scattering-static light scattering (DLS-SLS) set-up and in a SAXS experiment it is possible to measure easily the structure and the dynamics at q vectors significantly larger than the first neighbour peak. However, since their size is quite close to the wavelength of the visible light, performing a DLS experiment on concentrated samples is prohibitive due to the multiple scattering. On the other hand, the smaller particles when concentrated form a nearly transparent sample that can be probed even with visible light and a SAXS experiment gives complementary information in a wide q range.

## 5.2 Sample preparation

The colloidal nanoparticles were purchased by Micromod under the commercial name of Sicastar®. They are plain silica nanoparticles dispersed in pure water with mass concentration of 100mg per 1 ml of solution and a polydispersity index inferior to 0.2. Particles are synthesized using a modified Stoeber process [136] by hydrolysis of orthosilicates (TEOS). The producer declares a silica nanoparticles density of 2 $g/cm^3$. The lutidine, 99% purity, was purchased by Sigma-Aldrich.
To prepare the concentrated colloidal sample we start from an initial volume $(V_{SiO2} + V_{H_2O})$ of the silica-water suspension and then we add the lutidine (filtered with a 0.2 $\mu m$ PMMA filter) in order to reach the mass concentration of $C_L^m = 0.25$. The volume that one must add is obtained from

$$V_L = \frac{C_L^m}{1 - C_L^m} \frac{m_{H_2O}}{\rho_L}$$

where $\rho_L = 0.925 g/ml$ is the lutidine density and $m_{H_2O}$ is the initial mass of pure water [1]. Then the suspension is centrifuged, for 450 nm particles typically 2500 g for 5 minutes, to concentrate all the nanoparticles at the bottom of the cuvette. and then the excess liquid is removed in order to

[1] The mixing of water and lutidine is an exothermic process that in some cases can heat up the solution above the critical point. Before proceeding with the sample preparation it is then necessary to wait that the solution is cooled and completely mixed

reach the desired volume fraction $\phi_{fin}$. The volume of the solution to be removed can be computed with the formula

$$V_{remove} = V_{H_2O} + V_L - V_{SiO2}\frac{1-\phi_{fin}}{\phi_{fin}}$$

At this point we have a strongly inhomogeneous sample, with a very concentrated colloidal glass at the bottom and the remaining solvent on top. To obtain again a homogeneous sample it is then necessary to disperse again the nanoparticles. To do so, the cuvettes are placed on a vortex mixer until the sample appears again homogeneous. We can think of this step as a shear melting of the colloidal glass. The time required for the complete recovery of the homogeneity is strongly dependent on the total area of the silica-solvent interface, i.e. higher $\phi_{fin}$ and smaller particle radius requires longer times on the vortex mixer. For 450 nm nanoparticles typically 20 minutes were sufficient to obtain acceptable samples.
Once the homogeneous concentrated sample is obtained then the colloidal glass is transferred inside borosilicate capillaries. To obtain bubble-free homogeneous samples, the capillaries are again mildly centrifuged at 100 g for 30 seconds. Once filled, the capillaries are sonicated before the beginning of the experiment.
The samples for the X-ray experiments were prepared in thin walled capillaries purchased from Hilgenberg (wall thickness 0.01 mm, nominal diameter 0.5 mm) and sealed with a hot glue cap. The samples for DLS experiments were prepared inside capillaries produced in house starting from standard Pasteur pipettes (wall thickness $\sim$ 1 mm ,diameter $\sim$ 1-2 mm), sealed with Teflon and parafilm. All the steps listed above were carried out at temperatures below $20°C$, i.e. in the repulsive glass region.

## 5.3 SAXS experiments

Silica nanoparticles have a refraction index close to the one characteristic of bulk $SiO_2$ and, for visible wavelengths, there is not a good match with the refraction index of the water-lutidine mixture (with our concentration it can be estimated using [137] to be 1.37 [2]). Thus, even if the 450 nm nanoparticles have a form factor that can be easily measured with a visible DLS set-up, once concentrated the samples result completely opaque to visible light, making it impossible to correctly measure the structure factor due to the large amount of multiple scattering. When changing the water-lutidine ratio

[2] $n_{WL} = n_{Lut}C_L + n_{H_2O}(1-C_L)$

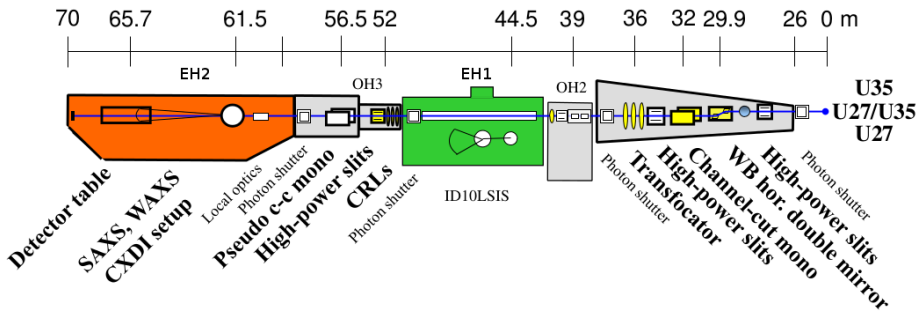


Figure 5.2: sketch of the ID10 beamline. The X-ray source is located in the far end on the rigt, while the experimental hutch used in this experiment is at the end of the X-ray-path, image taken from *http://www.esrf.eu*

it is possible to obtain a better index matching, but the resulting sample will have inevitably completely different physical properties (the lutidine concentration necessary for the index matching is $C_L \sim 0.68$).
The most effective way to overcome this opacity limit is to radically change the wavelength of the coherent radiation illuminating the sample; in other words, performing an X-ray photo-correlation (XPCS) experiment in small angle x-ray scattering (SAXS) configuration.

### 5.3.1 Experimental set-up

The SAXS experiments reported in this Thesis have been performed at the beamline ID10 EH2 at the European synchrotron radiation facility (ESRF) in Grenoble, France. The photon source is a third-generation synchrotron radiation light source placed 61.5 m from the sample environment. More precisely the light source is an insertion device composed of three undulator segments in series: one with a period of 27 mm (U27), one of 35 mm (U35), and a revolver unit carrying both U27 and U35 undulators. The source size is $928X23\mu m^2$ (H×V) FWHM, and the source divergence is $28X17\mu rad^2$ (H×V) FWHM, the overall brilliance is $B > 10^20ph/s/0.1\%bandwidth/mm^2/mrad^2/100mA$ at 8 keV. We can see in fig 5.2 a sketch of the ID10 beamline. After being generated in the undulators, the X-ray photons enter in the first safety hutch (optics-hutch) dedicated to the optical components common to both experimental hutches. In this sector the relevant devices for our set-up are the high-power slits, a beam diagnostics device, a white beam double mirror in horizontal reflection geometry (to produce a first filtering), a channel cut monochromator ( composed of two sets of liquid nitrogen cooled $Si(111)$ crystals working in symmetric Bragg-Bragg reflection which provide

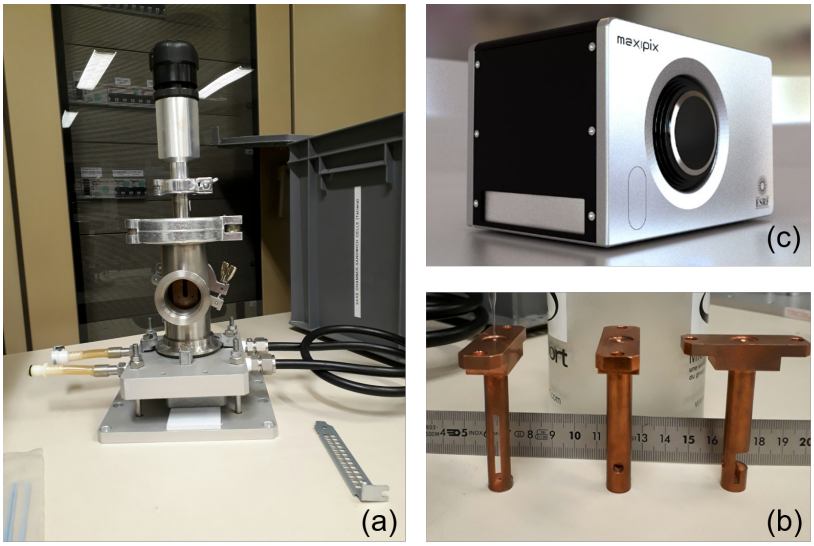


Figure 5.3: (a): SAXS vacuum chamber. (b): three sample holders with different possible apertures,the central one is the model most widely used in the present experiment. (c): Maxipix detector, image taken from *http://www.esrf.eu*

monochromatic beam in the energy range 7-25 keV), a pair of secondary slits, a white beam transfocator (for the focusing), and finally the attenuators and a photon shutter unit. The aims of these components are mainly the optimization of the transverse coherence, a first filtering of the incoming radiation and a first diagnostic of the beam properties. Another fundamental piece of equipment that can be found in this hutch is the set of absorbers, namely $Si$ slabs that can be inserted or removed from the beam path, each absorber reduces the total flux by a factor $1/e$. The white beam is now ready to be monochromatized and focused onto the sample, it is thus sent through a pipe across the experimental hutch EH1 and enters inside the optics hutch OH3. Here the beam is focused by a set of beryllium compound refractive lenses, further polished by another set of high power slits and filtered by a pseudo channel cut Si(111) monochromator. The beam can then finally enter in the second experimental hutch (EH2) with a spot size at the sample position of $10X10\mu m^2$ and an energy resolution of $\Delta\epsilon/\epsilon = 1.4 * 10^{-4}$ giving us a longitudinal coherence of $\xi_L \sim 1\mu m$ at 8.1 keV. The total flux on sample in this configuration is then $\sim 4 \cdot 10^{10}$ photons per second (value measured at the beginning of the experiment). The sample environment is composed by a cylindrical vacuum chamber, fig. 5.3-(a) in which the sample holder is hosted (fig. 5.3-(b)) and its temperature controller. The vacuum chamber is

directly connected to a 5 meters long pipe that the scattered photons cross to reach the detector, a fast readout, photon-counting pixel detector system named Maxipix shown in fig 5.3-(c). This device is composed of 4 chips in a 2X2 arrangement, each chip has 256 pixels and a single pixel has an area of $55X55\mu m^2$. The system achieves up to 1.4 kHz frame rate with 290 $\mu s$ readout dead time. The total distance separating the scattering volume to the centre of the detector is $D = 5.225m$, that combined with the scattering volume's transverse dimension of $d = 10\mu m$ give us a linear speckle size of $\sigma_{sp} = 1.22 * \lambda * D/d \approx 97\mu m$. To protect the detector, the direct beam was blocked by a beam stopper.
Attenuating the incident photon flux with an appropriate number of absorbers, it was possible to record the direct beam with the Maxipix, without causing any harm to the detector. Then scanning the sample's position, it was possible to measure of the sample's X-ray transmission, in fig. 5.4, we can see an example of such scans. Adopting the Lambert-Beer equation the recorded intensity can be described with:

$$I(x) = I_0 exp\left(-\left(s(x)/\mu_{capillary} + L(x)\phi/\mu_{SiO_2,NP} + L(x)(1-\phi)/\mu_{WL}\right)\right)$$

with: $1/\mu_{WL} = C_L^v/\mu_{lutidine} + (1 - C_L^v)/\mu_{H_2O}$; $s(x)$ is the thickness of the crossed capillary wall, $L(x)$ is the length of the crossed sample's volume, and $\mu_{capillary} = 136.7\mu m$, $\lambda_{SiO_2,NP} = 149.8\mu m$, $\mu_{H_2O} = 1034.95\mu m$ and $\mu_{lutidine} = 1081.3\mu m$ are the attenuation lengths of the materials constituting the sample (values taken from the database of CXRO, http://www.cxro.lbl.gov/).

At the centre of the capillary, the above equation is simplified since $s$ is equal to the wall thickness and $L$ to the difference between the capillary diameter $D$ and $2s$. Knowing all the previous parameters it is possible to perform a measurement of the volume fraction $\phi$ as:

$$\phi = \frac{log(I/I_0) + s/\mu_{capillary} + (D-2s)/\mu_{WL}}{(D-2s)(1/\mu_{WL} - 1/\mu_{SiO_2,NP})} \tag{5.1}$$

All the measurements of $\phi$ presented in this chapter are carried out employing eq. 5.1.
During the experiment it was not possible to thermalize correctly the sample, thus, to avoid the phase separation of the water and lutidine due to an excessive heating, it was decided to perform all the measurements at a fixed nominal temperature of $32°C$. Hence all the results reported below, correspond to a mildly repulsive hard sphere colloidal glass, and all the efforts are devoted to a complete comprehension of the colloidal glass in this configuration.

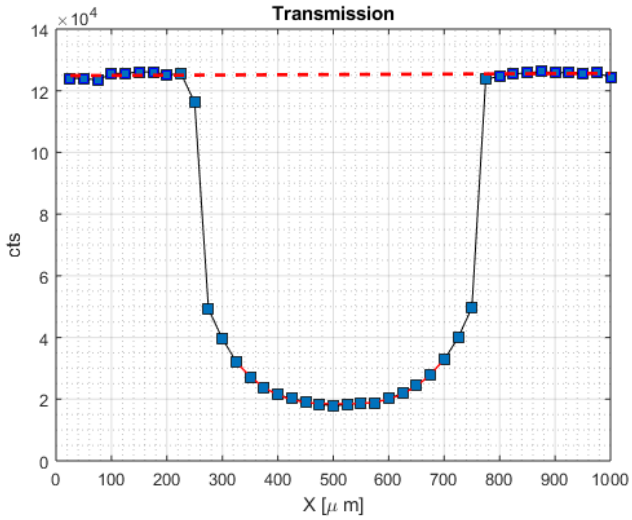


Figure 5.4: Example of a transmission scan to determine the volume fraction. From the width of the "shadow" projected by the capillary it is also possible to determine the real value of the diameter of the capillary.

## 5.4 Static structure factor

Performing XPCS experiments in small angle configurations has the great advantage that one is automatically performing also a measurement of the structure factor $S(q)$, on a wide range of $q$. In fact,

$$I(\mathbf{q}) \propto (\Delta\rho)^2 P(\mathbf{q}) S(\mathbf{q})$$

where $\Delta\rho$ is electron density difference between the colloidal particles and the surrounding liquid. For the present samples we have that $\rho_{SiO_2} \approx 600e/nm^3$, while $\rho_{solvent} \approx 330e/nm^3$ [138]. $P(q)$ is the form factor of a single particle and performing measurements on diluted samples it is possible to experimentally measure $P(q)$ once polydispersity and experimental $q$-resolution ($\delta q$) are taken in account.
For the diluted samples, the recorded intensity will be then:

$$I(q) \propto \int_{q-\delta q}^{q+\delta q} dq' \int_0^\infty f(R) P(R, q') dR + bkg \tag{5.2}$$

Where $bkg$ is the background due to the solvent and the capillary's walls independently measured[3], and $f(R)$ is the distribution of sizes. Typically,

[3]The water-lutidine mixture was measured in a silica capillary, while all the samples were prepared in borosilicate capillaries, thus the background for equation 5.2 was obtained with a combination of three backgrounds ($bkg_{water-lutidine} - bkg_{silica} + bkg_{borosilicate}$) see [138] for more details

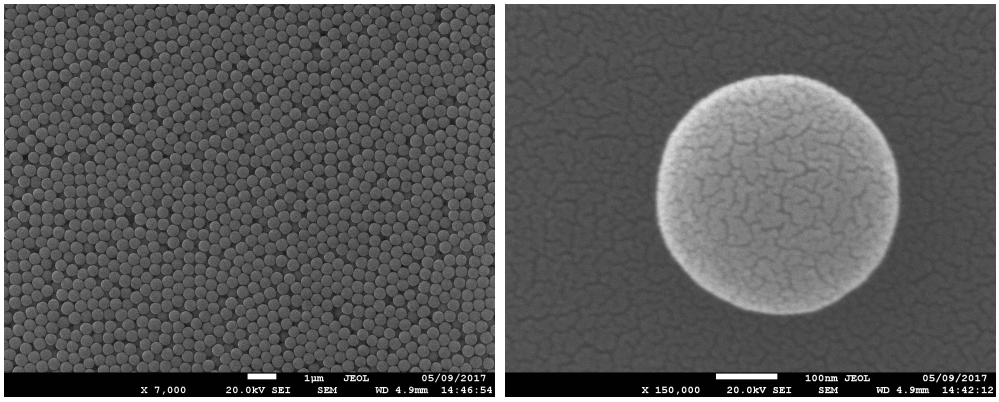


Figure 5.5: SEM images of dried nanoparticles. Since silica is a strong insulator it was necessary to cover the nanoparticles with an Au layer, 1 nm thick. Thus, the values obtained from a quantitative analysis of the images will be inevitably biased by the presence of such layer. Nevertheless, it is still possible to perform qualitative considerations, observing that the average shape is a reasonably well-formed sphere and that the radii distribution is quite narrow.

nanoparticles present a slightly skewed distributions that can be described by a Shultz distribution [139, 89]

$$F(R) = (z+1)^{z+1} R^z \frac{e^{-(z+1)\frac{R}{\mu}}}{\Gamma(z+1)\mu}$$

The parameter $\mu$ is the mean particle's radius, while the parameter $z$ is related to the width of the distribution by the relation $\langle R^2 \rangle - \langle R \rangle^2 = \mu/(1+z)$. In the present case, the nanoparticles have a quite large radius and thus, as can be seen from SEM images reported in fig. 5.5, they came with a quite narrow distribution and present a polydispersity index close to one [140].

In figure 5.6 an example of a measured form factor is reported. Knowing the exact location of the direct beam on the pixel detector it is possible to perform the average of the intensity over the azimuthal angles obtaining the intensity profile as a function of $\theta$ (or as a function of $q$). Then, after the subtraction of the background, it is possible to perform a fit to the experimental data with eq. 5.2 as reported in the right side of figure 5.6.

Knowing the form factor it is possible to finally dig out the $S(q)$. The followed procedure consits in: i) a normalization by the form factor of the background subtracted X-ray pattern produced by the concentrated sample, and then, ii) an average over the azimuthal angles is performed.

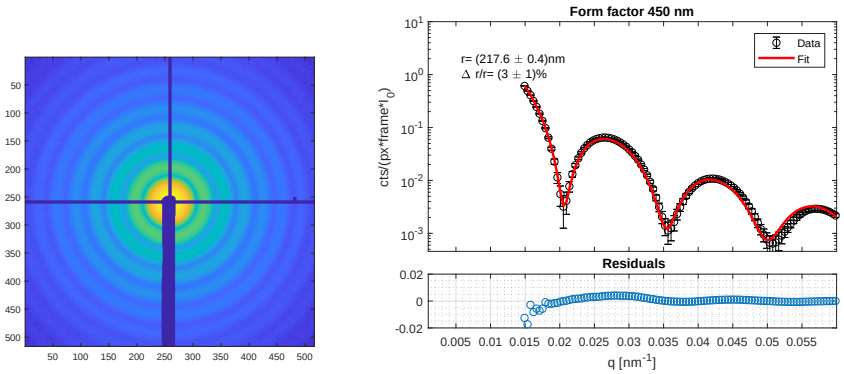


Figure 5.6: Left: image of the x-ray intensity pattern produced by a diluted suspension of colloidal particles in water and lutidine mixture. The cross shaped shadowed area is due to the connection of the Maxipix's chips and the beam stopper placed in correspondence of the direct beam. Right: intensity profile as a function of $q$ (black circles) and best fit to the data with eq. 5.2. The estimated radius is $R = (217.6 \pm 0.4)\mathsf{nm}$, while the polydispersity is estimated to be $\Delta r/r = (3 \pm 1)\%$ (the errors are attributed with the fitting algorithm).

This procedure is adopted in order to get rid more effectively of stray light contributions in the recorded backgrounds that affect critically the results at small q. In figure 5.7, the steps followed for the determination of a structure factor of a concentrated sample are reported. In the normalized background subtracted X-ray pattern, a set of small Bragg spots are visible on the second ring. Looking at the ratio between the peak intensity of those Bragg spots ($I_{cry}$), proportional to the square number of particles composing the crystal ($N_c$), and the peak of the $S(q)$ ($I_{am}$), proportional to the total number of particles in the scattering volume ($N$), it is possible to determine the relation $N_c \sim \sqrt{(I_{cry}/I_{am})N}$, which for $N = 6 \cdot 10^5$ gives $N_c \sim 190$, the volume occupied by the crystallite is then $\sim 0.024\%$ of the total scattering volume.

If we know the solution of equation 2.4 it would be possible to generate an analytical expression for $S(q)$. The solution of eq.2.4, can be made possible only applying a closure relation and some approximations. For our problem a good closure is typically given by the mean spherical approximation (MSA) which states

$$\begin{cases} g(r) = 0 & r < R \\ c(r) = -\frac{1}{k_b T} U(r) & r > R \end{cases}$$

where $U(r)$ is the potential energy between two particles. Analytical solutions

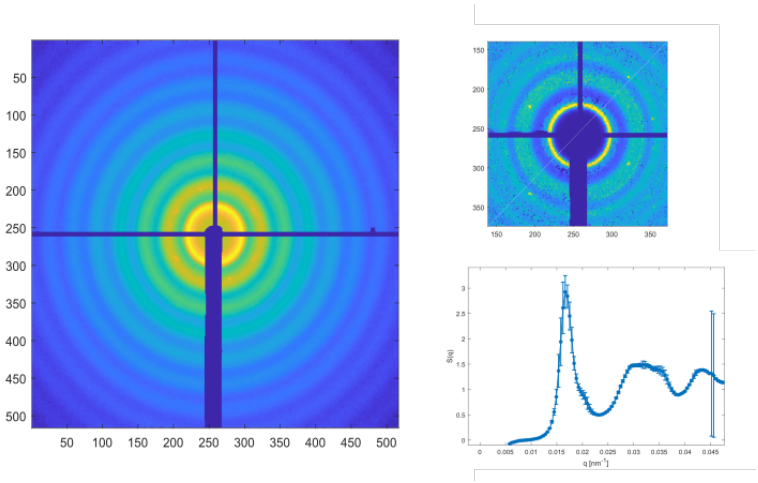

Figure 5.7: Left: x-ray pattern produced by the scattering from a colloidal glass. Right top: background corrected and normalized x-ray pattern. The small dots on the second ring are Bragg spots originating from a small cryistallite, during the whole measurement (lasted few ours) these spots does not show any significant change in position or intensity, in further analysis these regions were excluded with a software mask. Right bottom: azimuthal averaged structure factor.

with the MSA are available for a certain number of potential functions [141]. For the case of charged colloidal particles, a screened Coulomb interaction is often adopted for the description of the potential energy

$$U(r) = \begin{cases} \infty & r < R \\ \pi\epsilon_0\epsilon R^2\psi_0^2 \frac{e^{-k(r-R)}}{r} & r > R \end{cases}$$

Where $1/k$ is the Debye screening length, $\epsilon$ is the solvent's relative dielectric constant and $\psi_0$ is the surface potential.
Thanks to this closure relation it is now possible to attempt a fit to the experimental $S(q)$. In figure 5.8 the structure factor of the concentrated sample and the MSA fit is reported. It is evident that the MSA fit cannot completely reproduce the second structure factor's coordination shell, and this is possibly due to the presence of systematic errors in the evaluation of the background contribution. The right side of the second coordination shell falls in fact in correspondence to the second minimum of the form factor, which for monodisperse particles assumes values very close to zero. However, the results obtained from the fit to the structure factor ($R = (202 \pm 1)nm$ and $\phi = 0.45 \pm 0.02$) are compatiblewith the values obtained from independent measurements i.e. radius from the form factor and the volume fraction from

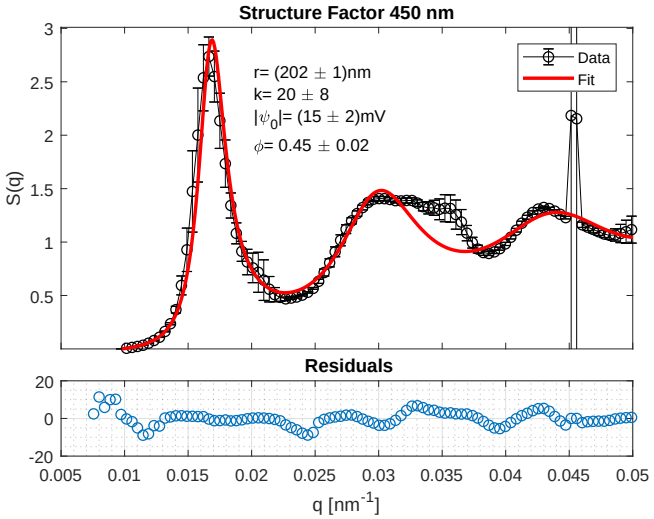


Figure 5.8: fit of the experimental structure factor using a model based on the MSA approximation, the first peak and the rise of the second ripple are well reproduced. The shape of this latter feature is probably distorted by irregularities in the background, since the second minimum of the form factor falls exactly on the right side of the second coordination shell. The $k$ parameter is the product between the particle radius and the Debye screening length, and its high value indicates that our system is very close to the hard sphere approximation (the Debye length results in fact to be $1/k = (10 \pm 4)nm$). The fitting procedure is extremely sensitive to the starting parameters, so the results here reported must be taken at a qualitative level.

transmission scans. The discrepancy in the radius arise from the fact that the model employed to describe the structure factor does not take in account the polydispersity of the colloidal particles inducing an underestimation of the $R$ value [138]. Also the value for the surface potential ($\psi_0$) is compatible with the $\xi$ potential obtained from a standard zeta sizing apparatus (*Malvern zetasizer*); the relation linking these two numbers is $|\psi_0| > \xi$, and indeed this is the case since at $T = 32°C$ $\xi = -6.8 \pm 0.4$ and $|\psi_0| = (15 \pm 2)mV$.

As can be seen from figure 5.6 and 5.5, the particle's size distribution is quite narrow, thus the presence of crystallization has to be expected. However, for samples "dense enough", the nucleation and growth of crystals can be extremely slow [60, 142]. Indeed, in our case this happened for samples with volume fractions higher than $\sim 0.45$ which maintained an amorphous structure for about 4 days. For comparison, in figure 5.9 two

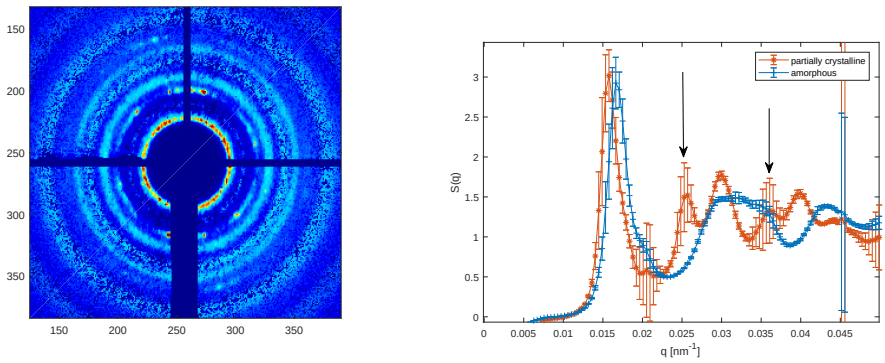


Figure 5.9: comparison between the structure factors of partially crystalline and amorphous samples. The first neighbour peak in the partially crystalline sample is shifted towards smaller q-values implying smaller concentrations. The crystalline peaks corresponding to the [1 1 1] and [2 0 0] planes.

structure factors are reported, one obtained on samples with $\Phi = 0.51 \pm 0.03$, and the other on samples with $\Phi = 0.41 \pm 0.05$. There is a clear difference in the shape starting from q values corresponding to the second peak of the $S(q)$, with the appearance of small sharp peaks in positions compatible with those expected for FCC crystal. Performing transverse scans, it was possible to observe how the crystallites are more abundant close to the capillary walls, thus suggesting a heterogeneous nucleation due to the sample-capillary interface. The less concentrated samples manifest the presence of small crystals already few hours after production, staining the measurements of the sample's dynamic.

## 5.5 Dynamic structure factor

The principal advantage in performing XPCS experiments in SAXS configuration, is the possibility to study the dynamics over a large q-range, described also in this case by a relaxation function of the kind $g_2(t) - 1 = A \cdot \exp(-(t/\tau)^{\beta})$. Our samples are dense enough to slow down the crystallization;they are in an out of equilibrium condition and aging is expected. The probed q range span portions of the reciprocal space that go from inverse lengths greater than the mean inter-particle distance to very localized motions, and the probed relaxation time varies by about one order of magnitude across the detector. Lastly, there might be anisotropic effects due to the reduced size of the capillary or the presence of gravitational effects on our relatively large particles.

Giving this wide variety of different phenomena that must be taken in account, the analysis of the data is organized as follows:

- q-dependence of $\tau$ and $\beta$ after azimuthal average;
- azimuthal dependence of $\tau$ and $\beta$;
- q-dependence of the aging dynamics at fixed azimuthal angles;
- study of the dynamical heterogeneities from the 2-times matrices;

The results presented in this chapter correspond to three datasets obtained from a single sample. Two datasets correspond to the sample at two well separated ages, let's call them young and aged sample, while the third corresponds to the same sample after tumbling, that lead to rejuvenation of the dynamics. In the following sections the results concerning the preliminary analysis and azimuthal dependence of the parameters will be referred to data from the aged sample, since the variation of $\tau$ during the measurements is relatively small. Conversely, for the study of the aging properties, the data presented here came from the young sample, where the aging effects are more evident. The dataset corresponding to the rejuvenated sample was collected over a wider time window with respect to the preceding ones, and offers a more complex time evolution described in more detail the next sections. This last dataset, in particular, presents a large time interval in which the system does not appear to age appreciably. For this reason the results concerning the dynamical heterogeneities will refer to mainly this dataset.

### 5.5.1 q-dependence of the dynamical quantities

We begin our description with a q-resolved analysis of various parameters needed to describe the dynamics. As can be seen from fig. 5.10 and fig. 5.11, the autocorrelation functions manifest a visibly compressed shape with a "stretching" exponent well above unity. Such compressed relaxations are observed in a certain number of experiments performed on a wide variety of disordered systems, colloidal glasses and gels [1, 2], polymers [3, 4], foams [5], aerogels [6] and in metallic glasses [7]. The wide assortment of disordered materials displaying these dynamics, suggests a common underlying mechanism. However, no clear consensus about its microscopic origin has yet emerged. One possibility, that can describe some experimental findings, is the continuous time Lévy flight model with a power-law distribution of waiting times [143], this model seems well suited for systems composed by large

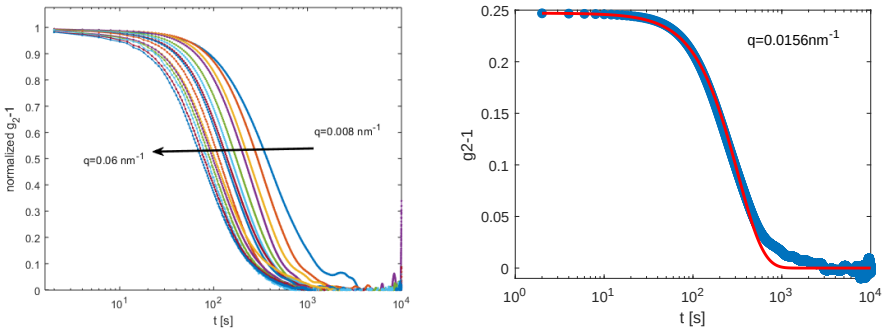


Figure 5.10: Left: normalized autocorrelation functions at q values between $q = 0.008nm^{-1}$ and $q = 0.06nm^{-1}$. In all cases we have a similar compressed shape with relaxation times decreasing with q. Right: Autocorrelation function with a compressed exponential fit. The fit can reproduce reasonably well only the first part of the decay, while the small stretched tail cannot be described without relying on more complex models, the results of the reported fit are $\tau = (508 \pm 4)s$, $\beta = 1.51 \pm 0.01$ $A = 0.247 \pm 0.003$.

particles dispersed in a glass forming medium [143]. Another model that has proven to be quite successful, is the one initially proposed by Cipelletti et al. and subsequently refined by Bouchaud and Pitard [144, 145]. This model, tailored for the description of collapsing gels, describe a system of attractive particles in which random micro-collapses occur producing point like dipole stress fields leading to a distribution of strain velocities.
The compressed exponential is usually accompanied by an anomalous scaling of $\tau(q)$ indicating non-diffusive processes; typically, is observed $\tau \propto 1/q$, which is often labelled as hyper-diffusive or ballistic regime. Indeed, this is also our case, as can be seen in fig. 5.12 where the relaxation times for the old sample as a function of q are reported. A good fit to the data is already obtained with the simple relation $\tau = 1/\omega_0 q$, however considering the possibility of a finite value for $\tau$ in the limit $q \to 0$ (namely $1/\tau = \omega_0(q + a)$) a much better fit is obtained. Good fits can also be obtained using a power-law of the kind $1/\tau = \omega_0 q^\mu$, and in this case a value of $\mu = 0.91 \pm 0.04$ is obtained ( $\mu = 0.80 \pm 0.04$ and $\mu = 0.82 \pm 0.02$ are obtained for the young and rejuvenated samples respectively). For comparison, the rescaled values of $\tau$ for the other runs are reported, and we can see a nearly-identical q-dependance, meaning that the sample's age does not alter this feature of the dynamics.

Since we are here to learn about the properties of the water-lutidine system in conditions close to the critical point, the solvent cannot offer a

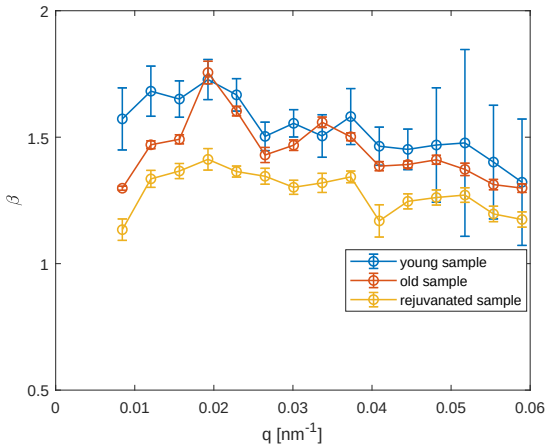


Figure 5.11: q-dependence of the compressing exponent $\beta$ for all three datasets (young,aged and rejuvenated). In all cases the values are always greater than 1 and do not show any appreciable change at different q.

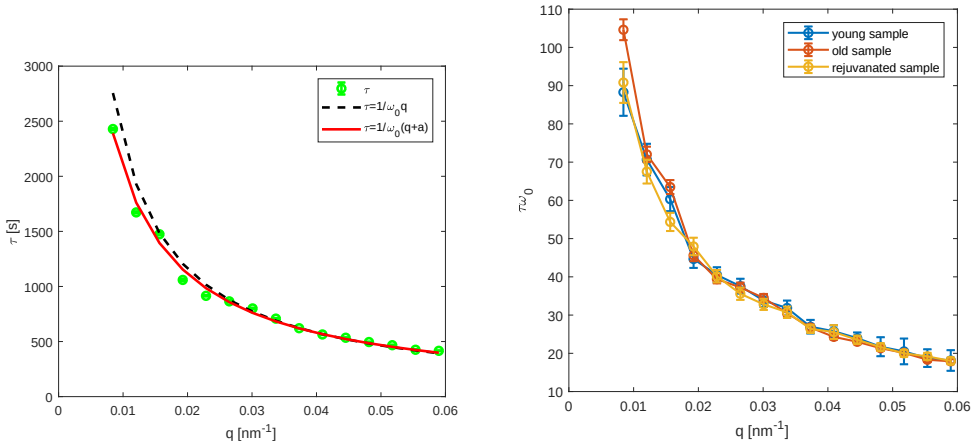


Figure 5.12: Left: Relaxation times as a function of the exchanged wavevector for the aged sample. The black dashed line is a fit using the law $1/\tau(q) = \omega_0 q$, while the red continuous line is the fit obtained with an extra parameter $(1/\tau(q) = \omega_0(q + a))$. Nearly identical results would be obtained with a two parameter fitting function of the kind $1/\tau(q) = \omega_0 q^a$. Both models describe well the behaviour at large q values, while the discrepancies become more and more evident as q approaches to zero.

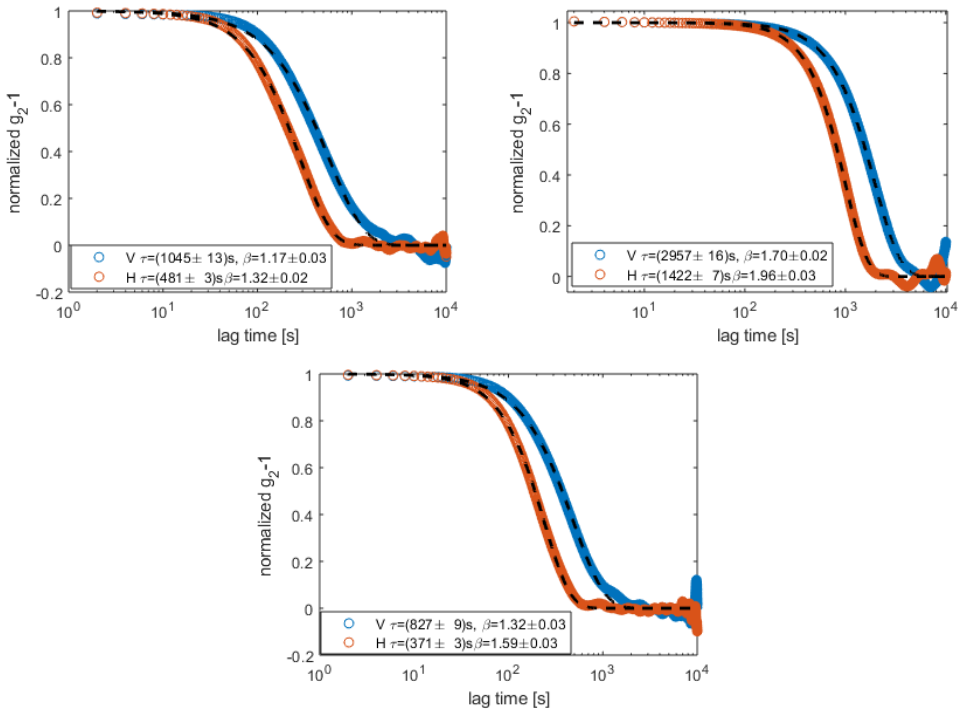


Figure 5.13: Comparison between the autocorrelation functions obtained from vertical and horizontal sectors. In all cases the horizontal functions manifest a faster and more compressed dynamics. Top left results for young sample, top right aged sample and bottom rejuvenated sample.

good match for the nanoparticle's density. Thus a priori, one could expect to observe detectable gravitational effects on our systems, and the typical signature would be an accelerated dynamics along the vertical direction. Thus one of the first test performed on our data was checking the presence of dynamical anisotropies. As can be seen from fig. 5.13 dividing the iso-q ring in quarters, a certain degree of anisotropy can already be observed, but it cannot be attributed to gravitational effects, since along the vertical direction the characteristic times are significantly longer.

The questions that immediately arise are: what is happening inside our samples? The dynamics observed along the horizontal plane is qualitatively the same to the one observed along the vertical direction? To begin answering the latter question, we can study the dependence of the dynamical parameters $\tau$ and $\beta$ on the azimuthal angle $\varphi$. As can be seen from fig. 5.14, approaching the vertical direction, the relaxation time increases quickly up to one order of magnitude more than the horizontal plane. At the same

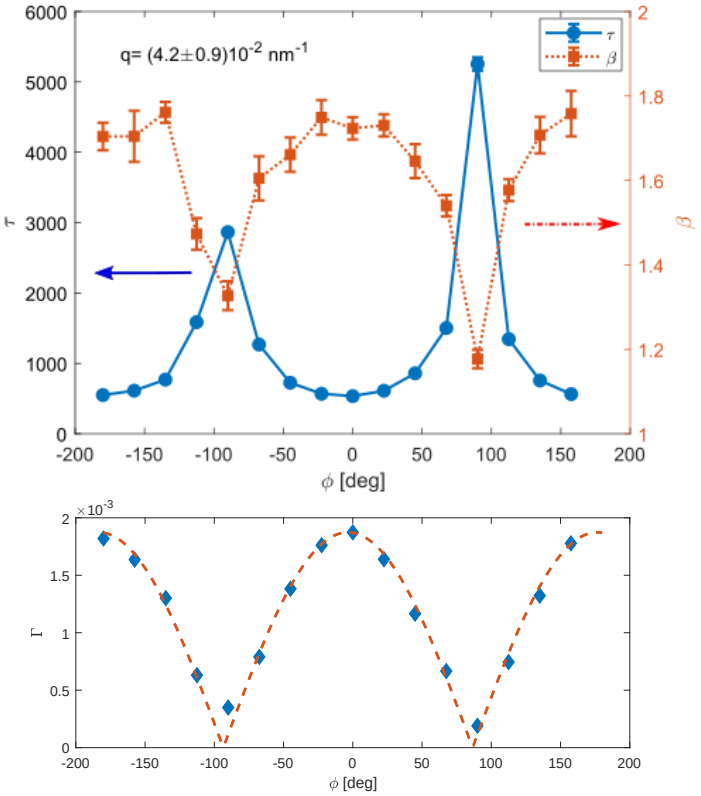


Figure 5.14: Analysis of the dynamical parameters for the aged sample. The relaxation time sharply rises at $\varphi$ values of $\pm\pi/2$ corresponding to the vertical direction, while the compressing exponent's value drops towards 1. In the bottom panel, the inverse of the relaxation time $\Gamma = 1/\tau$ is also reported as a function of $\varphi$, the red line is a simple $\Gamma_0|\cos(\varphi)|$ where $\Gamma_0$ is the maximal value of $\Gamma(\varphi)$. For the sake of clarity, the results for the other two datasets are not reported here but are qualitatively identical.

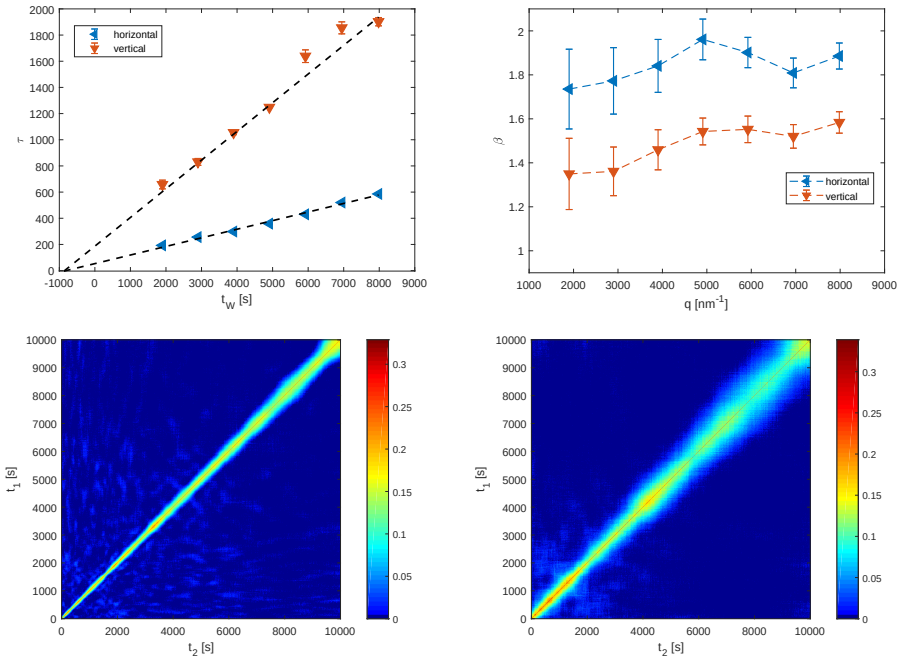


Figure 5.15: Results for the aging quantities from the young sample measured at q corresponding to the first neighbours peak. Top left: comparison between the relaxation times measured along the horizontal and vertical directions, the dashed lines are linear fits prolonged to the interception point before the beginning of the experiment. Top right: aging of the compressing exponent. Bottom: autocorrelation matrices for the horizontal (left) and vertical (right) directions.

time, the compression exponent sharply drops towards values close to one. The situation is clearer if we consider the rate $\Gamma = 1/\tau$, plotted as a function of $\varphi$ in the bottom part of fig. 5.14, and we immediately notice that it follows a simple cosine function $\Gamma \propto \cos(\varphi)$. This is an important piece of information, but before drawing any conclusion let's have look at another crucial aspect of our colloidal system, the aging dynamic.

### 5.5.2 Aging dynamics

For this purpose, it's better to focus our attention on the youngest sample, shown in fig. 5.15, as it displays a clear full aging with $\tau \propto t_W$. The data reported in fig. 5.15 are obtained taking sectors along the horizontal and

vertical direction with $\Delta\varphi = \pi/4$ which is a good compromise between good statistics and resolution in $\varphi$, and setting the origin of the waiting times ($t_W = 0$) as the beginning of the measurement. Both along the vertical and horizontal directions the relaxation time follows a simple linear law of the kind

$$\tau(t_W) = \alpha t_W + \tau_0 \tag{5.3}$$

Both $\tau_0$ and $\alpha$ are larger along the slow vertical direction than the fast horizontal one, implying a seemingly counter-intuitive behaviour of a fast aging for a slow motion. For the exponent we can see that the horizontal ones are systematically larger than the vertical ones and that both display a small growth with $t_W$. A last important thing that must be noted before proceeding further is that extrapolating the linear behaviours for negative waiting times, i.e. for the instants before the beginning of the experiment, the two lines intercept at a point that is about twenty minutes before $t_W = 0$ which is compatible with the end of the sample's preparation,meaning that this observed dynamics is initiated immediately after the sample preparation. Obviously these last considerations are only qualitative since it has been proven that the initial stages of aging in colloidal systems usually shows an exponential growth followed by a slower linear or sublinear behaviour [74, 75].

All these observations can be quickly explained thinking to the results of fig.5.14. In fact $\tau \propto 1/cos(\varphi)$ and the relaxation times along the vertical or the horizontal directions are the same quantity, simply scaled by a geometrical factor. In this case, the "genuine" relaxation function can be found when the term $1/cos(\varphi) \sim 1$, that in our case means $\varphi$ close to the horizontal plane.
In fact, focusing our attention on the q-dependence of the aging relaxation times taken considering only azimuthal angles close to zero ( fig. 5.16 and 5.17), we can see that both the aging rate $\alpha$ and the intercept $\tau_0$ follow closely a $q^{-1}$ dependence, as outlined in the plots of fig. 5.17, thus we can write $\alpha q = \delta$ and $\tau_0 q = \gamma$.

We are now ready to put together the information that we have collected. Let's start with the $\Gamma(\varphi) \propto \cos(\varphi)$; this kind of dependence in relaxation rates can be encountered in velocity fields where $\Gamma = |\mathbf{q} \cdot \mathbf{v}|$, where in this case the velocity is perfectly aligned along the radial direction. This suggests that what we are observing are strain velocities due to the shrinking of the colloidal glass, behaviour often observed in similar systems [146, 147, 148]. The other interesting result came from the aging of the relaxation time,

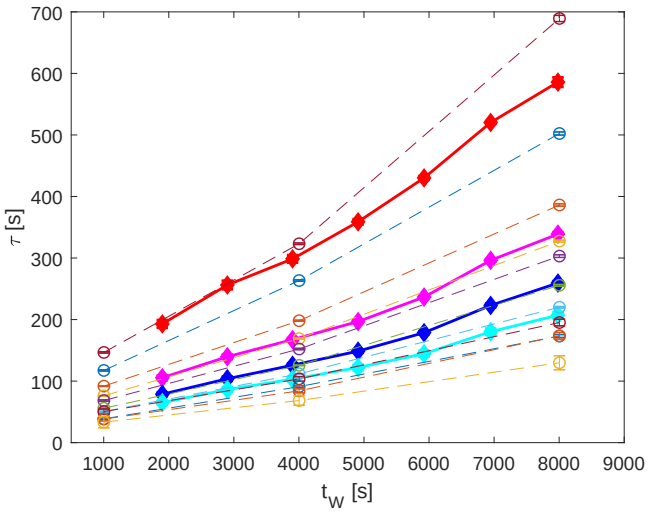


Figure 5.16: Relaxation times as a function of $t_w$ and q obtained following different complementary approaches. Empty symbols: aging obtained with a fine q-scan ($q \in [0.015nm^{-1}, 0.07nm^{-1}]$ but keeping a coarse $t_W$ resolution. Filled diamonds: relaxation times extracted from the 2-times at 4 well separated q-values. The q-resolution was kept constant in both methods, and all the analysis are performed along the horizontal direction.

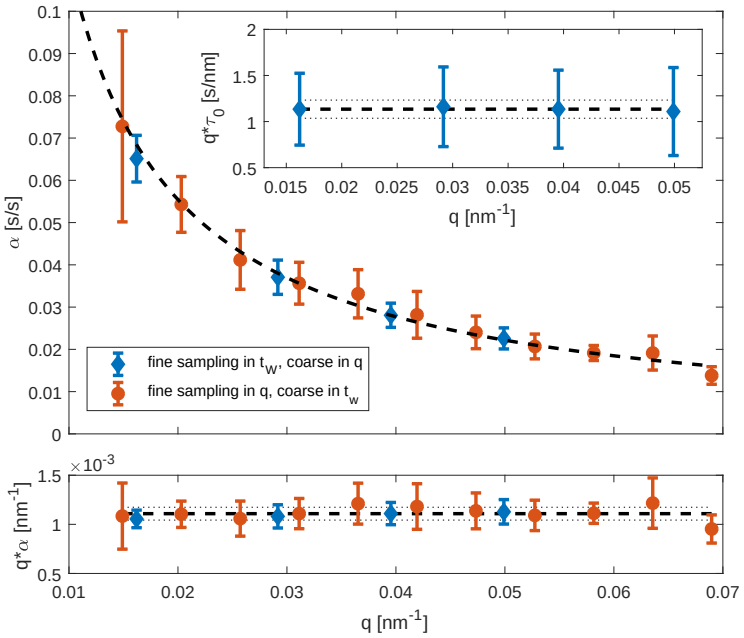


Figure 5.17: Results for the parameters of eq. 5.3 at different q-values. The orange filled circles corresponds to the empty symbol results of fig. 5.16, while the blue diamonds correspond to the filled symbols. Main panel: $\alpha(q)$ from different approaches, the dashed black line is a fit with equation $\alpha(q) = \delta/q$. Inset $\tau_0 q$ for the parameters obtained from the fine $t_w$ sampling, the results from the coarse sampling are omitted because, even if their nominal values are close to the ones reported here, they come with too large uncertainties. Bottom: $\alpha \cdot q$ for both samplings, here both results are consistent and with similar uncertainties.

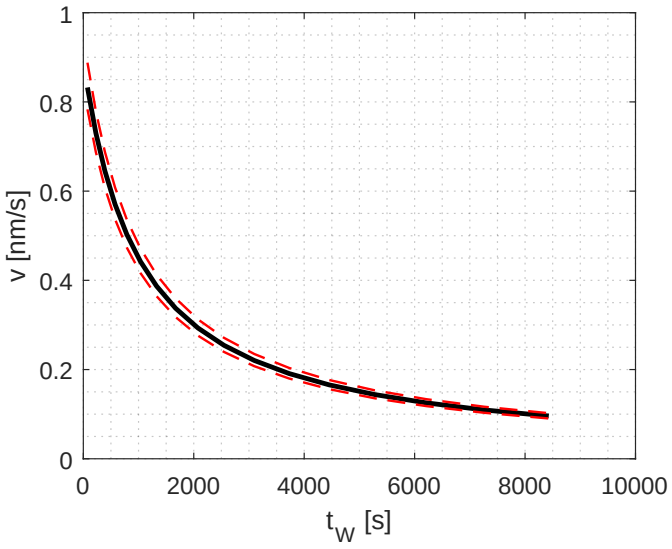


Figure 5.18: Velocity field as a function of $t_W$ computed with the values obtained from the young samples. The red lines are the confidence bands coming from the uncertainties of $\delta$ and $\gamma$ ($\delta = 1.11 \pm 0.07)10^{-3} nm^{-1}$ , $\gamma = (1.13 \pm 0.02) s/nm$ ).

that show us a close to $1/q$ dependence for $\alpha$ and $\tau_0$. Using the values obtained for the horizontal direction we can approximate $\mathbf{q} \cdot \mathbf{v} \sim qv$, and from $\tau(t_W) = (\delta t_W + \gamma)/q$ we obtain an expression for the aging velocity field:

$$v = \frac{1}{\delta t_W + \gamma} \tag{5.4}$$

In fig. 5.18 the values of $v(t_W)$ for the aging sample are reported, at the beginning of the measurement, the estimated velocity was $v = (0.88 \pm 0.04) nm/s$, which is close to other values obtained in other soft systems [144]. Now we can also explain why $\beta$ seems to grow with $t_W$. In fact, to obtain the $g_2 - 1$ we had to perform a time average on a finite interval of $t_w$ and a finite interval of $\varphi$. We observe in fact that looking at the two-times obtained with $\delta\varphi = \pi/4$ and reducing the integration time at values comparable to the relaxation time, the value of the exponent rise to values close to 2. this means that the autocorrelation function that we have seen in fig. 5.10 can be described by

$$g_2(t) - 1 \approx \frac{1}{2\pi} \int_0^{2\pi} d\varphi \frac{1}{\Delta t} \int_{t_w - \Delta t/2}^{t_w + \Delta t/2} dt'_w e^{-(qv(t'_w)\cos(\varphi)t)^2} \tag{5.5}$$

It's easy to demonstrate that the function arising form the averages in eq.

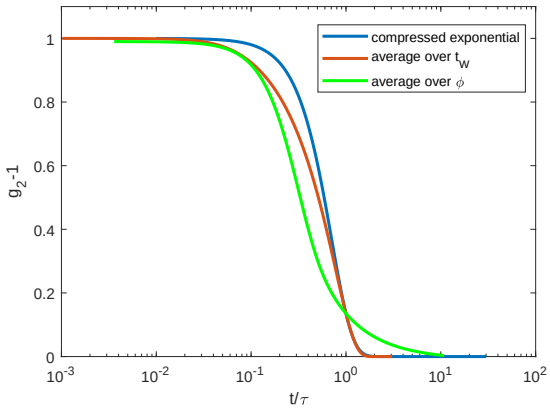


Figure 5.19: Relaxation functions computed using equation 5.5. Blue: simple compressed exponential with $\beta = 2$, red: average over 3000 seconds with aging parameters of the young sample, green: average over $2\pi$ for a fixed age. The average over different ages tends to stretch the decay, thus lowering the $\beta$ value, while the average over different angles give rise to a stretched tail.

5.5 can be easily mistaken for a compressed exponential with $\beta < 2$, and that when the $\varphi$ is not too large $\beta \to 2$ for $\delta t_W / < \tau > \to 0$. In figure 5.19 the computed autocorrelation functions that has to be expected for an average over a certain time interval at a small $\delta\varphi$ and on all the azimuthal angles with a non-aging relaxation time are reported.

Moreover, in the conditions $\delta t_W / < \tau > \to 0$, it is possible to compute analytically the average performed on the whole ring of eq. 5.5

$$g_2(t) - 1 = A * e^{-(tqv)^2} I_0((tqv)^2) \tag{5.6}$$

where $I_0((tqv)^2)$ is the modified Bessel function of the first kind. It is now possible to correctly fit the relaxations observed with the average over all the azimuthal angles, see fig. 5.20.

One more intersting question is, why the exponent is so close to two. We have seen that we are in presence of a velocity field, thus it is possible to employ the formalism developed for the autocorrelations detected in presence of flow which are expressed in terms of three contributions [149]

$$g_2 - 1 = |g_{1D}|^2 |g_{1T}|^2 |g_{1S}|^2$$

Here the first term is due to the free particle diffusion, which depends on the diffusion constant $D$, that since our samples are all in an arrested state, this

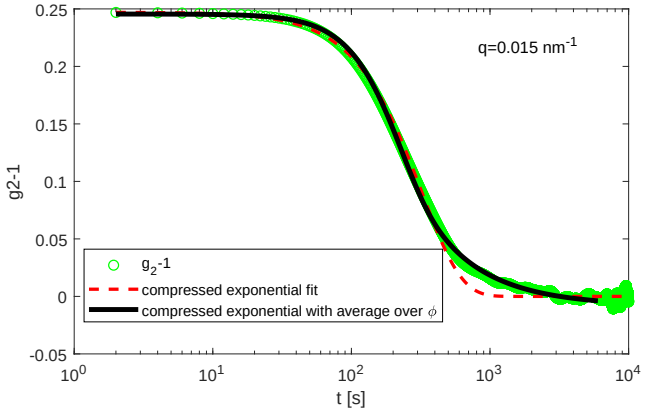


Figure 5.20: Experimental autocorrelation function computed over the whole ring from fig.5.10. Red dashed line :simple compressed exponential fit, black continuous line : fit using eq.5.6, it is now possible to describe also the stretched tail. The results obtained with this method are systematically smaller than the one obtained with compressed exponential functions along the horizontal direction (in this case the results using eq. 5.6 is $\tau = (261 \pm 1)s$, while from the compressed relaxation $\tau = (328 \pm 5)s$); this, in order to obtain reliable data, a certain $\delta\varphi$ must always be considered, hence the observed value of the relaxation time is an overestimate of the real value.

term does not contribute appreciably to the observed dynamic. The second term describes the exit of colloidal particles due to the flow. Here, since the motion is radial in a cylindrical symmetry this term does not contribute significantly to the overall $g_2 - 1$.
The last term describes the shear induced effect. The decorrelation is modulated by a self-beating frequency created by particles moving with different velocities inside the scattering volume. If the velocity difference between two particles separated by a distance $\mathbf{r} = \mathbf{r_2} - \mathbf{r_1}$, is $\delta\mathbf{v}$, then the beating frequency is given by $\mathbf{q} \cdot \delta\mathbf{v}$. The resulting autocorrelation function will be then subject to the modulation arising from the average over all Doppler shifts between all pair of particles inside the scattering volume, which can be written as

$$|g_{1S}|^2 = \frac{1}{4R^2} \int_{-R/2}^{R/2} d\mathbf{r_1} \int_{-R/2}^{R/2} d\mathbf{r_2} e^{-i\mathbf{q}\delta\mathbf{v}(\mathbf{r_1},\mathbf{r_2})t} \tag{5.7}$$

Knowing the expression for the velocity across the scattering volume it is possible to solve eq. 5.7, for a laminar shear [149]

$$|g_{1S}|^2 = \left[\frac{sin(\Gamma_S t)}{\Gamma_S t}\right]^2$$

or for a Poiseuille flow described by a parabolic velocity profile [150, 149]

$$|g_{1S}|^2 = \frac{\left[\frac{\pi}{4} erf(\sqrt{i\frac{\pi}{4}\Gamma_S t})\right]^2}{\Gamma_S t}$$

Where $\Gamma_S = \mathbf{q} \cdot \mathbf{v_0}$, with $\mathbf{v_0}$ the maximum shear velocity. Among these two solutions the one that is more likely to describe our data is certainly the latter, however in the limit of $\Gamma_S t \to 0$ both the expressions can be approximated by a a Gaussian function.

However, from the transmission scans performed at the beginning of every measurement it is not possible to detect any significant density gradient across the capillary, and the structure factor measured at the beginning of a measure with a young sample does not differ substantially from the ones observed at the end once the sample has aged. These facts indicate that here we are not in presence of a particle flow from the center of the capillary toward the walls or vice versa, but instead the situation appear more complex, with cluster of particles that move inward and outward the capillary, following a certain velocity distribution.

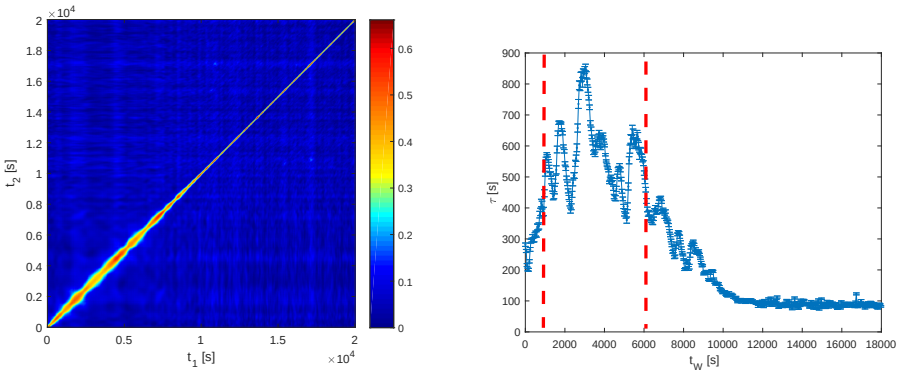


Figure 5.21: Left: autocorrelation matrix of the whole dataset for the rejuvenated sample. Right, evolution of the relaxation time, the region between the two red dashed lines, has a nearly constant $\overline{\tau}$.

## 5.6 Dynamical heterogeneities

From the autocorrelation matrices displayed in fig. 5.15 we can see small fluctuations along the diagonal, and one might wonder if they are the sign of dynamical heterogeneities. The scattering volume in this experiment is approximately $500X10X10\mu m^3$, and for volume fractions of $\sim 0.5$ and nanoparticles with radii of $217nm$, the number of probed particles is approximately $N \sim 6 \cdot 10^5$. This number is indeed quite high, and trying to extract the dynamical susceptibility from the aging sample is indeed quite difficult, since as we have seen in previous chapters, the aging can mimic the signal of the dynamical heterogeneity. So we need a sample in which aging is not too evident, and luckily, this is the case for the rejuvenated sample.

In fig.5.21 it is possible to see the complete dataset collected on the rejuvenated sample. Two very distinct regimes can be identified. A first regime, in which the dynamics is the same as the one described in previous sections displaying at first a rise in $\tau$, then a region where $\tau$ fluctuated around a fixed values and then a drop of $\tau$. The second regime is characterized by a perfectly Gaussian decay, nearly identical in both horizontal and vertical directions and weakly q-dependent. This latter dynamics is probably due to the term $g_{2T}$, thus it is not very interesting for our current objective. This last behaviour is the sign of a macroscopic collapse of the whole colloidal system and the general behaviour of fig. 5.21 is in qualitative agreement with other XPCS measures of collapsing gels [151]. What is important for the present discussion is that the first regime is still characterized by local motions, and that in this regime there exists a time sector in which the average relaxation time does not change with the sample's age. Focusing our attention on this

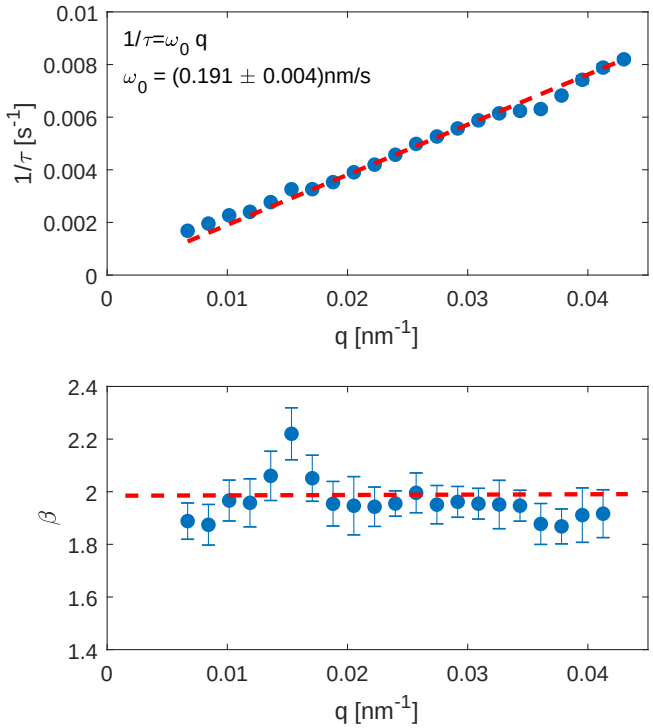


Figure 5.22: q-dependence of $1/\tau$ (top) and $\beta$ (bottom) for the "constant" time interval outlined in fig. 5.21 for the horizontal orientation. For this selection $\tau \propto 1/q$ without adding corrections as in fig. 5.12 and $\beta$ has values close to 2 at all the probed exchanged wavevectors.

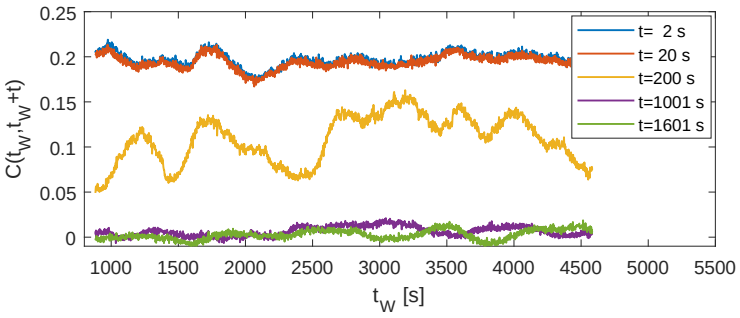


Figure 5.23: $C(t_W, t_W + t)$ at different values of the lag time t for $q = (0.028 \pm 0.008)nm^{-1}$. The dynamic appears fluctuating already at small lag times and the fluctuations remarably increase toward intermediate lag times, i.e. close to the relaxation time $\tau$. This behaviour is different in respect to the sudden rearrangements of [144], thus suggesting an intermittent dynamic of a different kind.

specific time sector is then possible to determine accurately the dynamical properties of our system without worrying too much of possible artefacts introduced by aging. The first quantities to be checked are the relaxation times and the exponents as a function of q, reported in fig. 5.22. The exponent is now very close to 2 (equal to 2 within the errobars) for nearly all the probed q values, while the inverse of the relaxation time is now well described by the ballistic assumption ($1/\tau = v_0 q$) that characterizes the dynamic governed by small local rearrangements. We are now ready to look at the experimental dynamic susceptibility. Adopting the extrapolation mechanism illustrated in chapter 3, it is possible to separate the statistical contribution to the $\chi_4$ from the real physical fluctuations. The results are functions peaked near $\tau$ as reported in fig. 5.24.

Even if the sample behaves like an attractive gel [144], the dynamic is not exactly of that kind. The main difference can be found looking at the $C(t_W, t_W + t)$, reported in fig. 5.23, in a similar way as the ones reported in [1, 104]. Differently from aging gels, we do not have sudden jumps, sign of sudden collapses, but instead large fluctuations. It is possible to filter out the gaussian contribution due to the stastistical noise with the procedure described in chapter 3 and in [2], obtaining the dynamical susceptibility $\chi_4(t, q)$ associated to the measured dynamics. In fig. 5.24 a representative curve for the susceptibility at fixed q compared to the corresponding $g_2 - 1$. This filtered susceptibility is, in principle, proportional to the true dynamical heterogeneity ($\chi_4^{het} = N\chi_4$, where $N$ is the number of particles in the scattering volume). With the exception of the lowest

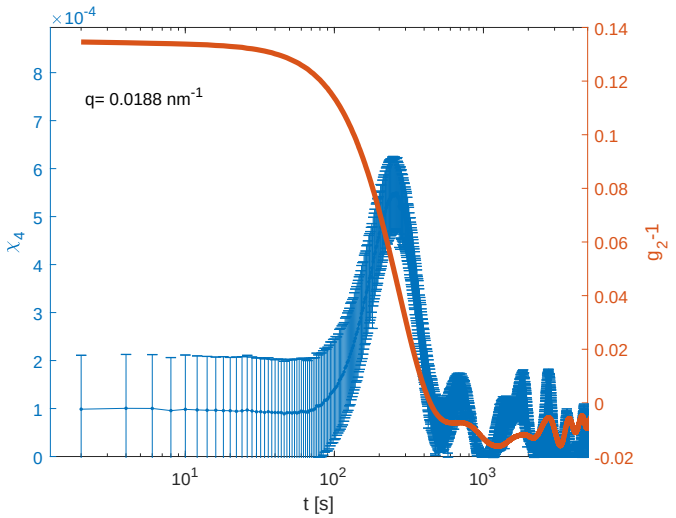


Figure 5.24: extrapolated $\chi_4$ and measured $g_2 - 1$ for a fixed q along the horizontal direction. The $\chi_4$ presents a sharp peak in the proximity of $\tau$ and smaller contributions in correspondence of the $g_2 - 1$ ripples at larger times, while it is consistent with 0 for small lag times.

q-values, the susceptibilities present a clear peaked shape with maximum values $\chi_4(t^*)$ located at times $t^* \sim \tau$. In fig. 5.25 a false color plot of $\chi_4(t, q)$ is reported, and it is easy to see how the $\chi_4$ signal develops with a bright peak at $q \sim 0.016nm^{-1}$ in correspondence to the first neighbour peak in the $S(q)$. This behaviour is more evident if we focus only on $\chi_4(t^*)$, as reported in fig. 5.26, and compare it to the structure factor. In this picture, the experimental dynamical susceptibility is multiplied by the estimated number of particles. Thus the numbers on the y axis of figure 5.26 represent the total number of particles participating a collective rearrangement. It must be pointed out that CRRs smaller than $\sim 100$ particles cannot be detected with these data as a consequence of the uncertainties over the extrapolated values. Nevertheless, we can infer that the number of particles, participating in a same collective motion is quite similar to the one observed in other structural rearrangements of colloidal samples. Normalizing the values of $\chi_4$ with the squared contrast of the $g_2$ ($A \propto f_q$) leads to a linear dependence on q, similar to the one observed on colloidal gels in refs.[1, 104]. This means that the structural information displayed by the dynamical susceptibility came from the non-ergodicity level ($f_q$). The drop of dynamical heterogeneity for larger length-scales can be related to the fact that increasing the probed lengths one is approaching the the macroscopic, and homogeneous, limit.

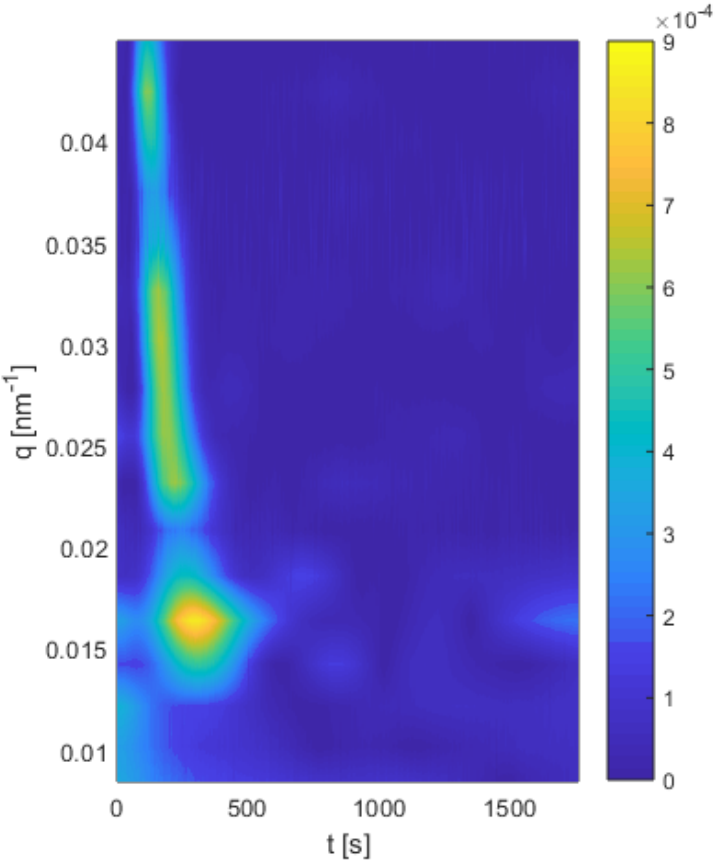


Figure 5.25: Map in false colours of $\chi_4(t, q)$. It is evident how the principal peak of the $\chi_4$ is present only a q-values larger than $q_{max}$, i.e. the q corresponding to the first neighbour peak. This means that the cooperative motion is limited only at very short distances. At q-values larger than $q_{max}$ we can observe that the maximum of the $\chi 4$ maintain itself approximately constant with the exceptions of two local minima, which are in correspondence of the structure's factor minima.

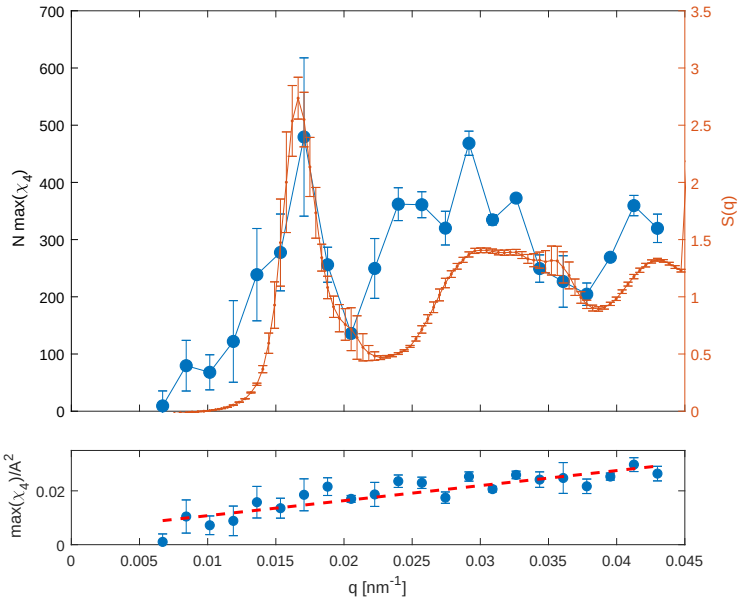


Figure 5.26: Top: maximum value of the observed $\chi_4$ multiplied by the total number of particles in the scattering volume. This number corresponds to the number of particles undergoing a collective motion. In our case we have a maximum in correspondence to the inter particle distance ($q_{max}$), where $\sim$ 500 particles are participating to the motion and after that the peak value stabilizes at $\sim$ 400 particles. Bottom: normalized values of $\chi_4/A^2$; this normalization emphasizes only the temporal fluctuations. In fact recalling what we have seen at the end of chapter 3, all the contribution to the dynamical susceptibility depends on the squared mean value of the contrast ($A^2$).

## 5.7 Visible PCS

We have seen that the mismatch in the refractive index causes the concentrated samples of the larger colloidal particles to be too opaque to be probed with visible light. However, colloidal glasses obtained with smaller particles (diameter $\sim$ 100 nm), immediately after production are reasonably transparent. The scattered light photons are enough to observe a reliable $g_2 - 1$ in multi-speckle PCS experiment allowing the study of the out of equilibrium glassy dynamics even for these colloidal glasses, however the presence of a non-negligible multiple scattering, poses limitations to the time-scale that can be effectively probed, since the more the sample ages, the more opaque it becomes, progressively enhancing the multiple scattering contribution. Qualitatively this can be seen by an increase of the Tyndall effect, i.e. illuminating the sample with white light it will appears lightly blue and the transmitted light will be orange, as can be seen from fig 5.27.

### 5.7.1 Experimental set-up

The experimental set-up employed in these measurements is similar, in principle, to the one described in cap. 4, i.e. we perform a multi-speckle experiment with a 532 nm CW laser. In fig. 5.27 the details for this new configuration are reported. The main difference with respect to the one described in chapter 4, comes from the collecting optics, now composed by a couple of lenses with focal lengths $f_1 = 50mm$ and $f_2 = 500mm$, arranged to magnify the scattering volume by a factor of $\sim 10$. The detector now is a ORCA-Flash4.0 V3 Digital CMOS camera from Hamamatsu. It is characterized by a chip of 2048 X 2048 pixels, each pixel is $6.5 \times 6.5\mu m^2$, and the frame rate can be at maximum 2655 fps (selecting a ROI of 2048 X 8 pixels). Here the limiting aperture is given by the collecting lens's diameter (39 mm), and the resulting speckle size is $l_c \approx 8\mu m$, thus slightly larger than the single pixel dimension.

### 5.7.2 Experimental results

The samples probed with this optical set-up was created following two different procedures. A first set of samples were created following the same preparation protocol described for the SAXS experiments, let's call it "slow procedure" since dispersing the colloidal glass with only the vortex mixer requires quite a long time. These samples were characterized by fast aging compressed functions, as it can be seen in fig. 5.28. The observed aging here follows a more complex behaviour than the one observed in SAXS

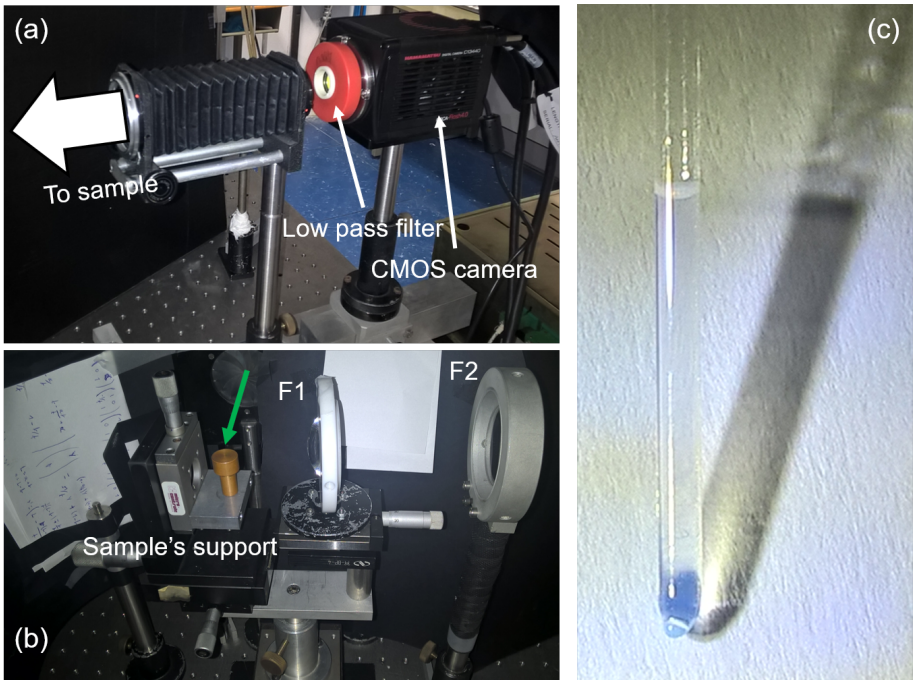


Figure 5.27: (a) details of the detection apparatus. A low-pass filter cuts off visible radiation with wavelength larger than 540 nm clearing the signal from the sample's luminescence. (b) details of the sample's stage and collecting optics. The green arrow indicates the optical path of the incoming laser beam, the sample is located on a XYZ movement inside a small container full of decalin (not shown here) to reduce the scattering at the sample's interfaces. The signal is collected at a scattering angle of 90° with a convergent lens $F_1 \sim 50mm$ and projected on the detector with a lens $F_2 \sim 500mm$. (c) picture of a sample prepared inside a thin walled capillary after 3 weeks from production ,the sample is still transparent but it is already visible the orange transmitted light and blue reflexes. During the measurements the optical path between $F_1$ and the low-pass filter is completely screened in order to reduce stray-light detection.

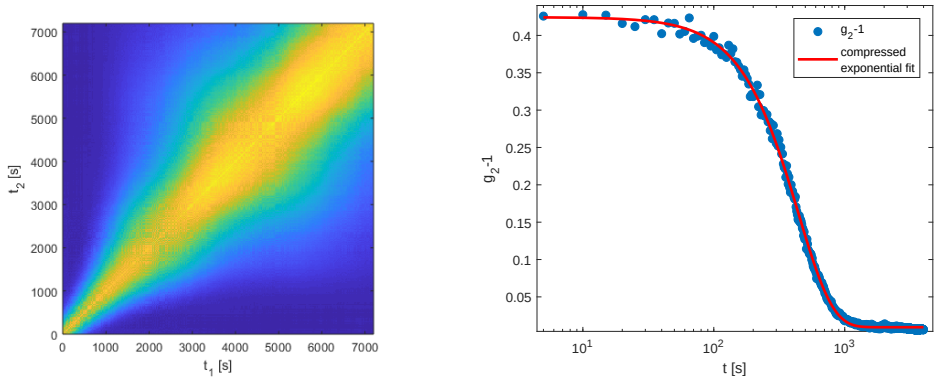


Figure 5.28: example for a fast-aging sample. Left autocorrelation matrix of the scattered intensity. Right $C(t_w, t_w + t)$ of the sample's early stages, time elapsed since the beginning of the measurement: $150s$. Even with visible light, the autocorrelation is described by a compressed exponential function with parameters: $\tau = (672 \pm 3)s$ and $\beta = 1.66 \pm 0.02$.The nominal concentration $\phi \sim 0.36$

experiments. The growth of the relaxation time follows an exponential law at the very beginning of the sample's life (red line in fig. 5.29). After a certain waiting time this regime is eventually replaced by a slower linear dependence similar to the one observed in SAXS experiments (green line in fig. 5.29). This articulated aging is not a novelty in soft disordered systems and has been observed in a wide variety of systems as clay suspensions [74, 75], colloidal glasses and gels [144, 147] and nanoemulsions [148]. This evolution typically follows a significant perturbation of the system, such as a quench from a fluid to a disordered solid or a large mechanical stress, and this dynamics therefore likely reflects the relaxation of internal stress introduced during the perturbation [147].

The second set of samples were produced adding a step in the previous protocol. Immediately after the colloidal system has been concentrated, it is mechanically stirred with a glass rod until all the larger clusters of densely packed particles are dispersed in the sample's volume. Then the couvette is again placed on the vortex mixer to obtain homogeneous sample. Since the time required for this last step is significantly shorter with respect to the first protocol, we call this latter approach "fast procedure". The most striking difference is that here, the intermediate scattering function appears always stretched with exponent $\beta \sim 0.42$. Another striking difference is the slow aging of this new kind of samples, with a growth in the relaxation time

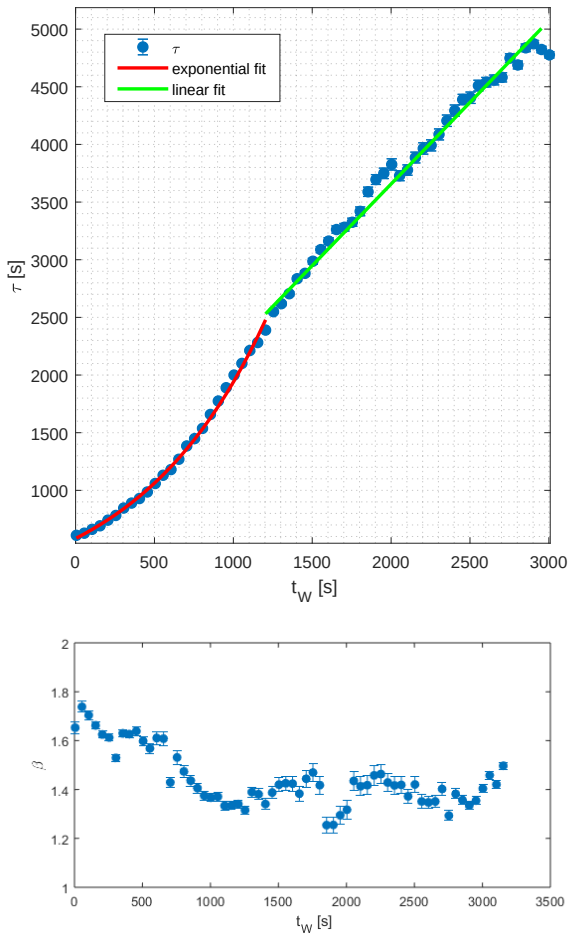


Figure 5.29: Top: aging of the relaxation time. The early stage is compatible with an exponential growth ($\tau(t_W) = t_0 \exp(\gamma t_W)$ with $\gamma = (1.20 \pm 0.03)10^{-3}s^{-1}$,$t_0 = (582 \pm 16)s$), while later $t_W$ are better described by a linear relation ($\tau(t_w) = at_W + b$ $a = 1.42 \pm 0.05$,$b = (826 \pm 113)s$). Bottom: Aging of the compressing exponent, it starts from values close to 2 and approach values close to 1.5.

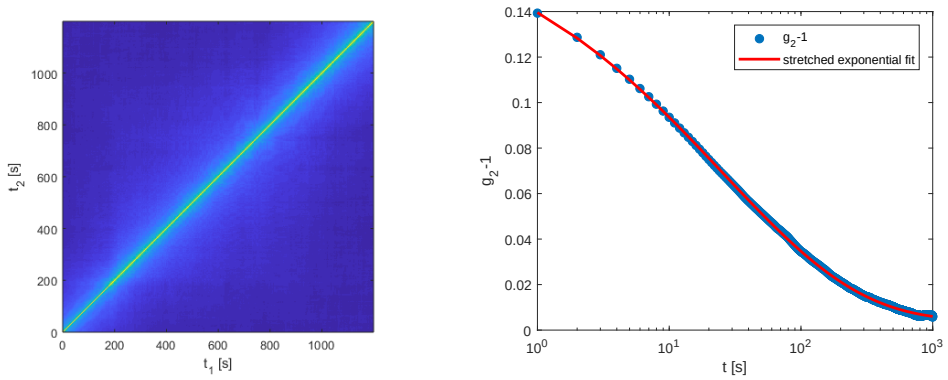


Figure 5.30: Example for a stretched autocorrelation observed in a colloidal glass obtained with the fast procedure. Relaxation time $\tau = (132.9 \pm 0.7)s$ and $\beta = 0.42 \pm 0.02$. The nominal concentration is $\phi \sim 0.37$

of about 1.7% per hour (de facto aging produces appreciable changes only comparing measures taken in different days). Despite the fact that these samples maintain quite fast dynamics, always in the range of hundreds or thousands of seconds, see figures 5.29 and 5.30, the time before the multiple scattering starts to significantly affect the signal is not much different than for samples displaying compressed relaxation, and is limited to 3-4 days.

Thus, the second preparation protocol gives rise to a dynamical response that one would expect in an undercooled liquid or in a glass. Unluckily, we do not have yet a study of the q-dependence for these samples, being the measurements carried out with an optical set-up at a fixed angle, so we cannot be sure if this dynamics is of diffusive origin.The presence of a "compressed" relaxation and the non diffusive dynamics is often explained taking in account the presence of internal stresses in the glass [144, 86]; hence the origin of this peculiar dynamics in the present case, could be related to the sample preparation protocol. This means that, thanks to the mechanical stirring adopted in the second preparation protocol, we are able to relax the stresses that had built up after the first densification. This interpretation can also explain the fact that a sample produced with the fast procedure can manifest again a compressed dynamics if placed again in a centrifuge for long enough time or with high enough acceleration.

The relation between the preparation protocols and the microscopic dynamic has been already observed in the past. A detailed investigation on this relation has been carried out by Angelini and coworkers [75, 152, 153] and it has been clearly observed that, for colloidal glasses of laponite in

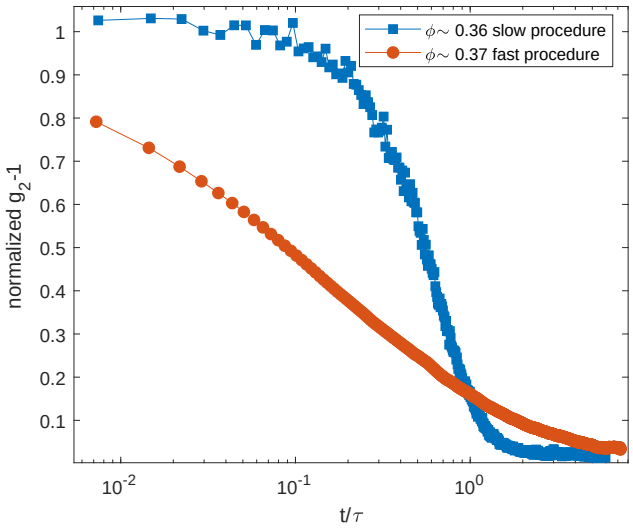


Figure 5.31: Comparison between stretched and compressed relaxations observed in two colloidal glasses with similar nominal concentrations. Since the compressed colloidal glass shows a very fast aging, the autocorrelation function here reported is taken with an average over rather narrow $\Delta t_W$ interval ($\Delta t_W = 50s$).

deionized water, the emergence of a compressed exponential is linked to the shear rejuvenation of sufficiently old samples [152]. These results have been related to a glass-glass transition expected for systems composed of highly charged and highly anisotropic colloidal particles [153] and thus, in principle, one should not generalize these findings to the whole world of colloidal glasses. However, the dichotomous behavior between compressed and stretched decay has been observed in other disordered systems [144, 4, 134].

## 5.8 Conclusions

In this chapter we have studied in detail the characteristics of a colloidal glass composed by silica nanoparticles in a water-lutidine binary mixture. All the reported measurements were carried out in the "repulsive" glass regime, where the particles interact with a long-range attractive and short range repulsive potential. We have discussed the structure and dynamics of large particles with diameter of 450 nm on very short length-scales with SAXS experiments. From these experiments we have seen that the dynamics in these systems arises mainly from a radial strain velocity, which is faster

along the horizontal plane and close to zero along the vertical axis. We have seen that the time average and angular average of this anisotropic decay can introduce significant changes in the shape of the final autocorrelation function, which is well approximated by a compressed exponential with exponent close to 2. This strain velocity tends to slow down with sample age, giving rise to a full aging regime for the relaxation times. From the complex time evolution of the rejuvenated sample we can infer that the dynamical mechanisms that can develop inside a colloidal glass are not always limited to only this velocity field (the final collapse observed in the measurement reported in fig.5.21), and that the slowing down of this velocity can be suspended for a significant time interval, i.e. the presence of a large "aging free" time sector highlighted in fig.5.21. From the dynamical susceptibility of this velocity induced decay we can observe that the dynamical heterogeneities manifest only at short length-scales (for distances shorter than the inter-particle separations), and that they involve several hundreds of particles.
From multi-speckle experiments based on visible light we are able to observe a qualitatively similar behaviour in samples composed by smaller particles (100 nm in diameter), with similar aging behaviour and highly compressed relaxations. Due to the limitations of the optical technique we weren't able to confirm the presence of the strain velocity field in the same way of the SAXS experiments. However we observed that modifying the preparation protocols, it is possible to change the dynamics, retrieving the diffusive-like stretched exponential behaviour.Moreover, from qualitative observations we observed that the strain induced dynamics is obtained when an equilibrated sample is "violently" centrifuged. This fact suggests the stresses introduced inside the sample's bulk during its preparation as origin of this non diffusive dynamics, and among the various processes the most critical appear to be the loading of the capillary. During the centrifugation, the colloidal glass, which has very weak mechanical properties, is subjected to a strong gravitational stress, this stress is transferred from the vertical axis to the radial and tangential directions, and here stopped by the pressure exerted by capillary walls. Once the centrifuge has stopped the stress along the vertical axis is released more quickly than the one accumulated on the radial direction, being the latter hindered by adhesive forces between the sample and the capillary walls. Thus after a transient initial time the dynamics of the sample is due principally to the residual radial and tangential stresses as depicted in the drawing of figure 5.32.

One last consideration comes from the observation that in the SAXS measurements, no sign of density gradients across the sample has been detected, and that the local structure didn't changed during the whole

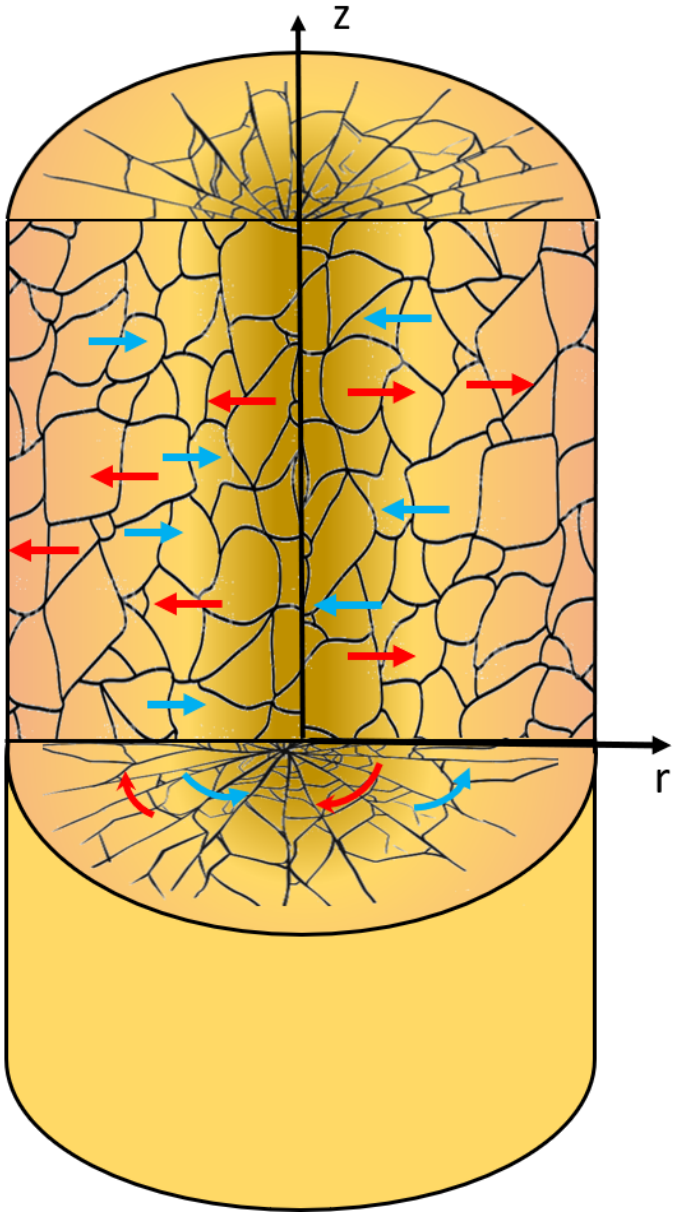


Figure 5.32: Pictorial representation of the dynamical structure developed inside a stressed colloidal sample. Different small regions composed by hundreds of particles move along radial direction toward (blue arrows) and from (red arrows) the vertical $z$ axis.

acquisitions. This fact, with the presence of clear signatures of dynamical heterogeneities, suggests that the dynamics developing inside the stressed colloidal samples is not originated from a macroscopic density gradient and that the particle's motions does not point all in a single direction, but instead group of particles wiggle along radial and/or tangential directions.
This is still a qualitative interpretation of the collected data, and even if the research is not in its earliest stages it is far to be considered concluded. In the near future we hope to characterize more accurately this phenomenon, with a development of a more rigorous theoretical framework, and extend our studies also to the fully attractive colloidal glass.

# Chapter 6

# XPCS on oxides

In previous chapters we have seen that performing photon-correlation experiments at various wave-vectors provides information on very different length-scales, and smaller $\lambda_{probe}$ grants access to larger q vectors. The limits to the accessible ranges are mainly due to the incident wavelength, and of course to practical constraints like beam divergence or geometry of the experimental chamber. Thus it is quite straightforward to see that in the hard X-ray regime with photon energies of $\sim$ 8keV ($\lambda \sim 0.15$nm) the interatomic distances (typically few $\dot{A}$) become accessible in transmission XPCS experiments. In this case, the angles necessary to reach these length-scales are larger than 10° and one refers to these configurations as Wide Angle X-ray Photon Correlation (WAXS) experiments. This chapter will be focused on the refinement of the research carried out by me and Pintori on borate glasses (the previous results can be found in [154] ) and to introduce some recent results on silica.

## 6.1 Beam-induced dynamics

The translatory motions in all glassy systems at temperatures well below $T_g$ are supposed to be completely "frozen", and this fact can be considered in a certain manner as a consequence of the glass state definition. Thus, it was very surprising when, probing the atomic motions at very short length-scales in a sodium silicate Ruta and coworkers discovered a strong departure from Arrhenius behaviour at low temperatures [155]. In their work a complete decorrelation of the intermediate scattering function was observed even at fractions of $T_g$ indicating a dynamics several orders of magnitude faster than the one measured with macroscopic probes like visible laser radiation or viscosity measurements.

As suggested in [154], this deviation can be described with a simple relation of the kind

$$\frac{1}{\tau} = \frac{1}{\tau_\alpha} + \frac{1}{\tau_{ind}} \tag{6.1}$$

where $\tau_\alpha$ is the natural, temperature dependent, structural relaxation time, and $\tau_{ind}$ is the characteristic time of a new process visible only with X-ray probes. This process was readily identified as a beam-induced effect [156] in which the observed relaxation time is strictly related to the total flux impinging on sample as it can be seen from the measurements performed on silica reported in fig. 6.1. The results found in [156] can be summarized as follows :

- The incident X-ray flux induces atomic motions at temperatures well below $T_g$. The time scale for this motion is inversely proportional to the photon flux absorbed by the sample.

- At fixed flux, the dynamics remain stationary and is independent of the accumulated dose.

- The decay time depends in a reversible way, and almost "instantaneously" on the incident flux.

- The shape of the autocorrelation function is independent of flux, suggesting that the observed phenomenon is strongly related to the intrinsic dynamics of the glass.

- This induced dynamics is observed for simple oxides glasses, while metallic glasses do not appear to be affected by X-rays in XPCS experiments.

These observations suggest the presence of a complex beam activated process which differs from the classical radiation damage reported in XPCS studies on soft materials under many aspects. The typical beam damage usually appears with a dynamics varying with the global absorbed dose resulting often in pronounced aging phenomena that are usually triggered by significant structural damage. For oxide glasses an alteration of the local structure is observed, qualitatively a reduction of the structure factor's peak and a increase of the intensity at low q, but it becomes evident only at high absorbed doses. Despite the occurrence of this structural alteration at larger accumulated doses, the observed dynamics is not strictly related to that damage. In fact, if that would be the case, the dynamics would evolve with the accumulated dose (and thus the decay time as well) and

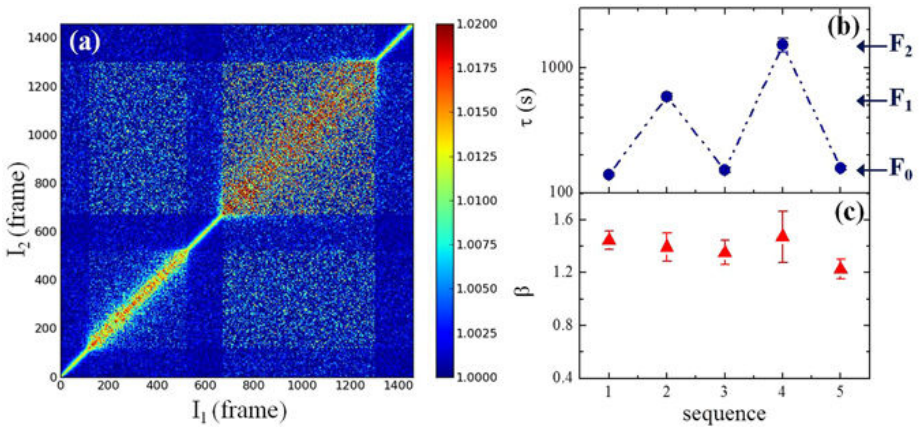


Figure 6.1: Instantaneous, reversible and stationary dynamics. (a) Two-time correlation function measured in vitreous silica at $T = 295K$ and $Q_p = 15nm^{-1}$ by varying the intensity of the incoming flux. Left to right in frame number: $F_0 \sim 1 \cdot 10^{11} ph/s$, $F_1 \sim 3 \cdot 10^{10} ph/s$, $F_0 \sim 1 \cdot 10^{11} ph/s$, $F_2 \sim 1.2 \cdot 10^{10} ph/s$, and $F_0 \sim 1 \cdot 10^{11} ph/s$. (b) Characteristic decay times $\tau$ as a function of the flux intensities used in panel (a). (c) Shape parameters $\beta$ as a function of the flux intensities used in panel (a). Figure taken from [156].

would not be reversible when the flux is changed. This kind of beam-induced dynamics (BID) closely resembles the one observed in transmission electron microscopy experiments performed on extremely thin silica samples [157], where the probing particles act also as a pump, fuelling the observed process. Depending on the specific intents this effect could represent an hindrance to the determination of some physical properties, for example the competition between the intrinsic and induced dynamics expressed by relation 6.1. However, given its close relation with the sample's properties, it can also represent an opportunity to study other physical properties, once a clear understanding of the BID mechanisms is provided.

## 6.2 Alkali-borate glasses

In the work carried out by Pintori and coworkers the role played by absorption and local structure to the determination of the beam induced relaxation time was inspected, and the materials of choice for this task were the borate glasses, because they are thoroughly studied in literature and offer a great control on the details of the microscopic structure.
Let's begin with the building block of this family of materials: the $B_2O_3$

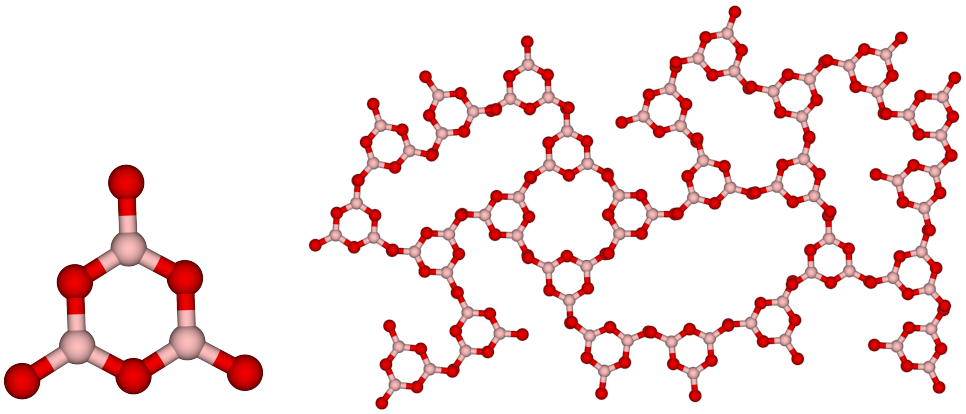

Figure 6.2: schematic representation of the atomic structure of a boroxol ring (left) and of the disordered network (right). The red circles represent the larger oxygen atoms, while the grey ones represent the smaller boron.

unit, already encountered in Chapter 4. At an atomic length-scale, the fundamental unit of this glass is composed by one boron atom linked to three oxygens as depicted in fig 6.2. These triangular units tend to arrange in intermediate structures called boroxol rings that finally build up all the atomic network, thus the elementary unit of $B_2O_3$ is composed by these flat, planar boroxol rings. However several studies demonstrated that not all the atoms are participating in the formation of such intermediate structure, and that the presence of boroxol rings markedly decreases in the high temperature melt [158, 159, 160]. The exact fraction of boron atoms contained in a boroxol ring in the glassy state is still debated. However, combining experimental data and molecular dynamic simulations it was possible to determine an upper limit of $\sim 75\%$[161].

Adding a certain fraction of alkali oxide $M_2O$ (where $M$ stands for a generic alkaline atom) to the glass, the physical properties of the obtained material will start to change and we can observe yet another anomaly involving $B_2O_3$. In fact it was early observed that increasing the alkaline molar fraction the thermal expansion coefficient does not increase monotonically as in the other glass formers, but instead presents a minimum at concentrations of $\sim 20\%$, and the sharpness of such minimum depends on the atomic species of the alkali mixed with the $B_2O_3$. This anomaly arises as a consequence of the formation of new kinds of structural units. In particular, the experiments show that the addition of metal oxide to $B_2O_3$ causes a progressive increase of the number of four-coordinated borons ($N_4$) at the expense of

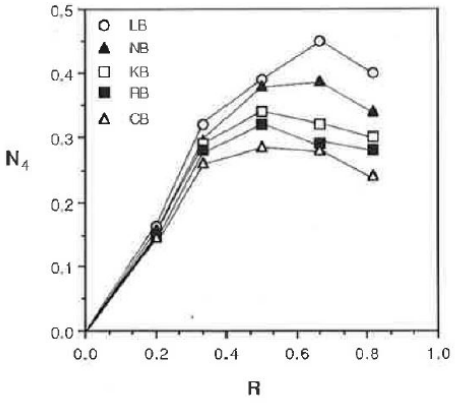


Figure 6.3: , Fraction of four coordinated borons in alkali borate glasses, LB=lithium borate, NB=sodium borate, KB= potassium borate etc. Image taken from [163]

three-coordinated ones, changes the network structures introducing new types of borate structural groups, and that the metal ions do not participate in the network formation [162]. In figure 6.3 the abundance of the $N_4$ groups at various molar ratios for different alkali borate glasses is reported. It is clearly visible that for alkaline atoms concentrations (R) up to $\sim 40\%$, we have a nearly linear dependence of $N_4$ on $R$. This abundance of tetrahedral groups can be explained considering that a four coordinated boron atom will constitute a negatively charged $BO_4^-$ unit in which the excess of negative charge is taken by the boron from the alkali ion to form the fourth $B-O$ bond. The positive alkali ion will then place itself near the $BO_4^-$ to provide local charge neutrality. Alongside this generation of $N_4$ sites, the alkaline ions provide the formation of non bridging oxigens on a $BO_3$ unit, and also in this case the charge neutrality is provided by an adjacent alkali ion. This latter process enters in competition with the $N_4$ formation explaining the local maximum of fig. 6.3.
Neutron diffraction experiments have shown that the short range boron-oxigen structures are nearly identical for different alkali atoms or different molar concentrations. A detailed analysis on the peak of the structure factor reveals two different nearest-neighbour distances 0.137nm and 0.147nm, which can be attributed to the $BO_3$ and $BO_4$ groups respectively [162].

## 6.3 Previous results and phenomenological model

The peculiar microscopic dynamics summarized in paragraph 6.1, is actually function to the incident photon flux. Thus speaking of relaxation times expressed in seconds could be misleading, and a clearer way to represent the decorrelation time can be defined as the number of frames necessary to produce a decorrelation $N_{frames} = \tau/t_{lag}$, where $t_{lag}$ is the lag time separating two different frames ($t_{lag} = t_{exp} + t_{read}$ where $t_{exp}$ is the exposure time and $t_{read}$ is the read-out time). A more quantitative relation between the relaxation time and the incident flux $F_0$ can be found to be [154]

$$\frac{\tau}{t_{lag}} = \frac{A}{F_0 \cdot t_{exp}\left(1 - e^{-\mu L}\right) \cdot \epsilon_{in}/U} \tag{6.2}$$

where $1/\mu$ is the X-ray attenuation length, $L$ is the sample's thickness, $\epsilon_{in}$ is the incident photon energy, and $A$ is a parameter that describe the sample's response do the induced dynamic. $U = \rho V N_a/M$ is the number of atoms (or elementary units) present in the scattering volume $V$, $\rho$ is the sample's density, $N_a$ is the Avogadro constant, and M is the molar mass.
After a time $\tau/t_{lag}$ a fraction of elementary units equal to $1/e$ has moved of a distance of $1/q$, in this amount of time $F_0 \cdot t_{exp}\left(1 - e^{-\mu L}\right)(\tau/t_{lag})$ photons have been absorbed by the sample, and then we can express the number of atoms (or atomic units) that move per absorption events as:

$$N_{units} = \frac{1}{e} \cdot \frac{U}{F_0 \cdot t_{exp}\left(1 - e^{-\mu L}\right)(\tau/t_{lag})} \tag{6.3}$$

thus $N_{units} \propto 1/\tau$,we will shortly see the relevance of this quantity.
To understand how the relaxation process was related to absorption it was decided to study a series of alkali borate glasses $(M_2O)_x(B_2O_3)_{1-x}$, where $M = Li, Na, K$ at fixed molar fraction $x = 0.14$. By varying the modifiers keep in its concentration fixed, the final network configurations were nearly the same, while the energy absorbed from the incident X-ray beam changed considerably. It was clearly demonstrated that the decay time does depend considerably on the number of photons absorbed by the sample, brutally summarizing, the heavier the atom faster the relaxation. For samples with similar local structure but different atomic weights, $\tau$ scales simply with absorption, but the number of units that has moved per photon ($N_{units}$) does not change appreciably for the three different borate glasses as reported in fig. 6.4, while it differs appreciably from the value estimated for pure

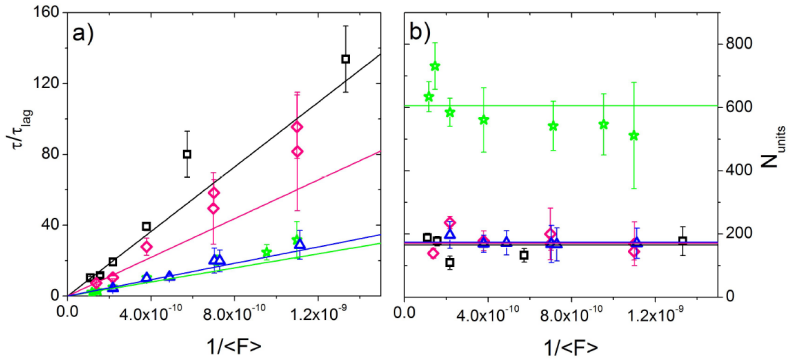


Figure 6.4: Left: decay times obtained from the XPCS measurements on $B_2O_3$ (green stars), $(K_2O)_{0.14}(B_2O_3)_{0.86}$ (blue triangles), $(Na_2O)_{0.14}(B_2O_3)_{0.86}$ (pink diamonds), $(Li_2O)_{0.14}(B_2O_3)_{0.86}$ (black squares) . The data were taken at the peak of the structure factor and plotted as a function of the mean flux $\langle f \rangle = F_0 t_{exp}/t_{lag}$. Right, $N_{units}$ for the different glasses, the solid lines represent the mean values of $N_{units}$:$\langle N_{B_2O_3} \rangle = 600 \pm 20$,$\langle N_{LBO} \rangle = 170 \pm 10$,$\langle N_{NBO} \rangle = 170 \pm 20$, $\langle N_{KBO} \rangle = 174 \pm 4$. Image from [154]

diboron trioxide.

This result suggested a link between the local structure and $N_{units}$, it was decided then to perform a series of measures on different lithium borate glasses ($(Li_2O)_x(B_2O_3)_{1-x}$) at different molar concentrations ($x$ =0.14, 0.22, 0.3, 0.5). As reported in fig. 6.5, it was observed a clear decrease in the value of those $N_{units}$ with the increasing number of tetrahedral units in the glass.

We can further refine this concept of the number of elementary units that had changed their position after the absorption of a photon, but we must discern between two equally plausible scenarios. The first one sees the generation of a photoelectron after the absorption of the X-ray photon. This photoelectron then starts to travel inside the atomic network interacting with the atoms through elastic and inelastic scattering events, and eventually it will loose all its energy. A certain fraction of the inelastic scattering events have produced an atomic displacement giving rise to the detected dynamical signal. We can refer to this interpretation as to the cascade-relaxation process.
In a second scenario, the absorption of a photon induces the breaking of

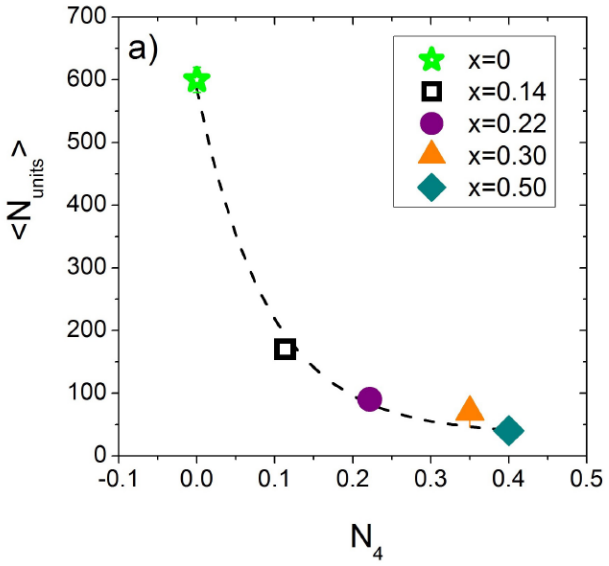


Figure 6.5: $N_{units}$ as a function of the fraction of $N_4$ units for $(Li_2O)_x(B_2O_3)_{1-x}$ glasses at different molar fractions. Image from [154]

an atomic bond and the initial displacement of a single atom. Because the formation of an atomic disordered network is always accompanied by the creation of local stresses, the initial rearrangement produces a cooperative motion in the neighbouring atoms in the attempt to release the stored elastic energy. In this case we have a stress-relaxation process.
With the present knowledge it is not possible to decide which one of the above mentioned models describes more precisely the experimental observations. Moreover one scenario does not exclude the other. In the stress-relaxation framework we can further discuss the meaning of $N_{units}$. Defining $v = V/U$ as the volume of a single elementary unit, where $V$ is the scattering volume, we obtain that the portion of scattering volume that has rearranged its internal structure per absorbed photon is given by $V_{corr} = N_{units} \cdot v$. Making the assumption that all the atoms contained in $N_{units}$ are clustered in the same volume, then it is possible to define a length-scale

$$\xi = \sqrt[3]{\frac{3}{4\pi}\frac{1}{e} \cdot \frac{V}{F_0 \cdot t_{exp}\,(1 - e^{-\mu L})\,(\tau / t_{lag})}}$$

that describes the rearranging region. $\xi$ would then describe the physical extension of the CRR induced by the X-ray interaction with the atoms constituting the glass, and a quite suggestive fact is that the numerical values obtained for this quantity are all of the order of few nanometers [154],

similar to the ones fond in literature for systems close to $T_g$ [164].

## 6.4 Sample preparation

To obtain alkali borate glasses with the desired final properties we had to establish a production procedure taking into account several constraints and complications not present in the preparation of pure $B_2O_3$ glasses. The most delicate complication comes from the necessity to introduce the alkali metals in the $B_2O_3$ glass. Typically alkali oxides are quite corrosive and react violently with water, thus it was decided to make alkali carbonates as a starting ingredient. These carbonates decompose in the alkali oxide and $CO_2$ at temperatures close to the melting point of $B_2O_3$, thus when loading the crucibles one has to keep in mind that at high temperatures the melt will be "inflated" by $CO_2$ suddenly released by the carbonate and if the starting volumes are too large, the alkali borate foam will exit the crucible contaminating the furnace. Another important constraint comes from the tendency of the alkali oxides to be expelled from the melt if the temperature is too high, thus limiting the amount of time in which the sample can be held well above $T_m$ to remove bubbles; and obviously, the alkali-borate glasses do not share the amazing stability against crystallization of pure $B_2O_3$, thus melt-quench techniques must be adopted. The detailed procedure to obtain these glasses can be found in [154]. After the annealing process the samples were polished to reach thickness of $\sim 40 - 50\mu m$ and immediately vacuum sealed.

## 6.5 Experimental set-up

In this chapter we will see results coming from different experiments performed at different synchrotron radiation sources. The experiments performed at ESRF, were realized at beamline ID10 in wide angle configuration. The beamline details are the same of the previous chapter. In particular we used a configuration with $10 \times 10\mu m^2$ spot size and $8.1keV$ incident radiation. The main difference is given by the different detector, now a deep depletion Andor Ikon-M camera able to detect single X-ray photons. The camera has 1024x1024 pixels and a pixel size of 13 $\mu m$, and was placed at a distance of $D \sim 750mm$ from the sample in order to match the speckle and pixel sizes. Due to the rather poor signal, for the computation of the two-times correlation matrix the whole 1024x1024 chip was used, leaving us with an angular resolution $\delta\theta \sim 1^\circ$.

The other XPCS measurements were performed at the Beampline P10 at the PETRA III synchrotron in Hamburg, Germany. An X-ray beam, produced by an undulator source, was focused by a Be compound refractive lens and the radiation was selected by a Si(111) monochromator. Hard X-rays originating from higher order monochromator reflections were suppressed by two Si mirrors reflecting at a grazing incident angle of 0.2°. The spatially coherent part of the beam was selected by rollerblade slits opened to $3 \times 3\mu m$, providing a flux of $\sim 6 \cdot 10^{10}$ photons per second per 100 mA. This configuration results in a longitudinal coherence length of $\sim 1.5\mu m$ and a transverse coherence length of $\sim 3 \times 3\mu m^2$. The speckle size is given by the usual formula $l_c = 1.22\lambda D/d$, where $\lambda = 0.15nm$, d is the beam diameter, and $D = 400mm$ the sample-detector distance, producing $l_c \sim 24\mu m$. The detector was a Princeton CCD ($1340 \times 12300$ pixels, $20 \times 20\mu m^2$ pixel size). The samples were mounted on a specifically designed sample holder with an circular hole (4-5 mm diameter with a 2 mm hole for the X-rays, and 120 $\mu m$ deep), see fig. 6.6. The temperature was kept fixed to $300K$ and monitored with a thermocouple inserted close to the sample holder. The total flux impinging on sample was controlled by means of a series of absorbers, each of them composed by a number, ranging from 0 to 8 of $Si$ foils $25\mu m$ thick. Right along the transmitted beam path a photodiode was placed to monitor the beam intensity and to measure the the sample thickness with the usual Lambert-Beer law $I = I_0 \exp(-\mu L)$.

## 6.6 Experimental results

Despite SAXS and WAXS experiments share nearly identical configurations, when ones goes to collect the photons at large angles the conditions that have to be fulfilled to perform an experiment change quite dramatically. As anticipated in chapter 3, the optimal sample thickness is dictated not only by the material's attenuation length but also by the longitudinal coherence. This latter condition is often the strictest, and then for all kinds of samples the final thickness is limited to be few tens of micrometers, thus smaller than the absorption length for most of the oxides glasses. This means that the measurements will be carried out with very low signals on the majority of samples. This drop in signal is partially compensated by larger detectors (with pixel arrays of $\sim 1000 \times 1000$ pixels) covering larger solid angles. Even with these expedients the final signal is still quite low, as can be seen from fig.6.7, where the histogram of the recorded analog-to-digital units (ADUs) obtained from 1000 images in a WAXS experiment is reported. It is evident the presence of three sharp peaks, above a monotonically decreasing

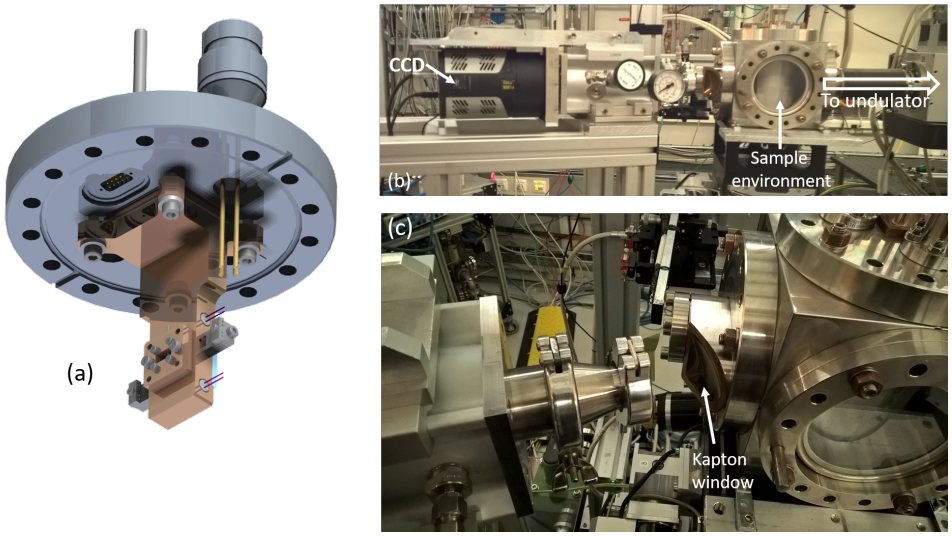


Figure 6.6: Some relevant components of the WAXS set-up at P10. (a): drawing of the sample holder for transmission experiments. The samples are held inside the small copper block fixed to the larger temperature-controlled support (also made of copper); image taken from http://photon-science.desy.de. (b) picture of the WAXS set-up, the Princeton CCD and the sample environment are clearly visible, (c) close-up of the signal's exit path; the scattered photons exit the sample chamber trough a kapton window, cross a small air gap and then enter the vacuum pipe connected to the CCD . This configuration does not allow to detect scattering angles between 7° and 14°.

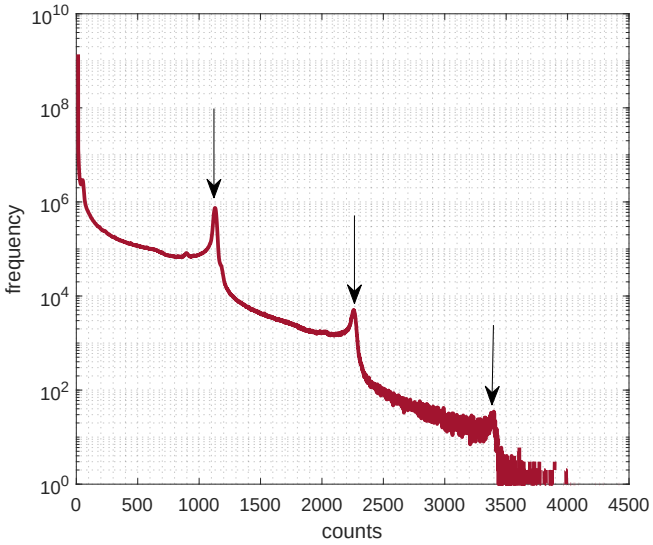


Figure 6.7: Histogram obtained from 1000 images of a WAXS experiment performed on $GeSe_2$, each image has been collected with an exposition of $0.6s$. The arrows point out the occurrence of one, two or three photons impinging on the same pixel during the acquisition. The most frequent ones are obviously the single photon events, here corresponding to approximately $C_{single} = 1120$ADUs, the other peaks are located at values multiples of $C_{single}$.

background due to electronic noise. The three peaks correspond to as much recorded events. The highest, located at $C_{single} = 1120$ADUs, represents the total number of single photon events wile the others correspond to two and three photons impinging on the same pixel at the same time. It is instructive to notice that these latter events are quite rare, if we consider the numbers shown in fig.6.7 normalized per number of images, then we clearly see that on a typical frame there are only $\sim 1000$ single photon events and less than ten double-photon events, while a three-photon event occurs approximately only once every 10 images. Given this shortage of photons it is useful to pre-elaborate the recorded images with a so called "dropletization algorithm". The tasks of this algorithm are to identify the pixels that have been struck by an elastically scattered X-ray photon and produce an image where the only non-zero pixels are the ones corresponding to a recorded photon. In all the WAXS analyses carried out in the present thesis it a dropletization algorithm developed by L. Lurio, M. Sutton and M. Sprung was used.

### 6.6.1 The short range structure and its response to strong irradiation

In the works of Ruta et al. [156] it is shown that, for silicates, the local structure remains initially stable against beam damage and starts to change only after a considerable amount of absorbed radiation. In the measurements performed at P10, this initial "stable" condition is not always encountered, since the smaller beam spot produces much higher fluences. The deformation of the structure factor can be qualitatively described by a slight change of the first peak position and a decrease and a broadening of the peak, accompanied by an increase of the scattered photons at low q. All these features are indicators of an increasing disorder in the glass, and suggest that after an initial transient the system can reach a (driven) equilibrium configuration. Obviously, for even higher absorbed doses, the X-rays will start to produce macroscopic defects visible in the $I(q)$ as a sharp increase of the small angle contribution. This latter phenomenon occurs on longer time-scales than the initial transient and it does not affect appreciably the dynamics at larger q. As a rule of thumb, we can divide the life of a glass subjected to intense X-ray radiation in three stages:

1. a first stage, in which the local structure changes and the induced dynamics is not stationary;

2. a second stage, in which the local structure is not affected anymore and the induced dynamics is stationary;

3. a third and last stage, in which the X-rays begin to produce significant damage and only the dynamics at short length-scales is unaffected.

In figure 6.8, the intensity profiles measured at two different values of the total absorbed dose are reported, it must be noted that the characteristic time of the first stage is much longer than the detected BID. The decrease and broadening of the structure factor's first peak is probably due to the damping in amplitude of the corresponding real-space oscillations at intermediate-range distances; this effect is qualitatively compatible with the heating of the scattering volume described in [165]. The slight change of the peak position however, was not observed in the work of Majérus et al. [165] and it seems to be a feature of the X-ray induced sample modification.
It is important to point out that all these phenomena are not explainable with heating of the sample alone. For the present case of lithium borate, the heat capacity is $C_{pg} \approx 1.77 J/g/K$ [166] and the mass of the sample is typically $m \sim 0.12 g$. In the extreme hypothesis that all the incoming

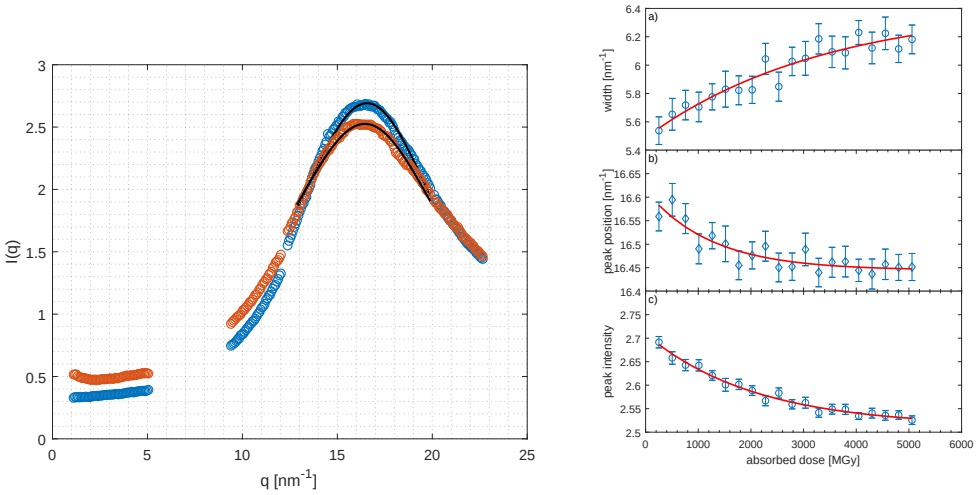


Figure 6.8: Left: $I(q)$ at different values of absorbed X-ray radiations blue circles $0.2 \cdot 10^9 Gy$, red circles $4 \cdot 10^9 Gy$. The general properties of the peak (position, width and height) have been tracked with a Lorentzian fit (black line). Right: time evolution of the first structure factor's peak width (a), position (b) and intensity(c), the red lines are exponential fits with characteristic times of $\tau_{width} = (500 \pm 170)$ frames ($\tau_{width} = (1.7 \pm 0.5)10^3$s), $\tau_{position} = (257 \pm 140)$ frames ($\tau_{position} = (0.8 \pm 0.4)10^3$s), $\tau_{intensity} = (340 \pm 70)$ frames ($\tau_{intensity} = (1.1 \pm 0.2)10^3$s) respectively.

X-rays are absorbed and that there is no thermal contact between the sample and the sample holder, the heat deposited on the sample is $\sim 0.68 mJ/s$ and after $10^4 s$ (the order of magnitude of the longest exposure time) the temperature of the sample would be increased by about $\sim 32K$, still well below the glass transition temperature $T_g \approx 700K$ [166]. These numbers are clearly an upper limit, here we haven't taken in account that only a small part of the incoming beam is actually absorbed, that the X-rays impinge on a small area and that the heat can be transferred outside the sample to the environment. They give us a superior limit for the real sample's temperature. So, temperature does not play a crucial role for this class of beam induced dynamics (BID):

### 6.6.2 Beam-induced dynamics

The low number of scattered photons in this class of experiments, lead to a very poor statistics when computing the autocorrelation matrix which results much less clear to read, as exemplified in fig. 6.9. To get a reliable

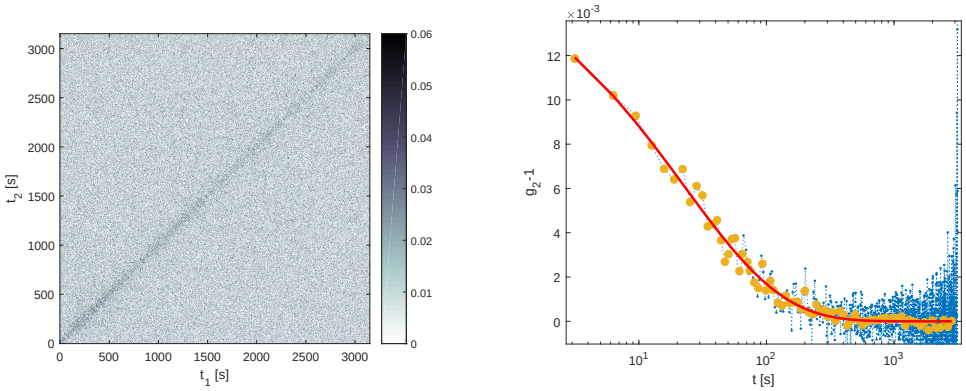


Figure 6.9: Example of a two-time autocorrelation matrix obtained in a WAXS measure on a $(Li_2O)_{0.5}(B_2O_3)_{0.5}$ sample (left), and its respective autocorrelation matrix (right). To improve the accuracy of the fitting algorithms, the autocorrelations were binned with a logarithmically spaced sampling (yellow dots). The best fit to the cure (red line) gives us a value for the contrast of $A = 0.017 \pm 0.002$, relaxation time $\tau = (78 \pm 8)s$ and stretching exponent $\beta = 0.55 \pm 0.08$.

autocorrelation function one has inevitably to average over conspicuous time intervals, thus, in contrast to what happened in previous chapters, a lot of the approaches adopted to exploit the advantages of the two-time autocorrelation function cannot be implemented here. We can still perform a measurement of the evolving dynamics relying on sub-matrices, but consecutive sub-matrices will result correlated, i.e. two consecutive time windows will be overlapped to a certain extent.

In the autocorrelation matrix of fig.6.9, it is possible to see a slight speeding up of the dynamics with time. This latter process is indeed related with the modification induced by the X-rays [154], and is not surprising that the change in local structure is reflected also in a change of the relaxation time since, as demonstrated in [154], the two are deeply connected.

A missing piece for the interpretation of the BID is a complete study of the q-dependence. To do so, we will recover the measurements performed at P10 on the borate glass $(Li_2O)_{0.5}(B_2O_3)_{0.5}$ taken at a fixed fluence for different exchanged wave-vectors, and the results will be put toghether whith oher measurements performed on the same system at ID10. Here the data from P10 are elaborated in a slightly different way whith respect to [154]. Since the detector covers a relatively large solid angle ($\delta\theta = 3.7°$), the detector area was divided in three regions, increasing the q resolution. To

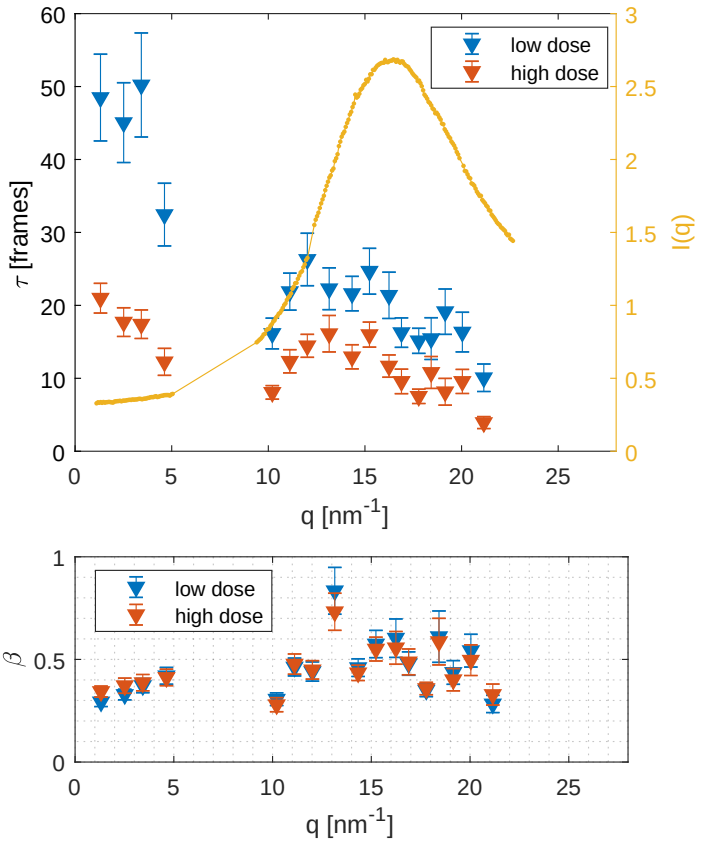


Figure 6.10: Top: relaxation times (expressed in frames) obtained for a $(Li_2O)_{0.5}(B_2O_3)_{0.5}$ sample at two different accumulated doses, as a reference the $I(q)$ of the non irradiated sample is reported (yellow dots). Bottom: stretching parameters at different q-values for the two different accumulated doses. The data points labelled as "low dose" correspond to a sample for which an amount of radiation ranging from $0Gy$ to $2.4 \cdot 10^9 Gy$ has been absorbed, while the points identified with "high dose" correspond to a sample for which the absorbed radiation ranges between $2 \cdot 10^9 Gy$ and $4.1 \cdot 10^9 Gy$. The measurements were carried out using full beam intensity with an exposure time of $1s$.

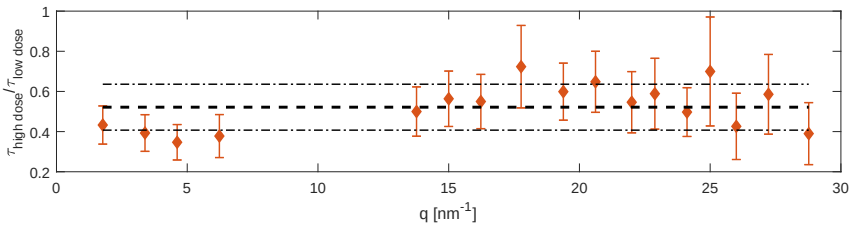


Figure 6.11: ratio between the relaxation times shown in fig.6.10, for all the investigated q values. The ratio is consistent within the uncertainty of $1\sigma$(dot-dashed line) with the mean value (dashed line)

prevent that the slowly varying structure factor could affect the results for the dynamics, each image was normalized with the instantaneous I(q), i.e. for each dropletized image an intensity profile was obtained, this profile was then smoothed and used to normalize the dropletized image an then sent into the autocorrelation algorithm. In fig. 6.10 the observed relaxation times (expressed in frames) and stretching exponents are reported, these results are obtained with such method for two different representative total absorbed doses (i.e. the dose absorbed at the end of the time window employed to compute the autocorrelation). The first time window corresponds to a fresh sample that starts slowly to rearrange its local structure, while the second to a sample whose pair distribution function has been already modified and has entered in the completely stationary regime.

These two sets of relaxation times appear to maintain the same general features, in both cases the dynamics is described by a stretched exponential, in both cases there is a slight slowing down in correspondence to the first neighbour's peak, reminiscent of a de Gennes narrowing effect, and in both cases more substantial slowing down at larger length-scales. The physical hidea behind the de Gennes narrowing is the fact that maxima in the structure factor of liquids and amorphous solids occur at scattering vectors corresponding to the most probable interatomic separation, i.e. they are due to the highly correlated and long-living atomic arrangements [167].The interesting thing is that, as shown in fig. 6.11, the ratio between the relaxation time of the fresh sample and that of the irradiated one appears to be substantially constant in q, suggesting a simple dependence between the local structure and the BID.
Because of the instrumental characteristics of the WAXS set-up at P10 it was not possible to acquire data at intermediate wave-vectors, thus the formulation of any q dependence of the relaxation time would result quite

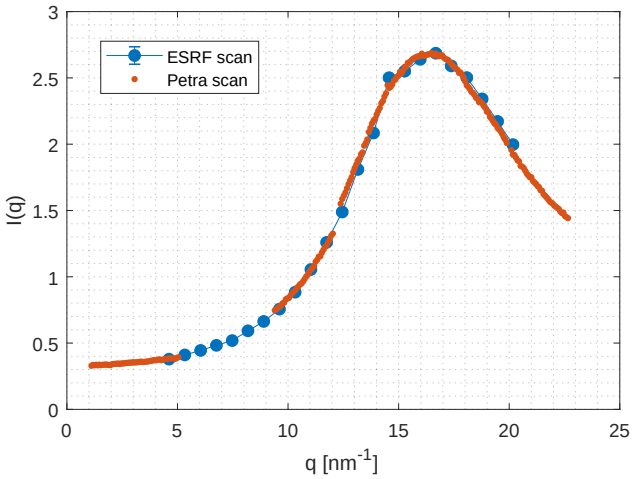


Figure 6.12: comparison between the scans performed at P10 (red dots), and ID10 (blue circles) of the structure factor's peak. The samples were $(Li_2O)_{0.5}(B_2O_3)_{0.5}$ glasses produced in two distinct periods. The reproducibility of the structural data, allow a comparison between the induced dynamics observed in the two experiments.

hasty without more details.

**comparison with ESRF data**

As found in [156] and [154] the BID strongly depends on the total absorbed dose, thus experimental parameters like the total flux produced by the unduators and the spot size of the focused X-ray beam play a crucial role. The best way to compare different data that come from different instruments is to rely on the number of units (or atoms) that move after the absorption of a single photon defined in eq.6.3. This latter quantity is a material's intrinsic property and thus should be independent of the particular beamline details. The only caveat might come from the way the beamline parameters are determined, since a precise determination of the spot-size and total flux is not an easy task, and some systematic errors could lurk behind the corners. To this purpose, a number of measurements on the same silica sample at the same scattering angle has been performed on the two different beamlines. The values obtained in different experiments with the same instrument have been averaged, and the ratio between the two values of $N_{units}$ has been found to be $N_{units}^{ESRF}/N_{units}^{Petra} = 1.3 \pm 0.3$.

Now that we know that the instrumental parameters of the two beamlines

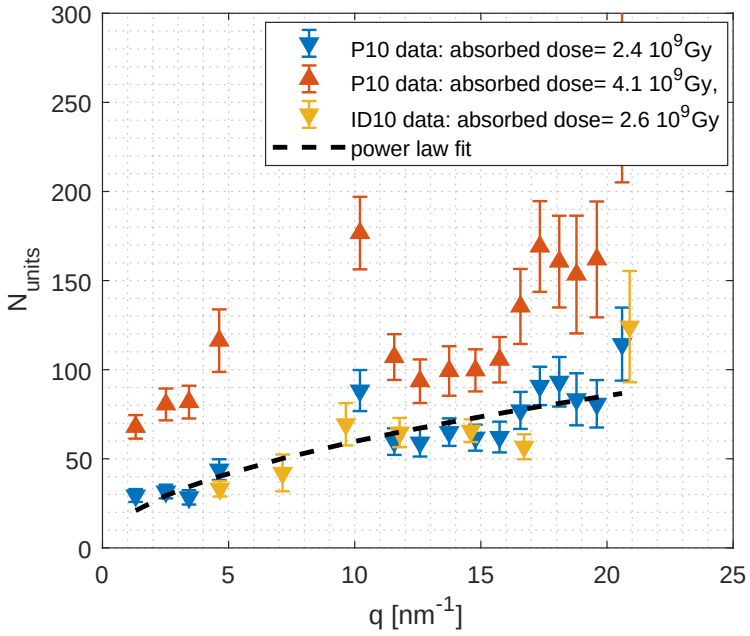


Figure 6.13: comparison between the measured $N_{units}$ obtained from the same kind of lithium-borate glass in two different beamlines. Blue and red triangles are obtained from the relaxation times reported in fig. 6.10, the yellow triangles are obtained from a set of measurements carried out at ID10. The dashed line is a power law fit ($N_{units} = N_0 \cdot q^{\alpha}$) on the datasets at low doses with $N_0 = 18 \pm 9$ and $\alpha = 0.5 \pm 0.2$.

are consistent, we can put together the results of $(Li_2O)_{0.5}(B_2O_3)_{0.5}$ glasses obtained from the two different instruments. Since the glasses studied in the two experiments were not prepared in the same batch, a scan of the $S(q)$ was taken before and after each run; the final shape of the structure factors differs between the experiments, because the total amount of absorbed radiation was in general different, but the shapes of the fresh samples overlap reasonably well, as shown in fig.6.12.

We can finally proceed to fill the gaps in the $\tau(q)$ dependence shown in fig.6.10. The measurements performed at ID10 were taken at q-values unreachable at Petra: two close to the edges of the inaccessible region and one in the middle of it, and other three around the first neighbour peak, to get additional reference points. Since the spot size at ID10 ($10 \times 10 \mu m^2$) is much larger than the one provided at P10 ($3 \times 3 \mu m^2$), the total fluence is decreased by about a factor ten, thus in the attempt to maintain the

same flux per frame it was decided to impinge on sample at full beam with exposition time of $5s$. Nevertheless, the total absorbed dose at the end of the measurements are lower than the total dose absorbed at Petra. For this reason it was decided to limit the comparison only to the lower irradiated samples. The result, reported in fig.6.13 shows a reasonably good agreement between the low dose data obtained at Petra (blue triangles) and the ones that came from ESRF (yellow triangles), combined these data can be described in first approximation by a power law $N = N_0 \cdot q^{\alpha}$ with exponent $\alpha = 0.5 \pm 0.2$. The de Gennes narrowing of $\tau$ is traduced in $N_{units}$ as a plateau region that begins with a small "peak" at the exchanged wave-vector $q_c \sim 10nm^{-1}$.

### 6.6.3 SAXS measurements on silica

Here we will introduce the first results from a very recent experiment performed on vitreous $SiO_2$ at P10. This time, the measurements were carried out in SAXS configuration with a large area detector called EIGER X 4M. The detector consists of $4 \times 2$ modules with $75 \times 75\mu m^2$ pixel size and an active area of $2070 \times 2167$ pixels ($155.2 \times 162.5mm^2$) placed at $5.05m$ from the sample. With a such enormous active area, the covered q range spans from $\sim 0.005nm^{-1}$ to $\sim 1nm^{-1}$, giving the opportunity to probe at the same time both the movements at large length-scales and the rearrangements happening at the nanoscale. Moreover, a smaller scattering angle means a more forgiving condition for the coherence length, thus a higher contrast, as it can be seen from the autocorrelation reported in fig.6.14, there the fitted value for the contrast is one order of magnitude larger then the one reported in fig.6.9.

The results, reported in fig.6.15, show that $\tau(q)$ is a monotonically decreasing function which can be described by a power law $\tau(q) = \tau_0 q^{\alpha_{SAXS}}$, with $\tau_0 = (0.37 \pm 0.03)10^3 s$, $\alpha_{SAXS} = 1.22 \pm 0.07$. The exponent of the relaxation function is compressed at all probed q values, and even here we can observe a markedly monotonically decreasing behaviour for $\beta(q)$, which seems to reach values compatible with a simple exponential. The large uncertainties over of $\beta(q)$ at large q values is due to the drop in contrast shown in the third panel of fig.6.15. This sudden drop can be readily described with the considerations reported in cap.3, in fact, in XPCS measurements, the contrast can be described, in first approximation, as the ratio between one coherent volume and the total scattering volume $contrast \approx V_{coh}/V_{scatt}$, using the relations of the path length difference we get $contrast \approx R/\sin(\theta)^2$ where $\theta$ is the scattering angle and $R$ is a quantity related to the ratio

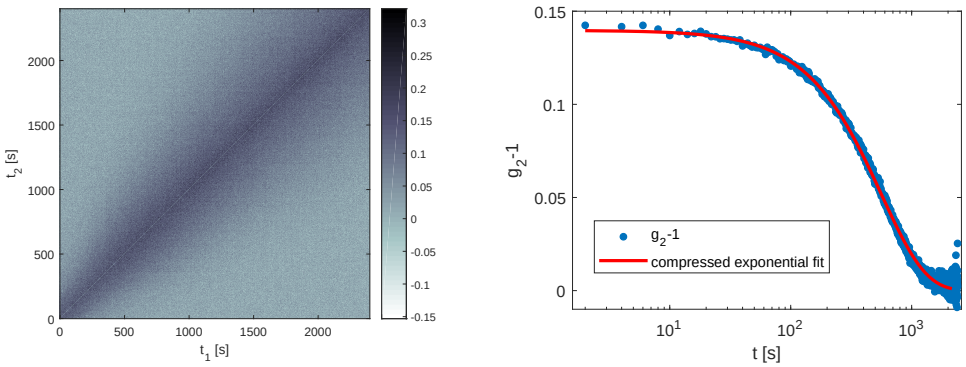


Figure 6.14: Left:autocorrelation matrix for the SAXS measurement on silica at $q = (0.47 \pm 0.06)nm^{-1}$. Right: autocorrelation function (blue line) with best fit to the data (red line). The fitted contrast is now $A = 0.140 \pm 0.002$,with relaxation time $\tau = (1.01 \pm 0.03)10^3 s$ and stretching exponent $\beta = 1.18 \pm 0.03$.

between the longitudinal coherence and the sample thickness. This rather simple model, being formulated on approximations valid for the SAXS regime, is able to describe reasonably well the contrast values at small angles, but fails (luckily) to describe the contrast at larger q-values.

We can attempt to compare these SAXS data with the WAXS results reported in [156]. In the latter dataset however, some details needed for a rigorous comparison between data produced on different beamlines are missing, but, thanks to the fact that silica was used to "tune" the two beamlines, we can rescale the values of [156] on a datapoint with well known experimental parameters (the yellow diamond in fig. 6.16), and we can obtain a robust comparison between the two datasets. Also at these large q-values the relaxation time is described by a power law of the kind $\tau = \tau_0/q^{\alpha}_{WAXS}$, with $\alpha_{WAXS} = 0.5 \pm 0.1$, quite similar to the one observed for $(Li_2O)_{0.5}(B_2O_3)_{0.5}$. This change means that the spatial length-scale becomes progressively less important for $\tau$ upon approaching sorter distances in qualitative agreement with what has been observed for the lithium borate glass. A direct comparison between the two glasses is reported in fig.6.17 and the intriguing similarities between the two materials confirm the general origin of the BID effect.

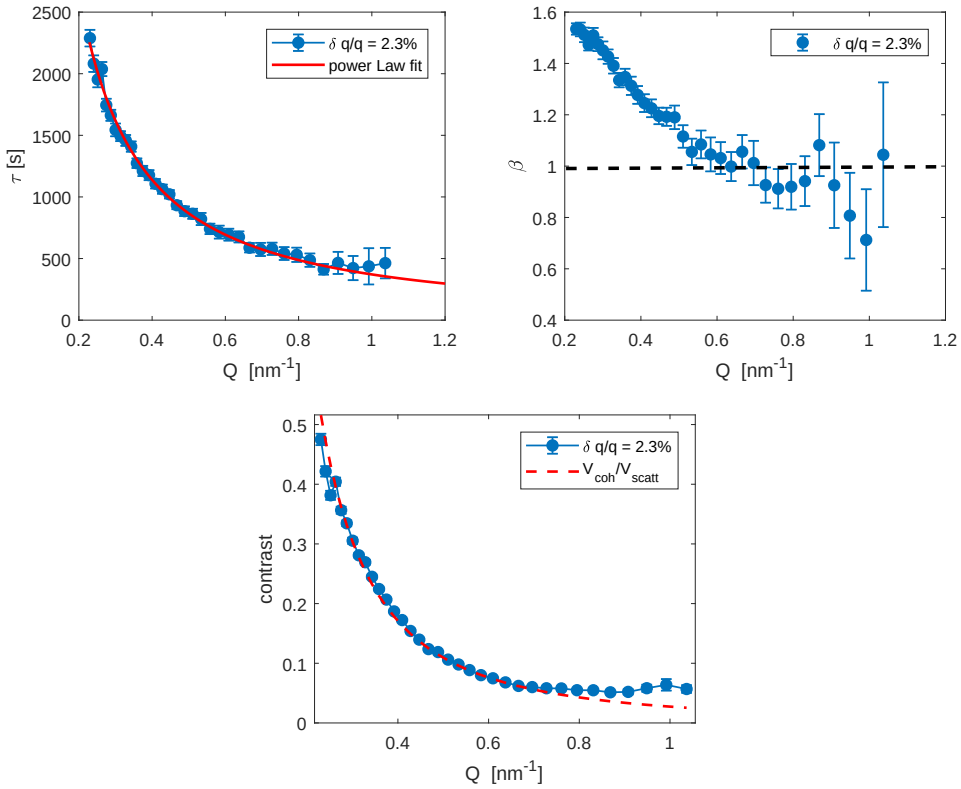


Figure 6.15: Results for $\tau(q)$ (top left panel) and $\beta(q)$ (top right) of the SAXS measure performed on amorphous silica. The analysis has been carried out keeping a fixed q-resolution of $\delta q/q = 2.3\%$. The increase of the uncertainty for $\beta$ at larger q-values is due to the decrease of about one order of magnitude in the contrast of the autocorrelation function (bottom). The red dashed line in the right panel is a simple fit of the contrast with $R/\sin(\theta)^2$ where $\theta$ is the scattering angle and $R = (33 \pm 1)10^{-6}$ is a quantity related to the ratio between the scattering volume and the coherence volume.

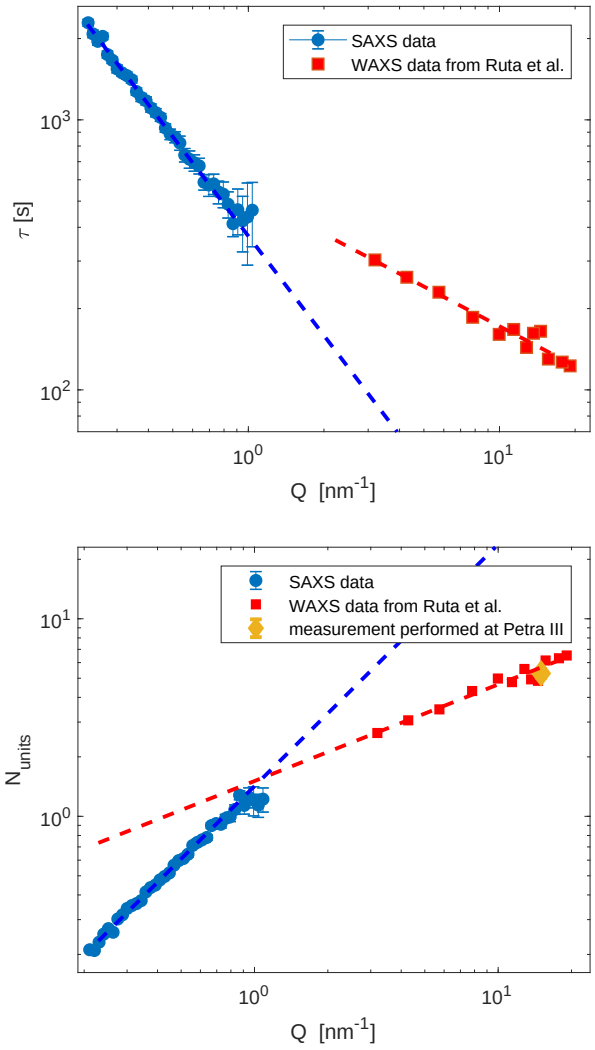


Figure 6.16: Comparison between the WAXS data reported in [156] (red squares) and the SAXS measurement (blue circles). In the top panel, are reported the relaxation times observed in the different experiments, on the bottom panel the same results are expressed as the number of units that has moved after the absorption of a photon, due to the lack of a precise measure of the photon flux and sample thickness in the WAXS data the conversion of the latter to $N_{units}$ is performed rescaling firstly the $\tau$ values on the relaxation time measured at a fixed q-value at P10 (yellow diamond), then all the data-points are converted in $N_{units}$. The data seem to evidence two distinct regimes described by a power-law with different exponents $0.5 \pm 0.1$ for the WAXS measure and $1.22 \pm 0.07$ for the SAXS one.

## 6.7 Final remarks

In summary, we have seen how intense X-ray irradiation can modify the local structure of a lithium borate glass. The absorption of X-rays at high doses induces also a change in the observed BID at all measured exchanged wave-vectors, nearly doubling the number of atoms that rearranges after the absorption of a photon, as can be seen in fig.6.11. This latter fact, in contrast with the structure factor's modification, is not compatible with a simple heating of the sample since, as outlined in [154], $N_{units}$ is seen to decrease with increasing temperature, in borate glasses. On the other hand, $N_{units}$ is seen to increase with decreasing the fraction of tetrahedrally bonded atoms (fig.6.5).From the q-dependence of $\tau$, or equivalently of $N_{units}$, of the lithium borate samples we observe a power-law scaling of the kind $N_{units} = N_0 \cdot q^{\alpha}$ with $\alpha = 0.5 \pm 0.2$.
A more trustworthy q dependence of the BID's characteristic time is found in the SAXS measurements recently performed on amorphous silica. Here it has been clearly observed that the relaxation times follow a power-law of the kind $\tau(q) = \tau_0/q^{\alpha}$ with an exponent of $\alpha_{SAXS} = 1.22 \pm 0.07$, and that approaching smaller distances this trend switches to a milder q-dependence. This tendency is in qualitative agreement with the WAXS results of Ruta et al.[156], where a power law with exponent $\alpha_{WAXS} = 0.5 \pm 0.1$ has been found. In this latter set of data there is no clear evidence of the plateau found in the lithium borate glass, but this can be a consequence of the coarser sampling adopted. Either way, in both regimes the dynamic cannot be attributed to diffusive processes. Another interesting fact comes from the strong similarity between the lithium borate data and the WAXS results for silica as can be seen in fig. 6.17 suggesting that the q-scaling, in WAXS regime, is independent of the probed system.
The stress-relaxation scenario is described more appropriately by the models developed for the intermittent dynamics in soft solids [145, 8] than the ones describing the atomic diffusion in undercooled liquids. The results obtained from the SAXS measurements on silica, show a compressed exponent $\beta$ that changes with q in qualitative agreement with what observed in simulations on soft materials [8]. Also the observed $\tau(q)$ in the SAXS regime matches what has been observed in [8]. Discrepancies arise in the WAXS regime and this can be due either to the fact that the probed q-range is different from the one covered by the simulations, or to the fact that the mechanisms involved in the BID at short length-scales are more complex.
Another interesting detail that could be explained by the theoretical models of [145, 8], is the different shape parameter of the autocorrelation function observed in different glasses. In the lithium borate reported in this Thesis

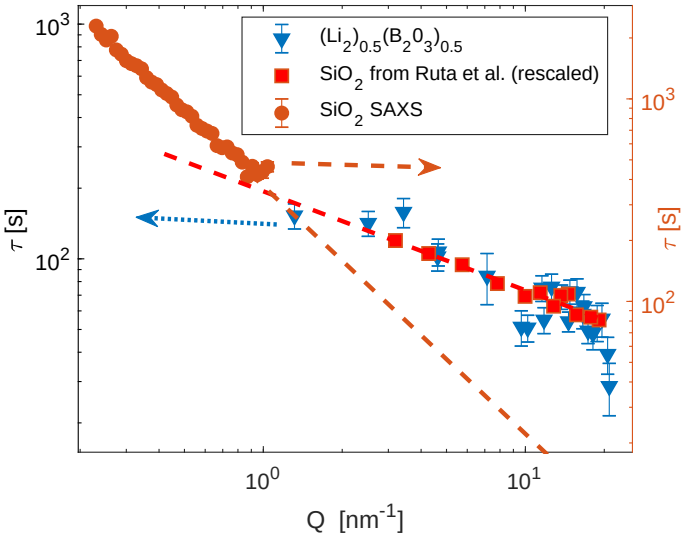


Figure 6.17: Qualitative comparison between the silica datasets and the $(Li_2O)_{0.5}(B_2O_3)_{0.5}$. The two samples shares the same general behaviour in the WAXS regime. Also the $(Li_2O)_{0.5}(B_2O_3)_{0.5}$ is compatible with the change of the power-law trend

the autocorrelations are stretched with $\beta \sim 0.5$, while in silica is compressed at all probed q-values; for more examples see [154]. In the simulations the shape parameter, as well as the q-dependence of $\tau$, depends on the ratio between the energy of the thermal bath (here replaced by the energy delivered by the X-rays) and the stress heterogeneity frozen-in during solidification. For certain values of this ratio $\beta$ can assume values smaller than 1, thus producing indeed a stretched exponential.

# Chapter 7

# Conclusions

In this Thesis we have studied the dynamics in three disordered systems under very different conditions; **a)** a strong glass former $B_2O_3$ in its glass transition region probed in the macroscopic limit, **b)** a colloidal suspension in its arrested state probed in a broad q-range with visible light and X-rays, and **c)** oxide glasses well below their glass transition temperature but under the influence of strong X-ray radiation. The main conclusions of the individual chapters are reported below.

**a)** The $B_2O_3$ glass was investigated with the intent to measure the $\alpha$ structural relaxation below the glass transition temperature with a PCS technique. During the measurements in the glass transition range the aging phenomenon was inevitably encountered, and the capabilities the two-time autocorrelation functions obtained in a multispeckle set-up were exploited to study in detail the time evolution of the structural relaxation. A campaign of dedicated experiments was then carried out to characterize the aging with a set of progressively deeper temperature jumps, and following the system until an almost complete recovery of the equilibrated undercooled liquid condition had been reached. It has been discovered that:

a.i) in the early stages of the glass's life, there is an apparent violation of the time aging-time superposition produced by the presence of mechanical stresses inside the sample's bulk originated as a consequence of the initial cooling;

a.ii) the presence of internal stresses does not alter the distribution of relaxation times that contribute to the stretched relaxation function, and with an appropriate choice of the experimental parameters or of the fitting function it is possible to obtain a stretching exponent $\beta$

compatible with the one of the equilibrated undercooled liquid (i.e. the time aging-time is retrieved);

a.iii) the time required by the system to reach the equilibrium condition and to completely dissipate the internal stresses (or equivalently the time necessary to recover the equilibrium value of the stretching exponent) is about $14 \cdot \tau_\alpha$, where $\tau_\alpha$ is the structural relaxation time of the equilibrated system;

a.iv) the evolution of the structural relaxation $\tau_\alpha(t_W)$ is described by the Tool,Moynihan,Narayanaswamy model [102, 35, 103], resulting strongly dependent on the fictive temperature;

a.v) the aging can heavily affect the dynamical susceptibility with signals similar to the ones related to the dynamical heterogeneity; however thanks to simple mathematical considerations and a detailed knowledge of the aging quantities it is possible to effectively model these aging-dependent contributions.

**b)** Silica nanoparticles dispersed in a near critical water-lutidine 2,6 mixture constitute a system with great potential for future applications in the studies of inter-particle interactions in disordered systems. Changing the temperature in a specific range it is possible to finely tune the energy potential between particles switching from a repulsive colloidal system to an attractive one and vice-versa. In this Thesis the efforts were dedicated to characterize the purely repulsive colloidal system in a set of photon-correlation experiments performed both in the visible and in the X-ray regime. In the X-ray experiment it was observed, similarly to what previously reported in literature, that:

b.i) samples of large colloidal particles are able to avoid crystallization preserving the amorphous structure only at volume fractions greater than $\sim 45\%$;

b.ii) the dynamics is intermittent, described by compressed relaxation functions ($\beta > 1$) with an hyper-diffusive behaviour ($\tau(q) \propto 1/q$);

b.iii) the samples are in an out of equilibrium condition displaying a relaxation time growing linearly with the sample's age.

From our data, we obtained also other new findings :

b.iv) the analysis of the autocorrelation functions at different azimuthal angles evidenced that the motions inside the sample are due to a radial

velocity field with cylindrical symmetry. Considerations concerning the stability of the structure factor's peak suggests a motion characterized by relaxation events sparse in the system and with velocity field directed radially both towards the centre of the sample and pointing outward, without a net particle's flux;

b.v) a sample with a stationary dynamic regime was obtained. From this stationary regime it was possible to extrapolate the dynamical susceptibility of the observed motion and relate its peak value to the number of particles participating in the cooperative rearrangement;

b.vi) a sharp increase of number of particles participating in cooperative rearrangements (from $\sim 20$ particles to $\sim 500$ particles) is observed in correspondence to the first neighbours peak, indicating that a typical cooperative rearranging region moves over an inter-particle distance in a relaxation time.

Visible PCS measures on analogous samples composed by smaller colloidal particles, confirmed the picture observed in the XPCS experiment and evidenced that the above considerations can be extended to all colloidal glasses of silica in water-lutidine. Moreover it was observed that the kind of dynamic developing in a colloidal glass is extremely sensitive to the preparation protocol. In fact, changing the procedure adopted for its preparation it was found that the autocorrelation functions can also be described by a slower than exponential (stretched) decay.

**c)** Several XPCS experiments performed on oxide glasses evidenced the presence of atomic motions even at room temperature, well below the glass transition temperature. It eventually was found that these motions are microscopic rearrangements induced by the X-ray beam, and thus that XPCS experiments on oxide glasses (but also chalcogenides and polymers) have to be interpreted as a pump-probe measurement where the same X-rays act both as a pump and as a probe. In this Thesis measurements on $(Li_2O)_{0.5}(B_2O_3)_{0.5}$ and silica glasses are reported. From these experiments it was possible to observe:

c.i) The relaxation time is inversely proportional with the absorbed flux ($\tau \propto 1/F$), in agreement with previous works [156, 154]

c.ii) The shape of the first structure factor's peak changes with increasing X-ray absorbed dose, indicating the occurrence of a modification of the local order. This alteration is associated with an initial non stationary

regime in the observed intermediate scattering function, followed by a stationary regime once the system's structure has ceased to change.

c.iii) The relaxation times in these regimes (initial non stationary and final stable) are observed to be proportional to each other, and the shapes of the autocorrelation functions are the same in both regimes.

c.iv) The relaxation times are a non monotonic decreasing function of q with a local maximum in the region near the structure factor's peak.

From this beam-induced dynamics it is possible to define the number of particles ($N_{units}$) that have moved over a distance $2\pi/q$ in a characteristic time $\tau$ after the absorption of a photon. This latter quantity appears to be a characteristics of the system under study and can be used to compare the results obtained in different experiments. For the lithium borate glass it was observed that this number of particles grows approximately linearly with q and then reaches a region with a weaker q-dependence. This qualitative result has been confirmed by a recent SAXS measurement on vitreous silica where we found that:

c.v) a clear nearly linear q-dependence of $N_{units}$ (or equivalently $1/\tau \sim q$) for q values up to $\sim 1nm^{-1}$;

c.vi) compressed relaxation functions with an exponent $\beta(q)$ described by a monotonically decreasing function of q.

Comparing these results with the measurements previously performed on silica at larger angles reported in [156] a cross-over region between $1nm^{-1}$ and $2nm^{-1}$ in which $1/\tau(q)$ acquires a sublinear dependence on the exchanged wave-vector can be identified. Currently a reliable model able to describe the mechanism of the beam induced dynamics is still lacking, but the prediction of models developed for soft collapsing systems seem to be able to qualitatively describe many of the observed features, suggesting that the stress-release mechanism plays a central role in this class of phenomena.

Combining the results of those individual chapters we can attempt to give an answer to some of the questions outlined in Chapter 1.

# I) Stress-release processes and compressed exponential relaxations

In all three experiments we have seen the contributions to the dynamics of a feature always present in glasses: the internal stresses trapped as a

consequence of the glass production. In the macroscopic limit studied in chapter 4, the presence of internal stresses produced a rigid shift of the whole speckle-pattern thus adding a Gaussian contribution to the detected intermediate scattering function. The autocorrelation functions appeared then with a mild initial slope, characteristic of the stretched exponentials, truncated by a sudden fast decorrelation compressing the overall intermediate scattering function's shape.
In the colloidal systems of chapter 5, the presence of anisotropic internal stresses on micrometer length-scales is at the basis of all the relaxations observed in XPCS and of a good number of visible PCS experiments. Even here, the relaxation is described by a compressed exponential, and once the anisotropic dependence has been identified the shape parameter $\beta$ is always very close to 2 at all length-scales.
Lastly, in the XPCS measurements on silica we have seen an induced process which can be described quite accurately by a stress-release scenario that takes place at nanometric length-scales. Also for $SiO_2$, the shape of the intermediate scattering function is compressed, and $\beta(q)$ shows to be a clearly decreasing function of q in the small angle regime.
Grouping these findings we can support the empirical conclusion stating that compressed relaxation functions are the signature of stresses embedded within the sample. It is intriguing, in fact, how the same process acting on diverse length-scales, macroscopic in $B_2O_3$, microscopic in the colloidal system and (most probably) nanoscopic in silica glass, comes always into play into the observation of the intermediate scattering function through the most disparate processes, and how at the end a compressed relaxation is always present, see fig.7.1. It has to be noted however, that in the case of the aging $B_2O_3$, the shape of the $\alpha$ structural relaxation is not affected by the presence of stresses (in fact the compressed term can be ruled out with an appropriate choice of experimental parameters). The q-dependence of the relaxation times observed in both the colloidal glass (chapter 5) and the oxides (chapter 6) indicate always a non-diffusive behaviour following a power law $\tau(q) \propto 1/q^{\alpha}$ with $\alpha$ close to 1, and also this nearly linear q-dependence is always associated with the stress-relaxation mechanisms in soft solids [144, 8].

# II) Spatial and temporal heterogeneity

The dynamical heterogeneity ($\chi_4$) is a key quantity for the glass transition. In this Thesis, a clear observation of $\chi_4$ can be found only in the chapter dedicated to the colloidal glasses in which is was possible to determine

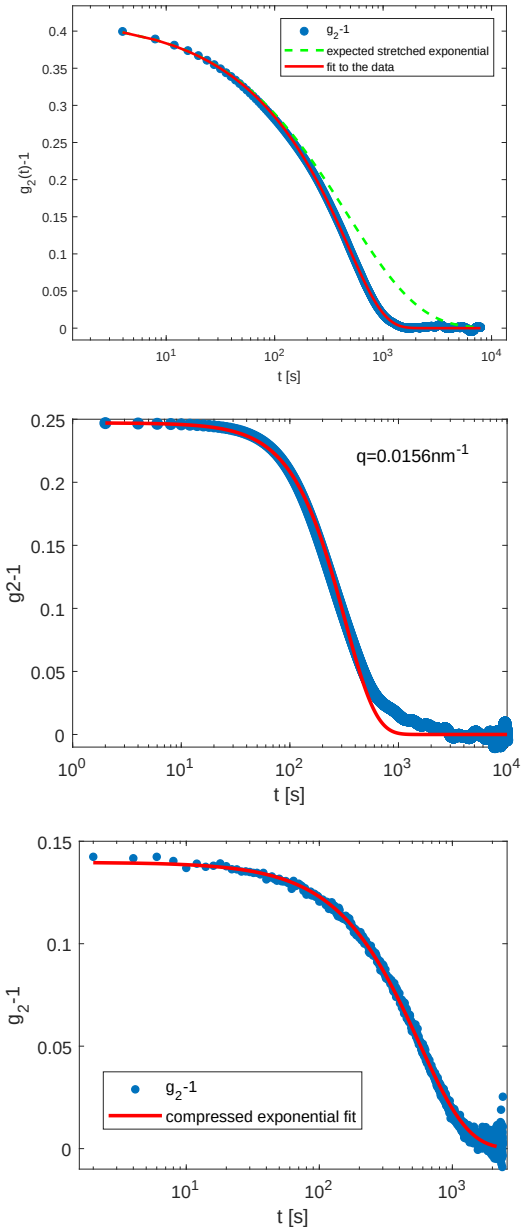


Figure 7.1: Examples of the various effects on the autocorrelation function of the stresses that can develop inside a glass. Top : aging autocorrelation function of boron trioxide truncated by the fast macroscopic relaxation, the latter manifests itself with a compressed relaxation with $\beta = 2$. Center: autocorrelation function at large q-values for a stressed colloidal sample, this autocorrelation is taken averaging over all the azimuthal angles and the compressing exponent is $\beta = 1.51 \pm 0.001$. Bottom: compressed relaxation function observed in the beam induced dynamics of a silica sample at small angles. The compressing exponent is here $\beta = 1.18 \pm 0.03$.

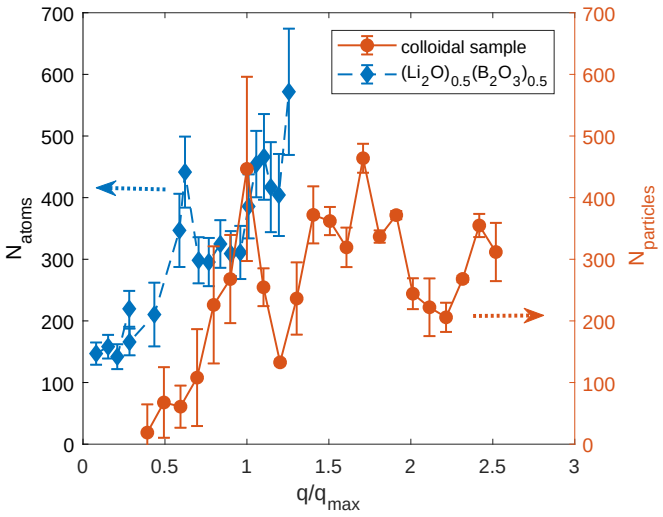


Figure 7.2: Comparison between the number of particles participating a coherent rearranging region in the colloidal sample (red circles) and the number of $(Li_2O)_{0.5}(B_2O_3)_{0.5}$ atoms that have moved after the absorption of a photon (blue diamonds). The q axes are rescaled with the value $q_{max}$, where $q_{max}$ is the position of the structure factor's peak for the colloids and for the borate glass.

the number of particles participating in a collectively rearranging region (CRR), see fig.5.26. In the stress-relaxation scenario of the beam induced dynamics we can obtain the quantity $N_{units}$, which is the number of atoms participating to the induced collective rearrangement obtaining an atomic equivalent concept to what observed in the colloidal glass. Moreover, in this interpretation we get another suggestive similarity between the behaviour of the number of particles of fig.5.26, and the number of $(Li_2O)_{0.5}(B_2O_3)_{0.5}$ atoms of fig.6.13. Looking at the general trend, we can see that $N$ rises from small values in the low q-limit and then reaches a sort of plateau at small-length scales. In fig.7.2 the two curves are reported and rescaled in q for a better comparison. This behaviour suggests that the dynamics in these samples is characterized by groups of $N_{max}$ particles moving over a characteristic distance (the inter-particle distance for colloids).

At the end of Chapter 4 we have seen that a clear signal of the dynamical susceptibility can also arise in presence of aging and that, provided a detailed knowledge of the time evolution of the physical quantities, it is possible to reproduce quite accurately the experimental $\sigma^2_{g_2-1}$. In principle one can then employ these considerations to get rid of the aging contribution in the

$\chi_4$ observed in out-of equilibrium systems (for example the aging colloidal samples). However, at present, it was not possible to perform such a task without obtaining large uncertainties in the final result. The principal limitation right now is due to the fact that in order to obtain $\chi_4$ we have inevitably to average over a certain time window and when the change of the relaxation time over this time window is too large, then the contribution due to the CRR's fluctuations will be inevitably cancelled by the growing relaxation time and cannot be retrieved with the simple model of Chapter 4. Thus the only way to preserve the information on the desired dynamical heterogeneity is to select small enough time windows, but in doing so, the statistics will inevitably limit the quality of the result.

# III) Aging and rejuvenation

Aging is a phenomenon common to all glasses and we have found it in many situations in Chapters 4 and 5 of this Thesis.

The aging of $B_2O_3$ can be described as the result of two distinct processes: the mechanical relaxation and the proper microscopic evolution. The latter can be described reasonably well by the phenomenological model of Tool, Moynihan and Narayanaswamy [102, 35, 103] where the evolution of the dynamical properties is completely described by the fictive and sample's temperatures and the memory of the past thermal history. Thus all the aging here is a thermally activated mechanism. For the colloidal sample, on the other hand, the dynamics is the consequence of the release of the elastic energy trapped inside the material during its production, and its slowing down is a consequence of the depletion of the mechanical energy reservoir. On the other hand, when one compares the mechanical relaxation of $B_2O_3$ with the colloidal sample's aging we can see a very similar behaviour of the velocity's time evolution [1], see fig.7.3. In fact in both cases we have a particle's motion that quickly slows down as the system looses its elastic stresses, eventually reaching a region where the stress-induced velocity is overrun by the $\alpha$ structural relaxation.

Also for the beam induced dynamics in $(Li_2O)_{0.5}(B_2O_3)_{0.5}$ of Chapter 6 a non stationary dynamics can be identified, but this time we observe a speed-up of the relaxation function and speaking of rejuvenation is more appropriate. This rejuvenation is accompanied with a progressive modification of the average local structure operated by the X-rays, thus suggesting a link between

[1] recalling briefly, in the aging $B_2O_3$ the Gaussian parameter of eq.4.8 is described by $\Gamma(t_W) = v(t_W)/\sigma$, where $\sigma$ is the squared sum of the speckle and pixel's sizes, while for the colloidal sample $\tau(t_W) = 1/(\mathbf{q} \cdot \mathbf{v}(t_W))$.

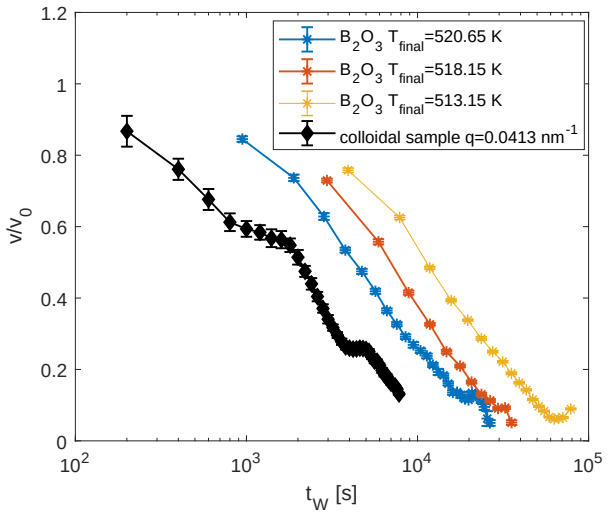


Figure 7.3: Comparison between the $v(t_W)/v(0)$ describing the mechanical relaxation in $B_2O_3$ at three different final temperatures and the velocity $v(t_W)/v(0)$ observed in the SAXS measurement of the aging colloidal glass. The time $t_W = 0$ corresponds to the beginning of the measurements, the data are rescaled in order to point out the similar shapes of $v(t_W)$. The initial velocities for the $B_2O_3$ are $v_0 = (35.1 \pm 0.3)nm/s$,$v_0 = (25.0 \pm 0.3)nm/s$,$v_0 = (17.7 \pm 0.2)nm/s$ for $T_f = 520.65K$,$T_f = 518.15K$ and $T_f = 513.15K$ respectively. The initial velocity for the colloidal sample is $v_0 = (0.66 \pm 0.04)nm/s$

these two processes.

## 7.1 Future perspectives

Within this Thesis it was possible to find an answer to some questions, but a number of other ones remains unanswered.
For some of the general questions formulated in Chapter 1 (i.e. the points iv) v) and vi) ), we have found only qualitative answers and a more complete explanation for these issues will require more experiments on more different systems. Moreover, from each individual chapter we can find several interesting paths to follow.
Regarding the PCS measures on the aging $B_2O_3$ it has yet to be found a model able to explain the interplay between the stress release and the microscopic aging of the structural relaxation. In fact, the parameters of the Tool,Moynihan,Narayanaswamy model [102, 35, 103] obtained for $\tau_\alpha$ are quite different from the ones obtained at higher temperatures, and among the possible explanations the influence of the external stresses cannot be excluded.
Regarding the colloidal glasses, the natural prosecution of the investigation is to exploit the water-lutidine properties to observe the change of the dynamical heterogeneity when changing the inter-particle interaction. For the repulsive glasses described in this Thesis, a piece that is still missing is a quantitative explanation for the compressed relaxation's origin; currently we have a qualitative picture in terms off stress-relaxation able to describe most of the features observed in these systems, but we are lacking of experiments able to provide a more detailed picture.
The phenomenon of the beam induced dynamics is still a young and mostly unexplored field. Currently, the main questions in this topic concerns the identification of the process (or processes) that make possible the beam induced dynamics, understanding which one between the cascade-relaxation and stress-relaxation models is able to better describe the experiments. Currently, some hints are tilting the scale towards the stress-relaxation process, but in practice the situation is far from being clear. A great help in this direction might came from experiments able to measure the time-scales over which the $N_{units}$ atoms rearrange after the absorption of a photon. Another important question is on the role is played by the stresses that are frozen in the glass once it has been produced.

The disordered systems are an ancient, yet largely unexplained field of condensed matter and material science. With the present Thesis I hope to provide even only a small step towards a better understanding of the

dynamical mechanisms governing the glassy state, and towards a more precise control on the physical properties of the materials that can be obtained from this class of extremely versatile systems.

# Bibliography


[1] A. Duri and L. Cipelletti. Length scale dependence of dynamical heterogeneity in a colloidal fractal gel. *EPL Europhys. Lett.*, 76(5):972, 2006.

[2] Agnès Duri, Hugo Bissig, Véronique Trappe, and Luca Cipelletti. Time-resolved-correlation measurements of temporally heterogeneous dynamics. *Phys. Rev. E*, 72:051401, Nov 2005.

[3] Hongyu Guo, Gilles Bourret, Muriel K. Corbierre, Simona Rucareanu, R. Bruce Lennox, Khalid Laaziri, Luc Piche, Mark Sutton, James L. Harden, and Robert L. Leheny. Nanoparticle motion within glassy polymer melts. *Phys. Rev. Lett.*, 102:075702, Feb 2009.

[4] H. Conrad, F. Lehmkühler, B. Fischer, F. Westermeier, M. A. Schroer, Y. Chushkin, C. Gutt, M. Sprung, and G. Grübel. Correlated heterogeneous dynamics in glass-forming polymers. *Physical Review E - Statistical, Nonlinear, and Soft Matter Physics*, 91(4):1–6, 2015.

[5] Luca Cipelletti and D. A. Weitz. Ultralow-angle dynamic light scattering with a charge coupled device camera based multispeckle, multitau correlator. *Rev. Sci. Instrum.*, 70(8):3214–3221, 1999.

[6] Anders Madsen, Robert L. Leheny, Hongyu Guo, Michael Sprung, and Orsolya Czakkel. Beyond simple exponential correlation functions and equilibrium dynamics in x-ray photon correlation spectroscopy. *New Journal of Physics*, 12, 2010.

[7] B. Ruta, Y. Chushkin, G. Monaco, L. Cipelletti, E. Pineda, P. Bruna, V. M. Giordano, and M. Gonzalez-Silveira. Atomic-scale relaxation dynamics and aging in a metallic glass probed by x-ray photon correlation spectroscopy. *Phys. Rev. Lett.*, 109:165701, Oct 2012.

[8] Mehdi Bouzid, Jader Colombo, Lucas Vieira Barbosa, and Emanuela Del Gado. Elastically driven intermittent microscopic dynamics in soft solids. *Nature Communications*, 8(May):1–8, 2017.

[9] Andrew Shortland, Nick Rogers, and Katherine Eremin. Trace element discriminants between Egyptian and Mesopotamian Late Bronze Age glasses. *Journal of Archaeological Science*, 34(5):781–789, 2007.

[10] Teófilo Vasconcelos, Bruno Sarmento, and Paulo Costa. Solid dispersions as strategy to improve oral bioavailability of poor water soluble drugs. *Drug Discovery Today*, 12(23-24):1068–1075, 2007.

[11] Guy Van Den Mooter. The use of amorphous solid dispersions: A formulation strategy to overcome poor solubility and dissolution rate. *Drug Discovery Today: Technologies*, 9(2):e79–e85, 2012.

[12] Stephen Byrn, Ralph Pfeiffer, Michael Ganey, Charles Hoiberg, and Guirag Poochikian. Pharmaceutical Solids: A Strategic Approach to Regulatory Considerations, 1995.

[13] Ping Gao. Amorphous Pharmaceutical Solids : Characterization , Stabilization , and Development of Marketable. *MOLECULAR PHARMACEUTICS*, 5(6):903–904, 2008.

[14] G. Tammann, Fr. Westerhold, B. Garre, Ernst Kordes, and H. Kalsing. Chemische reaktionen in pulverförmigen gemengen zweier kristallarten. *Zeitschrift für anorganische und allgemeine Chemie*, 149(1):21–98, 1925.

[15] G.J. Creus. *Viscoelasticity : basic theory and applications to concrete structures.* Lecture notes in engineering: 16. Berlin [etc.] : Springer, 1986 copyr, 1986.

[16] C. Masciovecchio, S. C. Santucci, A. Gessini, S. Di Fonzo, G. Ruocco, and F. Sette. Structural relaxation in liquid water by inelastic UV scattering. *Physical Review Letters*, 92(25 I):1–4, 2004.

[17] Jing Zhao, Sindee L. Simon, and Gregory B. McKenna. Using 20-million-year-old amber to test the super-Arrhenius behaviour of glass-forming systems. *Nature Communications*, 4:1783–1786, 2013.

[18] Edgar Dutra Zanotto. Do cathedral glasses flow? *American Journal of Physics*, 66(5):392–395, 1998.

[19] H. Vogel. *Phys.Zeit.22*, pages 645–646, 1921. Cited By :1.

[20] Gordon S. Fulcher. Analysis of recent measurements of the viscosity of glasses. *Journal of the American Ceramic Society*, 8(6):339–355, 1925.

[21] G. Tammann and W. Hesse. Die abhängigkeit der viscosität von der temperatur bie unterkühlten flüssigkeiten. *Zeitschrift für anorganische und allgemeine Chemie*, 156(1):245–257, 1926.

[22] C. A. Angell. Formation of glasses from liquids and biopolymers. *Science*, 267(5206):1924–1935, 1995.

[23] Jeppe C. Dyre. Colloquium: The glass transition and elastic models of glass-forming liquids. *Reviews of Modern Physics*, 78(3):953–972, 2006.

[24] M.D. Ediger, C.A. Angell, and S.R. Nagel. Supercooled Liquids and Glasses. *Journal of Physical Chemistry*, 100(95):13200–13212, 1996.

[25] R. Böhmer, K. L. Ngai, C. A. Angell, and D. J. Plazek. Nonexponential relaxations in strong and fragile glass formers. *The Journal of Chemical Physics*, 99(5):4201–4209, 1993.

[26] Andrea Cavagna. Supercooled liquids for pedestrians. *Physics Reports*, 476(4-6):51–124, 2009.

[27] F. H. Stillinger. A Topographic View of Supercooled Liquids and Glass Formation. *Science*, 267(5206):1935–1939, 1995.

[28] Martin Goldstein. Viscous Liquids and the Glass Transition: A Potential Energy Barrier Picture. *The Journal of Chemical Physics*, 51(9):3728–3739, 1969.

[29] H Frauenfelder, SG Sligar, and PG Wolynes. The energy landscapes and motions of proteins. *Science*, 254(5038):1598–1603, 1991.

[30] G. Ulrich Nienhaus, Joachim D. Müller, Ben H. McMahon, and Hans Frauenfelder. Exploring the conformational energy landscape of proteins. *Physica D: Nonlinear Phenomena*, 107(2):297 – 311, 1997. 16th Annual International Conference of the Center for Nonlinear Studies.

[31] Daniel J. Lacks. Localized mechanical instabilities and structural transformations in silica glass under high pressure. *Phys. Rev. Lett.*, 80:5385–5388, Jun 1998.

[32] Dennis L. Malandro and Daniel J. Lacks. Relationships of shear-induced changes in the potential energy landscape to the mechanical properties of ductile glasses. *The Journal of Chemical Physics*, 110(9):4593–4601, 1999.

[33] T. Keyes. Dependence of supercooled liquid dynamics on elevation in the energy landscape. *Phys. Rev. E*, 59:3207–3211, Mar 1999.

[34] Pablo G Debenedetti and H Stillinger Frank. Supercooled liquids and the glass transition. *Nature*, 410(6825):259–267, 2001.

[35] C. T. Moynihan, P. B. Macedo, C. J. Montrose, C. J. Montrose, P. K. Gupta, M. A. DeBolt, J. F. Dill, B. E. Dom, P. W. Drake, A. J. Easteal, P. B. Elterman, R. P. Moeller, H. Sasabe, and J. A. Wilder. Structural Relaxation in Vitreous Materials. *Annals of the New York Academy of Sciences*, 279(1):15–35, 1976.

[36] R. Brüning and K. Samwer. Glass transition on long time scales. *Physical Review B*, 46(18):11318–11322, 1992.

[37] Giorgio Parisi and Francesco Sciortino. Structural glasses: Flying to the bottom. *Nature Materials*, 12(2):94–95, 2013.

[38] Pierre Lucas. Energy landscape and photoinduced structural changes in chalcogenide glasses. *Journal of Physics Condensed Matter*, 18(24):5629–5638, 2006.

[39] Jean-Pierre Hansen and I.R McDonald. Theory of simple liquids. *Elsevier / Academic Pres*, (November), 2006.

[40] E. R. Weeks. Three-Dimensional Direct Imaging of Structural Relaxation Near the Colloidal Glass Transition. *Science*, 287(5453):627–631, 2000.

[41] Zexin Zhang, Peter J. Yunker, Piotr Habdas, and A. G. Yodh. Cooperative rearrangement regions and dynamical heterogeneities in colloidal glasses with attractive versus repulsive interactions. *Physical Review Letters*, 107(20):1–5, 2011.

[42] Pinshane Y, Simon Kurasch, Jonathan S Alden, Ashivni Shekhawat, Alexander a Alemi, Paul L Mceuen, James P Sethna, Ute Kaiser, and David a Muller. Imaging Atomic Rearrangements in Watching Silica ' s Dance. *Science*, 342(October):3–6, 2013.

[43] Ludovic Berthier and Giulio Biroli. Theoretical perspective on the glass transition and amorphous materials. *Reviews of Modern Physics*, 83(2):587–645, 2011.

[44] Walter Kob and Hans C. Andersen. Scaling behavior in the $\beta$-relaxation regime of a supercooled lennard-jones mixture. *Phys. Rev. Lett.*, 73:1376–1379, Sep 1994.

[45] C. Patrick Royall and Stephen R. Williams. The role of local structure in dynamical arrest. *Physics Reports*, 560:1–75, 2015.

[46] Ranko Richert. Heterogeneous dynamics in liquids: fluctuations in space and time. *Journal of Physics: Condensed Matter*, 14(23):R703, 2002.

[47] P. J. Carroll and G. D. Patterson. The distribution of relaxation frequencies from photon correlation spectroscopy near the glass transition. *J. Chem. Phys.*, 82(1):9–13, 1985.

[48] M.N. Berberan-Santos, E.N. Bodunov, and B. Valeur. Mathematical functions for the analysis of luminescence decays with underlying distributions 1. kohlrausch decay function (stretched exponential). *Chem. Phys.*, 315(1–2):171 – 182, 2005.

[49] J. Colmenero, A.A. Arbe, A. Alegría, and K.L. Ngai. Q-dependence of the relaxation times of the $\alpha$-relaxation as observed by quasielastic neutron scattering. *Journal of Non-Crystalline Solids*, 172-174:229 – 233, 1994. Relaxations in Complex Systems.

[50] J. Colmenero, A. Arbe, and A. Alegría. Crossover from debye to non-debye dynamical behavior of the $\alpha$ relaxation observed by quasielastic neutron scattering in a glass-forming polymer. *Phys. Rev. Lett.*, 71:2603–2606, Oct 1993.

[51] A. Arbe, J. Colmenero, M. Monkenbusch, and D. Richter. Dynamics of glass-forming polymers: "homogeneous" versus "heterogeneous" scenario. *Phys. Rev. Lett.*, 81:590–593, Jul 1998.

[52] Aaron S. Keys, Adam R. Abate, Sharon C. Glotzer, and Douglas J. Durian. Measurement of growing dynamical length scales and prediction of the jamming transition in a granular material. *Nature Physics*, 3(4):260–264, 2007.

[53] M D Ediger. Spatially Heterogeneous Dynamics in Supercooled Liquids. *Annu. Rev. Phys. Chem.*, 51:99–128, 2000.

[54] Ludovic Berthier. Dynamic heterogeneity in amorphous materials. 42, 2011.

[55] Ludovic Berthier, Giulio Biroli, Jean-Philippe Bouchaud, Luca Cipelletti, Djamel El Masri, Denis L'Hôte, Francois Ladieu, and Matteo Pierno. Direct experimental evidence of a growing length scale accompanying the glass transition. 2005.

[56] Cristina Toninelli, Matthieu Wyart, Ludovic Berthier, Giulio Biroli, and Jean Philippe Bouchaud. Dynamical susceptibility of glass formers: Contrasting the predictions of theoretical scenarios. *Physical Review E - Statistical, Nonlinear, and Soft Matter Physics*, 71(4):1–20, 2005.

[57] Ludovic Berthier, Giulio Biroli, Jean Philippe Bouchaud, and Robert L. Jack. Overview of different characterizations of dynamic heterogeneity. *Dynamical Heterogeneities in Glasses, Colloids, and Granular Media*, 9780199691, 2011.

[58] Peter J. Lu, Jacinta C. Conrad, Hans M. Wyss, Andrew B. Schofield, and David A. Weitz. Fluids of clusters in attractive colloids. *Phys. Rev. Lett.*, 96:028306, Jan 2006.

[59] David Chandler, Juan P. Garrahan, Robert L. Jack, Lutz Maibaum, and Albert C. Pan. Lengthscale dependence of dynamic four-point susceptibilities in glass formers. *Phys. Rev. E*, 74:051501, Nov 2006.

[60] W. C. K. Poon. Colloidal Suspensions. *The Oxford Handbook of Soft Condensed Matter*, pages 793–942, 2015.

[61] H.C. Hamaker. The london—van der waals attraction between spherical particles. *Physica*, 4(10):1058 – 1072, 1937.

[62] Jacob N. Israelachvili. 14 - electrostatic forces between surfaces in liquids. In Jacob N. Israelachvili, editor, *Intermolecular and Surface Forces (Third Edition)*, pages 291 – 340. Academic Press, Boston, third edition edition, 2011.

[63] Gary L. Hunter and Eric R. Weeks. The physics of the colloidal glass transition. *Reports on Progress in Physics*, 75(6), 2012.

[64] Antti Pekka Hynninen and Marjolein Dijkstra. Phase diagrams of hard-core repulsive Yukawa particles. *Physical Review E - Statistical Physics, Plasmas, Fluids, and Related Interdisciplinary Topics*, 68(2):8, 2003.

[65] Luca Cipelletti and Eric R. Weeks. Glassy dynamics and dynamical heterogeneity in colloids. *Dynamical Heterogeneities in Glasses, Colloids, and Granular Media*, 9780199691, 2011.

[66] Tomás Pérez-Castañeda, Rafael J. Jiménez-Riobóo, and Miguel A. Ramos. Two-level systems and boson peak remain stable in 110-million-year-old amber glass. *Physical Review Letters*, 112(16):1–5, 2014.

[67] Th. M Nieuwenhuizen Luca Leuzzi. *Thermodynamics of the Glassy State*.

[68] C. Chamon, P. Charbonneau, L. F. Cugliandolo, D. R. Reichman, and M. Sellitto. Out-of-equilibrium dynamical fluctuations in glassy systems. *Journal of Chemical Physics*, 121(20):10120–10137, 2004.

[69] Tomás S. Grigera and N. E. Israeloff. Observation of Fluctuation-Dissipation-Theorem Violations in a Structural Glass. *Physical Review Letters*, 83(24):5038–5041, 1999.

[70] Jean-Philippe Bouchaud. Aging in glassy systems: new experiments, simple models, and open questions. pages 0–25, 1999.

[71] E. Bertin and J. P. Bouchaud. Dynamical ultrametricity in the critical trap model. *Journal of Physics A: Mathematical and General*, 35(13):3039–3051, 2002.

[72] Mya Warren and Joerg Rottler. Quench, equilibration, and subaging in structural glasses. *Physical Review Letters*, 110(2):1–4, 2013.

[73] M. Paluch, Z. Wojnarowska, and S. Hensel-Bielowka. Heterogeneous dynamics of prototypical ionic glass ckn monitored by physical aging. *Physical Review Letters*, 110(1):1–5, 2013.

[74] M Bellour, A Knaebel, J L Harden, F Lequeux, and J-P Munch. Aging processes and scale dependence in soft glassy colloidal suspensions. *Physical Review E*, 67(3):031405, 2003.

[75] Roberta Angelini, Laura Zulian, Andrei Fluerasu, Anders Madsen, Giancarlo Ruocco, and Barbara Ruzicka. Dichotomic aging behaviour in a colloidal glass. *Soft Matter*, 9(46):10955, 2013.

[76] F. Ianni, R. Di Leonardo, S. Gentilini, and G. Ruocco. Aging after shear rejuvenation in a soft glassy colloidal suspension: Evidence for two different regimes. *Physical Review E - Statistical, Nonlinear, and Soft Matter Physics*, 75(1):1–7, 2007.

[77] A. Barrat, R. Burioni, and M. Mézard. Ageing classification in glassy dynamics. *Journal of Physics A: Mathematical and General*, 29(7):1311–1330, 1996.

[78] Vassiliy Lubchenko and Peter G. Wolynes. Theory of aging in structural glasses. *Journal of Chemical Physics*, 121(7):2852–2865, 2004.

[79] B. M. Oliver. Sparkling spots and random diffraction. *Proceedings of the IEEE*, 51(1):220–221, Jan 1963.

[80] J. W. Goodman. Some fundamental properties of speckle*. *Journal of the Optical Society of America*, 66(11):1145, 1976.

[81] Aristide Dogariu and Rémi Carminati. Electromagnetic field correlations in three-dimensional speckles. *Physics Reports*, 559:1–29, 2015.

[82] G. Grübel, A. Madsen, and A. Robert. *X-Ray Photon Correlation Spectroscopy (XPCS)*, pages 953–995. Springer Netherlands, Dordrecht, 2008.

[83] Robert Pecora Bruce J. Berne. *Dynamic Light Scattering*. Courier Corporation, 1976.

[84] D. L. Sidebottom, B. V. Rodenburg, and J. R. Changstrom. Connecting structure and dynamics in glass forming materials by photon correlation spectroscopy. *Phys. Rev. B*, 75:132201, Apr 2007.

[85] A. Duri, D. A. Sessoms, V. Trappe, and L. Cipelletti. Resolving long-range spatial correlations in jammed colloidal systems using photon correlation imaging. *Phys. Rev. Lett.*, 102:085702, Feb 2009.

[86] B. Ruta, Y. Chushkin, G. Monaco, L. Cipelletti, V. M. Giordano, E. Pineda, and P. Bruna. Relaxation dynamics and aging in structural glasses. *AIP Conference Proceedings*, 1518(1):181–188, 2013.

[87] H. Conrad, F. Lehmkühler, B. Fischer, F. Westermeier, M. A. Schroer, Y. Chushkin, C. Gutt, M. Sprung, and G. Grübel. Correlated heterogeneous dynamics in glass-forming polymers. *Phys. Rev. E*, 91:042309, Apr 2015.

[88] W Gotze and L Sjogren. Relaxation processes in supercooled liquids. *Rep. Progr. Phys*, 55(3):241, 1992.

[89] Heiko Conrad. *Dynamics of colloids in molecular glass forming liquids studied via X-ray photon correlation spectroscopy*. PhD thesis, Fakultat fur Mathematik, Informatik und Naturwissenschaften Fachbereich Physik der Universitat Hamburg, 2014.

[90] Francsco Dallari, B.H. Kintov, Giovanna Pintori, Francesco Riboli, Flavio Rossi, C. Armellini, Maurizio Montagna, and Giulio Monaco. The structural relaxation dynamics in the glass-former $B_2O_3$ : a multi-speckle dynamic light scattering study. *Philosophical Magazine*, 96(7-9):800–808, 2016.

[91] Claudio Maggi, Roberto Di Leonardo, Giancarlo Ruocco, and Jeppe C. Dyre. Measurement of the four-point susceptibility of an out-of-equilibrium colloidal solution of nanoparticles using time-resolved light scattering. *Physical Review Letters*, 109(9):1–4, 2012.

[92] Jennifer E Ward, Damien P Kelly, and John T Sheridan. Three-dimensional speckle size in generalized optical systems with limiting apertures. *Journal of the Optical Society of America. A, Optics, image science, and vision*, 26(8):1858–1867, 2009.

[93] D Attwood, K Halbach, and K J Kim. Tunable Coherent X-rays. *Science (New York, N.Y.)*, 228(4705):1265–72, 1985.

[94] P. Schmüser, M. Dohlus, and J. Rossbach. *Ultraviolet and Soft X-Ray Free-Electron Lasers: Introduction to Physical Principles, Experimental Results, Technological Challenges*. Springer Tracts in Modern Physics. Springer Berlin Heidelberg, 2008.

[95] Friso Van Der Veen and Franz Pfeiffer. Coherent x-ray scattering. *Journal of Physics Condensed Matter*, 16(28):5003–5030, 2004.

[96] Gerhard Grübel and Federico Zontone. Correlation spectroscopy with coherent x-rays. *Journal of Alloys and Compounds*, 362(1):3 – 11, 2004. Proceedings of the Sixth International School and Symposium on Synchrotron Radiation in Natural Science (ISSRNS).

[97] Manuel Ross. *Theory*, pages 13–36. Springer International Publishing, Cham, 2016.

[98] A. Duri, D. A. Sessoms, V. Trappe, and L. Cipelletti. Resolving long-range spatial correlations in jammed colloidal systems using photon correlation imaging. *Physical Review Letters*, 102(8):1–4, 2009.

[99] Cipelletti Bissig Trappe Ballesta1 Mazoyer1. Time-resolved correlation : a new tool for studying temporally heterogeneous dynamics Time-resolved correlation : a new tool for studying. *J. Phys.: Condens. Matter*, 15:S257, 2003.

[100] S. V. Nemilov and G. P. Johari. A mechanism for spontaneous relaxation of glass at room temperature. *Philosophical Magazine*, 83(27):3117–3132, 2003.

[101] Ranko Richert. Physical aging and heterogeneous dynamics. *Physical Review Letters*, 104(8):1–4, 2010.

[102] Arthur Q. Tool. Relation between inelastic deformability and thermal expansion of glass in its annealing range*. *Journal of the American Ceramic Society*, 29(9):240–253, 1946.

[103] O S Narayanaswamy. A model of structural relaxation in glass. *J. Am. Ceram. Soc.*, 54(10):491–498, 1971.

[104] E. Wandersman, A. Duri, A. Robert, E. Dubois, V. Dupuis, and R. Perzynski. Probing heterogeneous dynamics of a repulsive colloidal glass by time resolved x-ray correlation spectroscopy. *Journal of Physics Condensed Matter*, 20(15), 2008.

[105] S V Nemilov. Physical Ageing of Silicate Glasses at Room Temperature : General Regularities as a Basis for the Theory and the Possibility of a priori Calculation of the Ageing Rate. *Glass Physics and Chemistry*, 26(6):511–530, 2000.

[106] R. Brüning and M. Sutton. Volume of $b_2o_3$ at the glass transition. *Phys. Rev. B*, 49:3124–3130, Feb 1994.

[107] P. B. Macedo, W. Capps, and T. A. Litovitz. Two state model for the free volume of vitreous b2o3. *J. Chem. Phys.*, 44(9):3357–3364, 1966.

[108] E. Rössler, A. P. Sokolov, A. Kisliuk, and D. Quitmann. Low-frequency raman scattering on different types of glass formers used to test predictions of mode-coupling theory. *Phys. Rev. B*, 49:14967–14978, Jun 1994.

[109] M.A Ramos, J.A Moreno, S Vieira, C Prieto, and J.F Fernández. Correlation of elastic, acoustic and thermodynamic properties in {B2O3} glasses. *J. Non-Cryst. Solids*, 221(2–3):170 – 180, 1997.

[110] Giovanni Carini, Giuseppe Carini, Gaspare Tripodo, Gaetano Di Marco, and Edmondo Gilioli. Elastic and anelastic properties of densified vitreous $b_2o_3$: Relaxations and anharmonicity. *Phys. Rev. B*, 85:094201, Mar 2012.

[111] D. Sidebottom, R. Bergman, L. Börjesson, and L. M. Torell. Two-step relaxation decay in a strong glass former. *Phys. Rev. Lett.*, 71:2260–2263, Oct 1993.

[112] R. Brüning and K. Samwer. Glass transition on long time scales. *Phys. Rev. B*, 46:11318–11322, Nov 1992.

[113] A. Brodin, L. Börjesson, D. Engberg, L. M. Torell, and A. P. Sokolov. Relaxational and vibrational dynamics in the glass-transition range of a strong glass former $b_2o_3$. *Phys. Rev. B*, 53:11511–11520, May 1996.

[114] Michael J. Aziz, Eric Nygren, James F. Hays, and David Turnbull. Crystal growth kinetics of boron oxide under pressure. *Journal of Applied Physics*, 57(6):2233–2242, 1985.

[115] S. Kocakuşak, K. Akçay, T. Ayok, H. J. Koöroğlu, M. Koral, Ö T. Savaşçi, and R. Tolun. Production of anhydrous, crystalline boron oxide in fluidized bed reactor. *Chemical Engineering and Processing: Process Intensification*, 35(4):311–317, 1996.

[116] J. A. Bucaro, H. D. Dardy, and R. D. Corsaro. Strain relaxation in glass by optical correlation and pressure jump relaxation. *J. Appl. Phys.*, 46(2):741–746, 1975.

[117] R. Böhmer, K. L. Ngai, C. A. Angell, and D. J. Plazek. Nonexponential relaxations in strong and fragile glass formers. *J. Chem. Phys.*, 99(5):4201–4209, 1993.

[118] R. D. Corsaro and J. Jarzynski. Thermodynamic properties of boron trioxide in the glass transition region. *J. Chem. Phys.*, 60(12):5128–5129, 1974.

[119] W. Capps, P. B. Macedo, B. O'Meara, and T. A. Litovitz. Temperature dependence of the high-frequency moduli of vitreous b2o3. *J. Chem. Phys.*, 45(9):3431–3438, 1966.

[120] John Kieffer. Mechanical degradation and viscous dissipation in $b_2o_3$. *Phys. Rev. B*, 50:17–29, Jul 1994.

[121] S. V. Nemilov. Physical ageing of silicate glasses at room temperature: The choice of quantitative characteristics of the process and the ranking of glasses by their tendency to ageing. *Glass Physics and Chemistry*, 27(3):214–227, 2001.

[122] ROBERT GARDON and O. S. NARAYANASWAMY. Stress and volume relaxation in annealing flat glass. *Journal of the American Ceramic Society*, 53(7):380–385, 1970.

[123] N. V. Surovtsev, J. Wiedersich, A. E. Batalov, V. N. Novikov, M. A. Ramos, and E. Rössler. Inelastic light scattering in B2O3 glasses with different thermal histories. *Journal of Chemical Physics*, 113(14):5891–5900, 2000.

[124] Jan Gabriel, Thomas Blochowicz, and Bernd Stühn. Compressed exponential decays in correlation experiments: The influence of temperature gradients and convection. *Journal of Chemical Physics*, 142(10), 2015.

[125] Jan Gabriel, Florian Pabst, and Thomas Blochowicz. Debye Process and $\beta$-Relaxation in 1-Propanol Probed by Dielectric Spectroscopy and Depolarized Dynamic Light Scattering. *Journal of Physical Chemistry B*, 121(37):8847–8853, 2017.

[126] L Bremer, L Deriemaeker, R Finsy, E Gelade, and J Joosten. Fiber-optic dynamic light scattering; neither homodyne nor heterodyne. *Progr. Colloid Polym. Sci.*, 93(2):230, 1993.

[127] M. A. DeBolt, A.J. Easteal, P.B. Macedo, and C.T. Moynihan. Analisis of structural relaxation in glass using heating rate data. *Journal of The American Ceramic Society*, 59(1-2):16–21, 1975.

[128] John W Cahn and John W Cahn. Critical point wetting Critical point wetting. 3667(1977), 1977.

[129] J. W. Schmidt and M. R. Moldover. First-order wetting transition at a liquid-vapor interface. *The Journal of Chemical Physics*, 79(1):379–387, 1983.

[130] D. Beysens and D. Esteve. Adsorption Phenomena at the Surface of Silica Spheres in a Binary Liquid Mixture. *PHYSICAL REVIEW LETTERS*, 54(19):2123–2126, 1985.

[131] D. Pontoni, T. Narayanan, J.-M. Petit, G. Grübel, and D. Beysens. Microstructure and dynamics near an attractive colloidal glass transition. *Phys. Rev. Lett.*, 90:188301, May 2003.

[132] A. Gambassi, A. MacIołek, C. Hertlein, U. Nellen, L. Helden, C. Bechinger, and S. Dietrich. Critical Casimir effect in classical binary liquid mixtures. *Physical Review E - Statistical, Nonlinear, and Soft Matter Physics*, 80(6):1–27, 2009.

[133] C. Hertlein, L. Helden, A. Gambassi, S. Dietrich, and C. Bechinger. Direct measurement of critical Casimir forces. *Nature*, 451(7175):172–175, 2008.

[134] Xinhui Lu, S. G J Mochrie, S. Narayanan, A. R. Sandy, and M. Sprung. How a liquid becomes a glass both on cooling and on heating. *Physical Review Letters*, 100(4):1–4, 2008.

[135] K. N. Pham. Multiple Glassy States in a Simple Model System. *Science*, 296(5565):104–106, 2002.

[136] Werner Stöber, Arthur Fink, and Ernst Bohn. Controlled growth of monodisperse silica spheres in the micron size range. *Journal of Colloid and Interface Science*, 26(1):62 – 69, 1968.

[137] Olga Iulian, Amalia Stefaniu, Oana Ciocirlan, and Anca Fedeles. Refractive Index in Binary and Ternary Mixtures With Diethylene Glycol , 1 , 4-Dioxane and Water Between 293 . 15 - 313 . 15K. *Sci. Bull., Series B,*, 72, 2010.

[138] Alessandro Martinelli. Structural and dynamical investigation of a hard-sphere colloidal glass via multispeckle photon correlation techniques. Master's thesis, University of Trento, department of Physics, 2017.

[139] Michael Kotlarchyk and Sow-Hsin Chen. Analysis of small angle neutron scattering spectra from polydisperse interacting colloids. *The Journal of Chemical Physics*, 79(5):2461–2469, 1983.

[140] Ali Nematollahzadeh, Mohammad J. Abdekhodaie, and Akbar Shojaei. Submicron nanoporous polyacrylamide beads with tunable size for verapamil imprinting. *Journal of Applied Polymer Science*, 125(1):189–199, 2012.

[141] John B Hayter and Jeff Penfold. Molecular Physics: An International Journal at the Interface Between Chemistry and Physics An analytic structure factor for macroion solutions An analytic structure factor for macroion solutions. *Molecular Physics An International Journal at the Interface Between Chemistry and Physics MOLECULAR PHYSICS*, 42(1):109–118, 1981.

[142] W. Pusey, P. N. van Megen. Phase behaviour of concentrated suspensions of nearly hard colloidal spheres. *Nature*, (320):320– 340, 1986.

[143] Chiara Caronna, Yuriy Chushkin, Anders Madsen, and Antonio Cupane. Dynamics of nanoparticles in a supercooled liquid. *Physical Review Letters*, 100(5):8–11, 2008.

[144] Luca Cipelletti, S. Manley, R. C. Ball, and D. A. Weitz. Universal Aging Features in the Restructuring of Fractal Colloidal Gels. *Physical Review Letters*, 84(10):2275–2278, 2000.

[145] J. P. Bouchaud and E. Pitard. Anomalous dynamical light scattering in soft glassy gels. *European Physical Journal E*, 9(3):287–291, 2002.

[146] B. Chung, S. Ramakrishnan, R. Bandyopadhyay, D. Liang, C. F. Zukoski, J. L. Harden, and R. L. Leheny. Microscopic dynamics of recovery in sheared depletion gels. *Physical Review Letters*, 96(22):3–6, 2006.

[147] Hongyu Guo, S. Ramakrishnan, James L. Harden, and Robert L. Leheny. Gel formation and aging in weakly attractive nanocolloid suspensions at intermediate concentrations. *Journal of Chemical Physics*, 135(15), 2011.

[148] H. Guo, J. N. Wilking, D. Liang, T. G. Mason, J. L. Harden, and R. L. Leheny. Slow, nondiffusive dynamics in concentrated nanoemulsions. *Physical Review E - Statistical, Nonlinear, and Soft Matter Physics*, 75(4):1–8, 2007.

[149] S. Busch, T. H. Jensen, Y. Chushkin, and A. Fluerasu. Dynamics in shear flow studied by X-ray Photon Correlation Spectroscopy. *European Physical Journal E*, 26(1-2):55–62, 2008.

[150] Andrei Fluerasu, Pawel Kwasniewski, Chiara Caronna, Fanny Destremaut, Jean Baptiste Salmon, and Anders Madsen. Dynamics

and rheology under continuous shear flow studied by x-ray photon correlation spectroscopy. *New Journal of Physics*, 12, 2010.

[151] Andrei Fluerasu, Abdellatif Moussad, Anders Madsen, and Andrew Schofield. Slow dynamics and aging in colloidal gels studied by x-ray photon correlation spectroscopy. *Physical Review E - Statistical, Nonlinear, and Soft Matter Physics*, 76(1):3–6, 2007.

[152] R. Angelini and B. Ruzicka. Non-diffusive dynamics in a colloidal glass: Aging versus rejuvenation. *Colloids and Surfaces A: Physicochemical and Engineering Aspects*, 483:316–320, 2015.

[153] Roberta Angelini, Emanuela Zaccarelli, Flavio Augusto De Melo Marques, Michael Sztucki, Andrei Fluerasu, Giancarlo Ruocco, and Barbara Ruzicka. Glass-glass transition during aging of a colloidal clay. *Nature Communications*, 5(May):1–7, 2014.

[154] Pintori Giovanna. *Relaxation dynamics in borate glass formers probed by photon correlation at the microscopic and macroscopic length scale.* PhD thesis, University of Trento, 2017.

[155] B. Ruta, G. Baldi, Y. Chushkin, B. Rufflé, L. Cristofolini, A. Fontana, M. Zanatta, and F. Nazzani. Revealing the fast atomic motion of network glasses. *Nature Communications*, 5(May), 2014.

[156] B. Ruta, F. Zontone, Y. Chushkin, G. Baldi, G. Pintori, G. Monaco, B. Rufflé, and W. Kob. Hard X-rays as pump and probe of atomic motion in oxide glasses. *Scientific Reports*, 7(1):1–8, 2017.

[157] Pinshane Huang, Simon Kurasch, Jonathan Alden, Ashivni Shekhawat, Alexander Alemi, Paul McEuenand James Sethna, Ute Kaiser, and David Muller. Imaging Atomic Rearrangements in Watching Silica's Dance. *Science*, 342(October):3–6, 2013.

[158] Randall E. Youngman and Josef W. Zwanziger. Network modification in potassium borate glasses: Structural studies with nmr and raman spectroscopies. *The Journal of Physical Chemistry*, 100(41):16720–16728, 1996.

[159] Peter A.V Johnson, Adrian C Wright, and Roger N Sinclair. A neutron diffraction investigation of the structure of vitreous boron trioxide. *Journal of Non-Crystalline Solids*, 50(3):281 – 311, 1982.

[160] G. E. Jellison Jr., L. W. Panek, P. J. Bray, and G. B. Rouse Jr. Determinations of structure and bonding in vitreous b2o3 by means of b10, b11, and o17 nmr. *The Journal of Chemical Physics*, 66(2):802–812, 1977.

[161] Guillaume Ferlat, Thibault Charpentier, Ari Paavo Seitsonen, Akira Takada, Michele Lazzeri, Laurent Cormier, Georges Calas, and Francesco Mauri. Boroxol rings in liquid and vitreous $b_2o_3$ from first principles. *Phys. Rev. Lett.*, 101:065504, Aug 2008.

[162] J. Swenson, L. Börjesson, and W. S. Howells. Structure of borate glasses from neutron-diffraction experiments. *Phys. Rev. B*, 52:9310–9319, Oct 1995.

[163] Jianhui Zhong and P.J. Bray. Change in boron coordination in alkali borate glasses, and mixed alkali effects, as elucidated by nmr. *Journal of Non-Crystalline Solids*, 111(1):67 – 76, 1989.

[164] L. Hong, V.N. Novikov, and A.P. Sokolov. Is there a connection between fragility of glass forming systems and dynamic heterogeneity/cooperativity? *Journal of Non-Crystalline Solids*, 357(2):351 – 356, 2011. 6th International Discussion Meeting on Relaxation in Complex Systems.

[165] Odile Majérus, Laurent Cormier, Georges Calas, and Brigitte Beuneu. Temperature-induced boron coordination change in alkali borate glasses and melts. *Physical Review B - Condensed Matter and Materials Physics*, 67(2):1–7, 2003.

[166] G.D. Chryssikos, J.A. Duffy, J.M. Hutchinson, M.D. Ingram, E.I. Kamitsos, and A.J. Pappin. Lithium borate glasses: a quantitative study of strength and fragility. *Journal of Non-Crystalline Solids*, 172-174:378 – 383, 1994. Relaxations in Complex Systems.

[167] Manuel Ross, Markus Stana, Michael Leitner, and Bogdan Sepiol. Direct observation of atomic network migration in glass. *New Journal of Physics*, 16, 2014.

# Acknowledgements

First of all I want to say thanks to my parents and my sister, to have supported me in all these past years.
To my colleagues of the SDSC group, Giulio Maurizio, Aldo, Giacomo, Flavio, Giovanna.
A great thanks also to all the friends that I found here in Trento: Diana, Carmelo, Giacomo, Paolo, Martino, Fabrizio, Federico, Alessandro, Marco and all the fellow PhD students.
Another thanks goes also to the noisy crew of my flatmates during these years, in particular to Gabri, Otta, Elisa, Marzia, Nick, Angelo, Selma, Gregor, Sudipan, Salah, Kos and Willy.
And last but not least, to all mi old friends back in Sassuolo.